DOKUZ EYLÜL UNIVERSITY

GRADUATE SCHOOL OF NATURAL AND APPLIED SCIENCES

FINITE ELEMENT MODEL UPDATING AND DAMAGE IDENTIFICATION OF REINFORCED CONCRETE FRAMES WITH DIFFERENT INFILLS AND UNREINFORCED MASONRY WALLS

by

Umut YÜCEL

August, 2020

İZMİR

FINITE ELEMENT MODEL UPDATING AND DAMAGE IDENTIFICATION OF REINFORCED CONCRETE FRAMES WITH DIFFERENT INFILLS AND UNREINFORCED MASONRY WALLS

A Thesis Submitted to the
Graduate School of Natural and Applied Sciences of Dokuz Eylül University
In Partial Fulfillment of the Requirements for the Degree of Doctor of Philosophy in Civil Engineering, Structural Engineering Program

by

Umut YÜCEL

August, 2020

İZMİR

Ph.D. THESIS EXAMINATION RESULT FORM

We have read the thesis entitled **"FINITE ELEMENT MODEL UPDATING AND DAMAGE IDENTIFICATION OF REINFORCED CONCRETE FRAMES WITH DIFFERENT INFILLS AND UNREINFORCED MASONRY WALLS"** completed by **UMUT YÜCEL** under supervision of **PROF. DR. ÖZGÜR ÖZÇELİK** and we certify that in our opinion it is fully adequate, in scope and in quality, as a thesis for the degree of Doctor of Philosophy.

Prof. Dr. Özgür ÖZÇELİK

Supervisor

Prof. Dr. Serap KAHRAMAN

Thesis Committee Member

Asst. Prof. Dr. Mehmet Emre ÇEK

Thesis Committee Member

Prof. Dr. Oğuz Özgür EĞİLMEZ

Examining Committee Member

Assoc. Prof. Dr. Cemalettin DÖNMEZ

Examining Committee Member

Prof. Dr. Özgür ÖZÇELİK
Director
Graduate School of Natural and Applied Sciences

ACKNOWLEDGEMENTS

Studies carried out within this thesis were performed under the direction of Prof. Dr. Özgür ÖZÇELİK. His supervision, guidance, support, experience, and encouragement have been mandatory and irreplaceable for me to complete my Ph.D. study. I will always be thankful to him for his contributions to my academic growth and life experience.

I would like to thank my doctoral committee members, Prof. Dr. Serap KAHRAMAN and Asst. Prof. Dr. Mehmet Emre ÇEK. Their constructive and inspirational criticisms had an important place for the progression of my thesis. Specifically, I'm also grateful to Prof. Dr. Serap KAHRAMAN for being my temporary supervisor for one-year time.

I would like to express my great thanks to my temporary doctoral committee member Assoc. Prof. Dr. İbrahim Serkan MISIR for his support and encouragement. He did not leave any of my questions unanswered. I have benefited a lot from his experimental knowledge and experience.

I would like to thank Assoc. Prof. Dr. Sadık Can GİRGİN for his support and encouragement during my academic life. We shared the same office for a long time. He always treated me like a younger brother and helped me to overcome my problems.

Special thanks go to my best friends, Dr. Erkan DURMAZGEZER and M.Sc Özgür GİRGİN. I feel lucky to have the opportunity to work with these valuable people. Their friendship and support are invaluable to me. By this time, we have overcome many challenges and have accomplished lots of things. I believe that our collaboration will continue, and we will work together again in the future to succeed in many things.

I would like to state my thanks to Dr. Özgür BOZDAĞ for his patience against my everlasting questions. He never turned me down. I have learned a lot from his knowledge and experience.

I would like to express my thanks to my friends with whom we have shared lots of moments, Onur ÖZTÜRKOĞLU, Burak DURAN, Baran BOZYİĞİT, and Gökhan YÜCEL. Their support and encouragement had a critical role in my Ph.D. study.

I'm also grateful to Muhammed Emin DEMİRKIRAN, Onur BAŞKAYA, Üstün Can MERİÇ, Gökhan OKUDAN, Mazlum YAĞIZ, Umut CANDAN, Fahri TOKGÖZ, Filiz VARGÜN, Mustafa USLU, Bayram KAYA, Samet GÖYMEN, Duygu ŞENOL, İnci TERKAN, Egemen SÖNMEZ, and Baturay BATARLAR for their renunciant assistance during the experimental studies on the reinforced concrete frames; and to Fikret KURAN, Ercan TUNA, İsmael Bachabi YOUSSOUF, Önder DİZMAN, Beritan KAYA, Ayça AYDIN, Eren SÜLÜN, Selin ÇELEN, and Ömer ALDEMİR for their help during the tests on the unreinforced masonry walls.

Experimental studies on the reinforced concrete frames were performed by the financial support of the Scientific and Technological Council of Turkey (TÜBİTAK) under the grant #112M203 between the years 2013-2016, so I would like to express my thanks to TÜBİTAK for their support. Tests on the unreinforced masonry walls were conducted by the financial supports of the Disaster & Emergency Management Presidency of Turkey (AFAD) and National Earthquake Research Program (UDAP) under the grant #UDAP-Ç-16-05, and by the technical support of the Turkish Republic Directorate General of Foundations (VGM), so I would like to state my thanks to AFAD, UDAP, and VGM for their support.

Finally, I would like to express my great thanks to my family, Sevda, Alaattin, and Yonca Gamze YÜCEL for their endless love, encouragement, support, and guidance. They have always been by my side whenever I needed them. Additionally, I'm also thankful to my aunt Gülten YÜCEL for all her efforts on me since my childhood.

Umut YÜCEL

FINITE ELEMENT MODEL UPDATING AND DAMAGE IDENTIFICATION OF REINFORCED CONCRETE FRAMES WITH DIFFERENT INFILLS AND UNREINFORCED MASONRY WALLS

ABSTRACT

In recent years, finite element model updating (FEMU) methods have become attractive and popular tools that are used for finite element model verification and health condition assessment of civil engineering structures. In this thesis, system and damage identification studies conducted on half-scale, single-bay, single-story three reinforced concrete frames with different infill conditions are presented. The frames were tested along their in-plane directions under gradually increasing quasi-static cyclic loading. At predetermined drift levels (damage states), ambient vibration and white-noise tests were performed on the frames for the purpose of identifying their modal parameters by using three different output-only system identification methods. The modal identification results were correlated with detailed visual damage inspections made during quasi-static tests and were later used for damage identification of the frames by sensitivity-based FEMU method. At each progressively increasing damage state, stiffness reduction factors of the predetermined model parameters were obtained by minimizing the discrepancies between experimentally and numerically identified modal parameters. Comparative studies were carried out for the frames at different damage states in terms of system and damage identification results. In the final part of the thesis, system identification and model calibration work of the unreinforced masonry courtyard walls of the historical Isabey Mosque are presented. Dynamic characteristics of the structure were estimated from two sets of ambient vibration measurements. In order to obtain a much better correlation with in-situ tests, the uncertain model parameters of the initial numerical model were updated. Finally, a damage scenario study was performed on the calibrated numerical model.

Keywords: Reinforced concrete frame, infill wall, masonry structure, quasi-static cyclic test, system identification, model updating, damage identification

FARKLI DOLGULU BETONARME ÇERÇEVELERİN VE DONATISIZ YIĞMA DUVARLARIN SONLU ELEMANLAR MODELİ GÜNCELLEMESİ VE HASAR TANIMLAMASI

ÖZ

Son yıllarda, sonlu elemanlar modeli güncelleme yöntemleri (FEMU), inşaat mühendisliği yapılarının sonlu elemanlar modeli doğrulaması ve sağlık durumu değerlendirmesi için kullanılan ilgi çekici ve popüler araçlar haline gelmiştir. Bu tezde, farklı dolgu koşullarına sahip yarım ölçekli, tek açıklıklı, tek katlı üç adet betonarme çerçeve üzerinde yapılan sistem tanımlama ve hasar tespit çalışmaları sunulmuştur. Çerçeveler, kademeli olarak artan yarı-statik döngüsel yükleme altında düzlem içi doğrultuları boyunca test edilmiştir. Önceden belirlenmiş ötelenme seviyelerinde (hasar durumlarında), çerçevelerin üç farklı sadece-çıktı sistem tanımlama yöntemi kullanılarak modal parametrelerini belirlemek amacıyla ortamsal titreşim ve beyaz-gürültü testleri yapılmıştır. Modal tanımlama sonuçları, yarı-statik testler sırasında yapılan detaylı gözlemsel hasar incelemeleri ile ilişkilendirilmiş ve ardından çerçevelerin duyarlık-tabanlı FEMU yöntemi ile hasar tespiti için kullanılmıştır. Her bir gittikçe artan hasar durumunda, deneysel ve sayısal olarak belirlenen modal parametreler arasındaki farklılıklar minimize edilerek, önceden belirlenmiş olan model parametrelerin rijitlik azalma faktörleri elde edilmiştir. Farklı hasar durumundaki çerçeveler için sistem tanımlama ve hasar tespit sonuçları açısından karşılaştırmalı çalışmalar yapılmıştır. Tezin son bölümünde, tarihi İsabey Cami'sinin donatısız yığma avlu duvarlarının sistem tanımlama ve model kalibrasyon çalışmaları sunulmuştur. Yapının dinamik karakteristiği, iki ortamsal titreşim ölçümü setinden tahmin edilmiştir. Yerinde yapılan testlerle çok daha iyi bir korelasyon elde edebilmek üzere, ilk sayısal modelin belirsiz model parametreleri güncellenmiştir. Son olarak, kalibre edilmiş sayısal model üzerinde hasar senaryosu çalışması yapılmıştır.

Anahtar kelimeler: Betonarme çerçeve, dolgu duvar, yığma yapı, yarı-statik döngüsel test, sistem tanımlama, model güncelleme, hasar tespiti

CONTENTS

Page

LIST OF FIGURES

Page

LIST OF TABLES

CHAPTER ONE
INTRODUCTION

1.1 Introduction

In recent years, structural health monitoring (SHM) has become an attractive and popular tool for assessing the current states (i.e., health conditions) of civil engineering structures. After a damaging event like a natural disaster (e.g., earthquake, hurricane, etc.) or a human-made effect (e.g., explosion, fire, etc.), there exist many structures to be evaluated for safety purposes and the time is not abundant to give sound decisions about their states. In addition, rapid and reliable damage identification and classification are very important also for planning disaster relief operations.

Damage identification methods can be divided into four grades according to their development levels: (i) Level-I methods: those can detect the existence of damage, (ii) Level-II methods: those can detect the existence and location of damage, (iii) Level-III methods: those can detect the existence, location, and severity of damage, and (iv) Level-IV methods: those can detect the existence, location, and severity of damage together with the remaining life (prognosis) of the structure (Amani et al., 2007; Rytter, 1993; Park, 1997; Park et al., 2006; Stubbs et al., 2000).

There are many methods to determine the current states of the structural systems. The predominant method is the visual inspection method which is manual and subjective. However, the visual inspection method is insufficient and misleading as structural elements are often covered by non-structural elements like facades and walls. Another common method is the localized experimental method (e.g., acoustic, magnetic field, ultrasonic, eddy-current, thermal field, and radiograph methods) which focuses on the detection of localized damage and requires the approximate damage locations to be known. Recent developments have revealed that tracking changes in vibration characteristics of structural systems can be used for SHM purposes. These types of methods, which are more reliable and more objective than former ones, are known as vibration-based SHM methods.

In general, damage can be defined as the changes that affect the dynamic characteristics and performances of structural systems. It alters mass, stiffness, boundary condition, and energy dissipation properties. These effects result in detectable changes in the vibration characteristics of structural systems. Detecting these changes underlies the principles of the vibration-based SHM methods (Doebling et al., 1998; Farrar & Lieven, 2007; Sohn et al., 2003).

Vibration-based SHM is an essential tool that can be employed for performance assessment of existing structures, damage detection, and evaluation of structures before and after retrofit. It includes continuous and/or in different time monitoring of structural systems by using sensors, system identification by collected dynamic data, and assessing the present states of structures by extracting the damage sensitive properties from system identification results.

In literature, there exist different vibration-based damage identification methods based on damage index, Bayesian probabilistic approach, control theory, modal strain energy, and finite element model updating (Chase et al., 2005; Mottershead & Friswell, 1993; Shi & Law, 1998; Sohn & Law, 1997; Stubbs et al., 1992). In the scope of this thesis, only the finite element model updating (FEMU) based method is discussed.

FEMU method, which can be classified as a Level-III damage identification method, is basically based on updating numerical models of systems according to their experimental responses (mostly the system identification results). The method is also a powerful instrument that can be utilized to verify and/or calibrate the initial finite element (FE) models of systems developed under various assumptions and simplifications.

1.2 Literature Review

System identification of different types of engineering structures has been studied for a long time by many researchers. Some of them are briefly reviewed below.

He et al. (2009) performed dynamic field tests on a long-span suspension bridge, Alfred Zampa Memorial Bridge, located in San Francisco. This was one of the unique dynamic identification studies since the dynamic tests were conducted just before the bridge opening to traffic; so, no previous seismic excitation or traffic loadings were presented. Accordingly, forced vibration and ambient test data were processed with three modal identification techniques, namely MNEXT-ERA, SSI, and EFDD. The forced vibration tests were conducted by the application of vehicle-caused impact loading and controlled traffic effects. Identified vibration frequencies and mode shapes were found to be in good agreement for each type of test; however, damping ratios estimated by the use of forced vibration test data were higher than the ones estimated by ambient vibration test data. In addition, the estimation uncertainty of the damping ratios was higher than that of the vibration frequencies. Finally, the identification results were compared with the analytical results obtained from the 3-D FE model of the structure. Results were found to be in good agreement for a few contributing modes to the measured vibration of the bridge.

Magalhaes et al. (2012) performed a comprehensive system identification study on multi-span cable-stayed bridge Millau Viaduct located in southern France. In the study, two different dynamic test data were collected, namely ambient vibration and free vibration conducted by the sudden rupture of mass linking to deck member. In the study, the focus was to indicate the effectiveness of the ambient vibration testing performed for the in-service bridge and compare the modal identification results extracted by different methods and types of data. SSI-COV and p-LSCF methodologies were used for modal parameter identification. Moreover, the extracted vibration frequencies and mode shapes were correlated with the estimates of the developed numerical model. It was reported that ambient vibration testing enabled to identify more than twenty vibration frequencies and mode shapes. In addition, it provided damping ratio estimations in good agreement with ones obtained from the less practical and economical free vibration tests. Eventually, the efficiency of ambient vibration testing was revealed.

Astroza et al. (2016a) performed a comprehensive modal parameter identification study on a full-scale, 5-story R/C building which was tested on the NEES-UCSD shake table. The structure was exposed to a sequence of real earthquake excitations and between the seismic tests, white-noise dynamic test data were collected. These data were later used in five different system identification techniques (i.e., two input-output and three output-only techniques) in order to identify the modal parameters of the structure. The natural frequencies and mode shapes estimated by different identification techniques were found to be in good agreement, whereas the damping ratios exhibit higher variability. Besides, it was reported that the frequency and damping estimations were amplitude dependent. The global stiffness of the structure at each incremental damage level was calculated by using the identified natural frequencies, and the stiffness was found to be consistent with the reduction of the frequency of the first longitudinal mode. In this study, detailed visual inspection results of damage between the seismic tests were also reported and correlated with the system identification results. The identified modal parameters at different damage levels supplied information for finite element model updating based damage identification studies.

Finite element model updating and damage identification of different types of engineering structures have been studied for a long time by many researchers. Some of them are briefly reviewed below. Note that these studies also include system identification of the relevant structures.

Teughels & De Roeck (2004) used the FEMU technique for damage identification study of Z24 bridge located in Switzerland. Their study was based on the minimization of an objective function created by the discrepancies of the modal parameters obtained from the numerical model and experiments. Accordingly, damage was reflected by stiffness reduction factors of the structural members and identified by calibrating the numerical model. In this study, Gauss-Newton optimization method was used, and it was made more robust by the implementation of the trust region algorithm. Eighty-two 3-D elements were used in modeling of the girder, whereas forty-four elements were used in modeling of the abutments, columns, and piers. Moreover, the influence

of the soil was also taken into account by spring assignments. The study was performed in two subsequent steps: (i) Updating the initial numerical model to obtain the reference model and, (ii) updating the reference model for damage identification. The stiffness distribution of the bridge was approximated by damage functions which were useful to reduce the unknown parameters and improve the condition of the problem definition. Accordingly, the damage identification study was performed by updating Young's and shear moduli of the structural elements by using eight damage functions. As a result, realistic damage patterns were identified and good correspondence with the results of the direct stiffness calculation method was acquired. For both the undamaged and damaged bridge cases, the modal characteristics of the updated numerical model corresponded well with their experimental counterparts.

Bakir et al. (2007) performed sensitivity-based finite element model updating method using a trust region algorithm on a planar 4-story, 3-bay R/C frame where the stiffness values of the beam members near column-beam joints were numerically reduced in a damage scenario. Numerical model of the frame was developed according to strong column-weak beam approach, and the elements located at the beam ends, where the plastic hinges are expected to occur, were updated. The study was performed using eigenfrequency and eigenmode residuals. It was shown that the relative eigenfrequency differences and the MAC values improved after model updating and the predefined damages were accurately obtained by the updating algorithm. The algorithm was also examined in the existence of two noise levels in simulated measurement data in order to verify the robustness of the damage identification method. The updating algorithm was found to be promising in the existence of high noise level since it predicted most of the predefined damages with high accuracy.

Fang et al. (2008) applied the sensitivity-based FEMU method for damage identification study of an R/C planar frame. The method presented in this study is based on the minimization of the discrepancies calculated between experimentally identified and numerically obtained modal parameters. Bi-dimensional damage functions, which resulted in a significant enhancement of the optimization performance, were used in the updating process. The study was performed with two

subsequent steps: (i) The reference numerical model of the undamaged structural system was separated by a few damage functions so as to detect possible damage locations in a coarse manner and, (ii) the damaged parts were partitioned with finer damage functions for an accurate damage identification study. Moreover, a static based R/C damage model was proposed for remnant stiffness estimation of cracked segments and the results obtained using this method were later compared with the model updating based results. The bi-dimensional damage functions were found to be beneficial for a well-conditioned optimization problem. It was stated the updating method could detect the damage state of the structural system. In addition, the damage model approach was verified against the updating results and it was found to be feasible to estimate the remnant bending stiffness of a cracked R/C beam segment.

Weber et al. (2009) offered to apply known regularization techniques to have a better reliable and accurate model updating algorithm. Accordingly, two known techniques, truncated singular value decomposition and Tikhonov regularization were implemented in conjunction with the updating algorithm. It was emphasized that without using them, measurement errors may result in convergence problems. The effectiveness of the presented techniques was shown both on the numerical and experimental nonlinear model updating studies. In the numerical study, it was indicated that the offered techniques greatly improved the performance of the algorithm. In the final part of the presented study, damage identification studies of the laboratory tested 3-D, 2-story, 1-bay R/C structural frame subjected to incremental earthquake levels were performed using six design variables. Elements located on the beam-column joints, where the damage is most expectedly to occur, were selected as updating parameters and damage identification results were presented in terms of stiffness reductions of them. In this research work, the sensitivity values of the modal parameters with respect to design variables were also shown. It was demonstrated that both regularization techniques gave similar results. In addition, the identified stiffness reduction factors compared well with the damage observations.

Chen et al. (2011) performed analytical and experimental system identification studies on Guangzhou TV Tower in China. Accordingly, a very complicated system

including over 800 sensors was mounted on the structural system for both in-construction and in-service real-time monitoring; so, the ambient vibration testing was realized by long-term continuous monitoring. Modal parameters of the tower were extracted by SSI and EFDD methods. In this study, the analytical and experimental system identification works of the structure and the ambient vibration measurements at various construction stages and under various excitation conditions principally addressed these four topics: (i) a reduced order FE model for the tower by model updating, (ii) ambient vibration testing and modal parameter estimation of the tower under construction and two different environmental excitations such as earthquake and typhoon, (iii) comparing the findings from various excitation circumstances, and (iv) correlation study between air temperature and dynamic properties of the tower by the usage of linear regression analysis. In this study, a better baseline numerical model of the structural system was obtained for further SHM and damage identification studies. Besides, a linear relationship was observed between the vibration frequency estimations and air temperature.

Ji et al. (2011) carried out a set of full-scale tests on a high-rise steel building by using the E-Defense shake table facility to simulate a realistic damage scenario. The structure was densely instrumented with acceleration sensors, whereas the local and global deformations of the structure were also recorded extensively. During the tests, beam-column joints, non-structural walls, and concrete slabs were damaged. Floor accelerations were processed with the autoregressive exogenous term and FRF curve fitting methods to estimate the dynamic characteristics of the building. The application of three successive excitations to the structure resulted in reductions for natural frequencies, whereas no remarkable change in mode shapes was observed. Herein, mode shapes did not alter much since the damage was distributed in the beam ends at multiple levels over height. Two simplified FE models, the shear spring model and the fishbone model, were also used to ensure more information about the variances in dynamic characteristics of the structure. The shear spring model gave natural frequencies that were different from those obtained from experimental studies due to the bending effect of the lower steel frame. On the other hand, a reasonable FE model was obtained by the fishbone model since it was able to simulate both shear and

bending behavior of the structural system. Consequently, the modal analysis of the fishbone model ensured admissible correspondence with the experimental results.

Moaveni et al. (2013) presented a damage identification study based on finite element model updating of a 3-story, 2-bay masonry infilled R/C frame. Damage was progressively given to the structure by the UCSD-NEES shake table using scaled historical earthquake records of incremental severity. Between different damage states, low-amplitude white-noise tests were performed on the structure. Modal identification work was conducted by deterministic SSI technique using input-output data. Damage identification study was performed using a reduced number of design variables; i.e., three columns and the infills in two bays for each story were treated as subgroups in itself; and the results were obtained by updating the FE model by sensitivity-based FEMU algorithm and represented in terms of stiffness loss of structural members. Two vibration frequencies and thirty-two mode shape components were employed in the updating process. The reliability of the methodology was found to be satisfactory since the results showed correspondence with the damage observations. However, it was seen that the level of identified damage did not accurately reflect the loss of structural strength. In this context, the importance of nonlinear FE model updating to predict both stiffness and damage degradations was highlighted. It was expressed that the damage factors (identified damages) were sensitive to the amplitude of the excitation, whereas their spatial distribution was not sensitive. Finally, it was highlighted that the damage identification results depend on the accuracy and completeness of the estimated modal characteristics.

Garcia-Palencia et al. (2015) studied on three-span Powder Mill Bridge with the aim of obtaining a reference baseline numerical model of the structure. The initial numerical model was developed by two-node rigid link elements in order to support the composite concrete deck-steel girders. In experiments, strain gauges, accelerometers, pressure plates, temperature sensors, and bi-axial tilt-meters were used for the instrumentation. Frequency response function based model updating technique was conducted by using the experimentally collected data. A simulation study was performed and stiffness, mass, damping parameters were obtained using noise

contaminated data. Dynamic characteristics of the bridge extracted by using in-situ dynamic test data, which were obtained by linear sweep tests, were used for experimental validation. In this study, the requirement of a numerical model that reasonably represents the real structural behavior was emphasized for a successful model updating process. For the presented method, forced-vibration tests on short-span to medium-span bridges were found to be more appropriate than the ambient tests.

Iban et al. (2015) studied on a lively steel footbridge for FEMU purpose. The initial FE model was developed in ANSYS environment by using various cross-sections for steel skeleton and but only one constant thickness element for the deck. Ambient vibration and static loading tests were conducted on the structure. First, the initial FE model was calibrated manually to match with the experimentally obtained static response by adjusting the flexibility of the joints and Young's modulus of the concrete deck. After, the manually calibrated FE model was updated in an automatic way by using FEMtools software. At this stage, mass distribution along the deck was selected for updating. Consequently, a good match was captured between the experimental and analytical results.

Masciotta et al. (2016) focused on a damage identification technique based on second-order spectral characteristics of the nodal responses. The technique was applied to the well-known case study of Z24 Bridge in Switzerland in order to validate its reliability. Assessment of the variability of this spectrum-driven technique according to both the position and type of the excitation source was performed through numerical simulation studies of the dynamic response of the bridge exposed to various excitation types. These simulations allowed building the power spectrum matrix from which the main eigen parameters of the reference and damage scenarios were identified. Next, through weighing and combining the complex eigenvectors and real-valued eigenvalues, a damage index, which uses the discrepancies between spectral modes, was calculated for damage identification purposes. The obtained results demonstrated good agreement with the numerical model. In addition, the spectrum-driven method was found to be robust in damage localization. It was stated that the method was always able to detect the existing damage.

Goksu et al. (2017) conducted forced vibration tests on two full-scale substandard R/C buildings to identify their dynamic characteristics. For each of them, dynamic test data were collected before and after the application of quasi-static lateral loading cycles given in one direction from 2nd and 3rd stories. Forced vibration tests were conducted with eccentric mass shaker using sinusoidal forces. The study primarily concentrated on the investigation of the rates of alterations in the dynamic properties of the structural system with the damage. As expected, reduction in vibration frequencies and increment in damping ratios were observed for the various modes. Besides, effective slab width and Young's modulus of concrete were updated to get a reliable numerical model. Finally, a comparison of the FE modal parameters with the ones experimentally identified was made and the results were found to be consistent with the damages observed in the tests.

Nozari et al. (2017) conducted a damage identification research on a ten-storey R/C building by finite element model updating method using ambient vibration data. Accordingly, six perimeter infill walls were removed in order to induce structural damage. Vibration data were recorded both for undamaged and damaged cases; and the data were later processed for identifying the modal parameters. The initial numerical model of the building was developed by considering the material tests and in-situ observations. This model was calibrated later by utilizing the modal characteristics representing the undamaged case to obtain a reliable reference model of the building. In this study, it was also aimed to reveal the change in damage identification results by the variation of modal parameters. Multiple reference models obtained by using forty sets of modal parameters were used for damage identification purposes since the structural model parameters were obtained with high level of variations. Damage identification study was later performed (i) by using the reference model of which the average modal parameters were used and, (ii) based on the specific reference models. The position and severity of the structural damage were detected by calibrating the equivalent stiffness parameters of the twelve wall substructures. Although the detected damages were in good agreement with the existing damages of the structure, the results were found to be sensitive to the variation of the estimated modal properties. In this context, the need to use a probabilistic framework following

a Bayesian or a frequentist approach, which considers the variability and uncertainty of the modal properties and determines the uncertainty level in the model updating results, was emphasized.

Ding et al. (2019) suggested a novel damage detection methodology by utilizing the C-TSA algorithm, which takes into account both the measurement noise and FE modeling errors. The methodology was used both on the numerical studies on benchmark functions (Sphere, Griewank, Ackley, Rastrigin, Rosenbrock, and Schaffer equations) and experimentally tested 61-bar steel truss type of structure to evaluate the robustness and accuracy of the technique. The objective function was created based on natural frequency and modal assurance criterion discrepancies. In the experimental work, a modal hammer was used to generate the impact excitation for modal parameters which were required for damage identification. The results were later compared using several latest revolutionary algorithms and the approach was found to be promising even when modeling errors and measurement noise exist. In addition, it was stated that the proposed approach was more robust with faster convergence speed.

Park et al. (2019) introduced a model updating method for damage detection purposes without the necessity of using system identification techniques for the extraction of dynamic characteristics. Accordingly, the presented method uses the modal participation ratios (MPR), which can be determined from dynamic measurements by sensors, as an indicator of the extent of modal contribution. The MPR extraction assumes that the structure under investigation is subjected to ambient vibrations and no other additional loading on the structure is required. In the model updating phase, the objecting functions established by the differences between MPRs estimated from a model and extracted from the sensors, are minimized by a multi-objective optimization technique. The effectiveness of the method was shown by a simulated shear type structure that has four DOFs; whereas MPRs were obtained using the structural response of the system subjected to white-noise excitation. Herein, damage scenario studies were also performed on the updated model (baseline model). The results indicated that the baseline model was effective in the sense of representing

modal properties and predicting the structural response. In addition, the predefined damages for the damage scenarios were accurately detected by the presented method.

Finite element model updating and damage identification of masonry structures have been studied for a long time by many researchers. Some of them are briefly reviewed below. Note that these studies also include system identification of the relevant structures.

Bayraktar et al. (2010) performed numerical modeling, dynamic testing, and finite element model updating studies on an Ottoman masonry arch bridge. The initial FE model of the bridge was established by using three structural elements, namely stone arches, side walls, and timber blocks. Material properties of these parts were determined from the literature. All the boundary conditions at the abutments and side walls were assumed to be fixed for the initial FE model. Ambient vibration tests were conducted on two setups and the vibration characteristics of the bridge were estimated from peak picking and SSI methods. The initial FE model was calibrated with the manual tuning procedure by changing only the boundary conditions at the abutments. After the model updating process, good agreement was obtained between the experimental and analytical dynamic properties.

Ramos et al. (2010) studied on structural and modal identification of two historical monuments, a church and a restored clock tower, with the aim of detecting damage at an earlier stage. The monuments were monitored with vibration, temperature, and relative air humidity sensors. For the clock tower, by using the dynamic tests performed before and after the restoration, the effectiveness of the strengthening work was revealed. The entire structure was divided into eight parts, and the FE model of the actual state (after retrofitting) was obtained by updating the Young's moduli of these parts. For the church, the boundary conditions and the Young's modulus values of the column members and the main nave were selected as updating parameters. In this study, frequency monitoring was found to be reliable for the damage identification process. The findings of the research work revealed the non-negligible effect of the humidity and the well-known effect of the temperature on the dynamic characteristics

of masonry structures. During the monitoring period, apparently no damage was detected in both structures.

Bartoli et al. (2013) performed static and dynamic tests on a monumental masonry tower. Static tests including flat-jack and laboratory tests on cored samples extracted from the multi-layered masonry walls were employed to determine the material characteristics of the tower. Dynamic vibration tests were performed under sinusoidal forces at various frequencies generated by two vibrodynes. The numerical model of the tower was established in ANSYS analysis software by using the macro modeling approach. Uncertain parameters such as the Young's modulus of the infill material between wall layers and boundary conditions offered by nearby buildings were chosen as updating parameters and they were iteratively calibrated to reduce the discrepancies between the experimental and numerical behaviors. The calibrated numerical model was a good candidate to be employed for further structural analysis to research the structural behavior of the tower under severe loading conditions.

Costa et al. (2015) worked on two old and one recently constructed stone masonry arch bridges. Initial FE models of the bridges were constituted by the usage of micro modeling strategy with solid elements and zero thickness joint elements. Material characteristics were determined from field and laboratory tests, visual inspection, and historical research. To identify the vibration characteristics of the bridges, a series of ambient vibration measurements were performed by using portable tri-axial macro-seismographs. Model calibration of the initial FE model was performed to capture better agreement between experimentally and numerically obtained dynamic characteristics. In this context, engineering judgment and trial-and-error approach were adopted instead of a sophisticated optimization algorithm. After the model calibration process, good agreement was acquired between the numerically and experimentally estimated modal parameters.

Costa et al. (2016) studied on model updating of a stone masonry arch railway bridge. The initial numerical model was established by using in-situ (e.g., flat-jack, ménard pressuremeter, and ground penetrating radar) and laboratory tests. Dynamic

tests were performed in two setups by thirty-two measurement points under ambient vibration conditions. System identification was done by EFDD method available in ARTeMIS commercial software. To identify the model parameters that were more effective on modal responses, sensitivity analyses with three different approaches were performed. For each approach, different updating parameters were selected. Then, the updating methodology was conducted by changing the elastic properties of the materials with a genetic algorithm for a reliable bridge model Comparing with the initial numerical model, the updated numerical model demonstrated considerable improvements in modal parameters. The results indicated a trend of reducing the stiffnesses of structural members of the bridge which was compatible with the visual observation studies. The updated (reliable) numerical model was planned to be used for dynamic behavior assessment of the train-tack coupled system.

Cabboi et al. (2017) performed a damage assessment process on a historical masonry tower. Two series of ambient vibration test data were measured in fifteen selected locations. System identification was performed by SSI-DATA method available in ARTeMIS software. In the modeling stage, the tower was separated into two different partitions with a constant Young's modulus value for each partition, the footing was assumed as fixed, and the effect of the nearby church was simulated by elastic springs. Young's modulus, shear modulus, and elastic springs were calibrated for a reliable baseline FE model. By using this baseline model, two damage scenarios were simulated. In this study, the damage identification analysis was found to be sensitive enough to detect the damage scenarios.

Compán et al. (2017) worked on the structural safety assessment of a historical chapel. Dynamic properties of the chapel were extracted from ambient vibration data collected by eight uni-axial accelerometers. Tests were realized in twenty-five setups and fifty-one measuring points. For the system identification, EFDD and SSI methods implemented in ARTeMIS software were used. The initial FE model was developed by solid elements in ABAQUS software. This model consisted of two main components, namely the walls and vaults. Material properties were determined from the literature. Connections between the chapel and nearby building were considered

by spring elements. Young's moduli of masonry stone and masonry brick, connections represented by springs, and the inertial mass of the nearby building were selected as updating parameters in order to calibrate the initial FE model. Herein, the dynamic characteristics of the FE model were adjusted to the experimental results. Once the calibrated model was obtained, it was utilized to perform structural safety analyses and to estimate the collapse load of the structure.

Conde et al. (2017) worked on masonry arch bridges for model updating purposes. Laser scanning, ground penetrating radar, and sonic tests were performed to determine the mechanical characteristics. The macro modeling strategy was adopted by assigning homogeneous material having equivalent mechanical properties. Thus, the entire FE model was constituted by five main structural partitions. Boundary conditions were represented by fixed supports at the base of the bridge, whereas only the movements in transverse and longitudinal directions were restrained at both sides of the bridge. Ambient vibration measurements were carried out by three portable tri-axial macro-seismographs having GPS time synchronization. Tests were performed in twelve setups because of the limited number of measurement equipments, and each setup was designed by keeping one of the macro-seismographs as reference (i.e., was kept fixed) and roving the others. Dynamic data were processed using EFDD method by ARTeMIS software. Only the Young's moduli of the prescribed structural partitions were selected as updating parameters for model updating purposes. After model updating, satisfactory results were obtained for the frequencies and mode shapes of the first four modes. The updated FE model of the bridge was used to perform detailed structural assessment analyses under various conditions. Results exhibited the remarkable effect of tensile nonlinear properties of masonry and the vital role of the fill materials on the performance of the structural system. Finally, the importance of three-dimensional modeling was emphasized since the constituted numerical model enabled to capture the critical transverse effects in the response of the structure.

Torres et al. (2017) focused on the model updating study for the finite element model of a masonry cathedral. Ambient vibration tests were realized in twenty-two setups to cover the entire structure, and two reference measurement devices were used

in all setups. Modal analysis was performed by EFDD and SSI methods in ARTeMIS software. Material characteristics of the structure were described as representative values, neglecting the high variability in different zones. Thus, three main materials were defined for the entire structure, namely the Young's moduli of brick masonry, stone masonry, and reinforced masonry. Besides, boundary conditions, caused by adjacent structures, were represented by elastic elements. In order to determine the boundary conditions and initial material features, a preliminary updating procedure was conducted. Afterwards, the Young's modulus values for the main materials were calibrated within physical intervals. The updated finite element model allowed to conduct structural behavior assessment in the current condition and possible future research scenarios.

Altunisik et al. (2018) performed FE model updating on a historical masonry bastion. Ambient vibration measurements were carried out by eight uni-axial accelerometers. Dynamic characteristics were extracted by EFDD and SSI techniques. The initial FE model was established with ANSYS software by using four main components such as steel columns, R/C floors, masonry walls, and masonry arches and vault. Characteristics of these components were determined from the literature. Boundary condition at the base was assumed to be fixed and it was excluded from the updating scheme. Manual (by trial-and-error method) and automated (by an optimization algorithm embedded in FEMtools software) updating procedures were used to obtain a calibrated FE model. In this context, material properties such as Young's modulus and density were adjusted. The automated model updating procedure was performed by using local and global parameter approaches. After model updating, the discrepancies between the numerical and experimental dynamic properties were considerably reduced, and a calibrated FE model was obtained for SHM purposes.

Bassoli et al. (2018) studied on a medieval fortress which had suffered severe damage due to seismic events. Ambient vibration measurements were performed by ten uni-axial accelerometers to determine the dynamic properties of the damaged structural system. The FE model was constituted by considering a non-standard mesh

generation procedure called CLOUD2FEM. In order to take into account the influences of the damaged parts, different material characteristics were assigned to them. Model updating analyses were repeated in three stages in order to detect the damaged parts precisely. At each following stage, updating parameters were defined in more detail by using the results of the former stage. The updated numerical model of the structure was able to ensure better accuracy of modal properties and preserved the physical meaning of the updated parameters.

Ercan (2018) investigated the effects of retrofitting in a historical building comprising masonry and timber elements. 3-D solid model of the building was established in ABAQUS environment using the material properties obtained by ultrasonic pulse velocity, Schmidt Hammer, Archimedes' density test methods, and the formulas in the literature. Dynamic properties of the building were determined from ambient vibration measurements performed for both before and after retrofitting processes. Outputs of the dynamic tests were used to update the initial FE models (i.e., before and after retrofitting conditions). Here, Young's modulus and boundary conditions were chosen as updating parameters and assumed to be common for the entire structure. In addition, the updated FE models for both before and after retrofitting conditions were used to conduct earthquake performance analyses. The results demonstrated that the stiffness of the retrofitted structure increased three times with respect to the initial state. Operational modal analysis was found to be a reliable method to investigate the effects of retrofitting solutions with respect to earthquake performance of masonry structures, Besides, it was stated that the method was capable of damage identification as well as model updating of the historical structures.

1.3 Objectives and Scope

Similar to the studies in the literature, the research work presented in this thesis focuses on the topics of system identification, finite element model updating, model calibration, and damage identification studies performed on reinforced concrete (R/C) and unreinforced historical masonry structures, which represent the significant part of the building inventory in Turkey. Different from the existing state of the art, for R/C

structures, the effects of different infill conditions on system and damage identification results as a function of increasing structural damage are investigated. Herein, a novel infill wall system made of locked brick units is discussed and its efficiency is revealed comparatively.

The research work presented in this thesis mainly aims to

- perform system identification studies by different output-only system identification methods in order to identify dynamic characteristics,
- investigate the performance of different output-only system identification methods in identifying modal parameters,
- follow the evolution of the estimated modal parameters as a function of increasing structural damage,
- investigate the system identification results obtained by different excitation types and levels,
- examine the influences of different infill conditions on induced damages and modal identification results,
- correlate the modal estimation results with visual damage inspections,
- perform damage identification by using sensitivity-based finite element model updating method to identify the existence of damage, its location, and extent,
- investigate the effects of different infill conditions on damage identification results,
- perform model calibration in order to obtain numerical models that are more representative of the actual structural behavior,

- conduct damage scenario studies and identify the predefined damages.

Based on the objectives stated above, the following research work was performed in the scope of the presented thesis:

Extensive experimental studies were conducted on half-scale, single-bay, single-story three R/C frames with different infill conditions, namely bare, locked type infilled, and standard type infilled. The frames were tested along their in-plane directions under gradually increasing quasi-static cyclic loading. At predetermined drift levels (i.e., different damage states), ambient vibration and white-noise (having different excitation levels) tests were performed on the frames for the purpose of identifying their modal parameters. White-noise tests were conducted by an electro-dynamic shaker positioned on top of the frames (i.e., on the slab level). The recorded dynamic response data at different damage states were processed by using three different output-only system identification methods. The damages developed were classified by detailed visual damage inspections made during quasi-static tests, and their evolutions with respect to increasing damage levels were coupled with the corresponding modal identification results.

Damage identification of the frames at gradually increasing damage states was performed by the sensitivity-based finite element model updating method. The initial FE models of the frames were developed in MATLAB based FEDEASLab software by using 3-D Bernoulli-Euler frame elements (Filippou & Constantinides, 2004; MATLAB, 2017). Support conditions were represented by simple supports at column(s) bottom ends together with three rotational springs. Structural damages of the frames were represented by relative stiffness reduction factors. At each progressively increasing damage state, stiffness reduction factors of the predetermined model parameters were obtained by minimizing the discrepancies between experimentally and numerically identified modal parameters. The model updating process was performed in two steps: (i) first a reliable reference model was obtained by using the experimentally identified modal parameters at the undamaged state, and then (ii) the procedure was repeated by updating the reference model at each

progressively increasing damage state to identify the damage, its location, and extent. The number of model parameters used for the updating procedure was reduced to ensure a well-conditioned optimization problem by taking into account symmetry conditions, detectability indices, and internal moment levels occurred in the frame elements. The identified damage results were verified using the visual damage observations made during the quasi-static tests. A comparative study was performed for the frames at different damage states to reveal the effects of the different infill conditions.

Modal parameter identification and sensitivity-based finite element model updating studies were performed on the courtyard walls of the historical Isabey Mosque. Modal parameters of the walls were estimated from two sets of ambient vibration measurements using EFDD output-only system identification method. The initial numerical macro model was developed in ABAQUS (ABAQUS, 2017) by using the material properties obtained from the flat-jack tests and the relevant literature. Boundary conditions of the numerical model were defined through four regions by taking into account their locations. Each region was defined as translational springs in three directions. Initial stiffnesses of these springs were determined by manual updating so that a numerical model having modal parameters representative of the actual courtyard wall system was obtained. Mass density, Young's modulus, and boundary conditions (i.e., translational springs) of the initial numerical model were calibrated using a global parameter updating method. Thus, a reliable FE model that was more representative than the initial one was obtained to be used in future numerical assessment studies. Finally, a damage scenario study was performed on the calibrated numerical model, and the predefined damages were identified.

1.4 Organization of the Thesis

The presented thesis consists of seven chapters and two appendices which are organized as follows:

- In Chapter One, introduction to vibration-based structural health monitoring and literature review of the previous studies are presented. The objectives and scope of the thesis research are highlighted.

- In Chapter Two, system identification and operational modal analysis are discussed. Highlights of data acquisition and signal processing are discussed. Theoretical backgrounds of the commonly used operational modal analysis methods are presented.

- In Chapter Three, finite element model updating concept, its intended use, and commonly used methods are discussed. Theoretical background of the sensitivity-based finite element model updating method is detailed with its components. The developed model updating code is introduced, and its effectiveness is presented through numerical simulation studies.

- In Chapter Four, the experimental studies conducted on the half-scale, single-bay, single-story three R/C frames with different infill conditions are discussed. Descriptions of the frames, quasi-static test program, and dynamic tests are given. The static and dynamic test results of the frames are presented comparatively.

- In Chapter Five, damage identification studies of the R/C frames at progressively increasing damage states performed by sensitivity-based finite element model updating method are given. The results are correlated with the visual damage inspections made during quasi-static tests. The effects of different infill conditions on damage identification results are presented.

- In Chapter Six, experimental work performed on the unreinforced courtyard walls of the historical Isabey Mosque is discussed. Descriptions of the structure and dynamic test program are presented. System identification and model calibration studies conducted are detailed. A damage scenario study performed on the calibrated model is presented.

- In Chapter Seven, the overall research work is summarized, the important findings are highlighted, and some recommendations for future research are provided.

- In Appendix-1, the list of symbols that contains the symbols used throughout the thesis is presented.

- In Appendix-2, the publications made from the research work of the thesis are provided.

CHAPTER TWO
SYSTEM IDENTIFICATION & OPERATIONAL MODAL ANALYSIS

2.1 Introduction

In the most general sense, system identification is the process of constituting a mathematical model of a physical system to identify its dynamic characteristics (i.e., vibration frequencies, damping ratios, and mode shapes, a.k.a. modal parameters), whose values depend on material, geometry, and boundary properties of the system, by using experimental measurements. In the last decades, system identification methods have become attractive and popular tools for vibration-based SHM in order to assess the current states (i.e., health conditions) of engineering structures. Besides, they are also powerful instruments that can be used to verify numerical FE models developed under various assumptions (Rainieri & Fabbrocino, 2014).

System identification methods which are used in vibration-based SHM can be divided into two groups as input-output and output-only methods (Moaveni, 2007). Input-output methods, which are also known as experimental modal analysis (EMA) methods, require measuring both the excitation acting on the system and the reaction of the system to this excitation (e.g., acceleration, strain, displacement, etc.). They have been used in several areas, such as industrial machinery, aerospace engineering, civil engineering, and automotive engineering. Note that the implementation of measurable and controllable excitation is generally a difficult task that needs heavy and expensive equipments, especially for large-size systems. Therefore, the EMA methods are generally used for small and medium-size systems. In contrast, output-only methods do not require the measurement of the excitation acting on the system. Because of being large-scale, it cannot be practical and economic to excite the civil engineering structures with properly measurable excitations. In this situation, using ambient vibration effects (micro tremor, traffic, wind, etc.), that arise because of the normal usages of structures, becomes the only way to excitation. That's why using output-only methods, which are also known as operational modal analysis (OMA) methods, is more convenient for system identification in civil engineering structures

(Ozcelik et al., 2013; Rainieri & Fabbrocino, 2014). In the scope of this thesis, OMA methods are used for system identification purposes. Details are presented in the following sections.

2.2 Operational Modal Analysis (OMA)

Since the testing techniques are relatively cheap, fast, and do not affect the normal usage of the structure, OMA is very popular and attractive in civil engineering society. Moreover, the identified dynamic characteristics represent the actual structural system behavior under operational conditions (i.e., vibration levels that are not artificially generated and actually present in the structure). This means, for example, that during a bridge test, the traffic and normal operation need not be interrupted, and they can even be used as excitation sources. On the other hand, OMA testing requires low-noise and sensitive sensors, and high performance equipments due to the low vibration levels under ambient conditions. While ambient vibration tests are performed under operational conditions, the collected data are more prone to be polluted by environmental effects; therefore, longer test durations are necessary for healthy results. In return, longer data lead to complex and time-consuming analysis tasks, and storage problems (Rainieri & Fabbrocino, 2014). Since the excitation is unmeasured, it is possible to confuse its characteristics with the dynamic properties of the test specimen. Moreover, independent information in the test data is essential in order to excite vibration modes sufficiently and identify closely-spaced modes. This can be satisfied by using uncorrelated inputs (i.e., not generated by a dominant excitation source) and measurement points (i.e., data from multiple sensors measuring different degrees of freedom). Note that OMA does not provide mass-normalized mode shapes since the excitation is unmeasured. This situation causes problems for damage identification methods that require mass-normalized modes, such as flexibility-based methods. However, this limitation can be overcome by mode shape scaling approaches, such as mass change method, mass-stiffness change method, and using the FE model mass matrix (Brincker & Ventura, 2015; Rainieri & Fabbrocino, 2014).

A fundamental assumption in OMA methods is that the system to be examined is excited by a random broad-band excitation source (i.e., having white-noise characteristics), or at least band-limited white-noise (WN) characteristics. This is necessary so that the excitation does not drive the system at a specific frequency and enables various structural modes to be excited sufficiently. Accordingly, in operational cases, no need to measure the input excitation is justified by the assumption that the excitation does not contain any specific information (Sohn et al., 2003). It is possible to acquire broad-band excitation from various sources, such as ambient conditions, shake tables (or shakers), and impact hammers. If shake tables are preferred for this purpose, the trajectory tracking problem (i.e., the signal reproduction fidelity of the shake table) is a situation that has to be taken into account. Definition of the problem and the solving procedure are detailed at the end of this chapter.

Natural Excitation Technique combined with Eigensystem Realization Algorithm (NExT-ERA), Data-Driven Stochastic Subspace Identification (SSI-DATA), and Enhanced Frequency Domain Decomposition (EFDD) are the commonly used OMA methods in structural engineering applications. These methods can be categorized into two groups based on the domains they operate. From this perspective, NExT-ERA and SSI-DATA are time domain methods and EFDD is a frequency domain method. Regardless of how they are classified, these methodologies are based on the assumptions that the response of the system to a given combination of inputs is equal to the same combination of the corresponding outputs (a.k.a. linearity, which means that the system behaves within a linear range), the dynamic characteristics of the system do not change over time (a.k.a. stationarity or time-invariance, which means that the response of the system is independent of time), the sensor layout is convenient to capture the modes of interest (a.k.a. observability), and the excitation source is uncorrelated with the response of the system, having, for instance, broad-band characteristics (Brincker et al., 2001b; Brincker & Ventura, 2015; Caicedo et al., 2004; James III et al., 1993; Juang & Pappa, 1985; Rainieri & Fabbrocino, 2014; Reynders, 2012; Van Overschee & De Moor, 1996). The theoretical backgrounds of these methods are presented in the following sections.

Data acquisition and processing are the most significant stages for all experimental cases. In OMA, these are especially important since the responses are often weak. Improper decisions may cause challenges and misleading modal identification results; therefore, these sessions should be planned carefully in advance. In this context, there exist some highlights that can improve the quality of the measurements and the test results. Some of them are briefly discussed in the following sections (Brincker & Ventura, 2015; Rainieri & Fabbrocino, 2014).

2.2.1 Highlights for Data Acquisition

2.2.1.1 The Required Sensor Amount

In OMA tests, decision of the sensor amount is a critical factor. Using more than enough sensors causes economic issues. Besides, more sensor usage means more workmanship and time-consuming tasks. On the other hand, using an insufficient number of sensors may lead to missing some of the vibration modes and/or to encountering spatial aliasing problems, where the mode shapes appear very similar to each other and therefore discrimination of the modes becomes difficult (Ewins, 2000). That's why the optimum number of sensors should be carefully determined.

The easiest way to determine the required sensor amount is to investigate the rank of the spectral density (SD) matrix (i.e., the number of independent rows or columns) estimated from measurements. This process enables to determine the maximum number of modes that contribute to the response in any frequency band. For example, if only three closely-spaced modes are available in the considered frequency band, then the rank is three. If there exist four closely-spaced modes, then the rank is four, and so forth. In addition, existing noise sources have to be included in the rank calculation. Such as, if three noise sources are available along with four closely-spaced modes, then the rank becomes seven. Notice that this rank value is limited by the number of measurement points (i.e., number of used sensors), and it is required to select a higher number of measurement points than the problem rank to be able to capture all the vibration modes in the considered frequency band. Otherwise, the

closely-spaced modes can be partially hidden (i.e., only one of the modes or their combinations are revealed). In the case where the measurement points are close to each other and/or providing almost the same information, only one of the measurement points affects the rank of the matrix.

As a result, it is essential to use more measurement points (sensors) than the rank of the problem (sum of the physical modes and noise sources in the considered frequency band), and these points should be distant enough to obtain different information. In addition, no sensor should be located at node points of the modes since these points are motionless and do not include any information. For this purpose, previously developed finite element models are useful tools. In practice at least five or six sensors are recommended in OMA testing.

2.2.1.2 The Appropriate Excitation

In general, random excitation in time and space is desired for OMA tests. Let it rain on the structure, let some dogs chase some cats on it, let somebody walk on it, or let somebody drive a car on it. All of these are the examples of appropriate random excitations essential for good testing practices.

In OMA, the number of independent excitations has effects on limiting the rank of the problem (see Section 2.2.1.1). In the case where there is only one independent excitation, the rank is one. In other words, if there exists only one excitation source, then it may not possible to excite vibration modes sufficiently and identify the closely-spaced modes (i.e., only some of the modes or their combinations may be identified). Therefore, experiments with single excitation sources, such as shakers and hammers, are not recommended for OMA. Instead, multiple shakers or hammers can be used at the same time to overcome this problem. Note that using multiple excitation sources having different characteristics than broad-band (e.g., different characteristics than white-noise for shaker tests) might also result in a single excitation case. Moving loads or environmental loads, such as traffic and wind, are the other excitation options to obtain rank values larger than one. Note that this statement is valid only when the

investigated structure is large enough compared to the correlation length of the excitation, where the excitation source can be assumed to be comprised of several independent sources (e.g., wind or wave load acting on a structure). However, in the case of a small-scale structure, where the structure is small compared to the correlation length of the excitation, the number of independent excitations may be close to one due to the occurrence of correlated excitations which limits the rank of the problem. Therefore, it can be said that the larger the better, because the larger the structure, the more independent excitations occur. For small-scale structures, using a scraping or brushing equipment, which is moved around randomly and is in contact with the structure all the time, is the appropriate way for excitation. Another important point is that the investigated structure should be close enough to the excitation source in order to excite the structure in many points (e.g., traffic on a road nearby a structure); otherwise, the structure is excited by a single excitation. It should be stated that keeping the correlation length of the excitation and/or the distance to the excitation source the same as for the prototype may lead to a single excitation case for the scaled models of the structures being tested in laboratory conditions. Therefore, an adjustment should be performed on the excitation.

If the natural excitation is too small to obtain a signal of admissible magnitude (i.e., in the case of low signal-to-noise ratio), the excitation is limited to a single excitation source, or the experimental studies are conducted in laboratory conditions, a complementary artificial excitation should be used. Driving a car up and down a bridge, having people moving around inside the different stories of a building, using brushing or scraping equipments, and using multiple shakers or hammers are some of the examples of the artificial excitations. Note that the excitation method should be selected so as not to alter the dynamic characteristics of the system (e.g., if heavy traffic is used for exciting a bridge, the dynamic properties may change due to too much additional mass).

2.2.1.3 Sensor Placement

In OMA tests, generally, a limited number of sensors are used since the sensors and cables are expensive. Therefore, finding the optimum sensor placement becomes substantial in order to extract more information from the collected experimental data. In literature, there exist many criteria for determining the optimum sensor placement, such as Fisher information matrix, modal kinetic energy, information entropy, and effective independence (Guo et al., 2017; Kammer, 1991; Leyder et al., 2018; Meo & Zumpano, 2005; Papadimitriou et al., 2000; Papadopoulos & Garcia, 1998; Qureshi et al., 1980; Udwadia, 1994; Yi et al., 2012; Zhang et al., 2017). In addition, computational algorithms, such as genetic, heuristic, and meta-heuristic algorithms, have been studied by many researchers in order to enhance the efficiency, especially in the case where the number of possible sensor locations is large (Abdullah et al., 2001; Joshi & Boyd, 2009; Papadimitriou, 2004; Yao et al., 1993; Yi et al., 2012; Yuen & Kuok, 2015).

A basic way to determine the approximate optimum sensor placement is shown by Ibanez et al. (1976). In the method, first, the modal decomposition of the dynamic response $\mathbf{y}(t)$ is considered as given in Equation 2.1.

$$\mathbf{y}(t) = \mathbf{A}\mathbf{q}(t) \tag{2.1}$$

where the matrix $\mathbf{A}$ and vector $\mathbf{q}(t)$ are the true mode shapes and the true modal coordinates of the system, respectively. If the estimated modal matrix $\hat{\mathbf{A}}$ is available, the estimated modal coordinates $\hat{\mathbf{q}}(t)$ can be obtained by Equation 2.2.

$$\hat{\mathbf{q}}(t) = \hat{\mathbf{A}}^{+}\mathbf{y}(t) \tag{2.2}$$

where $\hat{\mathbf{A}}^{+}$ is the pseudo inverse of $\hat{\mathbf{A}}$. By combining Equations 2.1 and 2.2, Equation 2.3 is obtained.

$$\hat{\mathbf{q}}(t) = \hat{\mathbf{A}}^{+}\mathbf{A}\mathbf{q}(t) \tag{2.3}$$

The matrix product $\hat{\mathbf{A}}^{+}\mathbf{A}$ indicates the closeness between the estimated and true modal coordinate vectors. The closer the product $\hat{\mathbf{A}}^{+}\mathbf{A}$ is to the identity matrix, the better is the sensor placement. Since $\det(\mathbf{I})=1$, $\det\left(\hat{\mathbf{A}}^{+}\mathbf{A}\right)=1$ expression can be used to measure the deviation of $\hat{\mathbf{A}}^{+}\mathbf{A}$ from the identity matrix. $\det\left(\hat{\mathbf{A}}^{+}\mathbf{A}\right)$ can be either smaller or larger than one, therefore a positive measure of the deviation from identity can be obtained by calculating $\left|1-\det\left(\hat{\mathbf{A}}^{+}\mathbf{A}\right)\right|$. Consequently, the value of the sensor placement (V) is obtained as follows

$$\mathrm{V}=1-\left|1-\det\left(\hat{\mathbf{A}}^{+}\mathbf{A}\right)\right| \tag{2.4}$$

where the optimum sensor placement is satisfied when Equation 2.4 is close to one. To determine the $\hat{\mathbf{A}}$ matrix, a noise model is established by considering how accurately the mode shapes can be estimated (Equation 2.5).

$$\hat{\mathbf{a}}=\mathbf{a}+\{\mathrm{X_i}\} \tag{2.5}$$

In Equation 2.5, $\hat{\mathbf{a}}$ is the each of the estimated mode shapes in $\hat{\mathbf{A}}$ and $\{\mathrm{X_i}\}$ is the random vector where each of the elements is a stochastic variable with standard deviation given by Equation 2.6.

$$\sigma=\varepsilon\ \max\left(\mathrm{a_i}\right) \tag{2.6}$$

where $\mathrm{a_i}$ represents the elements of the true mode shape $\mathbf{a}$ and ε is the relative uncertainty parameter that describes different accuracies of mode shape estimation. This simple approach can be used to perform simulations considering different sensor amounts, sensor locations, and relative uncertainty parameters. By comparing the outputs of these simulations (i.e., V values of different simulations), it is possible to determine the optimum sensor amount and sensor placement.

Another commonly used way to determine the sensor placement is to evaluate the mode shapes of the developed numerical model of the system. By this way, the sensors should be placed in order to capture more modes as possible.

Since a limited number of sensors are used in OMA, sometimes it is required to perform the tests in multiple setups (therefore multiple datasets are obtained) in order to measure all the desired degrees of freedom (DOFs) of the structure in interest. Since the mode shapes are unscaled due to the unmeasured excitation and the scaling factor between the mass-normalized and unscaled mode shapes can vary from setup to setup, the mode shape estimations extracted from different setups cannot be simply combined together. In this context, some of the sensors are used as references (i.e., they are kept in the same place during all setups, reference sensors) in order to be able to assemble (merge) the mode shapes estimated by different setups, and the remaining sensors are roved progressively over the structure (i.e., roving sensors). A simple method to merge the mode shapes from different setups are described below.

Let the test is performed in D setups, and the mode shape estimations extracted from each dataset can be separated into two groups: N_{ref} components represent the common (overlapping) set of DOFs (i.e., the reference sensors) and N_{rov} components are the remaining (non-overlapping) set of DOFs (i.e., the roving sensors). The N_{ref} components of the mode shapes obtained from first and i^{th} setups are related through a scaling factor.

$$\left\{\phi^{k}_{ref,1}\right\} = \alpha^{k}_{1,i}\left\{\phi^{k}_{ref,i}\right\} \tag{2.7}$$

where $\left\{\phi^{k}_{ref,1}\right\}$ and $\left\{\phi^{k}_{ref,i}\right\}$ indicate the partitions of the k^{th} mode shape identified from the first and i^{th} setup at the N_{ref} reference DOFs, respectively, and $\alpha^{k}_{1,i}$ is the scaling factor between these mode shapes. If the number of reference sensors is larger than one, then the scaling factor can be determined by the least squares solution (Equation 2.8)

$$\alpha_{1,i}^{k} = \left\{ \left(\phi_{ref,1}^{k} \right)^{\mathrm{T}} \phi_{ref,1}^{k} \right\}^{-1} \phi_{ref,i}^{k} \tag{2.8}$$

and the total (merged) mode shape $\left\{ \phi^{k} \right\}$ is obtained by using these scaling factors as follows

$$\left\{ \phi^{k} \right\} = \begin{Bmatrix} \left\{ \phi_{ref,1}^{k} \right\} \\ \left\{ \phi_{rov,1}^{k} \right\} \\ \alpha_{1,2}^{k} \left\{ \phi_{rov,2}^{k} \right\} \\ \cdots \\ \alpha_{1,i}^{k} \left\{ \phi_{rov,i}^{k} \right\} \\ \cdots \\ \alpha_{1,D}^{k} \left\{ \phi_{rov,D}^{k} \right\} \end{Bmatrix} \tag{2.9}$$

The numbers of the reference and roving sensors are determined based on the desired spatial resolution of the mode shapes to be identified. The selection of the reference sensors should be performed so that all the modes of interest are clearly identifiable in all datasets. Sensors close to the nodes of the mode shapes are not appropriate to be reference sensors since they do not provide any information (i.e., roving sensors cannot be adequately scaled with respect to a reference sensor which is close to a node of a mode). In addition, if the considered mode shape vector has small components in the reference points, noise can significantly penetrate the scaling factor value; therefore, it is recommended to use more reference sensors as possible in order to provide a sufficient number of reasonably large mode shape components for all the modes. Additional information and methodologies to assemble the mode shape estimations from several datasets are available in the literature (Döhler et al., 2011a, 2011b; Felber, 1993; Peeters, 2000; Reynders et al., 2009).

2.2.1.4 Sampling Rate

The sampling rate or sampling frequency (i.e., the collected number of samples per second) of a test is determined based on the maximum valued vibration frequency that

wanted to be estimated from the collected data. This also states an upper limit for the frequency band of the data. For instance, if the sampling frequency is selected to be F Hz, then the collected data are limited up to F/2 Hz and does not involve any information beyond this limit (a.k.a. Nyquist frequency). Therefore, the sampling frequency should be chosen at least to be 2 times the maximum valued vibration frequency. If the sampling frequency is too low (i.e., if the data are sampled too slowly), higher frequencies than the Nyquist frequency are reflected in the interested frequency range and induce amplitude and frequency errors in the spectrum of the signal. This is known as the aliasing effect in signal processing. For example, assume that a signal involves f_c=50 Hz frequency component; when this signal is sampled at f_s=30 Hz, the frequency f_c is aliased, and the alias frequency f_a occurs as a frequency component of the signal at the absolute value of the difference between the input frequency f_c and the closest integer multiple of the sampling frequency f_s. In the present case, the alias frequency f_a=|50-2*30|=10 Hz. Note that it is difficult to distinguish the alias frequency from the actual frequency components of the signal. The only way to prevent the aliasing effect is removing all the frequency components in the analog signal that are above the Nyquist frequency by an anti-aliasing filter before the analog-to-digital conversion.

Note that some of the data acquisition systems have anti-aliasing filters that influence the frequencies in the environs of the Nyquist frequency. That's why the recommended sampling frequency should be larger than 2.4 times the higher frequency of interest. On the other hand, using very large sampling frequencies than the needed ones may cause memory and storage problems, especially for very long observation periods.

2.2.1.5 Measurement Duration

Identification problems in OMA mostly occur because of too short test data; therefore, it is beneficial to keep the test duration as long as possible. However, longer data require more memory and storage space which mean more cost. Processing this type of data is another problem due to time-consuming tasks. In this context, an

optimum measurement duration can be determined to be at least $T = 10/(\xi f_{min})$; where ξ is the modal damping factor, f_{min} is the lowest vibration frequency value in Hz, and T is the measurement duration in seconds.

2.2.2 Highlights for Signal Processing

2.2.2.1 Inspection of the Data Quality

Inspection of the test data is performed to decide whether the data are appropriate or not for OMA. Ideally, this check should be done during data collection in order to interfere and correct unwanted situations. This control stage includes checks for dropouts (i.e., large deviations towards zero), spikes (i.e., large deviations towards higher values), and clippings (i.e., signal saturation). Here, visual inspection is the commonly used method. In addition, by comparing the average and standard deviation values of the windowed data segments, it is possible to detect whether there exist undesired situations.

2.2.2.2 Detrending

Detrending is a process that compels a signal to have zero mean by removing its direct current (DC) offsets. It is significant since the DC component in the signal is not trustable due to the overabundant noise level in the low frequency region. Detrending is performed by dividing the signal into overlapping data segments and then removing the mean value of each segment. Note that each data segment should be tapered by using a window in order to minimize discontinuities between data segments and to reduce leakage (a.k.a. spectral leakage), which occurs when the signal is not periodic in the sample interval. The existence of leakage causes the energy at a certain frequency to spread to nearby frequencies and due to these additional frequency components, it becomes difficult to determine the actual frequency components of the signal in interest.

2.2.2.3 Filtering

Filtering is the process to eliminate the undesired and/or unnecessary frequency components of the signal. In general, filters are divided into two groups, such as analog and digital filters. In OMA, analog filters are only encountered as anti-aliasing filters that are applied prior to an analog-to-digital converter (i.e., digitalization). After digitalization, since everything is digital, only digital filters are used.

Digital filters can be grouped into two main types, namely the finite impulse response (FIR) filters (a.k.a. moving average filters), defined by finite impulse responses, and the infinite impulse response (IIR) filters (a.k.a. autoregressive filters), whose impulse responses are available indefinitely. The main difference between FIR and IIR filters is that the output of an FIR filter is based only on the current and past inputs, whereas the output of an IIR filter is based also on the past outputs. FIR filters are always stable (as the FIR name indicates) and have a frequency independent phase shift but need many coefficients to obtain a sharp filter cut-off. In contrast, IIR filters require a limited number of coefficients for a sharp filter cut-off (i.e., less computational demanding), whereas they have a frequency dependent phase shift. Both filter types ripple close to the cut-off frequency. Mathematical presentations for FIR and IIR filters are given in Equations 2.10 and 2.11, respectively. Here, $y(n)$ is the filtered signal, $a(k)$ represents the filter coefficients, na is the number of filter coefficients, and $x(n)$ represents the input to the filter.

$$y(n) = \sum_{k=0}^{na-1} a(k)\, x(n-k) \tag{2.10}$$

$$y(n) = \sum_{k=0}^{na} a(k)\, y(n-k) \tag{2.11}$$

In general, four filter types are commonly utilized in OMA depending on the frequency content that is intended to pass:

- Low-pass filters are defined by a single cut-off frequency and let to pass all frequency content below this cut-off frequency.

- High-pass filters are defined by a single cut-off frequency and let to pass all frequency content above this cut-off frequency.

- Band-pass filters are defined by two cut-off frequencies and let to pass all frequency content inside these cut-off frequencies.

- Band-stop filters are defined by two cut-off frequencies and let to pass all frequency content outside these cut-off frequencies.

The frequency response functions of these filters are presented in Figure 2.1 with f_1 and f_2 cut-off frequencies. In general, low-pass filters are often utilized to eliminate high-frequency components (e.g., in the case of decimation process), high-pass filters are generally preferred to remove the frequency components near DC, and band-pass filters are often employed to divide a frequency band with many modes into smaller frequency bands with a smaller number of modes in each band. Note that it is important to perform the same filtering operation on all measurement channels in the dataset, otherwise, the modal parameters are affected because of the phase and amplitude errors caused by filters.

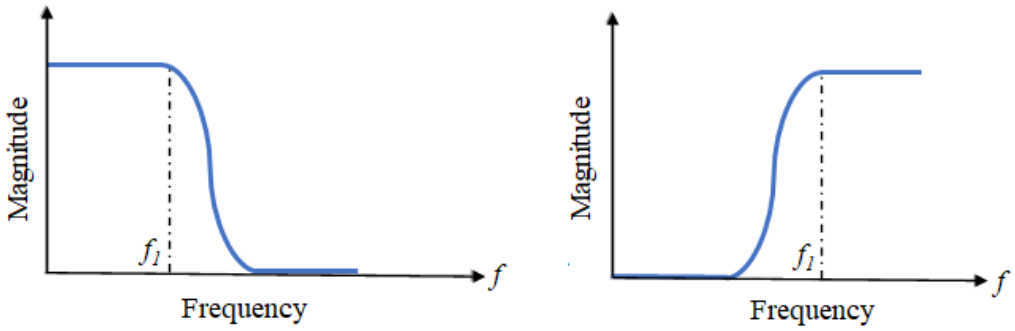

Figure 2.1 Frequency response functions of (a) low-pass, (b) high-pass, (c) band-pass, and (d) band-stop filters

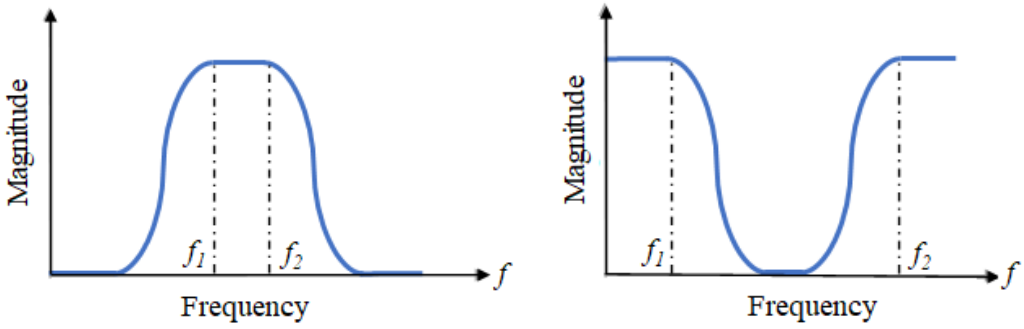

(c) (d)

Figure 2.1 continues

2.2.2.4 Down-Sampling (Decimation) and Up-Sampling (Interpolation)

A vibration test is generally performed by using a higher sampling frequency value than needed for the analysis. Therefore, resampling is required to obtain more appropriate sampling frequency which provides a better focus on the frequency bandwidth of interest. This process is called as down-sampling or decimation. Note that the energy above the new Nyquist frequency (related to the reduced sampling frequency) must be removed first by low-pass filtering in order to prevent aliasing problems. Afterwards, data omitting (e.g., every second data when reducing the sampling frequency by half, decimation factor is equal to two) can be realized without any problems. In the case of a higher resolution is desired, it is possible to increase the sampling frequency by generating new samples between the existing samples (a.k.a. up-sampling or interpolation) without any problems.

2.2.3 Review of Operational Modal Analysis (OMA) Methods

As stated before, OMA methods can be categorized into two groups based on the domains they operate (i.e., time domain and frequency domain methods). In time domain methods (e.g., NExT-ERA and SSI-DATA), analyses are performed using correlation functions that have the same characteristics with free decays. On the other hand, in frequency domain methods (e.g., EFDD), modal decomposition is realized by considering spectral density functions. It should be stated that the time domain methods are generally better conditioned than frequency domain methods due to the

influence of the powers of frequencies in frequency domain equations (e.g., spectral density estimates suffer from bias, whereas the time domain methods depend on the information that is bias-free or nearly bias-free). In addition, time domain methods enable to separate physical and noise modes from each other using stabilization diagrams. The main advantage of the frequency domain methods is considering the different frequency bands where different modes dominate (i.e., each mode has a small frequency band where it dominates), whereas the time domain methods deal with free responses that are present over the full examined time span (i.e., all the existing modes in the signal are present at any time during the considered free decay).

In the scope of this thesis, NExT-ERA, SSI-DATA, and EFDD methods are employed for modal parameter estimation. Herein, NExT-ERA and EFDD methods were programmed in MATLAB environment, and SSI-DATA method was used through a commercial software (ARTeMIS, 2016; MATLAB, 2017). In the following sections, the theoretical backgrounds of these methods are presented.

2.2.3.1 Natural Excitation Technique (NExT) Combined with Eigensystem Realization Algorithm (ERA)

The NExT-ERA modal identification method is a combination of the NExT and the ERA. NExT is the stage where the excitation data are processed to obtain a signal with the same characteristics of a free vibration data, whereas ERA is utilized to develop a numerical model of the investigated system in steady-state form based on the free vibration data obtained by the NExT. In this section, firstly the theoretical background of the NExT is presented, and then the ERA is detailed. In this sense, studies performed by Brincker & Ventura (2015), Caicedo (2011), Caicedo et al. (2004), Chang & Pakzad (2013), and Juang & Pappa (1985) are taken into account.

Consider the differential equation for a linear time-invariant (LTI) multi-degree-of-freedom system presented in Equation 2.12.

$$\mathbf{M}\,\ddot{\mathbf{x}}(t) + \mathbf{C}\,\dot{\mathbf{x}}(t) + \mathbf{K}\,\mathbf{x}(t) = \mathbf{f}(t) \tag{2.12}$$

where **M**, **C**, and **K** are the mass, damping, and stiffness matrices, respectively; $\mathbf{x}(t)$, $\dot{\mathbf{x}}(t)$, and $\ddot{\mathbf{x}}(t)$ represent the displacement, velocity, and acceleration vectors, respectively; and $\mathbf{f}(t)$ is the externally applied force vector. If it is assumed that the responses and the excitation are stationary random processes, Equation 2.13 can be written.

$$\mathbf{M}\,\ddot{\mathbf{X}}(t) + \mathbf{C}\,\dot{\mathbf{X}}(t) + \mathbf{K}\,\mathbf{X}(t) = \mathbf{F}(t) \tag{2.13}$$

where $\mathbf{X}(t)$, $\dot{\mathbf{X}}(t)$, and $\ddot{\mathbf{X}}(t)$ are the displacement, velocity, and acceleration stochastic vector processes, respectively; and $\mathbf{F}(t)$ represents the stochastic excitation vector process. Under the assumption that the system parameter matrices are deterministic, multiplying Equation 2.13 by a reference scalar response process $X_i(s)$ and taking the expected value of each side gives Equation 2.14.

$$\mathbf{M}\,E[\ddot{\mathbf{X}}(t)X_i(s)] + \mathbf{C}\,E[\dot{\mathbf{X}}(t)X_i(s)] + \mathbf{K}\,E[\mathbf{X}(t)X_i(s)] = E[\mathbf{F}(t)X_i(s)] \tag{2.14}$$

where $E[.]$ represents the expectation operator. Equation 2.14 can be rewritten as follows

$$\mathbf{M}\,\mathbf{R}_{\ddot{X}X_i}(t,s) + \mathbf{C}\,\mathbf{R}_{\dot{X}X_i}(t,s) + \mathbf{K}\,\mathbf{R}_{XX_i}(t,s) = \mathbf{R}_{FX_i}(t,s) \tag{2.15}$$

where $\mathbf{R}(.)$ indicates the correlation function vector. It should be stated that Equation 2.16 is satisfied if $\dot{A}(t)$ and $B(t)$ are stationary processes (Bendat & Piersol, 2000).

$$R_{\dot{A}B}(\tau) = \dot{R}_{AB}(\tau) \tag{2.16}$$

where $\tau = t - s$. It is possible to extend the relationship in Equation 2.16 as follows

$$R_{A^{(m)}B}(\tau) = R^{(m)}_{AB}(\tau) \tag{2.17}$$

where $A^{(m)}$ and $R^{(m)}_{AB}$ are the m^{th} derivatives of $A(t)$ and $R_{AB}(\tau)$ with respect to t and τ, respectively. Since the responses are uncorrelated to the disturbance (i.e., excitation) for $\tau > 0$, Equation 2.15 can be rewritten as follows

$$\mathbf{M}\,\ddot{\mathbf{R}}_{\mathrm{XX_i}}(\tau)+\mathbf{C}\,\dot{\mathbf{R}}_{\mathrm{XX_i}}(\tau)+\mathbf{K}\,\mathbf{R}_{\mathrm{XX_i}}(\tau)=0 \tag{2.18}$$

Equation 2.18 means that the displacement process correlation functions ($\ddot{\mathbf{R}}_{\mathrm{XX_i}}(\tau)$, $\dot{\mathbf{R}}_{\mathrm{XX_i}}(\tau)$, and $\mathbf{R}_{\mathrm{XX_i}}(\tau)$) satisfy the differential equation of motion (i.e., the correlation functions have the same characteristics as the free vibration data). Based on a similar approach, it can be said that the acceleration process correlation functions also satisfy this equation. This result is important and useful for civil engineering society since the acceleration responses of the structural systems are often measured.

In the application of NExT, one of the responses (i.e., one of the sensor channels) is chosen as a reference, and the correlation functions are computed with respect to this reference channel (i.e., denoted as $\mathrm{X_i}(s)$ in Equation 2.14). Therefore, it is essential to select a reference channel with a high signal-to-noise ratio (SNR) value and far from a node of any mode to ensure that all of the modes can be observed in the data.

In general, the ERA uses the impulse response (or the free vibration data) of a system without taking in to account the external forces. The discretized state-space representation for an LTI system is shown in Equation 2.19.

$$\begin{aligned}\mathbf{x}(\mathrm{k}+1)&=\mathbf{A}\,\mathbf{x}(\mathrm{k})+\mathbf{B}\,\mathbf{u}(\mathrm{k})\\ \mathbf{y}(\mathrm{k})&=\mathbf{C}\,\mathbf{x}(\mathrm{k})+\mathbf{D}\,\mathbf{u}(\mathrm{k})\end{aligned} \tag{2.19}$$

where $\mathbf{u}(\mathrm{k})$, $\mathbf{x}(\mathrm{k})$, and $\mathbf{y}(\mathrm{k})$ represent the vector of system inputs (i.e., forces applied to the system), the vector of states, and the vector of system outputs (e.g., acceleration measurements) at the k^{th} step, respectively. The **A**, **B**, **C**, and **D** coefficients (a.k.a. discrete-time state-space matrices) are the state, input, output, and feed-through matrices of the state-space model.

The ERA is based on the minimum realization principles to constitute a state-space representation of the system. Here, realization is the estimation process of the system

matrices (**A**, **B**, **C**, and **D**) from the response. Note that there exists an infinite number of system matrices having different dimensions that define the input-output relationship of the system. However, the case with the smallest number of states is taken into consideration (i.e., minimum realization). Since the input to the system is unknown (i.e., generally unmeasured), **B** and **D** matrices cannot be determined. Nevertheless, **A** and **C** matrices are used to calculate the modal parameters of the system. The first step of the ERA is constituting the Hankel matrix as presented in Equation 2.20.

$$\mathbf{H}(k)=\begin{bmatrix} \mathbf{Y}(k+1) & \mathbf{Y}(k+2) & \dots & \mathbf{Y}(k+m) \\ \mathbf{Y}(k+2) & \mathbf{Y}(k+3) & & \vdots \\ \vdots & & \ddots & \vdots \\ \mathbf{Y}(k+s) & \dots & \dots & \mathbf{Y}(k+m+s) \end{bmatrix} \tag{2.20}$$

where **Y**(k) is the impulse response vector (i.e., the free vibration data) with Nx1 dimensions at the k^{th} step. Here, N represents the number of sensors. The parameters s and m are the numbers of rows and columns in the Hankel matrix. For good results, m should be chosen to be approximately 10 times the number of modes to be identified, and s should be chosen to be 2-3 times m (Juang & Pappa, 1985). In the second step of the ERA, the singular value decomposition (SVD) of **H**(0) is carried out as presented in Equation 2.21.

$$\mathbf{H}(0)=\mathbf{R}\boldsymbol{\Sigma}\mathbf{S}^{T} \tag{2.21}$$

where **H**(0) represents the Hankel matrix at k=0, **R** and **S** are the left and right eigenvectors of **H**(0), respectively, and $\boldsymbol{\Sigma}$ is the diagonal matrix of singular values. Under ideal conditions, the matrix $\boldsymbol{\Sigma}$ is in the form presented in Equation 2.22.

$$\boldsymbol{\Sigma}=\begin{bmatrix} \boldsymbol{\Sigma}_g & 0 \\ 0 & 0 \end{bmatrix} \tag{2.22}$$

where $\boldsymbol{\Sigma}_g$ is a g by g matrix and g represents the system order (number of poles, or model order). However, in reality, the $\boldsymbol{\Sigma}_g$ matrix contains nonzero (or relatively small)

terms along the diagonal due to the measurement noise and the numerical truncation process. By eliminating these terms, it is possible to obtain the minimum system order (i.e., minimum realization). Note that higher model order selection causes fictitious modes to occur, whereas, in the case of smaller model order, some of the modes might not be identified. In order to determine the correct system order, stabilization diagrams are effective tools. These diagrams are plotted by repeated (iterative) identification processes with different number model orders. Herein, stable (i.e., physical) modes are constant and identifiable for all or most of the identification runs.

A and **C** matrices can be determined by Equations 2.23 and 2.24 as follows

$$\mathbf{A} = \mathbf{\Sigma}^{-1/2}\mathbf{R}^{T}\mathbf{H}(1)\mathbf{S}\mathbf{\Sigma}^{-1/2} \tag{2.23}$$

$$\mathbf{C} = \mathbf{E}^{T}\mathbf{R}\mathbf{\Sigma}^{1/2} \tag{2.24}$$

where the small singular values are excluded from the matrix $\mathbf{\Sigma}$ and $\mathbf{E} = [\mathbf{I}\ 0]$. The eigenvalue decomposition of the matrix **A** is utilized to determine the poles (eigenvalues), which is $\mathbf{\Lambda} = \mathrm{diag}(\lambda_i)$. Note that these eigenvalues are complex conjugates where their imaginary parts represent the damped vibration frequencies. Eventually, the vibration frequencies (ω_i) and damping ratios (ξ_i) of the system are calculated by the expressions presented in Equation 2.25.

$$\mu_i = \frac{\ln(\lambda_i)}{\Delta t} \qquad \mu_i, \mu_i^* = -\omega_i\xi_i \pm j\omega_i\sqrt{1-\xi_i^2}$$
$$\omega_i = \sqrt{\mu_i . \mu_i^*} \qquad \xi_i = -\frac{\mathrm{Real}(\mu_i)}{\omega_i} \tag{2.25}$$

where i is varied from 1 to N_s (number of modes), Δt is the sampling period, and the symbol "*" represents the conjugate form. To determine the mode shapes (ϕ_i), the relationship in Equation 2.26 is used.

$$\phi_i = \mathbf{C}\,\mathbf{\Gamma} \tag{2.26}$$

where $\mathbf{\Gamma}$ represents the eigenvectors of the matrix **A**.

2.2.3.2 Enhanced Frequency Domain Decomposition (EFDD)

The main idea behind the EFDD method is determining the modal parameters of a system from the singular value decomposition of the spectral density matrix of the responses which represents auto-spectral density functions of a single-degree-of-freedom system (SDOF) with the same dynamic characteristics. In other words, decomposition of the spectral matrix of the responses is used to obtain the physical information of a system. In this section, firstly the theoretical background of the FDD method is presented, and then its enhanced version, the EFDD method is discussed. In this sense, studies performed by Astroza et al. (2016a), Brincker et al. (2001a, 2001b), Brincker & Ventura (2015), Gentille & Gallino (2008), and Magalhães et al. (2010) are taken into account.

Consider the response of a system given in Equation 2.27, $\mathbf{y}(t)$ can be written in terms of the mode shape matrix **A** (i.e., modal matrix) and modal coordinates $\mathbf{q}(t)$.

$$\mathbf{y}(t) = \mathbf{a}_1 q_1(t) + \mathbf{a}_2 q_2(t) + ... = \mathbf{A}\,\mathbf{q}(t) \tag{2.27}$$

where $\mathbf{A} = [\mathbf{a}_1, \mathbf{a}_2 \cdots]$ and $\mathbf{q}^T(t) = \{q_1(t), q_2(t) \cdots\}$. Accordingly, it is also feasible to state the response of a system in terms of the modal matrix **A** and the correlation function matrix of the modal coordinates $\mathbf{R}_q(\tau)$ as given in Equation 2.28.

$$\mathbf{R}_y(\tau) = E[\mathbf{y}(t)\ \mathbf{y}^T(t+\tau)] = \mathbf{A}\,E[\mathbf{q}(t)\ \mathbf{q}^T(t+\tau)]\ \mathbf{A}^T = \mathbf{A}\,\mathbf{R}_q(\tau)\ \mathbf{A}^T \tag{2.28}$$

where $E[.]$ represents the expectation operator and $\mathbf{R}_y(\tau)$ is the correlation function matrix of $\mathbf{y}(t)$. The corresponding spectral density matrix is later obtained by taking the Fourier transform of both sides of Equation 2.28, and presented in Equation 2.29.

$$\mathbf{G}_y(f) = \mathbf{A}\,\mathbf{G}_q(f)\,\mathbf{A}^T \tag{2.29}$$

where $\mathbf{G}_y(f)$ and $\mathbf{G}_q(f)$ are the spectral density matrices of the response $\mathbf{y}(t)$ and the modal coordinates $\mathbf{q}(t)$, respectively. In $\mathbf{G}_y(f)$, the real-valued auto-spectral densities are formed as diagonal elements, whereas the off-diagonal terms represent the cross-spectral densities. If the system is excited by a signal with broad-band (e.g., white-noise) characteristics, then the spectral matrix can be decomposed as given in Equation 2.30.

$$\mathbf{G}_y(\omega) = \sum_{n=1}^{N} \left(\frac{\mathbf{a}_n \gamma_n^T}{-i\omega - \lambda_n} + \frac{\mathbf{a}_n^* \gamma_n^H}{-i\omega - \lambda_n^*} + \frac{\mathbf{a}_n^T \gamma_n}{i\omega - \lambda_n} + \frac{\mathbf{a}_n^H \gamma_n^*}{i\omega - \lambda_n^*} \right) \tag{2.30}$$

where $\mathbf{a}_n$, γ_n, and λ_n are the mode shapes, modal participation vectors, and poles, respectively. The symbol "*" and the superscript "H" represent the conjugate form and the Hermitian (i.e., complex conjugate transpose), respectively. Since the modal participation vectors are the weighted forms of the mode shapes ($\gamma_n = c_n^2 \mathbf{a}_n$ where c_n is a positive constant) and only the two midterms in Equation 2.30 (i.e., the second and third terms) are dominant in the case of lightly damped systems, Equation 2.30 can be arranged more simply as presented in Equation 2.31.

$$\mathbf{G}_y(\omega) = \sum_{n=1}^{N} \left(\frac{c_n^2 \mathbf{a}_n^* \mathbf{a}_n^H}{-i\omega - \lambda_n^*} + \frac{c_n^2 \mathbf{a}_n \mathbf{a}_n^T}{i\omega - \lambda_n} \right) \cong \sum_{n=1}^{N} 2c_n^2 \mathrm{Re}\left(\frac{\mathbf{a}_n \mathbf{a}_n^T}{i\omega - \lambda_n} \right) \tag{2.31}$$

In FDD, decomposition of the spectral density matrix estimated at each distinct frequency value is performed through singular value decomposition (SVD) as presented in Equation 2.32. The diagonal matrix **Z** holding the singular values z_n^2 is interpreted as auto-spectral densities of the modal coordinates (Equation 2.33), whereas the mode shape information can be extracted from the matrix **U** for each distinct frequency value (Equation 2.34). Note that the SVD allows separation of the noise modes from the physical ones which helps analysts to understand the structural related information. The first singular value that becomes flat compared to the modal response indicates the noise level; thus, lower singular values compared to that one can be eliminated in the process of modal parameter identification. Analysts can use this merit in the identification of the closely-spaced modes.

$$\mathbf{G}_y(f) = \mathbf{U}\,\mathbf{Z}\,\mathbf{U}^H = \mathbf{U}[z_n^2]\,\mathbf{U}^H \tag{2.32}$$

$$[\mathbf{Z}] = \mathrm{diag}(z_1^2, z_2^2, ..., z_n^2) = \begin{bmatrix} z_1^2 & 0 & ... & 0 \\ 0 & z_2^2 & & \vdots \\ \vdots & & \ddots & \vdots \\ 0 & \dots & \dots & z_n^2 \end{bmatrix} \tag{2.33}$$

$$[\mathbf{U}] = [\{U_1\}, \{U_2\}, ..., \{U_n\}] \tag{2.34}$$

In FDD, since the first singular value at each distinct frequency reflects the strength of the dominated vibration mode at that frequency, it is suitable to plot a frequency-singular value curve that can be used as a modal indicator. Accordingly, vibration frequencies are estimated by selecting the frequency values where the frequency-singular value curve has peaks. It is possible to estimate the vibration frequencies with higher accuracy by using the enhanced version of the FDD method (i.e., EFDD method), in which the singular value information around the considered peak is also used. Herein, the selection of the singular value segment around the peak is performed by assessing the similarity between the singular vector estimates related to the peak and the points around the peak. Modal assurance criterion (MAC) can be utilized to state the similarity between the singular vectors (Allemang, 2003) (formulation is presented by Equation 3.3 in Chapter Three). Limits (borders) of the singular value segment are determined based on the points where the similarity between the singular vectors falls below a predefined threshold value (i.e., as long as the singular vector around the peak exhibits high similarity, that singular vector belongs to the same mode). The piece of the singular values around the peak (i.e., singular value segment around the peak) is taken back to the time domain by the inverse fast Fourier transform. By this way, the corresponding auto-correlation function of a SDOF system is obtained. Accordingly, the frequency and damping estimations can be simply obtained by performing crossing times (i.e., time intervals between zero crossings) and logarithmic decrement (i.e., by arranging an exponential decay) on this auto-correlation function, respectively. In both versions of the methods (i.e., FDD and EFDD), near a peak corresponding to a mode, the first singular vector $\{U_1\}$ reflects

the estimated mode shape. Note that in the case of closely-spaced modes, the first singular vector will always give the best estimate of the mode shape.

2.2.3.3 Stochastic Subspace Identification (SSI)

In general, the SSI method is based on establishing a linear state-space model of the system by using the output-only measured vibration responses. There are two main types of SSI formulations available, namely the data-driven SSI (SSI-DATA) and the correlation-driven SSI (SSI-COV). The SSI-COV is very similar to the ERA. It uses the correlations of the time series. Conversely, the SSI-DATA is directly based on the measured time series, and unlike the two-stage time domain methods, (e.g., NExT-ERA and SSI-COV) calculation of the covariance matrices is not required. In addition, SSI-DATA is more robust since it uses least squares, SVD, and QR factorization. In this section, the theoretical background of the SSI-DATA method is presented. In this sense, studies performed by Astroza et al. (2016a), Brincker & Andersen (2006), Brincker & Ventura (2015), Magalhães et al. (2010), Van Overschee & De Moor (1996), Peeters (2000), and Peeters & De Roeck (2001) are taken into account.

Any free decay $\mathbf{y}(k)$ can be expressed by a state-space formulation as shown in Equation 2.35.

$$\mathbf{y}(k) = \mathbf{P}\mathbf{G}^{k}\mathbf{u}_0 \tag{2.35}$$

where $\mathbf{P}$ and $\mathbf{G}$ are the observation and discrete time system matrices, respectively, and $\mathbf{u}_0$ is the state-space initial conditions of the free decay. In the first step of the SSI-DATA method, the output measurement responses in time domain $\mathbf{y}(k)$ are utilized to construct the block Hankel matrix with 2s number of block rows and np number of data points (Equation 2.36). The Hankel matrix is later split in the middle into two block Hankel matrices, namely $\mathbf{H}_1$ (the upper part) and $\mathbf{H}_2$ (the lower part) each having s number of block rows. Here, $\mathbf{H}_1$ and $\mathbf{H}_2$ are also known as “the past” and “the future”, respectively. In the SSI theory, the projection matrix $\mathbf{O}$ is defined with Equation 2.37, and the calculation of its components is presented in Equation 2.38.

$$\mathbf{H} = \begin{bmatrix} \mathbf{y}(1) & \mathbf{y}(2) & \dots & \mathbf{y}(np-2s+1) \\ \mathbf{y}(2) & \mathbf{y}(3) & \dots & \mathbf{y}(N-2s+2) \\ \vdots & \vdots & & \vdots \\ \mathbf{y}(s) & \mathbf{y}(s+1) & \dots & \mathbf{y}(np-s) \\ \mathbf{y}(s+1) & \mathbf{y}(s+2) & \dots & \mathbf{y}(np-s+1) \\ \mathbf{y}(s+2) & \mathbf{y}(s+3) & \dots & \mathbf{y}(np-s+2) \\ \vdots & \vdots & & \vdots \\ \mathbf{y}(2s) & \mathbf{y}(2s+1) & \dots & \mathbf{y}(np) \end{bmatrix} = \begin{bmatrix} \mathbf{H}_1 \\ \mathbf{H}_2 \end{bmatrix} \tag{2.36}$$

$$\mathbf{O} = E\left[\mathbf{H}_2 \middle| \mathbf{H}_1\right] \tag{2.37}$$

$$\mathbf{O} = \mathbf{T}_{21}\,\mathbf{T}_{11}^{+}\,\mathbf{H}_1 \quad \text{where} \quad \begin{matrix} \mathbf{T}_{21} = \mathbf{H}_2\,\mathbf{H}_1^{\mathrm{T}} \\ \mathbf{T}_{11} = \mathbf{H}_1\,\mathbf{H}_1^{\mathrm{T}} \end{matrix} \tag{2.38}$$

In Equation 2.38, $\mathbf{T}_{21}$ and $\mathbf{T}_{11}$ represent the block Toeplitz matrices. It should be stated that the calculation of the block Toeplitz matrices is memory consuming and requires high computational effort. Therefore, the projection is generally calculated by the QR decomposition (factorization) of the transposed block Hankel matrix presented in Equation 2.36. Note that the free decays are established in the calculated projection matrix which can be expressed as follows

$$\mathbf{O} = \boldsymbol{\Gamma}\mathbf{X} \tag{2.39}$$

where $\boldsymbol{\Gamma}$ and $\mathbf{X}$ are the observability matrix and the matrix of Kalman states (i.e., the matrix representing the initial conditions of the free decays in the projection matrix), respectively. The next step in the identification process is taking the SVD of the projection matrix as shown in Equation 2.40.

$$\mathbf{O} = \mathbf{R}\boldsymbol{\Sigma}\mathbf{S}^{\mathrm{T}} \tag{2.40}$$

Based on Equations 2.39 and 2.40, $\boldsymbol{\Gamma}$ and $\mathbf{X}$ can be estimated as presented in Equation 2.41.

$$\hat{\boldsymbol{\Gamma}} = \mathbf{R}_n \boldsymbol{\Sigma}_n^{1/2}$$
$$\hat{\mathbf{X}} = \boldsymbol{\Sigma}_n^{1/2} \mathbf{S}_n^T \tag{2.41}$$

where $\mathbf{R}_n$, $\boldsymbol{\Sigma}_n$, and $\mathbf{S}_n$ are the restricted forms of the SVD matrices corresponding to the first n singular values (i.e., first n/2 modes). Eventually, the discrete time system matrix **G** and the observation matrix **P** are computed by solving a least squares problem. The modal parameters (i.e., vibration frequencies, damping ratios, and mode shapes) can be determined in a similar way as presented in Equations 2.25 and 2.26.

It should be stated that various techniques can be formulated in the SSI by multiplying real-valued weight matrices $\mathbf{W}_1$ and $\mathbf{W}_2$ on each side of the projection matrix. Thus, a generalized projection matrix is obtained and the SVD is performed on this resultant matrix (Equation 2.42).

$$\mathbf{W}_1 \mathbf{O} \mathbf{W}_2 = \mathbf{R} \boldsymbol{\Sigma} \mathbf{S}^T \tag{2.42}$$

Different forms of the weight matrices constitute the SSI standard algorithms known as the unweighted principal component (UPC) algorithm, the principal components (PC) algorithm, and the canonical variate algorithm (CVA).

2.2.4 Increased Signal Reproduction Fidelity by Offline Tuning Technique (OTT)

As it was stated before, the frequency content of a dynamic excitation should cover a wide range of frequencies (i.e., having broad-band characteristics) to excite a system's modes properly. However, in a shake table test (or shaker test), if a control algorithm is not used, the total forward transfer function estimation (i.e., estimated between command and feedback signals) clearly indicates that the command signal cannot be reproduced properly in terms of target amplitude and frequency content (Twitchell & Symans, 2003; Yucel, 2014). In other words, a trajectory tracking problem occurs between the target (command) and achieved (feedback) signals which means that the shake table cannot track the command signal properly. Complex internal mechanisms of the shake table and the table-specimen interaction are the main

reasons for this issue. Since the command signal loses its broad-bandwidth property, which is intended to be, results of OMA, model updating, and vibration-based SHM are also affected. In literature, there exist many control methods, such as adaptive control, PID based displacement control, PID+ feedforward, and offline tuning methods to solve this problem (Luco et al., 2010; Mota, 2011). In this thesis, offline tuning technique (OTT), a command shaping control strategy, is used for this purpose (Ozcelik et al., 2015, 2018; Thoen & Laplace, 2004; Yucel, 2014).

In OTT, firstly the forward transfer function (FTF) of the shake table is experimentally estimated between the command and the feedback signals. FTF is a beneficial tool that provides information about the dynamic characteristics of shake tables and their effects on command signals. Namely, a unit FTF value at a specific frequency means that there is no effect on the command signal (i.e., there is no tracking problem), whereas other values are the indicators of the tracking problem. Afterwards, the command signal is multiplied by the inverse of the FTF in the frequency domain and then filtered by a high-pass filter to avoid large motions surpassing the shake table's operational limits. The modified command signal obtained this way is transformed back to the time domain by the inverse fast Fourier transform, and is used as the adjusted command to the shake table. This way the signal reproduction fidelity is increased and the achieved signal on the shake table would be in nature as the desired command signal (Ozcelik et al., 2015, 2018; Yucel, 2014).

In Figure 2.2, the trajectory tracking problem observed in a shake table test, where the command signal has white-noise characteristics, is presented (Ozcelik et al., 2015). From the FTF estimation (Figure 2.2 (a)), the minimization effect of the shake table on the command (input) signal is clear (amplitudes less than unit value). On the other hand, the tracking problem can be verified by comparing the command and feedback (output) signals in both time and frequency domains (Figure 2.2 (b)). After the application of OTT, the tracking problem is solved, and the signal reproduction fidelity is improved both in time and frequency domains (Figure 2.2 (c)).

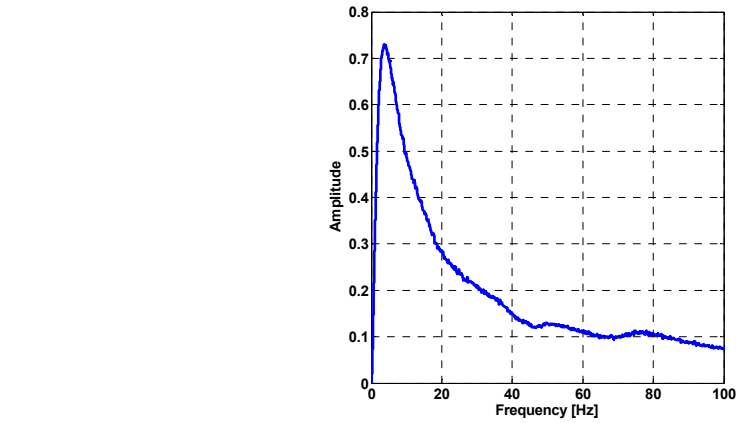

(a)

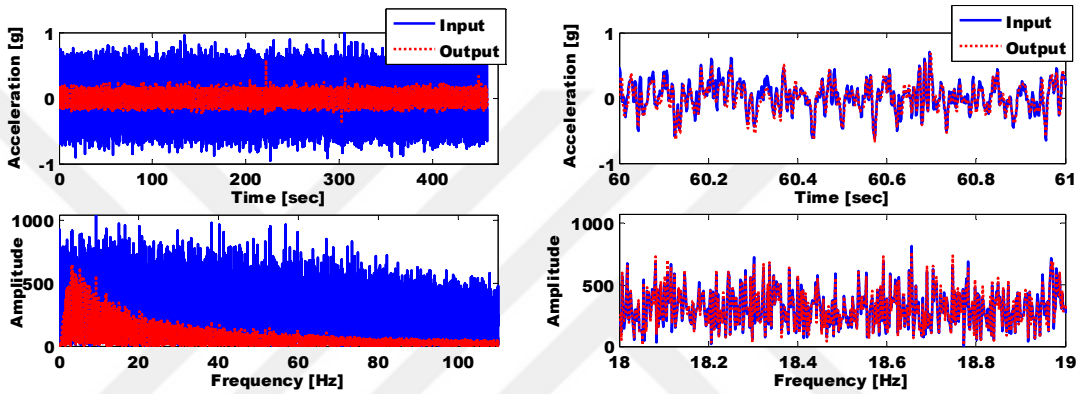

(b) (c)

Figure 2.2 (a) Forward transfer function estimation and signal reproduction fidelity (b) before and (c) after the application of OTT (zoomed) (Ozcelik et al., 2015)

The effects of OTT on the vibration frequency estimation results of a small-scale aluminum frame type structure are presented in Figure 2.3 (Yucel, 2014). Here, the values obtained by the impact hammer test can be considered as the exact results. It is explicit that the application of OTT for white-noise tests has significant effects and applying OTT, therefore broad-band excitation, is necessary to obtain more realistic system identification results.

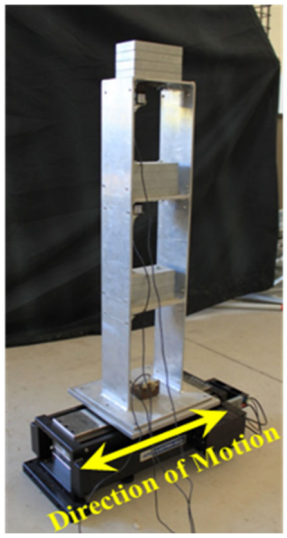

Excitation Type	1st Mode [Hz]	2nd Mode [Hz]	3rd Mode [Hz]
Impact Hammer	7.71	26.43	42.76
White-noise without OTT	11.92	29.98	43.80
White-noise with OTT	7.19	26.66	42.80

(a) (b)

Figure 2.3 (a) Small-scale aluminum frame type structure and (b) its system identification results under different excitation conditions (Yucel, 2014)

CHAPTER THREE
FINITE ELEMENT MODEL UPDATING

3.1 Introduction

In recent years, the finite element (FE) method has been commonly preferred by civil engineering society for structural analyses and designs. Within this scope, physical properties and behaviors of the structures are modeled by engineering judgements and insights. However, the constituted numerical models may not be convenient representatives of the real structural behaviors because of the modeling simplifications and assumptions made in model parameters such as material properties, boundary conditions, member connections, and meshing strategies. Therefore, these numerical models should be verified and corrected if necessary before further usages and analyses. This can be done by means of a finite element model updating (FEMU) procedure in which the initial FE model (i.e., numerical model) is calibrated based on the experimental data (a.k.a. model calibration). In this context, vibration frequencies, mode shapes, frequency response functions, acceleration time histories, modal strains, modal curvatures, modal strain energies, and modal flexibilities can be used as responses; but modal parameters such as vibration frequencies and mode shapes are the mostly preferred ones. In general, FEMU is the process where the unknown and/or uncertain properties of a FE model are adjusted such that the numerical results correspond well with the experimental ones. Note that experimental data is a better representation of the structural behavior than the FE model although it contains measurement errors. (Friswell & Mottershead, 1995; Teughels, 2003). Besides, FEMU methods are commonly used for damage identification purposes by adjusting model parameters that are related to structural stiffness (e.g., Young's modulus, shear modulus, Poisson's ratio, moment of inertia, etc.) to determine the location and the extent of the damage. In this context, experimental data before and after a damaging event are required.

FEMU methods are classified as model-based methods, in which a FE model is used to predict the observed changes. On the other hand, non-model methods are based

only on the changes of the measured data, and do not require a numerical model; therefore, they provide limited and coarse solutions and are not suitable for complex systems (Carden & Fanning, 2004). In literature, FEMU methods can be categorized into two main groups, namely direct (matrix) and indirect (iterative) methods. In direct methods, model updating is performed in a single step with a non-iterative approach. For this reason, the existence of measurement noise significantly reduces their efficiency and performance. This type of methods is mainly based on updating mass and stiffness matrices directly (i.e., without any regard to changes in model parameters), whereby their updated values deceive structural meanings and cause physically nonsense results. In addition, model connectivity and positive definiteness (i.e., a matrix is positive definite if it is symmetric an all its eigenvalues are positive) may not remain. Error matrix, optimal matrix, matrix-update, and the eigen structure assignment methods are the some of the direct methods (Alkayem et al., 2018; Carvalho et al., 2007; Friswell & Mottershead, 1995; Marwala, 2010; Mottershead & Friswell, 1993; Yang & Chen, 2009). For all these limitations, direct methods are less preferred, and indirect methods have mainly been used. In indirect methods, physical parameters (model parameters) of an initial FE model are calibrated (updated) until its dynamic characteristics (i.e., modal parameters) get sufficiently closer to that of the real structure. By the reason of the nonlinear relationship between the physical and modal parameters, the updating process is realized iteratively. Since the model parameters are updated, the mass and stiffness matrices preserve their physical meanings, and the model connectivity is ensured. The most commonly used iterative methods are sensitivity-based, computational intelligence, Bayesian/Monte Carlo, and response surface methods (Alkayem et al., 2018; Friswell & Mottershead, 1995; Marwala, 2010).

In linear FEMU methods (i.e., the methods that are discussed so far), always linear FE models are developed, and the structural damage is generally defined as loss of effective stiffness (a.k.a. damage indicator) based on linear responses. Therefore, the updated FE models can only reflect the behaviors of the structures in the linear range. However, all the real-life structures are inherently nonlinear, especially the damaged structures caused by strong excitations (e.g., earthquakes). Therefore, additional

nonlinear damage indicators are required (e.g., loss of ductility capacity, loss of strength, softening, residual deformations, etc.) for accurate damage identification. In this context, nonlinear FEMU methods, that are based on the nonlinear responses of the structural systems, can be used. Since the nonlinear responses include more information about damage than the linear responses, nonlinear FEMU methods can provide more accurate damage identification results and can be used for damage prognosis (i.e., predicting the remaining lives of the structural systems) studies (Asgarieh et al., 2014; Astroza et al., 2017; Ebrahimian et al., 2017; He et al., 2019). Note that the topic of nonlinear FEMU is not included within this thesis since it is aimed to focus on the linear FEMU methods, especially the sensitivity-based ones. Besides, model updating by linear methods is commonly used by civil engineering society for damage identification studies of nonlinear systems with reasonable success. In the following sections of the thesis, the sensitivity-based FEMU method is discussed in detail and used for model updating and damage identification purposes.

3.2 Sensitivity-Based Finite Element Model Updating Method

Sensitivity-based FEMU, which is in the category of inverse problems, is the most common method that can be utilized for model updating and damage identification purposes. In inverse problems, a FE model is constituted in order to represent the experimental data numerically, then the discrepancies between the experimentally and numerically identified quantities (i.e., modal parameters such as vibration frequencies and mode shapes are commonly used for this purpose) are minimized by adjusting (calibrating, updating) the unknown model parameters (e.g., mass density, Young's modulus, shear modulus, spring stiffness, moment of inertia, thickness, boundary conditions, etc.). In other words, in inverse problems, the output (i.e., modal parameters) is known, whereas the input (i.e., model parameters) is unknown. On the other hand, in forward problems, outputs are determined directly from the mathematical model with known parameters (i.e., model parameters). For example, damage is modeled numerically and the experimentally identified modal parameters are compared with the numerically obtained ones to verify the predefined damage. Note that typical engineering problems are generally in the form of forward problems

(Boller et al., 2009; Brownjohn, 2007; Carden & Fanning, 2004; Fan & Qiao, 2011; Marwala, 2010; Sohn et al., 2003; Teughels, 2003).

In general, sensitivity-based FEMU can be considered as an iterative optimization process at minimizing the discrepancies between the experimentally identified and numerically obtained (from FE model) quantities (modal parameters), which is defined by an objective function (a.k.a. cost function), by updating the selected model parameters of the numerical model (Friswell & Mottershead, 1995; Mottershead et al., 2011; Teughels, 2003; Teughels & De Roeck, 2004; Teughels et al., 2003). The iterations are continued until an absolute minimum (a.k.a. global minimum) of the objective function is acquired. In practice, material characteristics, geometrical properties, boundary conditions, and member connections are the mostly selected model parameters for updating purposes (a.k.a. updating parameters, design variables, or design parameters). The updating procedure can be conducted by a manual or automated way. Manual updating is a conventional method that depends on the trial-and-error approach. It has a slow convergence speed (i.e., more time and trials may be required for ultimate results) and does not guarantee a global minimum; therefore, this method is non-practical for complex systems. On the other hand, automated updating is performed by using a computer-aided optimization algorithm. Thus, it has faster convergence and provides more objective and accurate results. In practice, performing manual updating prior to an automated one is recommended. By this way, it is possible to ensure more reasonably accurate numerical models for the automated updating stage, which in return improves its convergence performance.

The general procedure of the sensitivity-based FEMU method is presented by a flowchart in Figure 3.1. Steps of the method can be summarized as follows: (i) Initially, selection of the unknown model parameter set of the investigated system is realized ($\mathbf{p}_k$). (ii) Appropriate and physically meaningful initial values are assigned to these model parameters ($\mathbf{p}_0$). (iii) FE analysis is realized to determine the numerical quantities of the system. (iv) Residual vector ($\mathbf{r}$) is calculated by the discrepancies between the numerically ($z(\mathbf{p}_k)$) and experimentally ($\tilde{z}$) obtained quantities. (v) A nonlinear least squares problem is defined by an objective function using the residual

vector. (vi) Sensitivity (Jacobian) matrix ($\mathbf{J}_{\mathbf{P}_k}$) is constituted by calculating the sensitivity of the residual vector with respect to the model parameters. (vii) Minimization process of the nonlinear least squares problem is performed by an optimization algorithm, thus updated model parameter values ($\mathbf{p}_{k+1}$) are obtained. (viii) Steps iii to vii are repeated by using the updated model parameter values ($\mathbf{p}_{k+1}$) until the convergence is satisfied (i.e., discrepancies between the numerical and experimental quantities are sufficiently minimized). By this way, the initial FE model is corrected such that it better represents the actual system, and the unknown model parameters are identified as to be $\mathbf{p}_{k+1}$.

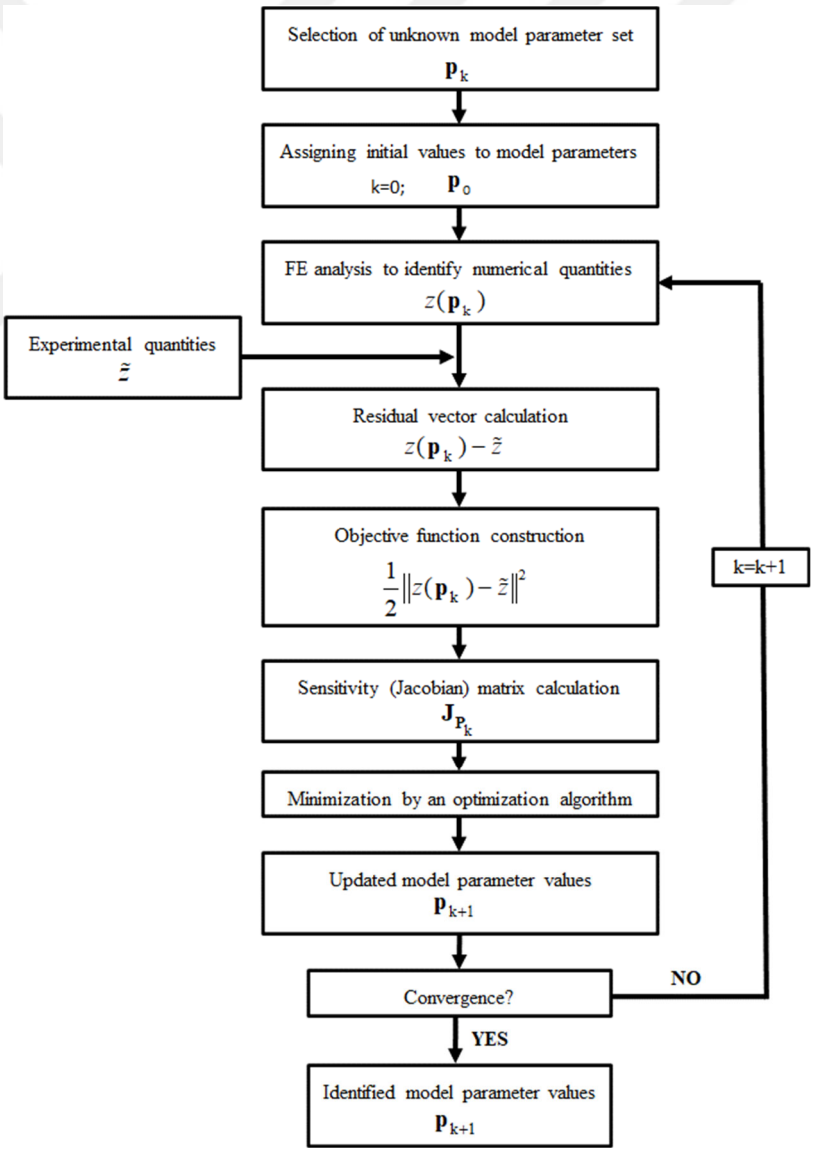

Figure 3.1 Flowchart of the sensitivity-based finite element model updating method

The theoretical background of the sensitivity-based FEMU method is presented in the following sections. In this sense, studies performed by Fang et al. (2008), Moaveni et al. (2013), Teughels (2003), and Teughels & De Roeck (2004) are considered.

3.2.1 Objective Function and Residual Vector

The first step of the sensitivity-based FEMU is to construct an objective function. The least squares approach is used for this purpose as given in Equation 3.1. Note that the problem is nonlinear due to the nonlinear relationship between the modal parameters and design variables $\mathbf{p}$.

$$\mathrm{f}(\mathbf{p}) = \frac{1}{2}\sum_{\mathrm{j}=1}^{\mathrm{m}}\left[z_{\mathrm{j}}(\mathbf{p}) - \tilde{z}_{\mathrm{j}}\right]^2 = \frac{1}{2}\sum_{\mathrm{j}=1}^{\mathrm{m}}\left[\mathrm{r}_{\mathrm{j}}(\mathbf{p})\right]^2; \quad \mathbf{l_b} < \mathbf{p} < \mathbf{u_b} \tag{3.1}$$

where $\mathbf{p} \in \mathbb{R}^{\mathrm{n}}$ represents the design variables (n is the number of design variables), $z_{\mathrm{j}}(\mathbf{p})$ and $\tilde{z}_{\mathrm{j}}$ are the numerically and experimentally obtained modal quantities, respectively, j indicates the component number of any variable (e.g., the j^{th} component of $\tilde{z}_{\mathrm{j}}$), r_{j} presents the residuals, and m is the number of components that are considered (i.e., number of residuals). $\mathbf{l_b}$ and $\mathbf{u_b} \in \mathbb{R}^{\mathrm{n}}$ are the lower and upper bounds (i.e., constraints), respectively, that the design variables have to satisfy during the updating process. In the case of an unconstrained optimization problem, physically nonmeaningful results may be obtained for the design variables.

The residual vector $\mathbf{r}$ indicates the discrepancies between numerically and experimentally obtained quantities (e.g., frequency response functions, vibration frequencies, mode shapes, modal curvatures, modal strains, modal strain energies, modal flexibilities, etc.). Herein, it should be stated that the modal flexibility residual, which is basically a combination of vibration frequencies and mode shapes, is more sensitive to the local changes of the systems (e.g., local damages). This is because the flexibility matrix (inverse of the stiffness matrix) is dominated by the lowest modes of the system, which can be easily identified, whereas the stiffness matrix is dominated by the highest modes, which are difficult, if not impossible to identify (Jaishi & Ren,

2005, 2006; Reynders & De Roeck, 2010). Since the vibration frequencies and mode shapes (the commonly used ones in civil engineering) are focused only in this thesis, equations are given in accordance with these quantities. Thus, the residual vector containing the frequency residuals $\mathbf{r}_f(\mathbf{p})$ (a.k.a. eigenfrequency residuals) and mode shape residuals $\mathbf{r}_s(\mathbf{p})$ can be defined as Equation 3.2.

$$\min \frac{1}{2}\left\|\mathbf{r}(\mathbf{p})\right\|^2 = \min \frac{1}{2}\left\|\begin{matrix}\mathbf{r}_f(\mathbf{p}) \\ \mathbf{r}_s(\mathbf{p})\end{matrix}\right\|^2 \tag{3.2}$$

where $\|.\|$ denotes the Euclidean norm, $\mathbf{r}_f : \mathbb{R}^n \to \mathbb{R}^{m_f}$ and $\mathbf{r}_s : \mathbb{R}^n \to \mathbb{R}^{m_s}$. Consequently, $\mathbf{r}: \mathbb{R}^n \to \mathbb{R}^m$ includes $m = m_f + m_s$ components. The uniqueness of Equation 3.2 can only be achieved by constituting an overdetermined problem, where m (number of residuals) is higher than n (number of design variables) (n<m). Otherwise, there exist infinitely many solutions that make Equation 3.2 minimum (underdetermined case). In practice, having significantly higher m values (n<<m) is essential to improve the updating performance. An overdetermined problem can be ensured by considering more response values than design variables and/or limiting the number of design variables (i.e., not assigning design variables to each finite element of the model). One way to do is to group a set of neighboring and/or symmetric finite elements, that are expected to undergo similar changes during updating, as substructures, and to assign a single design variable for them. Herein, engineering judgement is necessary to determine where or/and how to assign design variables. Another way is to use a parameterization method (e.g., using damage functions), which is detailed in the following sections of the thesis.

Note that experimentally and numerically obtained modal data must be matched correctly before the usage of Equation 3.2. For this purpose, the modal assurance criterion (MAC), which is a useful tool to determine the similarity between differently obtained modal vectors, can be utilized (Allemang, 2003). Formulation is presented in Equation 3.3.

$$\mathrm{MAC}\left(\phi_i, \overline{\phi}_j\right) = \left(\cos\theta\right)^2 = \frac{\left(\phi_i^T \, \overline{\phi}_j\right)^2}{\left(\phi_i^T \phi_i^T\right)\left(\overline{\phi}_j^T \, \overline{\phi}_j\right)} \tag{3.3}$$

where ϕ_i and $\overline{\phi}_j$ represent the i^{th} numerical and j^{th} experimental modal vectors, respectively, and θ is the angle between these modal vectors. MAC value always lies between 0 and 1, and the closeness of the criterion to unit value, which means that the angle between the vectors is zero (i.e., overlapping), is the indicator of the higher similarity (i.e., good correlation) between the vectors, whereas a value close to 0 designates bad correlation. However, in cases with similar modes or many closely-spaced modes, the MAC concept may result in erroneous mode matching. That's why an alternative formulation as given in Equation 3.4 can be used (Simoen et al., 2015).

$$1 - \mathrm{MAC}\left(\phi_i, \overline{\phi}_j\right) + \left|1 - \frac{\lambda_i}{\overline{\lambda}_j}\right| \tag{3.4}$$

where λ_i and $\overline{\lambda}_j$ are the numerical and experimental eigenvalues (see Equation 3.5 for the formulation), respectively. Here, a value close to zero indicates a perfect match between two modes.

It is essential to state that mode matching can cause non-smooth behaviors in the objective function. For example, with the change of the model parameter values after each iteration step, the modes might get matched differently (a.k.a. mode-crossing) due to occurrences of new modes and/or disappearances of existing modes. This situation leads to sudden jumps in the objective function which may inhibit the effectiveness of the optimization algorithm dramatically. To overcome this problem, modes must be matched again at the beginning of each iteration step.

3.2.1.1 Eigenfrequency Residuals

Eigenfrequency residuals include the differences between the numerical and experimental undamped eigenfrequencies. Formulation is given in Equation 3.5.

$$\mathbf{r}_f(\mathbf{p}) = \frac{\lambda_j(\mathbf{p}) - \bar{\lambda}_j}{\bar{\lambda}_j} \quad \text{with} \quad \lambda_j = \left(2\pi f_j\right)^2 \quad \mathbf{r}_f : \mathbb{R}^n \rightarrow \mathbb{R}^{m_f} \tag{3.5}$$

where j indicates the mode number, f_j is the eigenfrequency, $\lambda_j(\mathbf{p})$ and $\bar{\lambda}_j$ represent the numerical and corresponding experimental eigenvalues, respectively, and m_f is the number of eigenfrequencies utilized in the updating procedure. Here, relative differences are calculated to provide a similar weight for each eigenfrequency. The eigenfrequencies can be accurately identified, are very sensitive with respect to stiffness properties, and supply global information of the system; therefore, they are indispensable quantities for the updating process and have beneficial effects on the convergence performance of the optimization problem.

3.2.1.2 Mode Shape Residuals

Mode shapes contain valuable spatial information about the dynamic characteristic of a system. That's why including the mode shape residuals into the residual vector is beneficial to improve the updating performance. Each mode shape residual is calculated as

$$\mathbf{r}_s(\mathbf{p}) = \frac{\phi_j^l(\mathbf{p})}{\phi_j^{ref}(\mathbf{p})} - \frac{\tilde{\phi}_j^l}{\tilde{\phi}_j^{ref}} \qquad \mathbf{r}_s : \mathbb{R}^n \rightarrow \mathbb{R}^{m_s} \tag{3.6}$$

In Equation 3.6, j indicates the mode number, ϕ_j and $\tilde{\phi}_j$ are the numerical and corresponding experimental modal vectors, respectively, ϕ_j^l and ϕ_j^{ref} represent the l^{th} (any arbitrary) and reference component of vector ϕ_j, and m_s is the number of modal displacements (components of the mode shape vector) used in the updating process. For example, if "$ndof_j$" indicates the number of DOFs used for mode ϕ_j and N_{mode} is the number of considered modes, then the mode shape residual vector includes $m_s = \sum_{j=1}^{N_{mode}} ndof_j$ components. Note that each mode shape component "l" is divided by a reference component "ref" (generally the maximum component) to enable similar

weighting since the numerically and experimentally obtained mode shapes can be scaled in a different way (i.e., normalization).

Note that the mode shape estimations are less sensitive to structural changes (e.g., changes because of damage) as compared to vibration frequencies. Besides, they are more prone to be polluted with noise (i.e., they include higher estimation uncertainty). However, they should be involved in the updating process owing to their spatial information.

3.2.1.3 Weighting Factors for Residuals

It is possible to weight the components of the nonlinear least squares problem (i.e., frequency and mode shape residuals) given in Equation 3.2 by judging their confidence, importance, and/or estimation quality. Accordingly, the objective function can be reformulated to establish a weighted least squares problem as given in Equation 3.7.

$$\min \frac{1}{2}\mathbf{r}(\mathbf{p})^{T}\,\mathbf{W}\,\mathbf{r}(\mathbf{p}) = \frac{1}{2}\left\|\mathbf{W}^{1/2}\,\mathbf{r}(\mathbf{p})\right\|^{2} \tag{3.7}$$

Here, $\mathbf{W}$ is the weighting matrix. If $\mathbf{W}$ is a diagonal matrix, $\mathbf{W} = \mathrm{diag}(\ldots, w_j^2, \ldots)$, Equation 3.7 can be equivalently written as

$$\frac{1}{2}\left\|\mathbf{W}^{1/2}\,\mathbf{r}(\mathbf{p})\right\|^{2} = \min \frac{1}{2}\sum_{j=1}^{m}\left(w_j r_j(\mathbf{p})\right)^{2} \tag{3.8}$$

where w_j is the weighting factor of r_j. A well-known statistical method to select the weighting matrix is taking the inverse of the covariance matrix of the experimental errors, which gives the minimum variance Gauss-Markov estimate (Friswell & Mottershead, 1995; Simoen et al., 2015; Teughels & De Roeck, 2004). However, this statistical information is often not available; therefore, in practice, the appropriate weights are determined by engineering judgement and/or by carrying out some trial runs. Such as, in the case where eigenfrequencies match well but the mode shapes still

have discrepancies, it can be concluded that too much weights are assigned to eigenfrequency residuals; or in the case where the eigenfrequency residuals are not minimized enough, their weights should be increased.

Another important point is assigning relatively higher weighting factors to reliable and accurately identified residuals. As it was mentioned before, eigenfrequencies can be identified more accurately than mode shapes; therefore, it is convenient to use relatively higher weights for them. In addition, mode shape estimations generally include higher uncertainty than frequency estimations because of the limited number of sensors available for testing and measurement noise. That's why relatively lower weighting factors should be assigned to the mode shape residuals if they are thought to be unreliable. Notice that only the relative values of the weighting factors are significant, not their absolute values. It is possible to obtain different updating results for different weighting factors; therefore, the ultimate result should be decided based on engineering judgement and intuition.

3.2.2 Variables of the Updating Method

3.2.2.1 Design Variables

In FEMU, material and geometrical properties of FE models (e.g., mass density, Young's modulus, shear modulus, spring stiffness, moment of inertia, thickness, boundary conditions, etc.) are generally the unknown and uncertain (i.e., erroneous) physical parameters that are updated to identify their actual values. Typically, the amount of the potential erroneous parameters is huge for a FE model, especially for detailed and complex models, which results in the optimization problem to be ill-conditioned. An ill-conditioned optimization problem increases the computational expense, has convergence difficulties, and does not guarantee for a solution. In order to ensure a well-conditioned problem, the number of parameters should be relatively small and only these parameters, which are actually erroneous, should be updated; otherwise, physically unrealistic results may be obtained. Engineering insight is therefore essential to decide which parts of the FE model and which physical

parameters have to be updated. In literature, there exist regularization and parameterization (i.e., using damage functions) methods to overcome the ill-conditioning state of the optimization problem (Fang et al., 2008; Grip et al., 2017; Li & Law, 2010; Mottershead et al., 2011; Teughels & De Roeck, 2004; Titurus & Friswell, 2008; Weber et al., 2007). In the scope of this thesis, only the parameterization method is discussed in the following sections.

Another important point that should be considered is the sensitivities of the residuals (responses) to the selected model parameters. Since the updating method is sensitivity-based, the parameters should affect the responses sensitively, otherwise, the updating results are likely to be erroneous. Note that a response sensitive to a parameter does not automatically imply that this parameter has to be included in the updating process. In other words, if the value of a parameter is already adequately representing the true value, then there is no reason to update it.

3.2.2.2 Correction Factors

Physical parameters (design variables) can have different orders of magnitude; therefore, it is convenient to use a dimensionless correction factor (i.e., a kind of normalization process) for each parameter according to a reference value (mostly the initial value before updating). If X^e is the value of a physical parameter X in element e and X^e_{ref} is its reference value, the dimensionless correction factor a^e_X can be formulated as in Equation 3.9.

$$a^e_X = -\frac{X^e - X^e_{ref}}{X^e_{ref}} \tag{3.9}$$

In other words, the updated value of the parameter X is determined by Equation 3.10.

$$X^e = X^e_{ref}\left(1 - a^e_X\right) \tag{3.10}$$

Note that a correction factor can affect one element or a group of elements (substructures) having similar values for a considered parameter. In theory, each

parameter in system matrices is a candidate for updating; however, stiffness properties are the mostly selected ones in civil engineering applications. Other parameters are assumed to be known and/or to remain unchanged after a damaging event; thus, they are excluded from the updating process. But sometimes mass density of the investigated structure is the unknown and/or it may vary throughout the structure (i.e., especially in the case of masonry structures). In such cases, performing model updating by adjusting mass density is mandatory to determine the mass distribution of the structure.

If the physical parameter is linearly related to the stiffness matrix of the element (e.g., Young's modulus), Equation 3.10 can be reformed as presented in Equation 3.11.

$$\mathbf{K}^{e} = \mathbf{K}^{e}_{ref}\left(1 - a^{e}\right) \qquad -\infty \le a^{e} \le 1 \tag{3.11}$$

where $\mathbf{K}^{e}$ and $\mathbf{K}^{e}_{ref}$ represent the updated and reference (initial) element stiffness matrices, respectively. Here, a negative a^{e} value indicates stiffening, whereas a positive a^{e} value indicates softening (i.e., stiffness loss) in element e (e.g., a^{e} equals to 1 in the case of fully damaged element). Eventually, the updated global system stiffness matrix can be assembled from element stiffness matrices as given in Equation 3.12.

$$\mathbf{K} = \mathbf{K}^{U} + \sum_{e=1}^{n_e} \mathbf{K}^{e}_{ref}\left(1 - a^{e}\right) \tag{3.12}$$

in which $\mathbf{K}$ represents the global system stiffness matrix, $\mathbf{K}^{U}$ is the stiffness matrix of the non-updated elements (i.e., the elements whose properties remain unchanged and are excluded from the updating process), and n_e is the number of elements (or group of elements, substructures) wanted to be updated. Note that similar approaches are valid for the case of the physical parameter is linearly related to the mass matrix of the element (e.g., mass density). Updating the submatrices using correction factors (as in Equation 3.12) provides two critical properties for the updating problem: (i) Connectivity of a FE model is preserved since the element stiffness matrices (i.e.,

submatrices of the global stiffness matrix) are updated, and (ii) sensitivities with respect to correction factors are easy to calculate.

3.2.2.3 Damage Functions

In FEMU, if a large number of design variables are selected for updating, then the optimization problem may become ill-conditioned. An ill-conditioning state increases the computational expense, has convergence difficulties, and does not guarantee for a solution. Therefore, it is desired to reduce the number of design variables for a well-conditioned problem. In this context, an additional parameterization method through damage functions, which describes a relationship between design variables ($\mathbf{p}$) and correction factors ($\mathbf{a}$), can be used. Herein, correction factors are specified with predefined damage functions instead of independent values for all elements; thus, the number of design variables is reduced. In addition to this effect, damage functions ensure to obtain more realistic and physically meaningful correction factor distributions by preventing neighboring elements to be updated independently from each other (i.e., presence of damage on an element also affects neighboring elements).

Mainly, there exist two types of damage functions. In the first type, damage functions are defined by piecewise functions (can be linear or higher order polynomials) that are formed by a combination of fixed shape functions (i.e., no shape parameters are required) which differ from zero only over a limited area of the FE model and equal to zero elsewhere. In the second type, parameterized shape functions with characteristic patterns, which are determined in the updating process, are used to form damage functions (i.e., shape parameters, that determine the center location and width of the shape function, are required). In the scope of this thesis, only the linear piecewise formed damage functions (i.e., the first type) are used; therefore, equations are simplified in accordance with this type.

According to this approach, correction factors are supposed to vary continuously over a FE model and approximated by a linear combination of damage functions as given in Equation 3.13.

$$a^e = \sum_{i=1}^{n} p_i N_i\left(x^e\right) \tag{3.13}$$

where p_i represents the multiplication factors (equals to the design variables p_i that are updated iteratively), N_i is the damage function, x^e is the geometrical coordinate of the center of element e, and n represents the number of damage functions. Consequently, $N_i\left(x^e\right)$ represents the value of the i^{th} damage function at point x^e of element e, which also defines a relationship between the correction factor and element. Remind that n should be much smaller than n_e (the number of elements wanted to be updated) for a well-conditioned problem. According to Equation 3.13, the continuous correction factor is discretized for each individual element (i.e., corresponding a constant value in the center of each element), and once the multiplication factor is determined, it is possible to calculate the correction factor. Equivalent matrix notation of Equation 3.13 is given in Equation 3.14.

$$\mathbf{a}_{n_e \times 1} = \left[\mathbf{N}\right]_{n_e \times n} \boldsymbol{p}_{n \times 1} \tag{3.14}$$

or the full-length expression is presented in Equation 3.15.

$$\begin{bmatrix} a^1 \\ a^2 \\ a^3 \\ a^4 \\ \vdots \\ a^{n_e} \end{bmatrix}_{n_e \times 1} = \begin{bmatrix} N_1(x^1) & \cdots & N_n(x^1) \\ N_1(x^2) & \cdots & N_n(x^2) \\ N_1(x^3) & \cdots & N_n(x^3) \\ N_1(x^4) & \cdots & N_n(x^4) \\ \vdots & \cdots & \vdots \\ N_1(x^{n_e}) & \cdots & N_n(x^{n_e}) \end{bmatrix}_{n_e \times n} \begin{bmatrix} p_1 \\ p_2 \\ p_3 \\ p_4 \\ \vdots \\ p_n \end{bmatrix}_{n \times 1} \tag{3.15}$$

In the case of independent damage functions for each element (i.e., updating all the elements separately), $\mathbf{N}$ becomes an identity matrix and n equals to n_e. Thus, Equation 3.15 can be reformed as in Equation 3.16. Here, a zero value indicates that there is no relationship between the relevant element and damage function (i.e., each element has only its own damage function).

$$\begin{bmatrix} a^1 \\ a^2 \\ a^3 \\ a^4 \\ \vdots \\ a^{n_e} \end{bmatrix}_{n_e \times 1} = \begin{bmatrix} 1 & 0 & \cdots & 0 \\ 0 & 1 & \cdots & 0 \\ 0 & 0 & \cdots & 0 \\ 0 & 0 & \cdots & 0 \\ \vdots & & \cdots & \vdots \\ 0 & 0 & \cdots & 1 \end{bmatrix}_{n_e \times n_e} \begin{bmatrix} p_1 \\ p_2 \\ p_3 \\ p_4 \\ \vdots \\ p_n \end{bmatrix}_{n_e \times 1} \rightarrow \begin{bmatrix} a^1 \\ a^2 \\ a^3 \\ a^4 \\ \vdots \\ a^{n_e} \end{bmatrix}_{n_e \times 1} = \begin{bmatrix} p_1 \\ p_2 \\ p_3 \\ p_4 \\ \vdots \\ p_n \end{bmatrix}_{n_e \times 1} \tag{3.16}$$

Sometimes it is desired to assign a single correction factor for a set of elements of a FE model (e.g., neighboring and/or symmetric elements that are expected to undergo similar variations during the model updating process, elements that are expected to have similar damage patterns, etc.). The effects of this case on damage functions can be easily clarified by an example. Assume a beam member consisting of 4 finite elements. In the case of updating all the elements independently, **N** matrix and corresponding corrections factors can be written as

$$\begin{bmatrix} a^1 \\ a^2 \\ a^3 \\ a^4 \end{bmatrix}_{4 \times 1} = \begin{bmatrix} 1 & 0 & 0 & 0 \\ 0 & 1 & 0 & 0 \\ 0 & 0 & 1 & 0 \\ 0 & 0 & 0 & 1 \end{bmatrix}_{4 \times 4} \begin{bmatrix} p_1 \\ p_2 \\ p_3 \\ p_4 \end{bmatrix}_{4 \times 1} \rightarrow \begin{bmatrix} a^1 \\ a^2 \\ a^3 \\ a^4 \end{bmatrix}_{4 \times 1} = \begin{bmatrix} p_1 \\ p_2 \\ p_3 \\ p_4 \end{bmatrix}_{4 \times 1} \tag{3.17}$$

If it is desired to assign a single correction factor for the 1st and 3rd finite elements (maybe they are expected to have similar damage patterns), Equation 3.17 becomes as follows

$$\begin{bmatrix} a^1 \\ a^2 \\ a^3 \\ a^4 \end{bmatrix}_{4 \times 1} = \begin{bmatrix} 1 & 0 & 0 \\ 0 & 1 & 0 \\ 1 & 0 & 0 \\ 0 & 0 & 1 \end{bmatrix}_{4 \times 3} \begin{bmatrix} p_1 \\ p_2 \\ p_4 \end{bmatrix}_{3 \times 1} \rightarrow \begin{bmatrix} a^1 \\ a^2 \\ a^3 \\ a^4 \end{bmatrix}_{4 \times 1} = \begin{bmatrix} p_1 \\ p_2 \\ p_1 \\ p_4 \end{bmatrix}_{4 \times 1} \tag{3.18}$$

It is clear from Equation 3.18 that the 1st and 3rd finite elements have the same correction factors (i.e., $a^1 = p_1$ and $a^3 = p_1$), and the number of design variables is reduced to 3 from 4.

Note that the accuracy of the updating results is based on the coarseness and number of the damage functions, and a continuous smoother correction factor distribution can be ensured by using more damage functions. Alternatively, higher order damage functions having different shapes can also be used for this purpose. Both increase the number of unknown parameters (design variables) which may lead to computational expense and ill-conditioned problem; therefore, a balance between the condition of the optimization problem and the desired accuracy should be maintained. In this context, model updating can be performed in two steps: (i) First, updating is performed by using coarse damage functions. (ii) Then, additional updating is conducted, in which only the elements wanted to be obtained in detail are corrected, by using finer damage functions.

For example, a set of seven mono-dimensional triangular-like damage functions (i.e., have one dimension along the FE model) are presented in Figure 3.2. The global damage function is constituted by combining them in a piecewise linear function. From this piecewise linear function, the continuous distribution of the correction factors can be approximated.

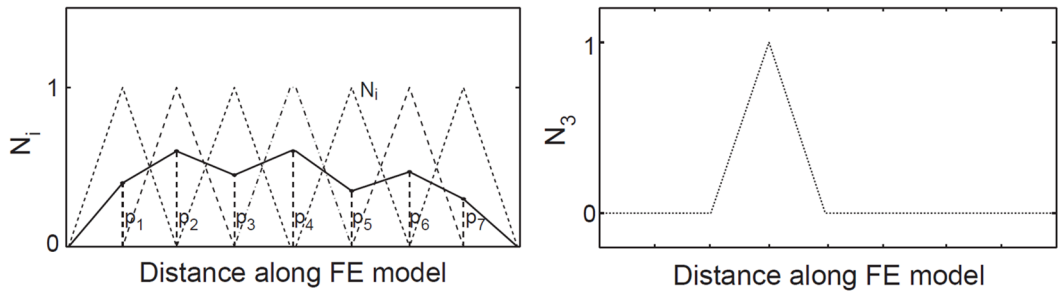

(a) (b)

Figure 3.2 (a) Set of seven triangular-like damage functions (dashed line) with continuous piecewise linear function (solid line) and (b) one isolated damage function (Teughels & De Roeck, 2004)

Note that mono-dimensional damage functions are not convenient for systems with planar elements (e.g., shell, membrane, etc.). In this context, bi-dimensional damage functions (e.g., bi-dimensional linear, bi-dimensional step, bi-dimensional-triangular, etc.) should be used to perform model updating.

3.2.3 Sensitivity (Jacobian) Matrix

Since the nonlinear least squares problem is solved with an iterative sensitivity-based optimization approach, the sensitivity matrix (a.k.a. the Jacobian matrix), which determines the rate of change in residuals with respect to changes in design variables, needs to be calculated in each iteration (Nocedal & Wright, 1999). In other words, sensitivities of residuals with respect to design variables should be calculated. The Jacobian matrix ($\mathbf{J_P}$) consists of the first-order derivatives of each residual r_j in residual vector with respect to each design variable p_i and calculated as follows

$$\left[\mathbf{J_P}\right]_{m\times n} = \begin{bmatrix} \frac{\delta r_1(\mathbf{p})}{\delta p_1} & \frac{\delta r_1(\mathbf{p})}{\delta p_2} & \cdots & \frac{\delta r_1(\mathbf{p})}{\delta p_n} \\ \frac{\delta r_2(\mathbf{p})}{\delta p_1} & \frac{\delta r_2(\mathbf{p})}{\delta p_2} & \cdots & \frac{\delta r_2(\mathbf{p})}{\delta p_n} \\ \vdots & \vdots & \ddots & \vdots \\ \frac{\delta r_m(\mathbf{p})}{\delta p_1} & \frac{\delta r_m(\mathbf{p})}{\delta p_2} & \cdots & \frac{\delta r_m(\mathbf{p})}{\delta p_n} \end{bmatrix}_{m\times n} \tag{3.19}$$

where $m = m_f + m_s$ (summation of the eigenfrequency and mode shape residual components), and n is the number of design variables $\mathbf{p}$. Based on the relationship between $\mathbf{a}$ and $\mathbf{p}$ presented in Equation 3.14, each component of the sensitivity matrix is determined by chain rule, and shown in Equation 3.20.

$$\frac{\delta r_j(\mathbf{p})}{\delta p_i} = \sum_{e=1}^{n_e} \frac{\delta r_j}{\delta a^e}\frac{\delta a^e}{\delta p_i} = \sum_{e=1}^{n_e} \frac{\delta r_j}{\delta a^e} N_i\left(x^e\right) \tag{3.20}$$

In the scope of this thesis, since the residual vector is discussed in terms of modal parameters (i.e., eigenfrequency and mode shape residuals), their sensitivities with respect to the design variables should be determined. It can be realized by taking derivatives of Equations 3.5 and 3.6 with respect to the correction factors. The resultant expressions are given in Equations 3.21 and 3.22 for eigenfrequency and mode shape residuals, respectively.

$$\frac{\delta \mathbf{r}_f}{\delta a^e} = \frac{1}{\tilde{\lambda}_j} \frac{\delta \lambda_j}{\delta a^e} \tag{3.21}$$

$$\frac{\delta \mathbf{r}_s}{\delta a^e} = \frac{1}{\phi_j^r} \frac{\delta \phi_j^l}{\delta a^e} - \frac{\phi_j^l}{\left(\phi_j^r\right)^2} \frac{\delta \phi_j^r}{\delta a^e} \tag{3.22}$$

In equations, $\frac{\delta \lambda_j}{\delta a^e}$ and $\frac{\delta \phi_j}{\delta a^e}$ terms are the eigenvalue and mode shape sensitivities, respectively (a.k.a. modal sensitivities), and can be calculated analytically with the formulas developed by Fox & Kapoor (1968). Note that the expressions are derived from an undamped eigenvalue problem under the mass-normalized mode shape assumption. All the equations are taken from Maia et al. (1997) and Teughels (2003).

Before the sensitivity equations, it is beneficial to recall some of the important expressions encountered in the dynamics of structures (Chopra, 2012). Let $\mathbf{K}$ and $\mathbf{M}$ be the system stiffness and mass matrices, respectively. Due to the orthogonality conditions of modes, Equation 3.23 can be written.

$$\phi_i^T \mathbf{K} \phi_j = 0; \quad \phi_i^T \mathbf{M} \phi_j = 0 \quad \text{with} \quad i \neq j \tag{3.23}$$

In the case of mass-normalized mode shapes, Equation 3.24 is satisfied.

$$\phi_i^T \mathbf{M} \phi_i = 1 \tag{3.24}$$

3.2.3.1 Sensitivity of Eigenvalues

Let ϕ_j and λ_j, which are the functions of correction factors, be a solution for the undamped eigenvalue problem as given in Equation 3.25.

$$\mathbf{K} \phi_j = \lambda_j \mathbf{M} \phi_j \tag{3.25}$$

Premultiplying Equation 3.25 by ϕ_j^T results in

$$\phi_j^T[\mathbf{K}-\lambda_j\mathbf{M}]\phi_j=0 \tag{3.26}$$

Differentiating Equation 3.26 with respect to a^e gives

$$\frac{\delta\phi_j^T}{\delta a^e}[\mathbf{K}-\lambda_j\mathbf{M}]\phi_j+\phi_j^T\frac{\delta[\mathbf{K}-\lambda_j\mathbf{M}]}{\delta a^e}\phi_j+\phi_j^T[\mathbf{K}-\lambda_j\mathbf{M}]\frac{\delta\phi_j}{\delta a^e}=0 \tag{3.27}$$

Since $\mathbf{K}$ and $\mathbf{M}$ are symmetric matrices, $[\mathbf{K}-\lambda_j\mathbf{M}]\phi_j$ and $\phi_j^T[\mathbf{K}-\lambda_j\mathbf{M}]$ terms are equal to each other. From Equation 3.25, first and third terms of Equation 3.27 are equal to zero and thus

$$\phi_j^T\frac{\delta[\mathbf{K}-\lambda_j\mathbf{M}]}{\delta a^e}\phi_j=0 \tag{3.28}$$

Equation 3.28 can be rewritten as

$$\phi_j^T\left[\frac{\delta\mathbf{K}}{\delta a^e}-\frac{\delta\lambda_j}{\delta a^e}\mathbf{M}-\lambda_j\frac{\delta\mathbf{M}}{\delta a^e}\right]\phi_j=0 \tag{3.29}$$

Due to the relationship given in Equation 3.24, Equation 3.29 becomes

$$\phi_j^T\frac{\delta\mathbf{K}}{\delta a^e}\phi_j-\frac{\delta\lambda_j}{\delta a^e}-\lambda_j\phi_j^T\frac{\delta\mathbf{M}}{\delta a^e}\phi_j=0 \tag{3.30}$$

Finally, the sensitivity of eigenvalues is obtained as

$$\frac{\delta\lambda_j}{\delta a^e}=\phi_j^T\left[\frac{\delta\mathbf{K}}{\delta a^e}-\lambda_j\frac{\delta\mathbf{M}}{\delta a^e}\right]\phi_j \tag{3.31}$$

3.2.3.2 Sensitivity of Mode Shapes

The mode shape sensitivity can be stated as a linear combination of the mode shape vectors themselves. The mode shape vectors are linearly independent and therefore can be used as basis vectors as given in Equation 3.32.

$$\frac{\delta\phi_j}{\delta a^e} = \sum_{q=1}^{d} \alpha_{jq}^e \phi_q \tag{3.32}$$

where d indicates the order of the analytical model (i.e., number of modes). Differentiating Equation 3.25 with respect to correction factor gives

$$\frac{\delta[\mathbf{K} - \lambda_j \mathbf{M}]}{\delta a^e}\phi_j + [\mathbf{K} - \lambda_j \mathbf{M}]\frac{\delta\phi_j}{\delta a^e} = 0 \tag{3.33}$$

Substituting Equation 3.32 in Equation 3.33 leads to

$$\frac{\delta[\mathbf{K} - \lambda_j \mathbf{M}]}{\delta a^e}\phi_j + [\mathbf{K} - \lambda_j \mathbf{M}]\sum_{q=1}^{d} \alpha_{jq}^e \phi_q = 0 \tag{3.34}$$

Alternatively

$$\sum_{q=1}^{d} \alpha_{jq}^e [\mathbf{K} - \lambda_j \mathbf{M}]\,\phi_q = -\frac{\delta[\mathbf{K} - \lambda_j \mathbf{M}]}{\delta a^e}\phi_j \tag{3.35}$$

Premultiplying Equation 3.35 by ϕ_s^T, where $s \neq j$, gives Equation 3.36.

$$\sum_{q=1}^{d} \alpha_{jq}^e \phi_s^T [\mathbf{K} - \lambda_j \mathbf{M}]\,\phi_q = -\phi_s^T \frac{\delta[\mathbf{K} - \lambda_j \mathbf{M}]}{\delta a^e}\phi_j \tag{3.36}$$

By the relationships given in Equations 3.23, 3.24, and 3.25, the left-hand side of Equation 3.36 is equal to zero except for $s = q$.

$$\alpha_{jq}^e \left[\lambda_q - \lambda_j\right] = -\phi_q^T \frac{\delta[\mathbf{K} - \lambda_j \mathbf{M}]}{\delta a^e}\phi_j \quad \text{for} \quad q \neq j \tag{3.37}$$

Expanding the right-hand side of Equation 3.37 gives

$$\alpha_{jq}^e \left[\lambda_q - \lambda_j\right] = -\phi_q^T \frac{\delta \mathbf{K}}{\delta a^e}\phi_j + \frac{\delta\lambda_j}{\delta a^e}\phi_q^T \mathbf{M}\phi_j + \lambda_j \phi_q^T \frac{\delta \mathbf{M}}{\delta a^e}\phi_j \tag{3.38}$$

As $q \neq j$, the second term of Equation 3.38 is zero and so

$$\alpha_{jq}^{e} = -\frac{1}{\left[\lambda_q - \lambda_j\right]} \phi_q^T \left[\frac{\delta \mathbf{K}}{\delta a^e} - \lambda_j \frac{\delta \mathbf{M}}{\delta a^e}\right] \phi_j \quad \text{for} \quad q \neq j \tag{3.39}$$

It can be seen from Equations 3.28 and 3.37 that the coefficient α_{jq}^{e} has to be calculated separately in the case of $q = j$. Differentiating $\phi_j^T \mathbf{M} \phi_j = 1$ with respect to a^e leads to

$$\frac{\delta \phi_j^T}{\delta a^e} \mathbf{M} \phi_j + \phi_j^T \frac{\delta \mathbf{M}}{\delta a^e} \phi_j + \phi_j^T \mathbf{M} \frac{\delta \phi_j}{\delta a^e} = 0 \tag{3.40}$$

Since $\mathbf{M}$ is a symmetric matrix, first and third terms of Equation 3.40 are equal to each other, thus Equation 3.41 can be obtained.

$$2\phi_j^T \mathbf{M} \frac{\delta \phi_j}{\delta a^e} = -\phi_j^T \frac{\delta \mathbf{M}}{\delta a^e} \phi_j \tag{3.41}$$

Substituting Equation 3.32 in Equation 3.41 gives

$$2\phi_j^T \mathbf{M} \sum_{q=1}^{d} \alpha_{jq}^{e} \phi_q = -\phi_j^T \frac{\delta \mathbf{M}}{\delta a^e} \phi_j \tag{3.42}$$

Alternatively

$$2\sum_{q=1}^{d} \alpha_{jq}^{e} \phi_j^T \mathbf{M} \phi_q = -\phi_j^T \frac{\delta \mathbf{M}}{\delta a^e} \phi_j \tag{3.43}$$

Using the relationships given in Equations 3.23 and 3.24, Equation 3.44 can be obtained.

$$\alpha_{jj}^{e} = -\frac{1}{2} \phi_j^T \frac{\delta \mathbf{M}}{\delta a^e} \phi_j \tag{3.44}$$

By assembling Equations 3.39 and 3.44, and substituting them into Equation 3.32, the sensitivity of mode shapes is calculated as

$$\frac{\delta\phi_j}{\delta a^e} = \sum_{q=1;\, q\neq j}^{d}\left(\frac{\phi_q}{\lambda_j-\lambda_q}\phi_q^T\left[\frac{\delta \mathbf{K}}{\delta a^e}-\lambda_j\frac{\delta \mathbf{M}}{\delta a^e}\right]\phi_j\right)-\frac{\phi_j}{2}\phi_j^T\frac{\delta \mathbf{M}}{\delta a^e}\phi_j \tag{3.45}$$

3.2.3.3 Sensitivities of Eigenfrequency and Mode Shape Residuals

By using the relationship in Equation 3.11, the following expressions can be written

$$\frac{\delta \mathbf{K}}{\delta a^e} = -\mathbf{K}_{ref}^e = \frac{-\mathbf{K}^e}{(1-a^e)}; \qquad \frac{\delta \mathbf{M}}{\delta a^e} = -\mathbf{M}_{ref}^e = \frac{-\mathbf{M}^e}{(1-a^e)} \tag{3.46}$$

Combining Equations 3.20, 3.21, 3.31, and 3.46 gives the sensitivity equations of eigenfrequency residuals (Equations 3.47 and 3.48).

$$\frac{\delta r_j(\mathbf{p})}{\delta p_i} = \sum_{e=1}^{n_e}\left(\frac{1}{\tilde{\lambda}_j}\frac{\delta\lambda_j}{\delta a^e}\right)N_i\left(x^e\right) \tag{3.47}$$

$$\frac{\delta\lambda_j}{\delta a^e} = \phi_j^T\left[\frac{-\mathbf{K}^e}{(1-a^e)}-\lambda_j\frac{-\mathbf{M}^e}{(1-a^e)}\right]\phi_j \tag{3.48}$$

In the case where the mass properties are assumed to be known and to remain unchanged during the updating process, the $\frac{\delta \mathbf{M}}{\delta a^e}$ term equals to zero. Hereby, Equation 3.48 transforms into Equation 3.49 (i.e., only stiffness parameter updating).

$$\frac{\delta\lambda_j}{\delta a^e} = \phi_j^T\left[\frac{-\mathbf{K}^e}{(1-a^e)}\right]\phi_j \tag{3.49}$$

Combining Equations 3.20, 3.22, 3.45, and 3.46 gives the sensitivity equations of mode shape residuals (Equations 3.50 and 3.51).

$$\frac{\delta r_j(\mathbf{p})}{\delta p_i} = \sum_{e=1}^{n_e}\left(\frac{1}{\phi_j^r}\frac{\delta\phi_j^l}{\delta a^e}-\frac{\phi_j^l}{(\phi_j^r)^2}\frac{\delta\phi_j^r}{\delta a^e}\right)N_i\left(x^e\right) \tag{3.50}$$

$$\frac{\delta\phi_j}{\delta a^e} = \sum_{q=1;\, q\neq j}^{d} \left(\frac{\phi_q}{\lambda_j - \lambda_q} \phi_q^T \left[\frac{-\mathbf{K}^e}{(1-a^e)} - \lambda_j \frac{-\mathbf{M}^e}{(1-a^e)} \right] \phi_j \right) - \frac{\phi_j}{2} \phi_j^T \frac{-\mathbf{M}^e}{(1-a^e)} \phi_j \qquad (3.51)$$

In the case of only stiffness parameter updating, Equation 3.51 transforms into Equation 3.52.

$$\frac{\delta\phi_j}{\delta a^e} = \sum_{q=1;\, q\neq j}^{d} \left(\frac{\phi_q}{\lambda_j - \lambda_q} \phi_q^T \left[\frac{-\mathbf{K}^e}{(1-a^e)} \right] \phi_j \right) \qquad (3.52)$$

In sensitivity analyses, order of the analytical model (d), which is independent of the modes that are used for residuals, should be selected as high as possible (i.e., much higher than the number of modes that is used for residuals) for a sensitivity matrix including contributions of more modes (i.e., including more information). By this way, the obtained sensitivity matrix is more accurate and more representative of the investigated system, which in return improves the updating performance. On the other hand, since the contributions of higher modes are low, the provided information decreases with the increasing mode number. Therefore, a sufficiently accurate but not inefficiently costly calculation should be performed.

Note that it is not possible to obtain element stiffness matrices $\mathbf{K}^e$ from all FE packages; however, nodal forces $\mathbf{F}_j^e$ are provided by any FE package. In such cases, the equations above should be revised by using the $\mathbf{F}_j^e = \mathbf{K}^e \phi_j$ transformation, which means substituting $\mathbf{K}^e \phi_j$ with $\mathbf{F}_j^e$ in all equations.

If the residual vector is weighted, as presented by Equation 3.7, the sensitivity matrix should also be weighted in a similar way. The weighted sensitivity matrix is calculated as in Equation 3.53.

$$\mathbf{W}^{1/2} \mathbf{J_P} \qquad (3.53)$$

If $\mathbf{W}$ is a diagonal matrix, Equation 3.53 can be equivalently written as

$$w_j \left(\mathbf{J_P} \right)_j \tag{3.54}$$

which means to multiply the j^{th} row of the sensitivity matrix (related to the j^{th} residual) by the corresponding weighting factor w_j.

It should be stated that an approximate calculation of the components of the sensitivity matrix can be obtained by the finite difference method. Formulation is presented in Equation 3.55.

$$\frac{\delta r_j(\mathbf{p})}{\delta p_i} = \frac{r_j(\mathbf{p}+\Delta\mathbf{p}) - r_j(\mathbf{p}-\Delta\mathbf{p})}{2\Delta\mathbf{p}} \tag{3.55}$$

where $\Delta\mathbf{p}$ is the sufficiently small design parameter step. It is clear that the method requires two additional modal analysis tasks (i.e., one for $\mathbf{p}+\Delta\mathbf{p}$ and one for $\mathbf{p}-\Delta\mathbf{p}$) for each column of the sensitivity matrix at each iteration. That's why this method is computationally expensive, especially for the systems with higher number of design variables, and commonly avoided in practice.

3.2.3.4 Detectability Index

Once the sensitivity matrix is calculated, it can be used to determine detectability indices of the design variables as follows (Weber et al., 2007)

$$D_j = \left\| \mathbf{S}_j \right\| \tag{3.56}$$

where $\|.\|$ denotes the Euclidean norm, D_j represents the detectability index of the j^{th} design variable, and $\mathbf{S}_j$ is the j^{th} column vector of the sensitivity matrix (i.e., corresponding to the j^{th} design variable). The detectability index provides information about the sensitivities of the residuals with respect to the design variables. In other words, detectable elements are more effective on the residuals (i.e., a unit change in a detectable element causes more changes in residuals). By the light of the detectability index, it is possible to get feelings on how responses of a model are influenced by

changes of model parameters, to decide whether a parameter should be selected for updating or not, and to determine where or/and how to assign design variables. As noted earlier, a response sensitive to a parameter (i.e., a detectable parameter) does not automatically imply that this parameter has to be included in the updating process. In other words, if the value of a parameter is already adequately representing the true value, then there is no reason to update it.

3.2.3.5 Condition of the Jacobian Matrix

In FE model updating, condition status of the Jacobian (sensitivity) matrix is an important issue. It can be quantified by computing the condition number of the Jacobian matrix (i.e., ratio of the largest and smallest singular values of the matrix), which measures the sensitivity of the solution to errors (or changes) in the data. A matrix with a small condition number (close to 1) is said to be well-conditioned and is far from being singular, whereas a matrix with a large condition number is said to be ill-conditioned and is nearly singular. In FE model updating, the ill-conditioning state is undesired since it increases the computational expense, has convergence difficulties, and does not guarantee for a solution.

An optimization problem has a unique solution if it is overdetermined (i.e., the number of residuals is higher than the number of design variables (n<m) and the Jacobian matrix has full-rank (i.e., having linearly independent columns), which means that the matrix $\mathbf{J}_\mathbf{P}^\mathrm{T}\mathbf{W}\mathbf{J}_\mathbf{P}$ is nonsingular or, equivalently $\det\left(\mathbf{J}_\mathbf{P}^\mathrm{T}\mathbf{W}\mathbf{J}_\mathbf{P}\right)\neq 0$.

If $\det\left(\mathbf{J}_\mathbf{P}^\mathrm{T}\mathbf{W}\mathbf{J}_\mathbf{P}\right)=0$ (which corresponds to rank deficiency), the case where some columns of the Jacobian matrix are linearly dependent, there is no unique solution (i.e., several minimum points exist). In the case of some columns are close to being linearly related, the problem has a unique minimum point, but this point is not very prominent. Near linear dependency of the columns makes the Jacobian matrix to be ill-conditioned. Unfortunately, the Jacobian matrix is prone to be ill-conditioned since changes in neighboring and/or symmetric elements of a FE model may have almost

same influences on residuals (i.e., having similar detectabilities). This situation causes linearly dependent columns in the Jacobian matrix. If the discretization becomes finer (a.k.a. over-parameterization), this effect gets stronger (Beck & Arnold, 1977; Fritzen et al., 1998). To remedy this problem, grouping elements as substructures is a good option. In addition, using a higher analytical model order (d) in sensitivity calculations enables to distinguish the effects of each element in the model, which in return serves to obtain linear independent columns in the Jacobian matrix.

Insensitive residuals (responses) also lead to an ill-conditioned Jacobian matrix. It is desired that small variations in design variables cause large changes in residuals (i.e., highly sensitive residuals with respect to design variables). Otherwise, it may be impossible to minimize the objective function and unrealistic results may exist. The problem of insensitive residuals can occur, for example, in the case of a design variable with too low or too high initial value, such that a small variation of the design variable does not alter the residuals.

As stated before, mode shapes are less sensitive to the stiffness parameters, are more difficult to accurately identify from measurements (i.e., they include higher estimation uncertainty), and are influenced more from noise than eigenfrequencies. All of these cases may result in an ill-conditioned Jacobian matrix. However, mode shapes are the indispensable components of the updating process due to their spatial information.

Existence of noise in experimental data can lead to an ill-conditioned problem. Besides, ill-conditioned problems are extremely sensitive to measurement noise. Even in the presence of low level of noise, significant changes may occur in the location of the minimum, which may result to obtain parameter values that are very different from their exact values. Therefore, the solution becomes inaccurate and said to be unstable.

Describing the non-updated model parameters (i.e., model parameters that are not aimed to be updated) by constraints (e.g., 0 and 0.00001 values for lower and upper bounds, respectively) may lead to an ill-conditioned Jacobian matrix. This is because they are still updated by the algorithm according to their bounds (i.e., in reality, they

are not updated because of their constraints) and are taken into account for sensitivity calculations together with the relevant finite elements. Therefore, only the model parameters that are really wanted to be updated should be considered, and the others should be excluded completely from the updating process.

Based on the statements above, the importance and necessity of limiting the number of design variables are revealed again. By this way, the probability to have linearly dependent columns and insensitive elements in the Jacobian matrix, which may lead to an ill-conditioned problem, can also be reduced.

3.2.4 Optimization Process

FEMU is an optimization process where a minimization problem of the objective function is solved. In this concept, definitions of the global and local minimum points are essential to interpret and evaluate the results. Namely, a global minimum (i.e., absolute minimum) is the point where the objective function has the absolute smallest value (i.e., there is not a smaller value that the objective function can have), whereas the local minimum is the point where the objective function has the smallest value in its neighborhood (i.e., there exist more smaller values that the objective function can have). In general, outcomes (solutions) of an optimization problem can be in three different forms based on the problem type (i.e., underdetermined or overdetermined, ill-conditioned or well-conditioned), which are visualized by Figure 3.3: (i) There exists one prominent global minimum point with several local minimum points. This is the case when the problem is overdetermined and well-conditioned (i.e., the desired case). It is easy to find the global minimum point (Figure 3.3 (a)). (ii) There exists one global minimum point, which is not prominent, with several local minimum points. This case may occur when the problem is ill-conditioned. It is difficult to find the global minimum point (Figure 3.3 (b)). (iii) There exist several global minimum points (i.e., infinitely many solutions). This is the case when the problem is underdetermined. It is difficult to determine which one of the global minimum points reflects the actual solution of the problem (Figure 3.3 (c)).

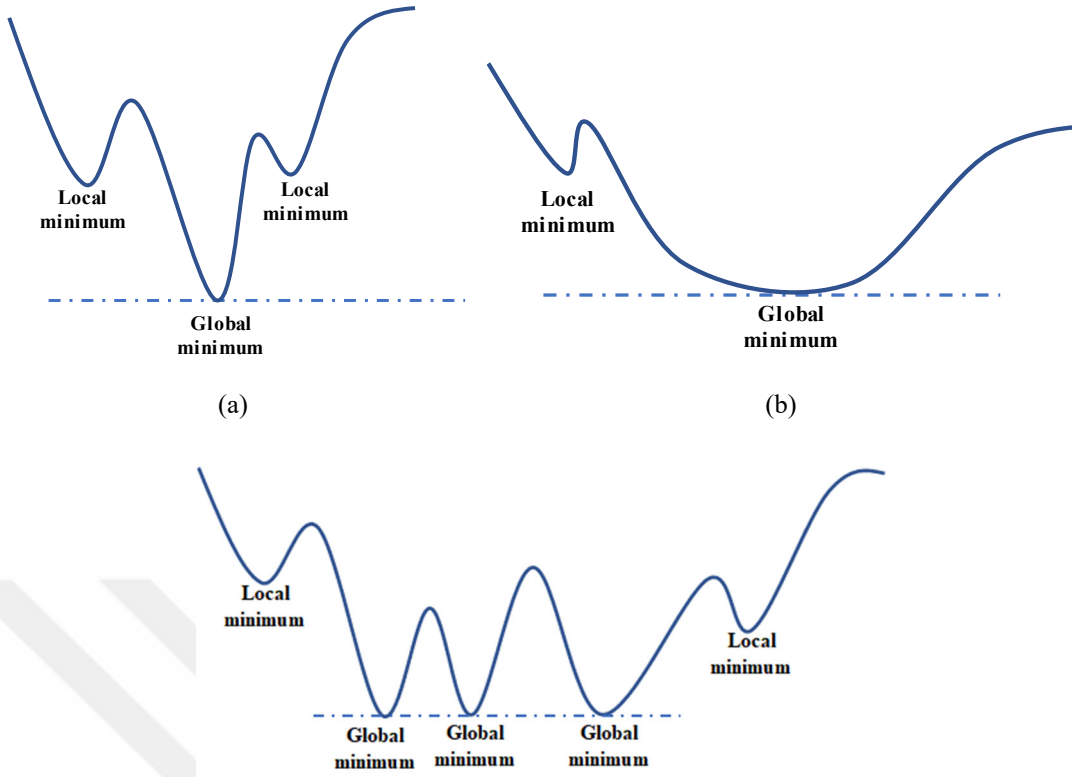

Figure 3.3 Outcomes of an optimization problem: (a) one prominent global minimum point with several local minimum points, (b) one global minimum point, which is not prominent, with several local minimum points, and (c) several global minimum points

Note that using an efficient and robust (even in the case of an ill-conditioned problem) optimization method is essential for the accuracy and reliability of the results. In this context, there exist local, global, and response surface methods in the area of optimization theory. Brief information for each method is given below.

Local optimization methods begin from a starting point (e.g., initial values of the design variables) and produce iteratively a sequence of improved estimates until a solution. They provide fast convergence since they are based on derivatives of the objective function. The basic local method is the Newton method in which the local curvature of the objective function is utilized to establish an approximate quadratic model function. The minimum of this function gives the successive point in the iterative process. Quasi-Newton, sequential quadratic programming, conjugate gradient, and augmented Lagrangian methods are the other commonly used local optimization methods. Line search and trust region strategies (algorithms) can be used

to improve their convergence (Conn et al., 2000; Nocedal & Wright, 1999). Due to their effectiveness and fast convergence property, local methods are very popular. However, they can be trapped in a local minimum and do not guarantee to find the global (absolute) minimum. Specific algorithms, which are more convenient for least squares problems, are enhanced from the general methods. They are mainly based on the fact that the Hessian calculations can be approximated by using only the first-order derivative information (Moré & Wright, 1993; Nocedal & Wright, 1999). Gauss-Newton method, which is derived from the Newton method, is known as the basic least squares method. Another commonly used method is the Levenberg-Marquardt method.

Global optimization methods are more robust methods that are more likely to find the global minimum and are less affected by the selection of the starting position (i.e., initial point). These methods are based on probabilistic searching without the usage of any gradient information. Requiring a large number of function evaluations is their main drawback. Genetic algorithms, simulated annealing, and coupled local minimizers are the commonly used global methods (Holland, 1975; Kirkpatrick et al., 1983; Suykens et al., 2001; Suykens & Vandewalle, 2002).

In response surface methods, the optimization algorithm is applied to an approximate surface of the real objective function instead of applying it directly to the objective function. The response surface is constituted by combining first- or second-order polynomials and corresponds with the real objective function in a set of sampling points. Because of these polynomials, it may be difficult to find the global minimum of an objective function having many local minimums. This issue can be overcome by using general response surface methods; however, they are feasible to the problems having a low number of design variables (Alotto et al., 1997; Pahner, 1998).

In this thesis, the optimization problem is solved iteratively by using Gauss-Newton method with trust region algorithm (Coleman & Li, 1996). A brief theoretical background of the method is presented in the following section. Herein, line search algorithm is also discussed for comparison with the trust region algorithm.

3.2.4.1 Gauss-Newton Optimization Method with Trust Region Algorithm

In Gauss-Newton method, the function $f(\mathbf{p}_k)$ to be minimized is approximated by a quadratic model $q_k(\mathbf{z})$ of truncated Taylor series about the current iterate $\mathbf{p}_k$.

$$q_k(\mathbf{z}) = f(\mathbf{p}_k) + \nabla f(\mathbf{p}_k)^T \mathbf{z} + \frac{1}{2}\mathbf{z}^T \nabla^2 f(\mathbf{p}_k)\mathbf{z} \tag{3.57}$$

where $\mathbf{z}$ indicates the step vector from $\mathbf{p}_k$, $\nabla f(\mathbf{p}_k)$ and $\nabla^2 f(\mathbf{p}_k)$ are the gradient and the Hessian of the objective function, respectively. When $\nabla^2 f(\mathbf{p}_k)$ is positive definite, $q_k(\mathbf{z})$ has a unique minimizer that can be obtained by solving the Newton equation presented in Equation 3.58.

$$\nabla^2 f(\mathbf{p}_k)\mathbf{z}_k^{GN} = -\nabla f(\mathbf{p}_k) \tag{3.58}$$

The next iterate is determined by performing the Newton step presented in Equation 3.59 and this process is repeated until the convergence is satisfied.

$$\mathbf{p}_{k+1} = \mathbf{p}_k + \mathbf{z}_k^{GN} \tag{3.59}$$

$\nabla f(\mathbf{p})$ and $\nabla^2 f(\mathbf{p})$ can be stated in terms of the Jacobian matrix and residual vector, and are presented in Equations 3.60 and 3.61.

$$\nabla f(\mathbf{p}) = \sum_{j=1}^{m} r_j(\mathbf{p}) \nabla r_j(\mathbf{p}) = \mathbf{J_P}(\mathbf{p})^T \mathbf{r}(\mathbf{p}) \tag{3.60}$$

$$\nabla^2 f(\mathbf{p}) = \mathbf{J_P}(\mathbf{p})^T \mathbf{J_P}(\mathbf{p}) + \sum_{j=1}^{m} r_j(\mathbf{p}) \nabla^2 r_j(\mathbf{p}) \approx \mathbf{J_P}(\mathbf{p})^T \mathbf{J_P}(\mathbf{p}) \tag{3.61}$$

In Gauss-Newton method, the starting point ($\mathbf{p}_0$) should be selected sufficiently close to a local solution ($\mathbf{p}^*$) where $\nabla^2 f(\mathbf{p}^*)$ is positive definite. Otherwise, convergence difficulties may occur. This kind of challenges can be overcome by the

implementation of the line search or trust region strategies which improve the robustness of the optimization method (Conn et al., 2000; Nocedal & Wright, 1999).

Line search methods are based on determining a direction at each iteration and searching along this direction for a new iterate with a lower function value. The iterates are generated by Equation 3.62.

$$\mathbf{p}_{k+1} = \mathbf{p}_k + \alpha_k \mathbf{z}_k \tag{3.62}$$

where $\mathbf{z}_k$ represents the search direction and α_k is the step length (i.e., the distance to move along $\mathbf{z}_k$), which is greater than zero and selected so that $f(\mathbf{p}_{k+1}) < f(\mathbf{p}_k)$. α_k can be determined by minimizing the function given in Equation 3.63. Once the new iterate is obtained ($\mathbf{p}_{k+1}$), the process is repeated by a new search direction and step length.

$$\min_{\alpha>0} \phi(\alpha) = f(\mathbf{p}_k + \alpha \mathbf{z}_k) \tag{3.63}$$

In the trust region approach, a model function m_k (Equation 3.64), which has similar behavior to that of the actual objective function f near the current point $\mathbf{p}_k$, is developed by the algorithm. In addition, a region that surrounds $\mathbf{p}_k$ and where the model function can be trusted is determined (i.e., trust region). The trust region is a sphere described by $\| \mathbf{z} \| < \Delta$, where $\Delta > 0$ is its radius (i.e., $\mathbf{z}$ lies inside the trust region). By minimizing the model function in Equation 3.64, it is possible to compute a candidate for the new iterate ($\mathbf{p}_{k+1}$).

$$m_k(\mathbf{z}) = f(\mathbf{p}_k) + \nabla f(\mathbf{p}_k)^T \mathbf{z} + \frac{1}{2} \mathbf{z}^T \nabla^2 f(\mathbf{p}_k) \mathbf{z} \quad \mathbf{z} \text{ lies inside the trust region} \tag{3.64}$$

If the candidate causes an insufficient decrease in f, which means that the model is not suitable for f, Equation 3.64 is solved again by using a smaller trust region; otherwise, the candidate is approved as a new iterate from which the process reiterates. Herein, the trust region is increased since the model is reliable.

According to the agreement between the actual and predicted reductions in f as measured by the ratio presented in Equation 3.65, Δ_k is adjusted at each iteration.

$$\rho_k = \frac{f(\mathbf{p}_k) - f(\mathbf{p}_k + \mathbf{z}_k)}{f(\mathbf{p}_k) - m_k(\mathbf{z}_k)} \tag{3.65}$$

If $\rho_k \approx 1$ (i.e., indicator of good agreement), then Δ_k is increased. If ρ_k is small or negative (i.e., indicator of poor agreement), then Δ_k is decreased. Else, Δ_k remains unchanged. In addition, ρ_k is used for the decision to accept a step $\mathbf{z}_k$. Namely, if ρ_k is greater than a small positive number (e.g., $\rho_k > 0.00001$), then the $\mathbf{z}_k$ is acceptable. Otherwise, $\mathbf{z}_k$ is recomputed with a smaller trust region. Generally, the step direction changes whenever the size of the trust region is changed. On the other hand, only a single search direction is used in line search strategy.

The main difference between the line search and trust region approaches is the selection of the direction and distance of the step to the next iterate. In line search algorithm, first the direction $\mathbf{z}_k$ is fixed and then the appropriate distance α_k (step length) is determined. On the other hand, in trust region algorithm, first the maximum distance (i.e., the trust region radius Δ_k) is chosen. Afterwards, the best direction and step are sought according to this distance. In the case of unsatisfactory results, the trust region radius is reduced and a new candidate is tried out. In general, the trust region strategy is more robust and exhibits better convergence performance since it prevents the iterates from taking large steps (even in the case of an ill-conditioned problem).

In the scope of this thesis, Gauss-Newton method with trust region algorithm is performed by using the *fmincon()* function in the MATLAB's optimization toolbox (MATLAB, 2017). The first- and second-order derivatives of the objective function (i.e., the gradient and the Hessian, respectively) are calculated and provided to the *fmincon()* to improve its convergence performance. In addition, it is possible to define constraints (i.e., lower and upper bounds that the design variables have to satisfy during updating process) and initial points $\mathbf{p}_0$ (i.e., the starting points of the

optimization algorithm) for the design variables. Note that it is very important to select suitable constraints and initial points, which are close to the actual parameter values, to converge to the optimal solution (i.e., global minimum of the objective function). Otherwise, it is possible to encounter convergence difficulties and/or to be trapped in a local minimum. In addition, existence of the constraints has a beneficial effect on the solution process since it reduces the search space of the optimization algorithm.

3.3 Applicability of the Sensitivity-Based FEMU Method to Different Types of Structural Systems

It is possible to perform the sensitivity-based FEMU method on different types of structural systems. Application of the method is independent of the structure type (e.g., building, bridge, tower, dam, airport, etc.), structure size/scale (e.g., small-scale or full-scale), material (e.g., reinforced concrete, steel, masonry, etc.), loading conditions (e.g., self-weight, earthquake, wind, laboratory tested, etc.), and damage mechanisms. In the literature, there exist numerous examples of the method being applied on different types of structures, such as reinforced concrete buildings (Behmanesh et al., 2018; Moaveni et al., 2013; Song et al., 2019), bridges (Garcia-Palencia et al., 2015; Petersen & Oiseth, 2017; Teughels & De Roeck, 2004), and masonry structures (Bassoli et al., 2018; Boscato et al., 2015; Compán et al., 2017; Foti et al., 2012; Torres et al., 2017).

Although this is the case, applications of the method on real complex structural systems come with certain challenges. Some of them are summarized here: (i) Advanced numerical modeling is necessary for representing the real structural behavior. For instance, appropriate modeling of an infilled frame to take into account frame-infill interaction is necessary to present the real behavior of the system accurately. (ii) Having a dynamic test grid providing high spatial resolution is often not possible as the number of existing sensors is usually limited. Therefore, for real-life structures, a large number of sensors may be necessary for accurate registration of their dynamic responses. In addition, broad-band excitation of real-life structures due to their larger sizes is another important issue. Especially for very rigid structures,

earthquake excitation may be the only option to reveal their dynamic characteristics. (iii) Damage identification using the FEMU method after a damaging event is not always possible because the dynamic characteristics of the undamaged state may not be readily available. Therefore, important structures must be monitored continuously to capture their undamaged and damaged states. Finally, (iv) numerical models of real structures usually contain a large number of finite elements, updating all of these elements in the framework of FEMU may not be feasible. Determination of which finite element(s) to update is usually not obvious and there are usually many possibilities to choose from. Different choices may result in different scenarios. Only one of these scenarios corresponds to the actual state of the system under investigation.

3.4 Developed Code for the Sensitivity-Based FEMU Method

In order to carry out model updating and damage identification studies, the sensitivity-based FEMU method was programmed in MATLAB environment by considering the details presented in the previous sections of the thesis. For FE model analyses and extracting the parameters that are required for model updating (e.g., numerical modal parameters, element mass and stiffness matrices, etc.), FEDEASLab FE software (Flippou & Constantinides, 2004) was utilized. Note that FEDEASLab is a MATLAB based program that consists of many codes (m-files) serving different purposes (e.g., m-files for 2-D frame element, 3-D frame element, construction of stiffness and mass matrices, modal analysis, static analysis, etc.).

In the scope of the research work presented in this thesis, some modifications and add-ons (e.g., related to the extraction of element stiffness and mass matrices, 3-D modal analysis, translational and rotational spring definitions, etc.) were performed on the existing FEDEASLab m-files in order to make them suitable for the updating code. Consequently, the updating code and FEDEASLab were arranged to work in harmony. Note that they are nested due to the iterative process of the updating method (i.e., the outputs of FEDEASLab are the inputs of the updating code, and then, the outputs of the updating code become the inputs of FEDEASLab, and continues so on).

3.5 Sensitivity-Based FEMU Studies Performed on Numerical Models

This section of the thesis includes sensitivity-based FEMU studies performed on numerical models. By this way, the effectiveness and accuracy of the previously developed code are revealed. Accordingly, a single-bay, single-story, three dimensional (3-D) structural frame model consists of 10 equal length finite elements was established in FEDEASLab environment by using 3-D linear elastic Bernoulli-Euler frame elements, which have 6 DOFs per node (i.e., 3 translational and 3 rotational DOFs) (Figure 3.4). Each finite element of the model has 80x80 cm cross-sectional dimensions and 100 cm length. Material properties were set to 214 GPa and 8000 kg/m^3 for Young's modulus and mass density, respectively (i.e., the frame is made of steel). Support conditions are fixed and pinned for the left and right columns, respectively. Note that this model is considered as a reference model that can be used for further studies.

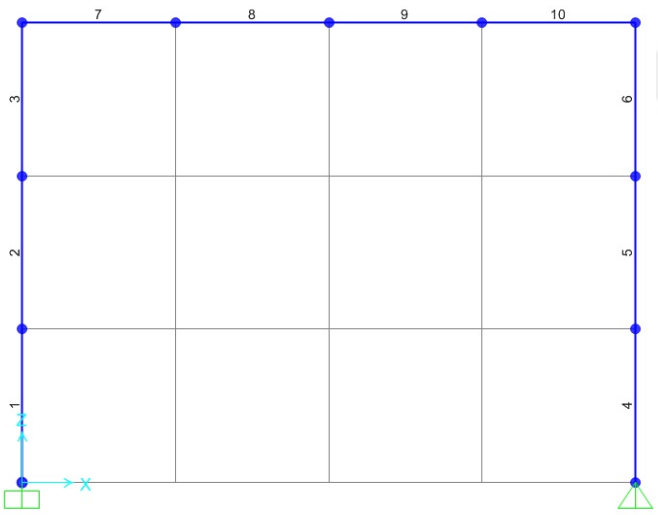

Figure 3.4 Single-bay, single-story, 3-D structural frame model

Model updating studies of this reference model were performed for 4 different cases: (i) Mass density updating, (ii) Young's modulus updating, (iii) Young's modulus updating by using less residuals, and (iv) Young's modulus updating by using less residuals and design variables. Each case is detailed in the following sections.

3.5.1 Case-I: Mass Density Updating

In this case, a new FE model was developed by reducing the mass density values of the beam member (i.e., elements denoted as 7, 8, 9, and 10 in Figure 3.4) of the reference model by 50%. Then, these changes were tried to be detected by updating the reference model. Updating was performed by using the frequency and mode shape estimations of the first 5 modes. Therefore, $\mathbf{r}_f$ has 1x5=5, $\mathbf{r}_s$ has (3x9)x5=135 (3 is the translational DOFs per node, 9 is the number of free nodes in the model), and $\mathbf{r}$ has 5+135=140 components (m=140). All of the finite elements were selected as design variables, thus n=10. Note that independent damage functions were assigned for each element (i.e., the finite elements were updated separately). Since n<m, an overdetermined problem occurs. The dimensions of the Jacobian matrix are 140x10. Model order (d) was selected as 27 (i.e., corresponding to all the numerical modes). Only reduction was allowed in design variables by defining constraints ($\mathbf{0} < \mathbf{p} < \mathbf{1}$). Weighting factors for all residuals were set to 1 in order to provide same weight. The optimization problem was solved by Gauss-Newton method with trust region algorithm. Model updating results are shown in Table 3.1.

Table 3.1 Model updating results for Case-I

Mode #	Case-I	Reference Model	Freq. Diff. [%]	MAC	Objective Function Value	Number of Iterations
	Freq. [Hz]	Freq. [Hz]				
1	18.30	15.31 (18.31)	-16 (0)	1.000 (1.000)	0.460 (8.64E-6)	5
2	53.28	44.01 (53.27)	-17 (0)	1.000 (1.000)		
3	62.79	53.56 (62.76)	-15 (0)	0.987 (1.000)		
4	200.18	152.52 (200.25)	-24 (0)	0.980 (1.000)		
5	209.50	172.73 (209.61)	-18 (0)	0.922 (1.000)		

In Table 3.1, the values in parentheses represent the ones obtained after model updating. It can be seen from the table that the optimization process is finished in 5 iterations. After the application of model updating, the objective function is minimized, frequency differences are zeroized (i.e., almost same frequency values as

the reference model are obtained), and MAC values (calculated between the reference model and Case-I) are increased. Percentage changes of the model parameters (design variables) with respect to their initial values are presented in Figure 3.5.

In the figure, the actual (i.e., 50% mass density reductions for the 7, 8, 9, and 10 numbered elements of the model) and detected (by the updating code) mass density reductions are given together. It can be concluded that the updating code detected the changes of the frame accurately in terms of location and severity. All these findings are the indicators of the success of the code.

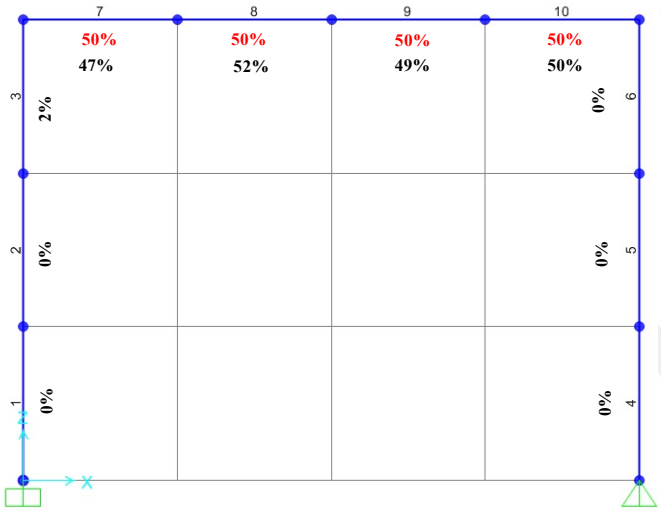

Figure 3.5 Actual (written in red) and detected (written in black) mass density reductions for Case-I

3.5.2 Case-II: Young's Modulus Updating

In this case, a new FE model was created by reducing the Young's modulus values of the reference model by different amounts (i.e., 70% for the elements #1 and #4, 40% for the elements #3 and #6, and 25% for the element #9). Then, these changes were tried to be detected by updating the reference model. It should be stated that the remaining updating conditions (e.g., residuals, design variables, weighting factors, constraints, etc.) are the same as the ones adopted in Case-I. Model updating results are shown in Table 3.2.

Table 3.2 Model updating results for Case-II

Mode #	Case-II	Reference Model	Freq. Diff. [%]	MAC	Objective Function Value	Number of Iterations
	Freq. [Hz]	Freq. [Hz]				
1	11.19	15.31 (11.19)	37 (0)	0.989 (1.000)	1.552 (7.23E-6)	11
2	32.37	44.01 (32.38)	36 (0)	0.998 (1.000)		
3	37.65	53.56 (37.64)	42 (0)	0.984 (1.000)		
4	124.76	152.52 (124.80)	22 (0)	0.985 (1.000)		
5	149.71	172.73 (149.61)	15 (0)	0.979 (1.000)		
Rank: 10 (10) **Condition Number:** 23.42 (74.42) **Determinant:** 1.20E-11 (1.10E-9)						

In Table 3.2, the values in parentheses represent the ones obtained after model updating. It can be seen from the table that the optimization process is finished in 11 iterations. After the application of model updating, the objective function is minimized, frequency differences are zeroized (i.e., almost same frequency values as the reference model are obtained), and MAC values (calculated between the reference model and Case-II) are increased. Based on the rank, condition number, and determinant calculations, the Jacobian matrix is said to be full-rank, well-conditioned, and non-singular (but nearly to be singular). Percentage changes of the model parameters (design variables) with respect to their initial values are presented in Figure 3.6.

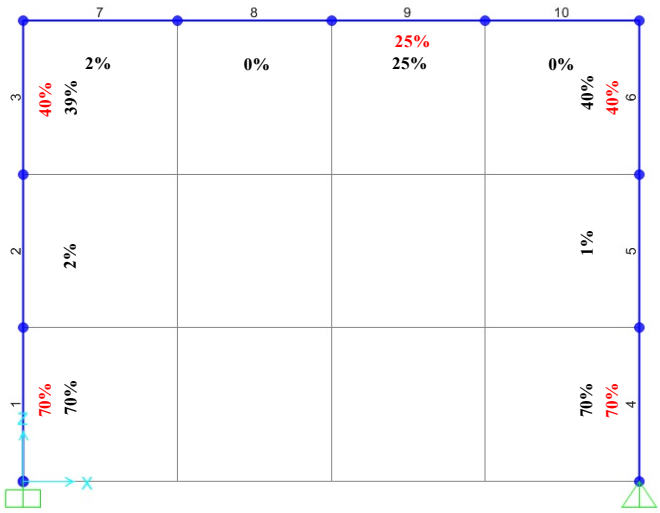

Figure 3.6 Actual (written in red) and detected (written in black) Young's modulus reductions for Case-II

In the figure, the actual (i.e., 70% for the elements #1 and #4, 40% for the elements #3 and #6, and 25% for the element #9) and detected (by the updating code) Young's modulus reductions are given together. It can be concluded that the updating code detected the changes of the frame accurately in terms of location and severity. All these findings are the indicators of the success of the code.

3.5.3 Case-III: Young's Modulus Updating by Using Less Residuals

In this case, the model used in Case-II was handled again. The only difference is the amount of the residuals; namely, only the frequency estimations of the first 5 modes were used. Therefore, $\mathbf{r}_f$ has 1x5=5 components. Since there are no mode shape residuals, $\mathbf{r}$ has 5 components too (m=5). All of the finite elements were selected as design variables, thus n=10. An underdetermined problem occurs since m<n; therefore, they may exist infinitely many solutions. The dimensions of the Jacobian matrix are 5x10. Remaining updating conditions are the same as the ones adopted in Case-II. Model updating results are given in Table 3.3.

Table 3.3 Model updating results for Case-III

Mode #	**Case-III**	**Reference Model**	**Freq. Diff. [%]**	**MAC**	**Objective Function Value**	**Number of Iterations**
	Freq. [Hz]	**Freq. [Hz]**				
1	11.19	15.31 (11.19)	37 (0)	0.989 (1.000)	1.441 (2.34E-9)	13
2	32.37	44.01 (32.37)	36 (0)	0.998 (0.999)		
3	37.65	53.56 (37.65)	42 (0)	0.984 (1.000)		
4	124.76	152.52 (124.76)	22 (0)	0.985 (0.999)		
5	149.71	172.73 (149.70)	15 (0)	0.979 (0.994)		
Rank: 5 (5) **Condition Number:** 15.40 (42.10) **Determinant:** -1.56E-90 (-2.20E-92)						

In Table 3.3, the values in parentheses represent the ones obtained after model updating. It can be seen from the table that the optimization process is finished in 13 iterations. After the application of model updating, the objective function is minimized, frequency differences are zeroized (i.e., almost same frequency values as

the reference model are obtained), and MAC values (calculated between the reference model and Case-III) are increased. Based on the rank, condition number, and determinant calculations, the Jacobian matrix is said to be full-rank, well-conditioned, and singular (i.e., there is no unique solution). Note that the Jacobian matrix is full-rank although it is singular. This occurs because of the underdetermined nature of the problem. Percentage changes of the model parameters (design variables) with respect to their initial values are presented in Figure 3.7.

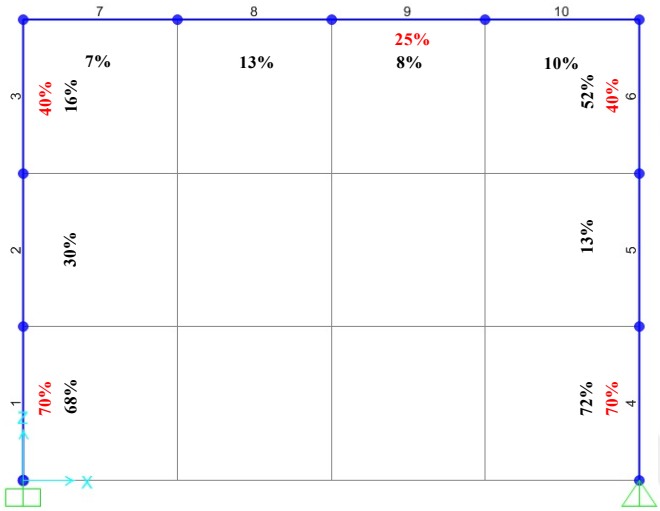

Figure 3.7 Actual (written in red) and detected (written in black) Young's modulus reductions for Case-III

In the figure, the actual (i.e., 70% for the elements #1 and #4, 40% for the elements #3 and #6, and 25% for the element #9) and detected (by the updating code) Young's modulus reductions are given together. It can be seen that the updating code couldn't detect the changes of the frame accurately despite the minimizations in the objective function and modal parameter discrepancies. This is an expected result since the problem is underdetermined. In other words, the optimization algorithm has found one of the infinite solutions.

3.5.4 Case-IV: Young's Modulus Updating by Using Less Residuals and Design Variables

In this case, the model used in Case-III was handled. The only difference is the amount of the design variables; namely, common design variables were assigned to different element groups (i.e., one for the elements #1 and #4, and one for the elements #3 and #6). Besides, only the elements, in which the predefined changes were made, were selected as design variables (i.e., the elements #1, #3, #4, #6, and #9). Consequently, 3 design variables are obtained: one for the elements #1 and #4, one for the elements #3 and #6, and one for the element #9. Since n<m (n=3, m=5), an overdetermined problem occurs. The dimensions of the Jacobian matrix are 5x3. Remaining updating conditions are the same as the ones adopted in Case-III. Model updating results are given in Table 3.4.

Table 3.4 Model updating results for Case-IV

Mode #	**Case-IV**	**Reference Model**	**Freq. Diff. [%]**	**MAC**	**Objective Function Value**	**Number of Iterations**
	Freq. [Hz]	**Freq. [Hz]**				
1	11.19	15.31 (11.19)	37 (0)	0.989 (1.000)	1.441 (7.16E-9)	12
2	32.37	44.01 (32.37)	36 (0)	0.998 (1.000)		
3	37.65	53.56 (37.65)	42 (0)	0.984 (1.000)		
4	124.76	152.52 (124.76)	22 (0)	0.985 (1.000)		
5	149.71	172.73 (149.71)	15 (0)	0.979 (1.000)		
Rank: 3 (3) **Condition Number:** 4.22 (7.09) **Determinant:** 0.09 (0.45)						

In Table 3.4, the values in parentheses represent the ones obtained after model updating. It can be seen from the table that the optimization process is finished in 12 iterations. After the application of model updating, the objective function is minimized, frequency differences are zeroized (i.e., almost same frequency values as the reference model are obtained), and MAC values (calculated between the reference model and Case-IV) are increased. Based on the rank, condition number, and determinant calculations, the Jacobian matrix is said to be full-rank, well-conditioned,

and non-singular. Note that the condition number is reduced significantly as compared to Case-III. This is because of preventing the linearly dependency of the columns of the Jacobian matrix by limiting the number of design variables. Percentage changes of the model parameters (design variables) with respect to their initial values are presented in Figure 3.8.

In the figure, the actual (i.e., 70% for the elements #1 and #4, 40% for the elements #3 and #6, and 25% for the element #9) and detected (by the updating code) Young's modulus reductions are given together. It can be concluded that the updating code detected the changes of the frame accurately in terms of location and severity. All these findings are the indicators of the success of the code.

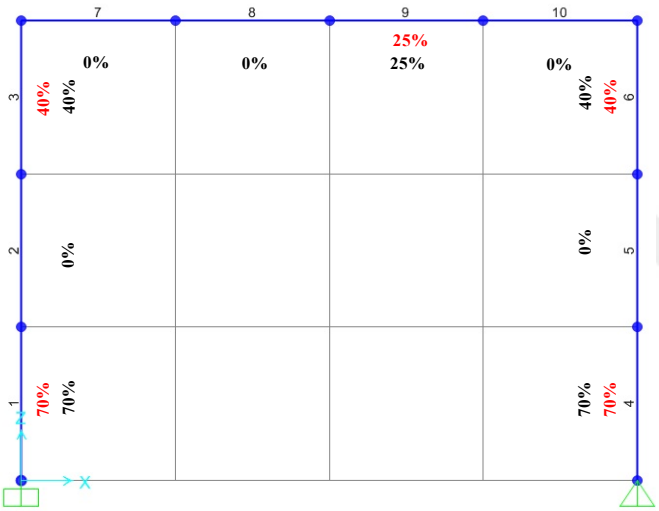

Figure 3.8 Actual (written in red) and detected (written in black) Young's modulus reductions for Case-IV

CHAPTER FOUR
STATIC AND DYNAMIC TEST RESULTS OF THE QUASI-STATICALLY TESTED REINFORCED CONCRETE FRAMES WITH DIFFERENT INFILL CONDITIONS

4.1 Introduction

In extensive studies conducted in Dokuz Eylul University Structural Mechanics Laboratory, half-scale, single-bay, single-story eight reinforced concrete (R/C) frames with different infill conditions, namely bare, locked type infilled, and standard type infilled, were tested. Studies were realized as part of a project which was supported by The Scientific and Technological Council of Turkey (TUBITAK) under the Grant #112M203. This chapter of the thesis aims to present static and dynamic test results of the frames which were quasi-statically tested under progressively increasing in-plane drifts, and after dynamically tested at some predetermined drifts. At different drift levels, therefore at different damage states, ambient vibration and white-noise (having different excitation amplitudes) tests were performed to estimate the modal parameters of the frames. An electro-dynamic shaker, positioned on the centerline of the slab for white-noise tests, was used to impose broad-band excitation. Three different output-only system identification methods, namely NExT-ERA, SSI-DATA, and EFDD were used to process the recorded dynamic response data at different damage states (i.e., theoretical backgrounds of these methods are presented in Section 2.2.3). A comparative study was performed for different frames at different damage states. Detailed visual damage inspections, which were made during quasi-static tests (i.e., discrete damage states), and their evolutions with respect to increasing drift ratios were coupled with the corresponding modal identification results. By this way, correlation studies could be performed between the identified modal parameters and occurred damages (with type, location, and extent information). Note that in the scope of this thesis, only three of the frames are discussed (i.e., one bare and two infilled frames) in the following sections.

4.2 Description of the Reinforced Concrete (R/C) Frames

One bare (i.e., no infill) and two infilled half-scale, single-bay, single-story R/C frames with partial slabs were tested under quasi-static loading conditions along their in-plane directions. The material tests provided that the concrete compressive strength is ~38 MPa (i.e., the 28-day average strength of 15x15x15 cm cubic samples) and the yield strength of the reinforcing bars are ~420 MPa. Both columns and beam members have cross-sectional dimensions of 15x25 cm, whereas the slab thickness is 6 cm. Height of the frames is 150 cm from the foundation top to the slab top, and column center-to-center span length is 225 cm (Figure 4.1 (a)). The reinforcement detailing was done using capacity design principles (Figure 4.1 (b)). Approximately 10% of the columns' axial load capacity (~120 kN load) was applied on each column to represent the upper story weights by using two separate hydraulic pistons. This axial load resulted in pre-compression effects on the columns instead of a direct increase in the mass of the frame systems. In addition to this load, 4 concrete pads (each weighing 1.38 kN) and 16 steel plates (each weighing 0.18 kN) were placed on the slab for representing a portion of the service loads. The tests were performed by applying a lateral force to the R/C frames with the usage of double-acting displacement-controlled servo-hydraulic actuator which was attached to the frames at the slab level (Figure 4.1 (c)). General views of the test setup with test equipments for one of the infilled frames are shown in Figure 4.2. Note that the same setup was used for all tests and frames.

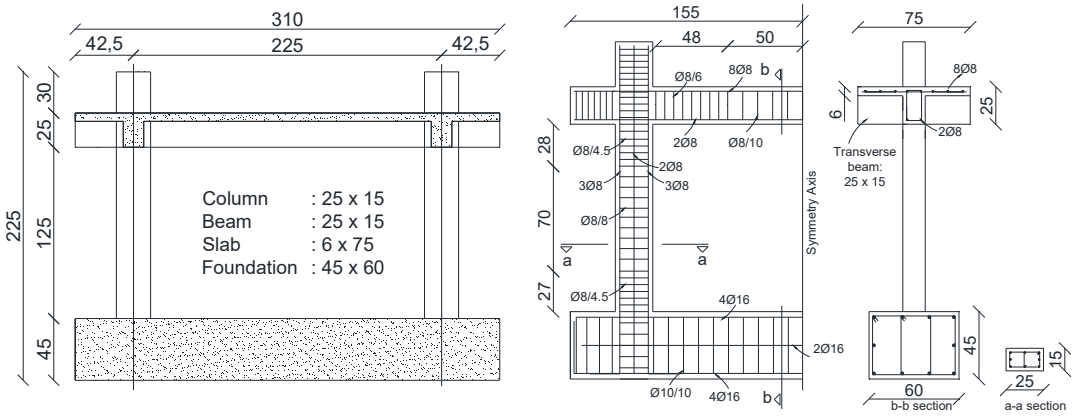

(a) (b)

Figure 4.1 Schematic view of the (a) frame, (b) reinforcing details, and (c) test setup (dimensions are in cm)

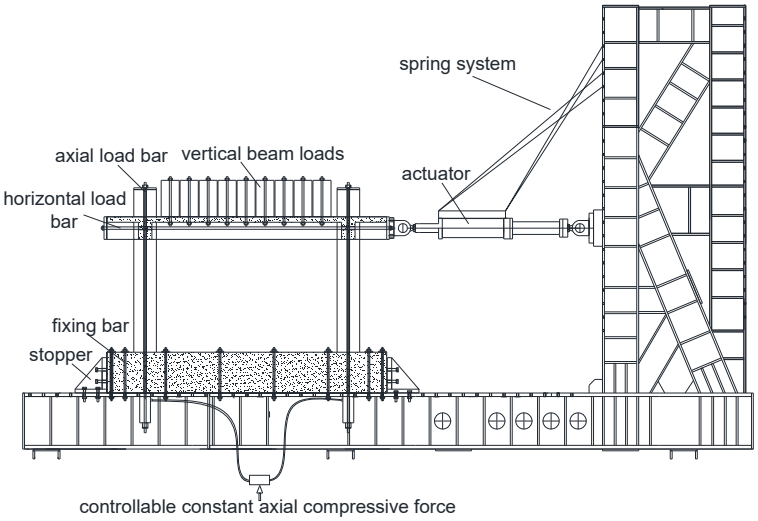

(c)

Figure 4.1 continues

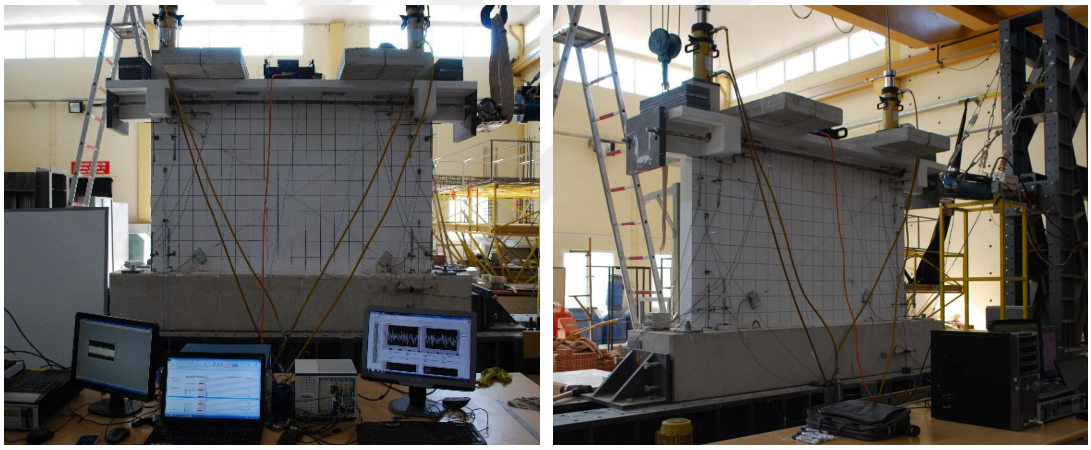

Figure 4.2 General views of the test setup with test equipments (Personal archive, 2016)

Two different types of brick units, namely standard and locked bricks as shown in Figure 4.3, were used to build the infill walls. The main difference between these bricks is that the former one uses mortar on the bed and head-joints (standard brick), and the latter one does not use mortar on any of these joints (locked brick). The locked bricks lock into each other while enabling sliding motion along their in-plane directions (along the strong axis of the R/C frames) due to their mortar-less feature. This novel feature of the brick enables low-to-moderate (mild) level panel action to develop within frame systems, and therefore has the potential of preventing soft or weak story mechanism (Misir et al., 2012). The out-of-plane stability (along the weak axis of the R/C frames) is provided by the brick's internal locking feature. Mortar was

used at all brick-to-brick and brick-to-frame interfaces for the infill wall constructed with standard bricks, whereas for the infill wall with locked bricks, mortar was used only at the brick-to-foundation interface. At the brick-to-beam interface, a foam-type material was used as it is the case in real-life applications. General views and interface details for the infill walls constructed with standard and locked type bricks are presented in Figure 4.4. In addition, types of infills used inside the frames are summarized in Table 4.1.

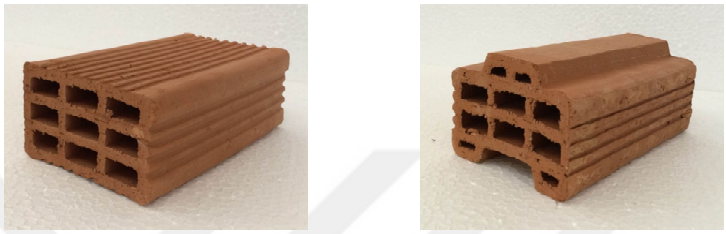

(a) (b)

Figure 4.3 (a) Standard and (b) locked type bricks (Personal archive, 2016)

(a)

(b)

Figure 4.4 General views and interface details for the infill walls constructed with (a) standard and (b) locked type bricks (Personal archive, 2016)

Table 4.1 Infill conditions of the frames

Frame #	Infill	Type of Infill
F1	No	-
F2	Yes	Locked
F3	Yes	Standard

4.3 Description of the Quasi-Static Test Program

Quasi-static tests were performed by imposing incrementally increasing story drifts to the frames (i.e., progressively increasing damage on the members of the frames were induced). Note that a single-cycle displacement pattern (history), which was determined in accordance with ACI 374.1.05 (2005), was used for each test and is shown in Figure 4.5. A total of 13 drift ratios (i.e., damage states) were defined, namely undamaged state, 0.075%, 0.15%, 0.20%, 0.35%, 0.50%, 0.75%, 1.00%, 1.40%, 1.75%, 2.20%, 2.75%, and 3.50%. The lateral displacements corresponding to these drift ratios can be calculated by multiplying the drift ratios with the specimen height defined as the length from the foundation to the actuator level (i.e., ~139 cm). Accordingly, the frames were subjected to in-plane (i.e., lateral) cyclic displacements ranging from 1.04 mm (0.075% drift) to 48.65 mm (3.50% drift).

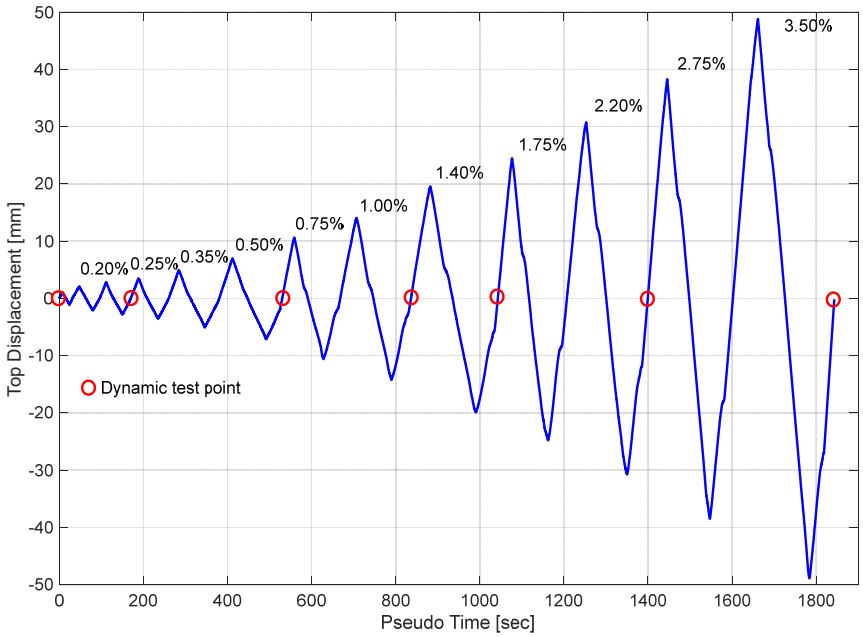

Figure 4.5 Single-cycle displacement pattern imposed on the frames

Twelve linear variable displacement transducers (LVDTs) and four string potentiometers (string pots) were used for static response measurements during quasi-static tests. The placement of these sensors is shown in Figure 4.6. Here, each LVDT and string pot is abbreviated as “L” and “S”, respectively. Note that S3 and S4 are available if there exists an infill wall. S1 measures the top displacement, therefore the imposed drift ratio on the frames, in order to cross-check the displacement given by the actuator, whereas S2 is used to track if there exists a movement in the foundation (i.e., sliding of the frame), which was desired to be avoided by the stoppers (Figure 4.1 (c)).

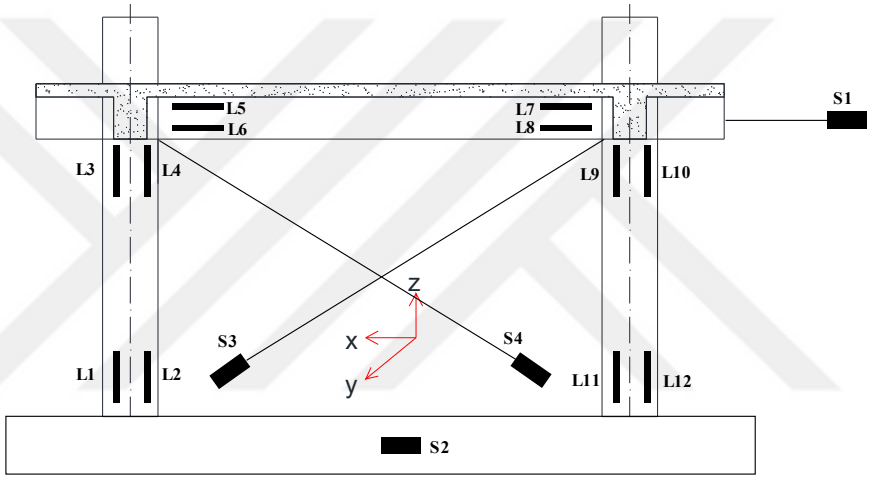

Figure 4.6 Placement of the static measurement sensors (L: LVDT, S: String pot)

4.4 Description of the Dynamic Test Program

At the end of each predetermined drift ratio: 0%, 0.20%, 0.50%, 1.00%, 1.40%, 2.20%, and 3.50% (i.e., at gradually increasing damage levels), a series of white-noise (WN) and ambient vibration (AV) tests were conducted on the frames. These dynamic test points, which were selected so that significant changes in modal parameters as damage level increases can be captured, are presented in Figure 4.5 with the circle symbol. The actuator was detached from the frames before the dynamic tests. This was done to prevent the restraining effect of the actuator on the frames, which may change the stiffness characteristics of the frames. It should be stated that once the frames went into severe nonlinear range, they retained different levels of residual deformations. When the actuator was detached before the dynamic tests, a certain amount of residual

deformation remained on the frames. In other words, the dynamics tests were performed at zero lateral force but not at zero residual displacement. It should be stated that the axial load applied on each column was also present during the dynamic tests; however, effects of this axial load (i.e., pre-compression effects on column members) on system identification results were not investigated within this study.

WN tests were performed by a uni-axial electro-dynamic shaker (with an increased reaction mass) which was placed on top of the frames (at the mid-line of the slab). The shaker was configured to move along the in-plane directions (along the x-axis) of the frames only. By this way, broad-band dynamic excitation was applied on the frames with an intention to excite their in-plane modes. The input signal to the shaker, the same one was used for all tests, was designed so that it had a frequency bandwidth of 0.1 – 100 Hz. This bandwidth was deemed sufficiently broad-band to excite the first few in-plane modes obtained based on preliminary numerical model studies. The signal amplitude was regulated manually by the gain knob of the signal amplifier unit but was set to a fixed value once sufficiently high vibration response was observed. Offline tuning technique (OTT), a command shaping control strategy, was used for WN tests to improve the signal reproduction fidelity of the shaker. This way the achieved signal on the shaker platen would be in broad-band nature as the designed input signal (details of OTT are presented in Section 2.2.4). Note that the implementation of OTT was necessary since the shaker itself has no built-in controller.

The frames were densely instrumented with 4 tri-axial and 5 uni-axial piezo-electric type accelerometers (i.e., 17 measurement points for each test). Also, one uni-axial accelerometer was mounted on the shaker in order to measure the WN excitation level imposed on the frames. Accelerometers used have ±5g amplitude range, frequency bandwidth of 0.25 Hz to 3000 Hz, sensitivity of 1000 mV/g, and 5e-4 broad-band resolution. The data acquisition system used is a NI-PXI system consisting of three 18-bit PXI-4472 A/D cards (each has 8 channels) with simultaneous sampling capability and anti-aliasing filters. Accelerometer layout (i.e., spatial distribution of the accelerometers) was determined from modal analysis studies performed on the initial numerical models of the frames. Since the responses of the frames are dominated

mainly by the modes in the frequency band of interest, sensor placement was performed in order to capture as many responses as possible. The accelerometer layout with positive polarities, the same one was used for all tests and frames, are presented in Figure 4.7. Note that each accelerometer station is abbreviated as "Sta" in the figure. As an example, accelerometers of Sta 1 (consists of one tri-axial accelerometer) and Sta 2 (consists of two uni-axial accelerometers) are shown in Figure 4.8 (accelerometers are marked with yellow circles). Here, it is also possible to see the static measurement sensors (i.e., LVDT, string pot) in this figure.

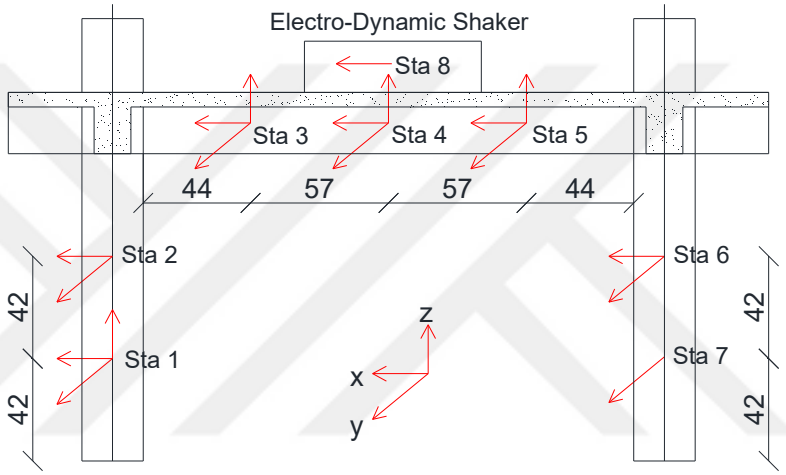

Figure 4.7 Accelerometer layout with positive directions (dimensions are in cm)

(a) (b)

Figure 4.8 Accelerometers of (a) Sta 1 and (b) Sta 2 (Personal archive, 2016)

For system identification purpose, 12 minutes long WN and AV response data at the end of the predetermined drift ratios (i.e., 7 sets for each frame) were recorded at a rate of 250 Hz. Before the modal analysis work, pre-processing of the recorded data was performed in MATLAB environment; namely the data were detrended, and then band-pass filtered between 0.5-100 Hz by using finite impulse response (FIR) filter in order to enhance the estimation accuracy by focusing on the frequency range of interest. This bandwidth was decided to be adequate to detect the first few modes of the frames (based on numerical models) and eliminate the undesired frequency content in the recorded data (e.g., environmental noise effects that pollute the data).

4.5 Damage Observations and Quasi-Static Test Results

Detailed visual damage inspections were made during the quasi-static tests and the observations were documented. A summary of these observations at specific drift ratio intervals is given in Table 4.2 for each frame. In addition, a set of photographs of the tested frames at 0.20% and 3.50% drift ratios are presented in Figure 4.9 as a complementary information for Table 4.2. Although detailed damage descriptions at each drift ratio are given in the table, some important characteristics of damage trends for the frames are summarized: For the frame with locked infills (F2), stepped and horizontal cracks were mainly formed at brick-to-brick interfaces over a large portion of the infill wall (panel) due to the sliding mechanism. Numerous and scattered plaster cracks (i.e., no concentration of crack patterns) occurred and no significant brick crushing was observed. On the other hand, for the frame with standard type infills (F3), cracks were concentrated at corner zones where a bi-axial compression-compression stress state developed due to lateral in-plane loading which caused brick members to crush and spall around these zones (i.e., concentration of cracks). Also, it can be said that the presence of the standard infills caused the number and width of the cracks induced on the surrounding frame members to increase (e.g., in the case of standard infilled frame, structural damage was observed throughout the column(s), whereas for the bare and locked infilled frames, structural damage was mainly concentrated on the column(s) bottom ends). From this perspective, it can be said that the infilled frames have different damage patterns.

Table 4.2 Summary of visual damage inspections for different frames (F: Frame, I: Infill)

Drifts (%)		Damage Description		
		F1 (no infill)	**F2 (locked infill)**	**F3 (standard infill)**
0.075-0.20	F	Minor flexural cracks on the beam (<0.2 mm). No cracks on column(s).	Minor cracks on column(s) ends (<0.2 mm). No cracks on beam.	Minor flexural cracks on beam - column(s) joints and column(s) ends (<0.2 mm).
	I		Separation between infill panel - frame interfaces started.	Separation started between infill panel - frame interfaces.
0.25-0.50	F	New beam flexural cracks. Flexural column(s) cracks. Minor cracks on the slab and beam (<0.5 mm).	Flexural cracks on various parts of column(s), beam ends, and slab (<0.2 mm). Cracks were increased in number.	Shear and flexural cracks arose at various zones of beam and column(s) ends.
	I		Minor diagonal cracks at corner zones. No considerable visible damage on infill.	Diagonal cracks at corner zones. Plaster spalled off due to crushing.
0.75-1.00	F	Moderate damage on frame joints. New minor flexural cracks on beam (<1 mm).	Flexural cracks on column(s), beam, and slab were increased in number (Crack width < 0.5 mm).	New diagonal shear cracks arose on column(s) ends. Some flexural cracks on beam and column(s) ends were propagated.
	I		Frame infill contact interface started to get lost (separation > 1cm). Minor cracks at corner. No considerable crack on infill.	No additional visible cracks. Gap between frame - infill panel became more than 10 mm.
1.40	F	Uplift between foundation - column(s) ends. Moderate flexural cracks on slab and beam - column(s) ends (>2 mm).	New slab cracks appeared.	New flexural cracks arose on beam and column(s) ends. Shear cracks appeared at bottom parts of column(s).
	I		Shear cracks arose in both diagonal directions. 2 cm gap formed between panel - frame interface. Plaster swelled.	More than 10 mm gap between panel - frame interface. Plaster spalled off due to crushing at corners.
1.75-2.20	F	Uplift between foundation - column(s) ends increased. Moderate - severe flexural cracks on column(s) - beam interfaces (>3 mm).	Moderate - severe frame cracks (> 5 mm).	New flexural cracks arose throughout the beam, on slab and column(s) bottom ends.
	I		Plaster spalled off at corner zone. Irregular horizontal crack formations. In some parts, gap between two brick > 10 mm.	Infill was crushed and spalled off only at corner parts. More than 25 mm gap between panel - frame interface.
2.75-3.50	F	Severe flexural damage on frame (>5 mm). Spalling and crushing at base of column(s) concrete. Buckling of reinforcing bars at column(s) bottom ends.	Reinforcing bars became visible and buckled. Concrete spalled off at bottom ends of column(s). New frame cracks were observed.	Reinforcing bars became visible and buckled. Cracks were propagated at column(s) bottom ends.
	I		Plaster spalled off throughout the wall.	More than 35 mm gap between panel - frame interface. No additional infill wall damage.

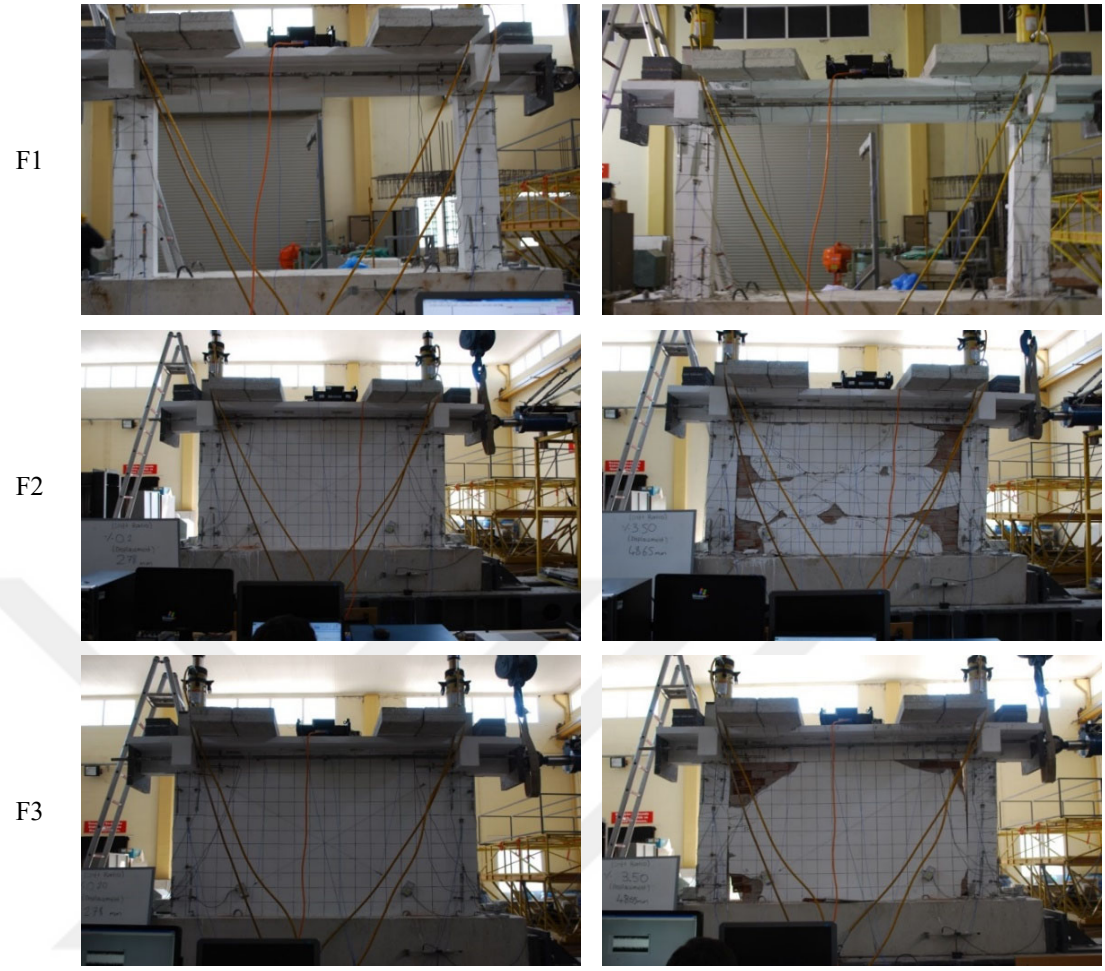

Figure 4.9 Damage states of the frames at the end of (a) 0.20% and (b) 3.50% drift ratios, respectively (Personal archive, 2016)

Hysteretic lateral force-displacement curves of the frames obtained from quasi-static cyclic tests are shown in Figure 4.10. By combining the peak points of the hysteretic curves, it is possible to plot the strength envelope curves of the frames which are presented in Figure 4.11. From the figures, it is clear that there exist strength and stiffness degradations as the drift ratio (i.e., displacement level) increases. As expected, the additional lateral resistance imposed on the frames by the standard type infills (F3) is much higher than the additional resistance by the locked type infills (F2) (i.e., F3 reaches relatively higher lateral load levels). Moreover, the frame with standard infills reaches its maximum lateral resistance earlier than other frames. The frame with locked infills contributes to the lateral resistance about 39% with respect to the bare frame (F1). For the standard type infills, this contribution is about 113%.

The frame with locked infills shows lower strength degradation than that of the frame with standard infills. Since the contribution of infills to the lateral strength of a frame structure is not considered in most of the seismic codes, the behavior of the frame with locked infills seems analogous to the bare frame.

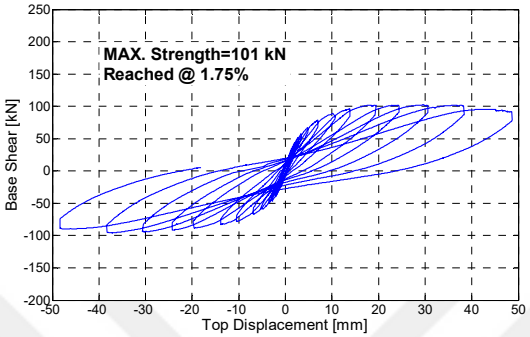

F1 (no infill)

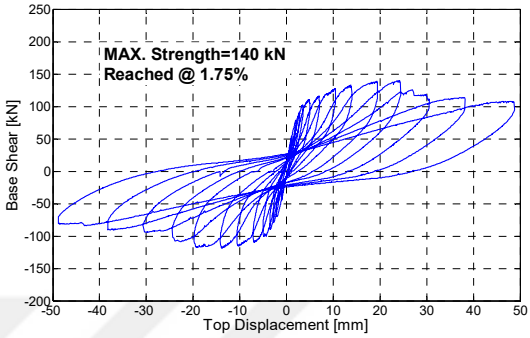

F2 (locked infill)

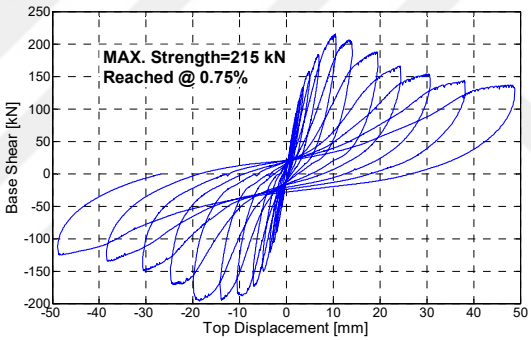

F3 (standard infill)

Figure 4.10 Hysteretic curves for the frames obtained from quasi-static cyclic tests

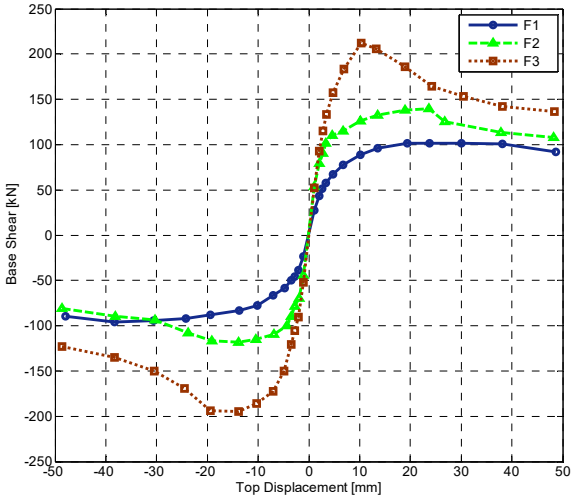

Figure 4.11 Strength envelope curves for the frames

Stiffness degradation curves of the frames are presented in Figure 4.12 (a). Herein, the peak-to-peak stiffness approach, which is described as the slope of the line that connects negative and positive peak points for a cycle of hysteretic curve, is adopted. In order to track the stiffness degradations clearly, the normalized peak-to-peak stiffness, which is calculated by dividing each peak-to-peak stiffness value by the one determined in the first cycle, is also presented in Figure 4.12 (b).

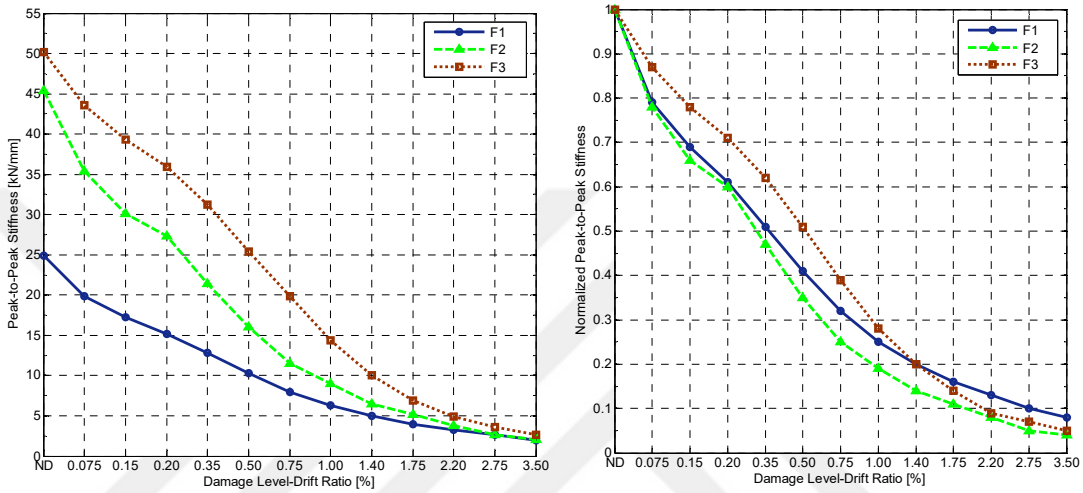

(a) (b)

Figure 4.12 Stiffness degradation curves for the frames in the sense of (a) peak-to-peak stiffness and (b) normalized peak-to-peak stiffness values

It can be seen from the figures that the bare frame (F1) has the lowest initial stiffness value. For the bare, locked type infilled (F2), and standard type infilled (F3) frames, initial stiffness values are obtained as 24.9 kN/mm, 45.4 kN/mm, and 50.2 kN/mm, respectively. The initial stiffnesses of the locked and standard type infilled frames are approximately 1.82 and 2.02 times than that of the bare frame, respectively. Notice that the frame with locked infills has higher stiffness values at early stages but exhibits significant drops with increasing drift ratios due to overcoming the static friction threshold of the locked bricks and the shear failure of the mortar. After about 2.20% drift ratio, all the frames show similar stiffness values. Since the contribution of infills to the stiffness of a frame structure is not considered in most of the seismic codes, here again, the behavior of the frame with locked infills seems analogous to the bare frame.

The cumulative dissipated energy curve, which is described as the summation of the area enclosed by each hysteretic curve, is given for each frame in Figure 4.13. This curve is important since it reflects the capacity of a structure to dissipate seismic input energy (i.e., a higher value represents better energy dissipation performance). By referring to Figure 4.13, it can be said that the bare frame (F1) has the minimum energy dissipation capacity, whereas the standard infilled frame (F3) has the highest. At 3.50% drift ratio, the cumulative dissipated energy values of the frames with locked and standard infills are approximately 1.34 and 1.65 times than that of the bare frame, respectively. Note that the behavior of the frame with locked infills seems analogous to the bare frame in the sense of dissipated energy.

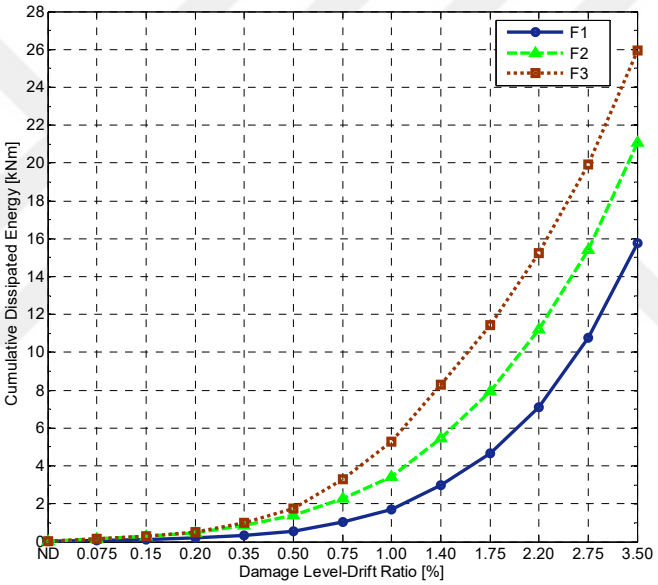

Figure 4.13 Cumulative dissipated energy curves for the frames

Some numerical information about the quasi-static test results that can be extracted from Figures 4.10 to 4.13 is summarized in Table 4.3.

Table 4.3 Numerical information about the quasi-static test results

Frame	Strength [kN]		Peak-to-Peak Stiffness [kN/mm]		Degradation [%]		Cumulative Energy Dissipation [kNm]
	Max.	@ 3.50%	Initial	@ 3.50%	Strength	Stiffness	@ 3.50%
F1 (no infill)	101 @1.75%	95	25	2	6	92	16
F2 (locked infill)	140 @1.75%	108	46	2	23	96	21
F3 (standard infill)	215 @0.75%	136	50	3	37	95	26

4.6 Dynamic Test Results

The system identification methods presented in Chapter Two (i.e., NExT-ERA, EFDD, and SSI-DATA) were used with the response data obtained from WN and AV excitations. Two different WN excitations, namely with the application of OTT (WN w/Offline) and without the application of OTT (WN wo/Offline), were used for all frames at different damage levels. The root mean square (RMS) response amplitudes of the shaker excitations measured by the accelerometer on the shaker (i.e., Sta 8, x-direction) were ~0.46 g and ~0.21 g for WN wo/Offline and WN w/Offline cases, respectively. Notice that the WN wo/Offline case has more than two times the RMS response amplitude of the WN w/Offline case. This is because of scaling the modified input signal according to the shaker's limitations before sending it to the shaker. Three different tests, namely WN wo/Offline, WN w/Offline, and AV, produced ~0.011 g, ~0.004 g, and ~4.17E-05 g RMS response amplitudes along the in-plane direction (along x-direction) at Sta 4, respectively. These values were almost the same for all the frames. Notice that the AV tests lead to very low-level response amplitudes. As a result, it is possible to designate, relatively, WN wo/Offline data as the "high-level", WN w/Offline the "medium-level", and AV data as the "low-level" response cases. Dependence of modal parameter identification results on the level of excitation will be discussed in the following sections.

The estimated modal parameters belong to the first in-plane (i.e., along x-direction) modes for different frames at progressively increasing damage levels. Note that the focus has been given to the first in-plane modes (i.e., fundamental in-plane modes) since the quasi-static tests were performed in this direction (i.e., first in-plane modes are the largest contributors to the frames' dynamic responses along this direction). In addition, since the shaker's excitation direction was along the in-plane direction (x-direction, see Figure 4.7), the recorded structural responses were predominately along this direction. Therefore, the WN tests were mainly used to track the changes in the in-plane modes with respect to gradually increasing damage levels. Here, WN w/Offline tests were preferred because of the broad-band nature of the excitation, as explained in the previous sections. In the scope of this thesis, unless otherwise stated, the presented estimation results are from the NExT-ERA method using WN w/Offline test data.

It must be emphasized that the fundamental in-plane modes at different damage states presented here are called the "in-plane modes" due their predominant motions being along the x-(longitudinal) direction; but these modes are not purely in-plane modes. In different intensities, some identified in-plane modes, at different damage states, are coupled modes, meaning that they have components also along y-(transversal) and z-(vertical) directions. Especially for the infilled frames at lower damage states, the in-plane fundamental modes are not at all purely in-plane modes; but as the walls progressively go through more damage, the estimated in-plane modes become more and more in-plane by losing their modal components along y- and z-directions. In order to facilitate the discussion of the results, the coupled modes with dominant in-plane components are designated as "in-plane modes".

System identification results (obtained by NExT-ERA method) for the fundamental in-plane modes at different damage states using three different excitation types (i.e., AV, WN w/Offline, and WN wo/Offline) are given in Tables 4.4 to 4.6. As a summary and to highlight the results visually, the results are also presented by bar plot format in Figure 4.14.

Table 4.4 Modal identification results for F1 (bare frame) under different excitation conditions

Excitation Type	Modal Params	No Damage	0.20%	0.50%	1.00%	1.40%	2.20%	3.50%
AV	ω [Hz]	15.26	14.62	13.72	12.04	11.15	9.81	8.44
	ξ [%]	0.59	0.59	0.81	0.88	0.98	0.73	1.51
	MAC	1.00	1.00	0.99	0.98	0.97	0.97	0.96
WN wo/ Offline	ω [Hz]	15.11	14.41	13.45	11.44	10.64	9.44	8.04
	ξ [%]	2.08	1.03	2.18	1.88	1.96	1.97	1.86
	MAC	0.99	0.98	0.98	0.98	0.97	0.97	0.97
WN w/ Offline	ω [Hz]	15.11	14.49	13.56	11.29	10.83	9.62	8.23
	ξ [%]	1.65	0.92	1.85	1.66	1.67	1.58	1.65
	MAC	1.00	0.98	0.99	0.98	0.97	0.97	0.97

Table 4.5 Modal identification results for F2 (locked infill) under different excitation conditions

Excitation Type	Modal Params	No Damage	0.20%	0.50%	1.00%	1.40%	2.20%	3.50%
AV	ω [Hz]	14.77	14.49	14.19	13.15	12.78	12.02	9.38
	ξ [%]	0.89	1.43	0.78	1.45	1.24	0.90	0.70
	MAC	1.00	0.99	0.99	0.95	0.93	0.90	0.80
WN wo/ Offline	ω [Hz]	14.31	14.09	13.82	12.53	12.35	11.46	8.44
	ξ [%]	1.47	1.07	1.36	1.71	2.06	2.02	3.73
	MAC	1.00	0.99	0.98	0.93	0.90	0.87	0.80
WN w/ Offline	ω [Hz]	14.43	14.22	13.95	12.85	12.60	11.80	8.94
	ξ [%]	1.54	1.09	1.28	1.51	1.67	1.57	2.58
	MAC	1.00	0.97	0.98	0.95	0.92	0.89	0.81

Table 4.6 Modal identification results for F3 (standard infill) under different excitation conditions

Excitation Type	Modal Params	No Damage	0.20%	0.50%	1.00%	1.40%	2.20%	3.50%
AV	ω [Hz]	14.42	14.19	13.94	12.60	12.00	11.00	-
	ξ [%]	0.91	0.78	1.46	2.08	1.07	0.81	-
	MAC	0.99	0.99	0.98	0.95	0.93	0.89	-
WN wo/ Offline	ω [Hz]	14.13	13.86	13.57	12.13	11.49	10.48	9.73
	ξ [%]	1.04	1.38	1.97	2.01	2.05	1.89	1.78
	MAC	1.00	1.00	0.99	0.93	0.91	0.88	0.85
WN w/ Offline	ω [Hz]	14.20	13.97	13.63	12.41	11.73	10.84	9.94
	ξ [%]	1.01	1.16	2.18	1.35	1.52	1.29	1.24
	MAC	1.00	1.00	0.98	0.95	0.92	0.89	0.86

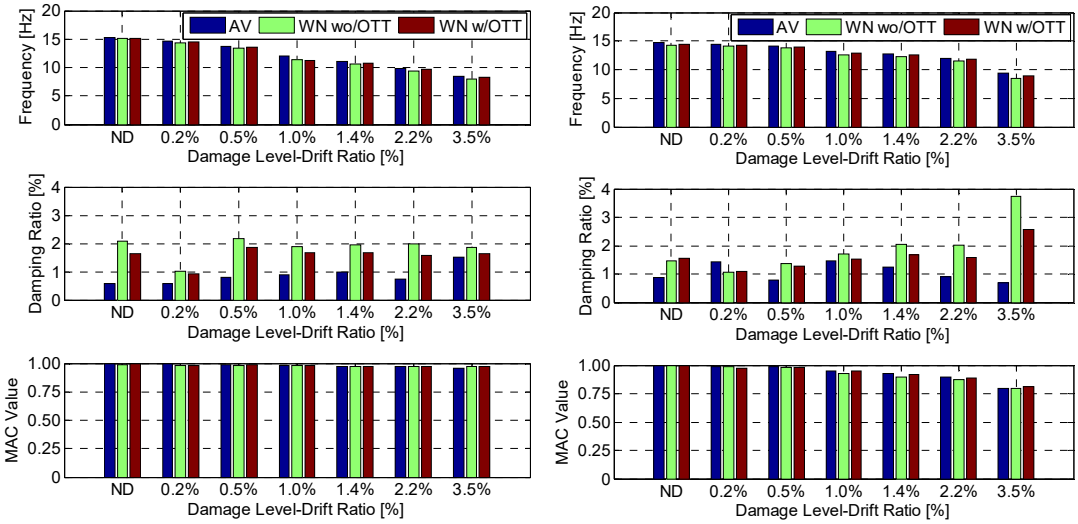

F1 (no infill) F2 (locked infill)

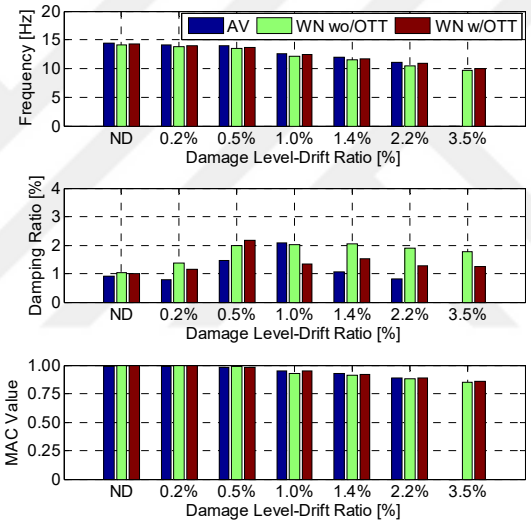

F3 (standard infill)

Figure 4.14 Estimated modal parameters for different frames using different excitation types (NExT-ERA results)

Note that the selection of the modes was realized by the use of stabilization diagrams, which are useful tools in determining proper system order and in distinguishing between stable and unstable modes for parametric system identification methods (e.g., SSI-DATA and NExT-ERA) (Peeters & De Roeck, 2001; Zhang et al., 2014). As an illustrative example, a stabilization diagram is shown in Figure 4.15 for WN w/Offline dataset of the bare frame (F1) at the undamaged state (i.e., 0% drift ratio). Herein, the stability criteria given in Equation 4.1 were used to plot the diagram.

$$\left|f_i - f_j\right| / f_j \le 1\% \; ; \qquad \left|\xi_i - \xi_j\right| / \xi_j \le 5\% \; ; \qquad \left|1 - MAC_{\phi_i,\phi_j}\right| \le 1\% \tag{4.1}$$

where (f_i, f_j), (ξ_i, ξ_j), and (ϕ_i, ϕ_j) represent the identified frequencies, damping ratios, and mode shapes, respectively for models of successive orders *i* and *j*. MAC_{ϕ_i,ϕ_j} is the modal assurance criterion calculated between ϕ_i and ϕ_j. The symbols presented in the stabilization diagram denote: "⊕" a pole with stable frequency, damping, and mode shape; ".d": a pole with stable frequency and damping; ".v": a pole with stable frequency and mode shape; and ".f": a pole with stable frequency only. In the figure, also smoothened and amplitude scaled power spectral density functions (PSDs), which were calculated using the response data recorded at "Sta 1" along x-, y-, and z-directions from a tri-axial accelerometer, are given. Note that the PSDs have different energy levels; therefore, they were scaled in a different way in order to plot them on the same figure. From the stabilization diagram, the model order of 14 was chosen for this particular case. It should be stated that too high model order selection leads to computational expense and non-physical mode occurrence, whereas in the case of too low model order, it is possible to miss some of the structural modes. Therefore, a balance should be maintained for model order selection.

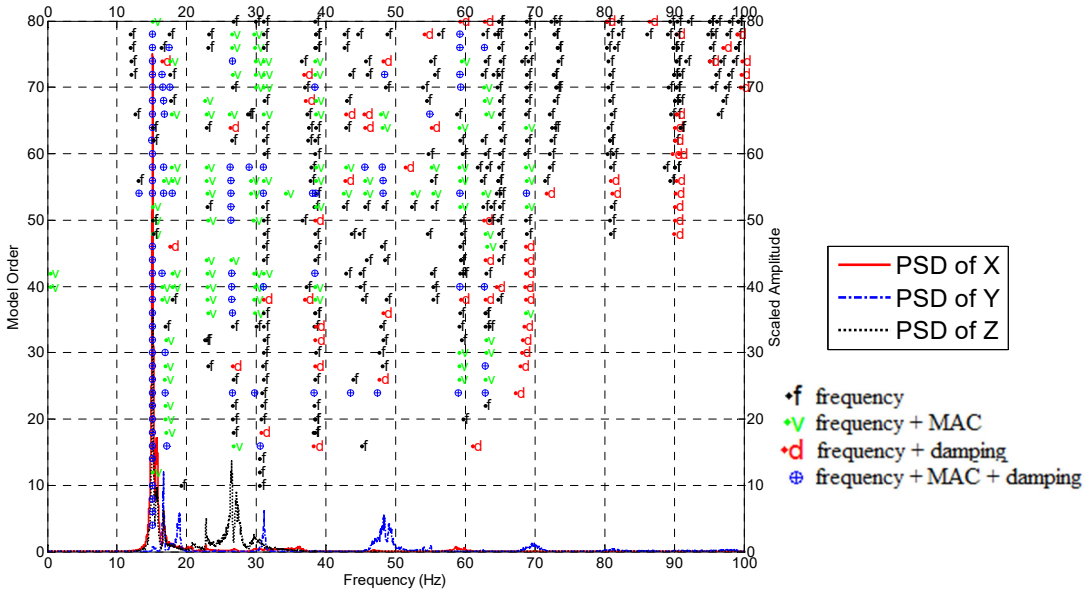

Figure 4.15 Stabilization diagram of F1 (bare frame) at the undamaged state (NExT-ERA results with WN w/Offline dataset)

From the results presented in Tables 4.4 to 4.6 and Figure 4.14, it can be said that for all frames subjected to different excitation conditions, similar frequency values are identified for a particular damage level and for that particular frame. In other words, the excitation level results in minor differences in frequency estimations. As damage level increases the identified frequency values become smaller. Notice that at the same damage level (e.g., 2.20%) for a particular frame, the frequency results from the WN wo/Offline case (relatively a higher level of excitation) are the smallest ones compared to the relatively lower level excitation cases (e.g., AV and WN w/Offline tests), and the highest values being the ones from the AV tests (the lowest level of excitation case). This is due to R/C frames behaving nonlinearly (or quasi-linearly) even at the level of WN wo/Offline case (refer above for their RMS amplitudes). Higher excitation levels, which are expected to widen pre-existing and/or newly emerged cracks in the members, lead to decreased in-plane stiffness which in turn results in smaller frequency estimations. A similar approach is adopted in the study of Astroza et al. (2016a). Note that the modal parameters could not be identified using the AV data set at 3.50% damage state for F3 (as indicated with the symbol "-"). This is due to low signal-to-noise ratio (SNR) seen in this particular data set; but for all the other frames and damage levels, no such problem was observed.

The results suggest that the damping ratio estimations exhibit significant scatter (variability) among different excitation and frame types. In addition, they do not have clear trends that can be utilized solely as a damage indicator. It is known that noise always exists in real-life measurements; therefore, SNR has an important role in accurate parameter estimation. Especially, damping estimations are very sensitive to measurement noise, and as the noise level increases, uncertainty in damping estimations increases as well (Bajric et al., 2014, 2015). Another peculiarity with damping estimations is the fact that they are amplitude dependent (Astroza et al., 2016a, 2016b). The damping values estimated from the WN data (especially the WN wo/OTT tests which have the largest RMS amplitudes) are consistently higher than the ones estimated from the AV data (which have the smallest RMS amplitudes) for all the frames at all damage states.

MAC values (shown in Tables 4.4 to 4.6 and Figure 4.14) were calculated between the mode shapes of the undamaged states (using the WN w/Offline test result as the reference) of F1, F2, and F3 and different damaged states of the same frame. These values indicate the changes occurred in mode shapes as damage level increases. MAC values for all frames consistently decrease as damage level increases, which indicates that the estimated mode shapes at different damage states differ increasingly more with respect to the mode shapes of the undamaged cases. Notice that the changes in mode shapes are more pronounced for the infilled frames (i.e., F2 and F3). This is due to the infill wall-frame interaction in out-of-plane direction. The reason for this is that the almost purely in-plane mode remains purely in-plane regardless of damage level for frame F1 (no infill, therefore no infill-frame interaction). This results in small variations in MAC estimations. On the other hand, the coupled modes, dominantly seen in the infilled frames at the undamaged and low-level damaged states, turn into purely in-plane modes as damage progresses, resulting in significant changes in MAC values. Details of the mode shapes will be discussed in the coming sections.

Method-to-method variability in estimation results was investigated by processing the recorded response data at different damage states using three different system identification methods. The obtained results are shown in Figure 4.16. The MAC values given in the figure were found between the undamaged mode shapes (using the WN w/Offline tests and estimated by NExT-ERA method) and the damaged ones (using the WN w/Offline tests and estimated by SSI-DATA and EFDD methods) for different frames. It is clear that the frequency estimations and MAC values by different methods are very similar for each damage state (i.e., negligible differences), therefore it can be concluded that the estimated values are independent of the method used. As a general trend for all methods, it can be said that the estimated frequencies and MAC values decrease as the damage increases. For damping estimations, it can be said that NExT-ERA and SSI-DATA methods give somewhat similar results; but the overall match among the methods is not as good as in the case of frequency and mode shape estimations. The damping results obtained by EFDD method differ considerably from the results obtained by other two methods. Subjectiveness of the peak-picking and logarithmic decrement processes can be attributed as the reasons behind this higher

variability in damping estimations by EFDD method. A clear trend for damping ratio estimations, as observed for the frequency and mode shape estimations at the level of excitations considered in this study, cannot be observed as damage increases. Nevertheless, a slight increasing trend in damping estimations is noticeable as the drift ratio, therefore the damage level, increases (e.g., F2).

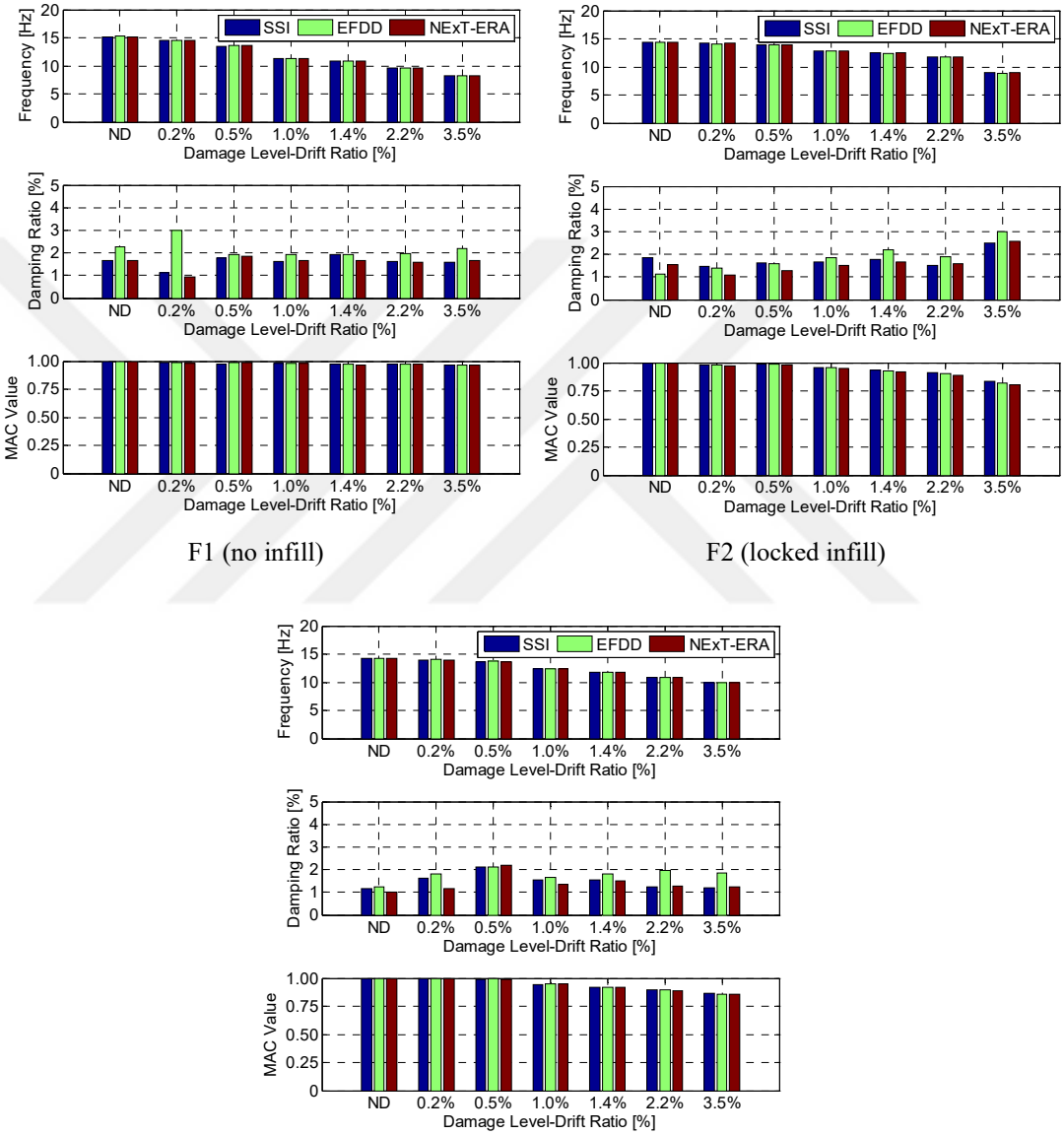

F1 (no infill) F2 (locked infill)

F3 (standard infill)

Figure 4.16 Estimated modal parameters for different frames by different system identification methods (WN w/Offline dataset)

Modal parameter estimations and evolution of mode shapes for all the frames are indicated comparatively in Figures 4.17 and 4.18, respectively, as a function of damage

level. For the undamaged state, the vibration frequencies of the bare (F1), locked infilled (F2), and standard infilled (F3) frames are identified as 15.11 Hz, 14.43 Hz, and 14.20 Hz, respectively. It is expected that the existence of infills would have stiffening effect along the in-plane direction and therefore the frequencies of the in-plane modes would increase; but it is interesting to note that F1 (the bare frame) has the highest frequency among the tested frames. This may be considered as a counter-intuitive result at a first glance; but there exist two main reasons underlying this issue: (i) It should be emphasized that the in-plane mode shapes of the infilled frames (i.e., F2 and F3) are coupled modes (i.e., the modes for these frames are not purely in-plane but have dominant in-plane components) especially at low damage levels (e.g., at the ND and 0.20% drifts), whereas F1 has purely in-plane mode shapes for all drift cases (refer to Figure 4.18). The coupled nature of the in-plane modes for the infilled frames is due to the frame-infill interaction in out-of-plane direction. Therefore, a direct comparison of the estimated frequencies for the frames with and without infills may be misleading. (ii) The infill walls couldn't be excited properly during the dynamic tests due to the low excitation levels even at the level of WN wo/Offline case (refer above for the RMS amplitudes of the excitation levels). Therefore, the identified modal parameters represent only the characteristics of the surrounding frame structures without the contributions of the infill walls. It should be stated that if the dynamic tests were performed under higher excitation conditions (e.g., large-size shake table tests, snap-back tests, etc.), it would be possible to excite the infilled frames properly; in return, the infilled frames would exhibit higher vibration frequency values than that of the bare frame. Note that the latter reason (i.e., item ii) will be discussed in detail in Section 5.3. At the undamaged state, all the frames with infills have similar frequencies for the predominantly in-plane modes (with coupled out-of-plane components). As these frames get damaged, they start to differentiate from each other depending on the infill condition, this starts at around 0.50% drift. It is clear from Figure 4.17 that a steady decrease takes place in the frequency estimations for all the frames as damage increases; but it is obvious that the lateral stiffness of the bare frame (F1) decreases at a faster rate than the frames with infills. Note that since the infill walls couldn't be excited properly at the dynamic excitation levels attained in this study, they cannot be the contributors to the in-plane stiffnesses of the frames. Therefore, the differences

observed in the frames' lateral stiffnesses (i.e., frequency estimations) can be attributed to the effectiveness of the infill walls on the damage formations and distributions that occurred at the surrounding frame structures during the quasi-static tests. Also, it is important to note that the decreasing trend in the frequency estimations for the frame with locked infills (F2) is slower than the other two. This might possibly be indicating that the additional damage that might be induced by frame-infill interaction is less severe for F2 (due to mild panel action) than F3 (the frame with standard infills). At 3.50% drift ratio, the identified frequencies for the frames F1, F2, and F3 are 8.23 Hz, 8.94 Hz, and 9.94 Hz, respectively. The percentage changes in the frequencies with respect to the undamaged states are calculated as 45% (F1, bare frame), 38% (F2, frame with locked infills), and 30% (F3, frame with standard infills). These results show that the frames with the locked type infills (F2) and without infills (F1) are somewhat similar. The frame with the standard type infills (F3) shows smaller frequency variations between the undamaged (ND) and the highest damaged (3.50% drift) states. Moreover, as shown in Figure 4.17, it can be said that at the excitation level (i.e., WN w/Offline) attained for these tests, the damping ratio estimations show no clear trend both for damage level and infill condition.

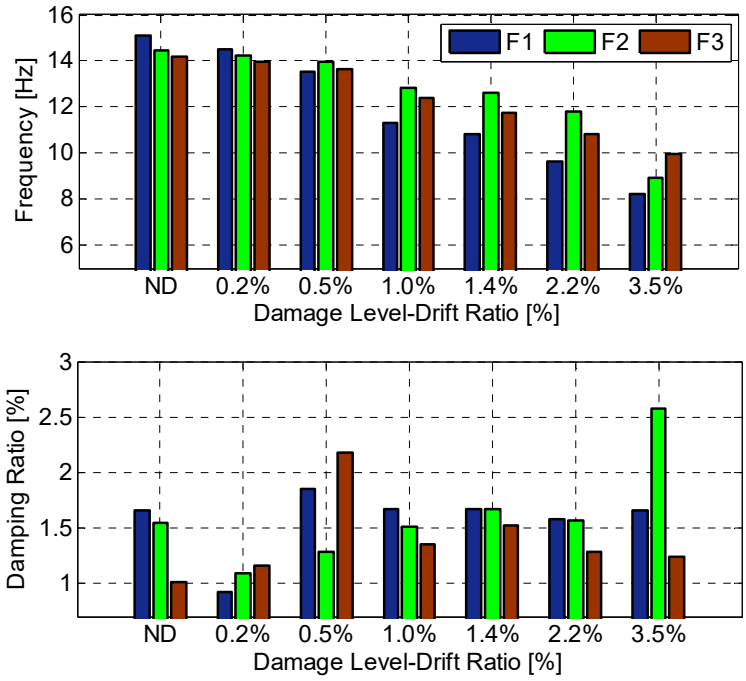

Figure 4.17 Modal parameter estimation results for the frames as a function of damage state (NExT-ERA results with WN w/Offline dataset)

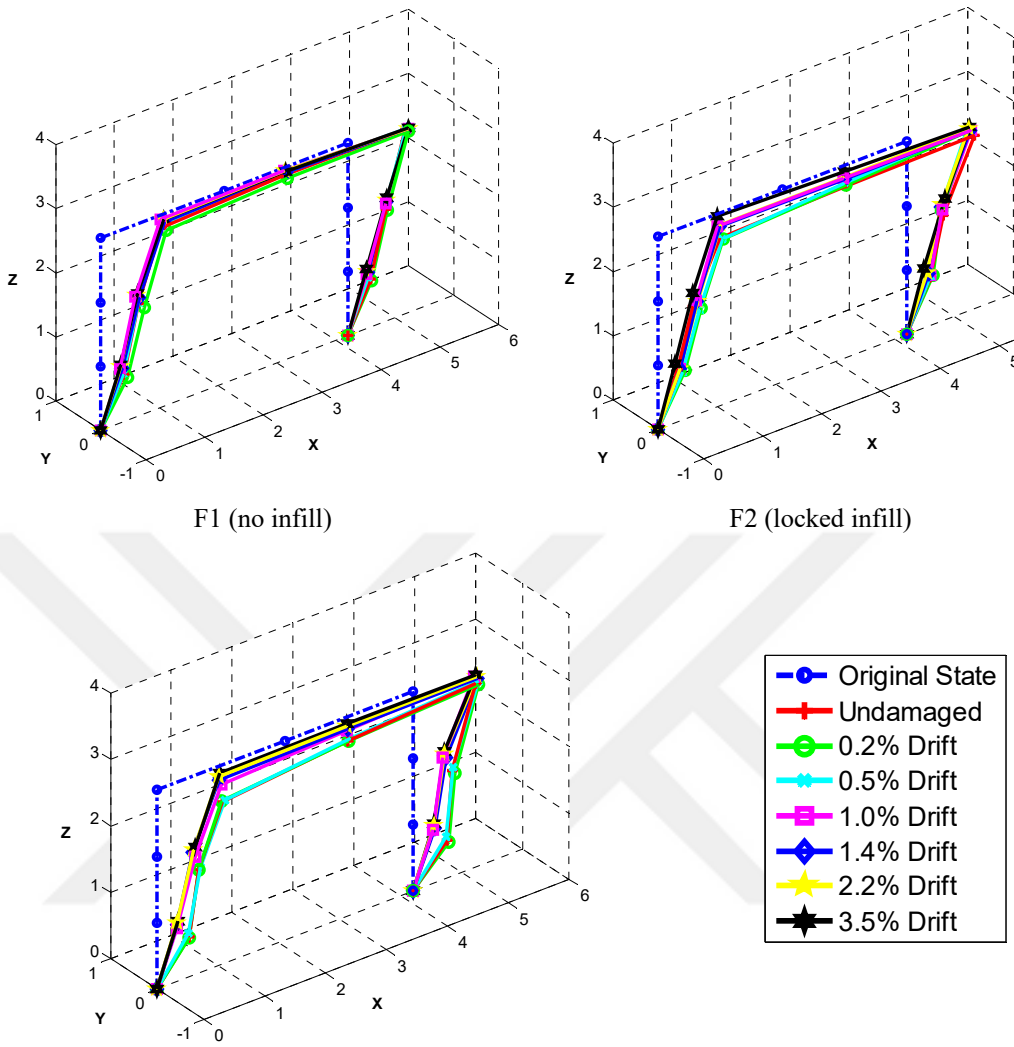

F1 (no infill)

F2 (locked infill)

F3 (standard infill)

Figure 4.18 Evolution of the mode shapes as damage level increases

It should be stated that the mode shapes shown in Figure 4.18 are plotted by using the real parts of the identified complex mode vectors. Note that complex mode shapes may occur because of many reasons, such as low SNR (i.e., high noise level and/or low signal level), aerodynamic effects, gyroscopic effects, nonlinearities of the systems, and non-classical damping mechanisms of the systems (Chopra, 2012; Ewins, 2000). It should be emphasized that the first in-plane mode shape of the bare frame (F1) is almost perfectly in-plane (i.e., almost no component along the y- and z-directions). On the other hand, infilled frames have mode shape components also along y- and z-directions; but as the structural damage level increases y- and z-components start to disappear. The modes estimated at higher damage levels (approximately 1.00%

and beyond) become almost perfectly in-plane. This result indicates that the effects of infills on the mode shape estimations diminish as damage increases. Figure 4.19 demonstrates the polar plot representations of the estimated mode shapes with complex components. These plots show the level of non-classical damping in the frames. Based on the results, it can be said that the mode shapes are classically damped (characterized by negligible complex parts) because the vector components are almost perfectly collinear and aligned along the real axis. This also serves as a justification in plotting the estimated mode shapes, which have complex components, using only their real parts (Figure 4.18). It can also be said that the damage level does not change the classically damped nature of the modes.

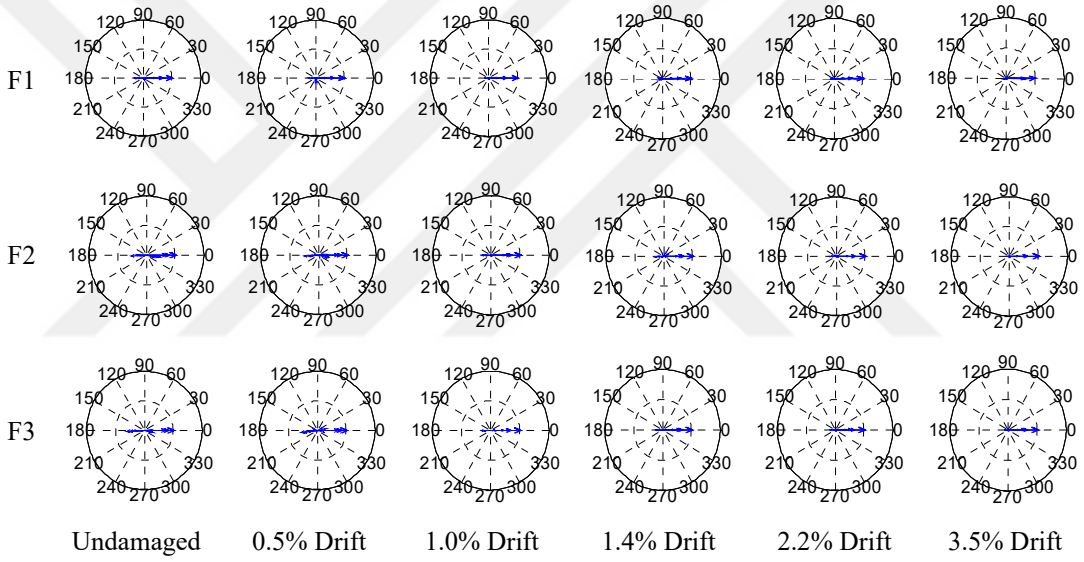

Figure 4.19 Polar plot representations of the mode shapes

Figure 4.18 shows that as the structural damage increases, the in-plane mode shapes go through very small changes. This observation can be used to justify that as damage increases, the effective modal masses corresponding to the fundamental in-plane modes remain unchanged for different frames (i.e., under the assumption that the mass properties of the frames remain unchanged during the tests). With this assumption, the stiffness degradations (SDs) corresponding to the in-plane modes with respect to the undamaged case can be approximated by Equation 4.2.

$$SD_i^j(\%) = \frac{(f_{ND}^j)^2 - (f_{D,i}^j)^2}{(f_{ND}^j)^2} \times 100 \quad (4.2)$$

where f_{ND}^j and $f_{D,i}^j$ are the identified frequencies for a particular frame *j* (*j*=F1, F2, and F3) at the undamaged and various damaged levels *i* (*i*=ND, 0.20%, 0.50%, 1.00%, etc.), respectively. The stiffness degradations calculated using Equation 4.2 at different drift levels for different frames were matched with the detailed visual damage inspections (refer to Table 4.2). The results were clustered into three dimensional plots and are presented in Figures 4.20 to 4.22 for frames F1, F2, and F3 (i.e., frames with different infill conditions), respectively. In these figures, damage types are categorized for column (subplot (a)), beam (subplot (b)), and infill (subplot (c)) members in three distinct groups, and subplot (d) shows the zones where damages are concentrated. The bars with red colors indicate that a particular damage type (as indicated on the longitudinal axis) occurred for the first time or that damage type increased significantly at that particular drift ratio (as indicated on the transversal axis). The bars with yellow colors indicate that no significant change in the existing damage type occurred, and the bars with green colors indicate that a particular damage type has not yet occurred at that drift ratio. The bars with gray colors indicate that the corresponding member damages do not exist for that frame (e.g., there is no infill wall in F1, therefore Figure 4.20 (c) is all in gray color). These figures are useful in determining what damage type (also its extent and location) is observed on the frames when stiffness degradation is seen as a function of increasing structural damage. Note that the stiffness degradation values are calculated using the frequency estimations obtained from dynamic tests and represent only the characteristics of the surrounding frames.

For F1 (the bare frame) in Figure 4.20, stiffness degradations are obtained as 8%, 19%, 44%, 49%, 59%, and 70% for 0.20%, 0.50%, 1.00%, 1.40%, 2.20%, and 3.50% drift ratios, respectively. The damages at beam ends due to the flexural action are effective until 0.20% drift ratio, and meanwhile ~8% stiffness degradation is observed. With increasing drift ratio, up to 1.00%, the damages at column(s) ends start to be more pronounced. The largest change in the stiffness degradation (~25%) is observed within the 0.50%-1.00% drift ratio interval along with mainly column damages (Figure

4.20 (a), damage types 1a, 2a, and 3a). Towards the end of the test, the separation at the column-foundation interface can be seen as the main damage type of the frame with ~11% stiffness degradation change.

For F2 (the frame with locked infills) in Figure 4.21, stiffness degradations are obtained as 3%, 7%, 21%, 24%, 33%, and 62% for 0.20%, 0.50%, 1.00%, 1.40%, 2.20%, and 3.50% drift ratios, respectively. Column and infill damages are effective until 0.20% drift ratio. The first significant change in the stiffness degradation is seen between 0.50%-1.00% drift interval where infill (e.g., concentrated cracks at the corner zones, distributed horizontal cracks) and various column damages occur. The largest stiffness degradation change (~29%) is observed between 2.20%-3.50% drift ratio interval. Meanwhile, separation at the frame-infill interface and various column damages (e.g., extension and deepening of existing cracks, crushing of concrete cover at columns' bottom ends, and buckling of reinforcement bars) (Figure 4.21 (c), damage types 6-7, Figure 4.21 (a), damage types 11a and 11b, etc.) are developed.

For F3 (the frame with standard infills) in Figure 4.22, stiffness degradations are obtained as 3%, 8%, 24%, 32%, 42%, and 51% for 0.20%, 0.50%, 1.00%, 1.40%, 2.20%, and 3.50% drift ratios, respectively. Various types of column cracks, frame-infill separation, and cracks at the corner zones of the infill wall are the main damage types seen within the 0.50%-1.00% drift ratio interval. The largest change in the stiffness degradation (~16%) is also observed within this interval. Within the drift ratios following this range, beam and infill member damages start to substantially increase without a sudden change in the stiffness degradation (i.e., a smoother, more gradual change has been observed for F3 also confirmed by the changes in the frequency estimations).

From the findings above, it can be said that the presence of infills initiated R/C member damages to occur earlier than the bare frame. The stiffness degradation values calculated at the ultimate damage state (i.e., 3.50%) are 70%, 62%, and 51% for the frames F1 (bare frame), F2 (frame with locked infills) and F3 (frame with standard infills), respectively. Here again, the behavior of the frame with locked infills seems

analogous to the bare frame in the sense of stiffness degradation values. It should be noted that the quasi-static tests let to perform detailed damage observations, whereas the dynamic tests let to calculate stiffness degradations by using the identified modal parameters. By combining the outputs of these two tests, it is possible to pair different damage types (from static tests) with stiffness degradation values (from dynamic tests).

1a) Flexural cracks at column bottom ends.
2a) Flexural cracks at column top ends.
3a) Flexural cracks at column central zone.
1b) Shear cracks at column bottom ends.
2b) Shear cracks at column top ends.
3b) Shear cracks at column central zone.
4a) Shear cracks at column – beam joint region.
11a) Crushing of cover concrete at left column bottom end.
11b) Crushing of cover concrete at right column bottom end.
12a) Uplift between left column and foundation.
12b) Uplift between right column and foundation.
13) Reinforcements at column bottom ends become visible.
15) Buckling of reinforcements at column bottom ends.
18) Rupture of reinforcement at column bottom ends.
22) 2 mm crack width at column ends.
23) 5 mm crack width at column ends.

4b) Flexural cracks at beam – column joint region.
5a) Flexural cracks at beam ends.
5b) Flexural cracks at beam central region.
10) Flexural cracks at slab.
14) Reinforcements at beam ends become visible.
16 Buckling of reinforcement at beam ends.
17) Rupture of reinforcement at beam ends.
19) 2 mm crack width at beam ends.
20) 5 mm crack width at beam ends.
21) 10 mm crack width at beam ends.

6) Separation starts between infill wall – beam interface.
7) Separation starts between infill wall – column interface.
6-7) Frame – infill interface separation.
8a) Horizontal shear cracks at central and edge zones.
8b) Diagonal shear cracks at central and edge zones.
8c) Cracks at upper and lower side of infill.
9a) Cracks at infill corner (a).
9b) Cracks at infill corner (b).
9c) Cracks at infill corner (c).
9d) Cracks at infill corner (d).
8-9-a) Crushing and spalling of plaster.
8-9-b) Spalling of infill wall.

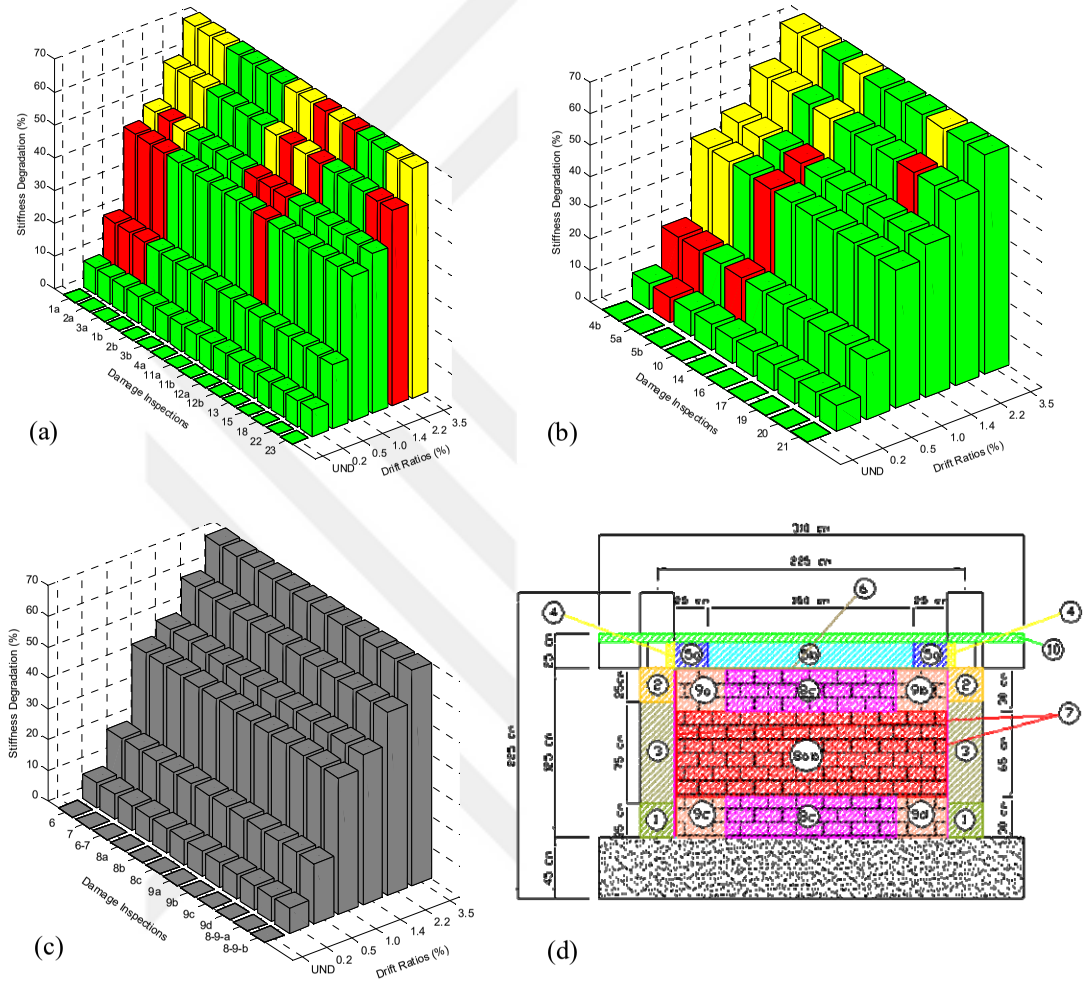

Figure 4.20 Combined stiffness degradation-visual damage inspection plots for F1: (a) column, (b) beam, (c) infill wall members, and (d) approximate zonation of different damage types

1a) Flexural cracks at column bottom ends.
2a) Flexural cracks at column top ends.
3a) Flexural cracks at column central zone.
1b) Shear cracks at column bottom ends.
2b) Shear cracks at column top ends.
3b) Shear cracks at column central zone.
4a) Shear cracks at column – beam joint region.
11a) Crushing of cover concrete at left column bottom end.
11b) Crushing of cover concrete at right column bottom end.
12a) Uplift between left column and foundation.
12b) Uplift between right column and foundation.
13) Reinforcements at column bottom ends become visible.
15) Buckling of reinforcements at column bottom ends.
18) Rupture of reinforcement at column bottom ends.
22) 2 mm crack width at column ends.
23) 5 mm crack width at column ends.

4b) Flexural cracks at beam – column joint region.
5a) Flexural cracks at beam ends.
5b) Flexural cracks at beam central region.
10) Flexural cracks at slab.
14) Reinforcements at beam ends become visible.
16 Buckling of reinforcement at beam ends.
17) Rupture of reinforcement at beam ends.
19) 2 mm crack width at beam ends.
20) 5 mm crack width at beam ends.
21) 10 mm crack width at beam ends.

6) Separation starts between infill wall – beam interface.
7) Separation starts between infill wall – column interface.
6-7) Frame – infill interface separation.
8a) Horizontal shear cracks at central and edge zones.
8b) Diagonal shear cracks at central and edge zones.
8c) Cracks at upper and lower side of infill.
9a) Cracks at infill corner (a).
9b) Cracks at infill corner (b).
9c) Cracks at infill corner (c).
9d) Cracks at infill corner (d).
8-9-a) Crushing and spalling of plaster.
8-9-b) Spalling of infill wall.

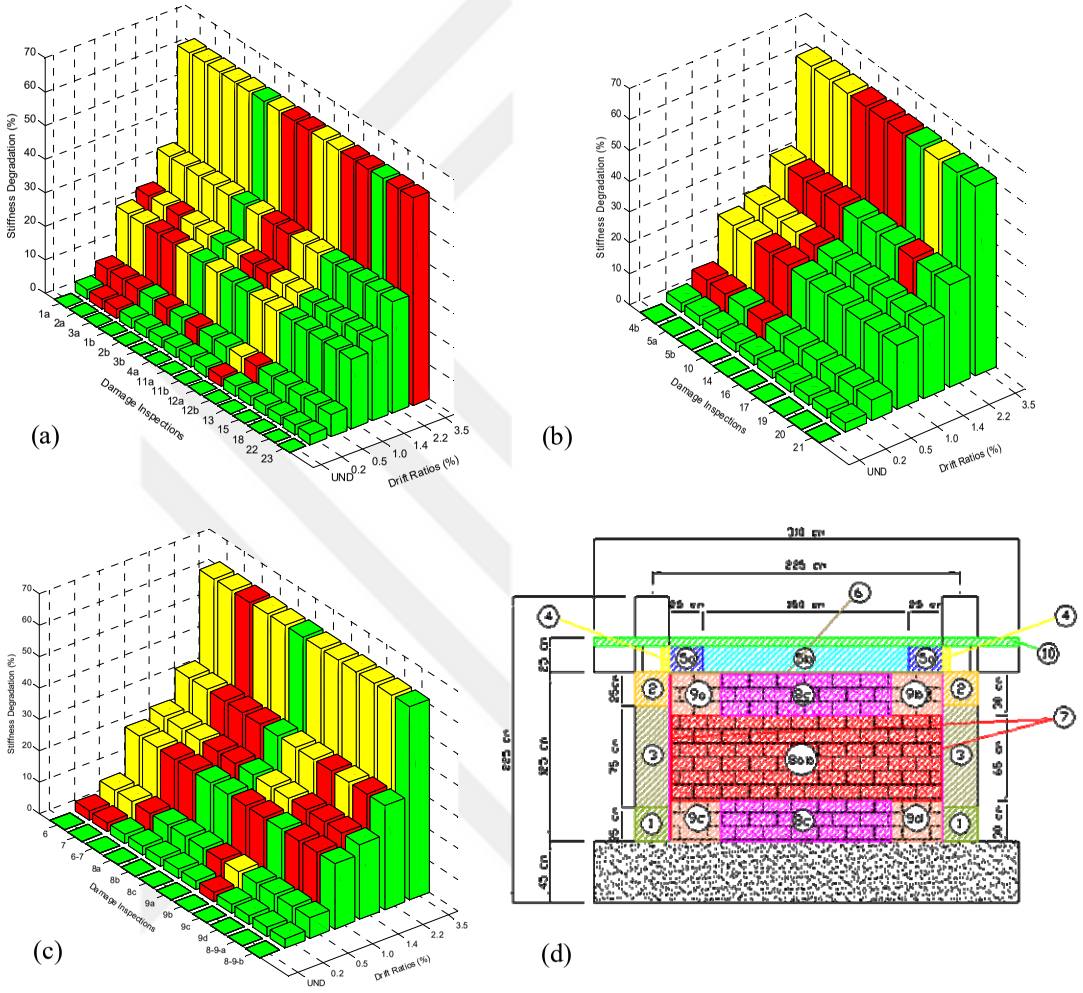

Figure 4.21 Combined stiffness degradation-visual damage inspection plots for F2: (a) column, (b) beam, (c) infill wall members, and (d) approximate zonation of different damage types

1a) Flexural cracks at column bottom ends.
2a) Flexural cracks at column top ends.
3a) Flexural cracks at column central zone.
1b) Shear cracks at column bottom ends.
2b) Shear cracks at column top ends.
3b) Shear cracks at column central zone.
4a) Shear cracks at column – beam joint region.
11a) Crushing of cover concrete at left column bottom end.
11b) Crushing of cover concrete at right column bottom end.
12a) Uplift between left column and foundation.
12b) Uplift between right column and foundation.
13) Reinforcements at column bottom ends become visible.
15) Buckling of reinforcements at column bottom ends.
18) Rupture of reinforcement at column bottom ends.
22) 2 mm crack width at column ends.
23) 5 mm crack width at column ends.

4b) Flexural cracks at beam – column joint region.
5a) Flexural cracks at beam ends.
5b) Flexural cracks at beam central region.
10) Flexural cracks at slab.
14) Reinforcements at beam ends become visible.
16 Buckling of reinforcement at beam ends.
17) Rupture of reinforcement at beam ends.
19) 2 mm crack width at beam ends.
20) 5 mm crack width at beam ends.
21) 10 mm crack width at beam ends.

6) Separation starts between infill wall – beam interface.
7) Separation starts between infill wall – column interface.
6-7) Frame – infill interface separation.
8a) Horizontal shear cracks at central and edge zones.
8b) Diagonal shear cracks at central and edge zones.
8c) Cracks at upper and lower side of infill.
9a) Cracks at infill corner (a).
9b) Cracks at infill corner (b).
9c) Cracks at infill corner (c).
9d) Cracks at infill corner (d).
8-9-a) Crushing and spalling of plaster.
8-9-b) Spalling of infill wall.

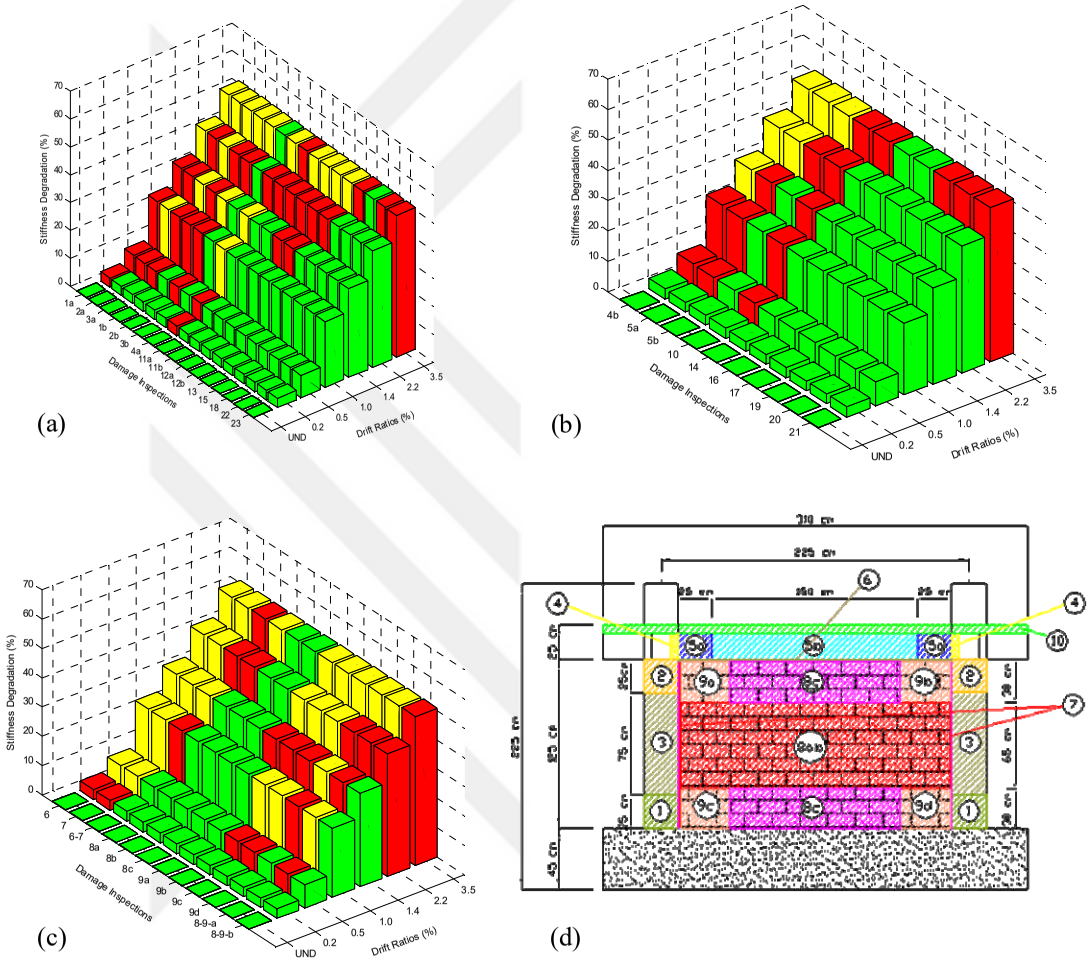

Figure 4.22 Combined stiffness degradation-visual damage inspection plots for F3: (a) column, (b) beam, (c) infill wall members, and (d) approximate zonation of different damage types

4.6.1 Identification of the Out-of-Plane Modes

As stated before, only the first in-plane modes of the frames are discussed so far. It should be stated that the higher modes couldn't be identified clearly from the dynamic data due to low excitation levels and SNR (i.e., even in the case of WN wo/Offline, the excitation level is low). In other words, the higher modes of the frames couldn't be excited sufficiently. However, the frames are most likely to have structural modes in their weakest directions (i.e., out-of-plane direction), which means that the frames have out-of-plane modes in lower frequency values than those of their in-plane modes. This statement can be supported by investigating the Fourier amplitude spectrum diagrams of the dynamic response data. As an example, for the bare frame (F1), Fourier amplitude spectrum of Sta 4 (with x-, y-, and z-components, see Figure 4.7) is presented in Figure 4.23 (WN w/Offline dataset at 3.50% drift ratio was used).

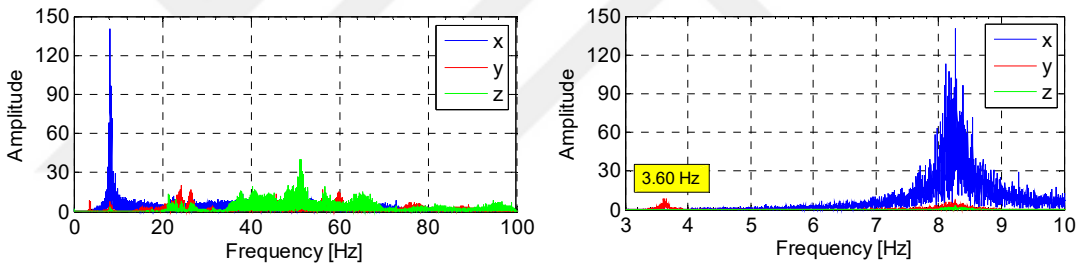

(a) (b)

Figure 4.23 (a) Fourier amplitude spectrum for Sta 4, (b) zoomed in 3-10 Hz bandwidth (for F1, by using the WN w/Offline dataset at 3.50% drift ratio)

In the figure, the peak value around 3.60 Hz for the y-component represents the out-of-plane mode. Note that the out-of-plane mode is not pronounced as much as the in-plane mode (x-component, around 8.23 Hz) since the excitation to the frames is in in-plane direction only. Therefore, higher estimation uncertainty is expected in the out-of-plane mode (i.e., lower SNR value along the non-excited direction).

It should be stated that the out-of-plane modes of the frames couldn't be identified by NExT-ERA and SSI methods (i.e., parametric methods). Therefore, identification was conducted by using EFDD method with a peak-picking process around the frequency of interest. The modal parameter estimation results of the frames at different

damage states are given in Table 4.7. Similar to the in-plane modes, the frequency values show a decreasing trend as structural damage increases, whereas no clear trend is observed for damping ratios. Herein, at the undamaged state, the bare frame (F1) has the highest frequency value among the tested frames. This is a reasonable result since the contribution of the infill wall to the out-of-plane stiffness of the frame system is relatively low compared to the increase in the mass of the frame system due to the presence of the infill wall.

Table 4.7 Modal parameters of the out-of-plane modes of the frames (WN w/Offline dataset by EFDD method)

Frame #	Modal Params	No Damage	0.20%	0.50%	1.00%	1.40%	2.20%	3.50%
F1 (no infill)	ω [Hz]	5.58	5.26	5.41	5.11	4.57	3.87	3.63
	ξ [%]	3.27	1.49	3.14	2.05	2.46	2.50	2.80
F2 (locked infill)	ω [Hz]	4.57	4.14	4.10	4.08	3.96	3.74	3.63
	ξ [%]	2.09	2.68	2.81	2.09	2.39	1.99	0.41
F3 (standard infill)	ω [Hz]	4.41	4.15	4.06	3.82	3.77	3.40	3.05
	ξ [%]	2.76	3.06	2.96	2.45	2.97	1.78	2.76

The polar plot representations of the identified out-of-plane mode shapes are given in Figure 4.24.

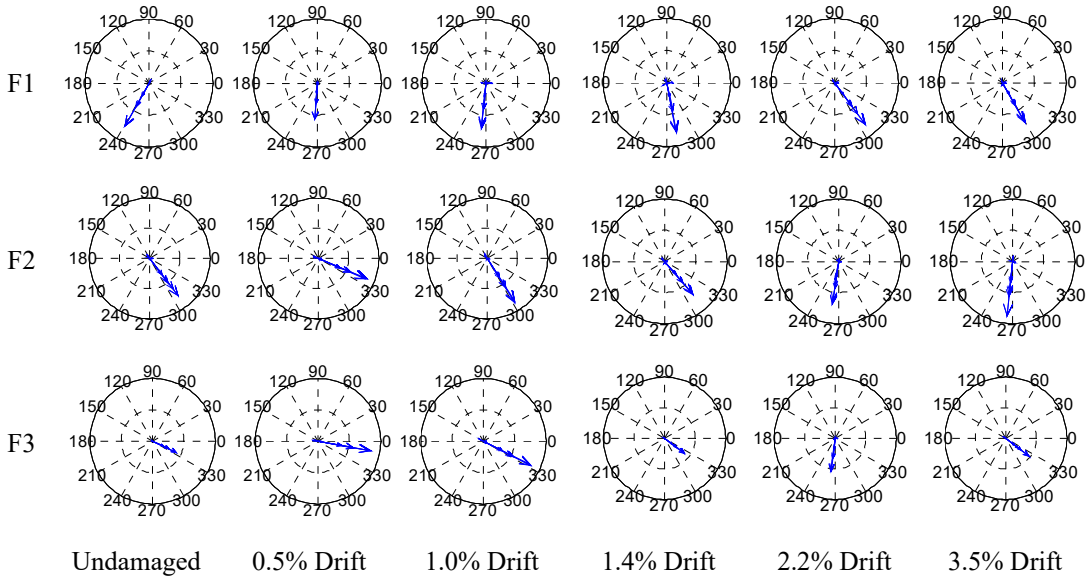

Figure 4.24 Polar plot representations of the out-of-plane mode shapes

It clear from Figure 4.24 that the modes are classically damped and have larger complex components due to low SNR values. That's why the out-of-plane mode shapes are considered as unreliable estimates and comparing their evolutions with respect to increasing damage levels may lead to unrealistic results (i.e., the evolution of the MAC values is not provided in Table 4.7 because of this reason).

CHAPTER FIVE
DAMAGE IDENTIFICATION OF THE QUASI-STATICALLY TESTED REINFORCED CONCRETE FRAMES WITH DIFFERENT INFILL CONDITIONS BY SENSITIVITY-BASED FINITE ELEMENT MODEL UPDATING METHOD

5.1 Introduction

In this chapter, sensitivity-based FEMU studies performed on the quasi-statically tested R/C frames with different infill conditions, namely bare, locked infilled, and standard infilled frames, for damage identification purposes are presented. Structural damages of the frames were defined by relative stiffness reduction factors (i.e., reduction in Young's modulus and/or spring stiffness values), and each progressively increasing damage state, the stiffness reduction factors of the predetermined elements (i.e., design variables) were obtained by minimizing an objective function constructed as the differences between the modal parameters of the real structure (from OMA results discussed in Chapter Four) and the numerical model (from FE model). In this context, modal parameter results of the EFDD method with WN w/Offline dataset were used. The updating process for each frame was conducted in two steps: (i) By using the experimentally identified modal parameters corresponding to the undamaged state, the initial FE model was updated to obtain a reliable reference model. (ii) The procedure was repeated by updating this reference model at each progressively increasing damage state (e.g., 0.50%, 1.00%, 1.40%, 2.20%, and 3.50%) to identify the damage, its location, and extent. The number of design variables used for the updating procedure was reduced to ensure a well-conditioned optimization problem by taking into account symmetry conditions, detectability indices, and internal moment levels occurred in the frame elements. Different from the existing state of the art, these three aspects were evaluated together to obtain damage identification results which are more consistent with the damage observations and are more realistic for increasing damage levels. Finally, the identified damage results were verified using the visual damage observations made during the quasi-static tests.

5.2 Damage Identification of the Bare Frame (F1)

This section presents the results of the sensitivity-based FEMU method carried out on the bare frame (F1) for damage identification purpose. The initial FE model of the frame was constituted in FEDEASLab environment by using 3-D linear elastic Bernoulli-Euler frame elements. Physical properties (i.e., model parameters) of the initial FE model were identified from measured geometric dimensions and material tests. Accordingly, Young's modulus and density values for concrete were chosen as 32 GPa and 25 kN/m^3, respectively. Note that it is very difficult (almost impossible) to attain perfect fixity at supports in real-life situations. Therefore, support conditions of the initial FE model were represented by simple supports at the column(s) bottom ends together with three rotational springs about x- (in-plane), y- (out-of-plane), and z- (vertical) axes. Other nodes of the FE model were set to be unconstrained. The initial spring stiffnesses were determined as 9807 kNm/rad by manual updating procedure (i.e., trial-and-error method) for the purpose of bringing the numerical modal analysis results close to the experimentally identified ones; however, the ultimate spring stiffnesses were determined by automated model updating approach presented in Section 5.2.1 (i.e., by performing manual updating before, it was aimed to improve the converge performance of the automated updating). Note that the distributed mass of the frame was supposed to be lumped at the nodes of the FE model (i.e., lumped mass assumption was made).

The vibration frequencies and mode shapes of the first two modes (i.e., out-of-plane and in-plane modes), which were obtained by EFDD method with WN w/Offline dataset, were selected as the experimental responses to be used in the updating process. This is because these modes were clearly identifiable from all response data collected at different damage levels, and therefore were considered as reliable estimations.

The initial FE model was divided into 12 substructures (i.e., 3 and 9 substructures for rotational springs and 9 frame elements, respectively) by considering the neighboring and geometrically symmetric finite elements that have similar effects (i.e., detectabilities) on modal parameters (e.g., substructure #1 for the bottom, substructure

#2 for the mid, and substructure #3 for the top elements of the column(s), see Figure 5.1 (b)). Note that independent damage functions were assigned for each substructure (i.e., the substructures were updated separately). It should be stated that the adopted substructuring strategy is also convenient for symmetric damage occurrence which is expected due to the cyclic quasi-static loading case (i.e., symmetric loading). In addition, the detectability indices of these substructures were calculated for the first mode only, for the second mode only, and for both modes together (Figure 5.1 (a)).

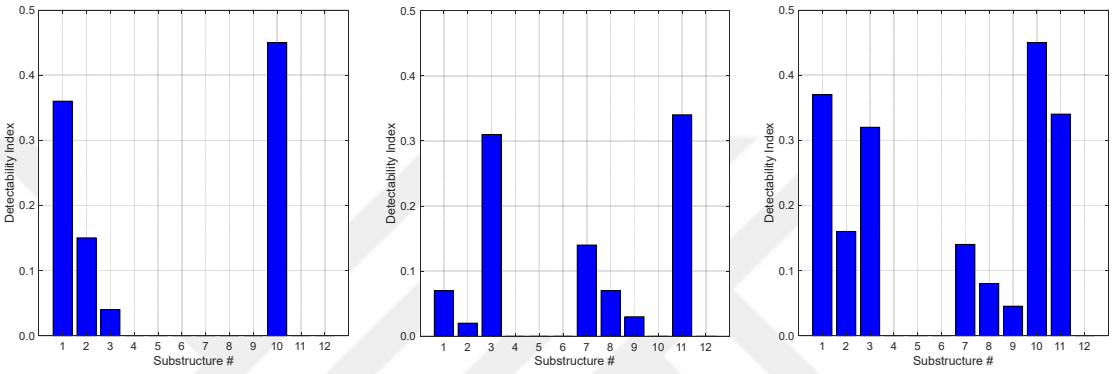

1st mode (out-of-plane) 2nd mode (in-plane) 1st and 2nd modes together

(a)

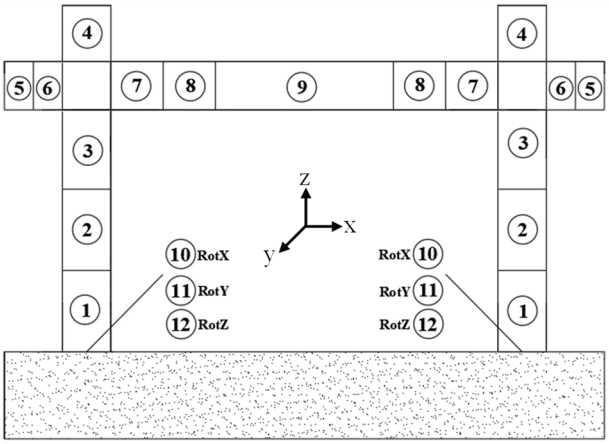

Detectable Elements

#1 Column(s) bottom ends

#2 Column(s) mid-zones

#3 Column(s) top ends

#7-8 Beam ends

#9 Beam mid-zone

#10 Rotational springs about x-axis (RotX)

#11 Rotational springs about y-axis (RotY)

(b)

Figure 5.1 (a) Detectability indices and (b) detectable elements

It can be concluded from Figure 5.1 that the sensitivity of a mode can change from one substructure to another (i.e., detectability of a substructure can vary from one mode to another). Besides, some of the modes are insensitive to variations in some substructures (i.e., having zero detectability index value). For example, the 2nd mode

(in-plane mode) is sensitive to the rotational springs about y-axis (i.e., substructure #11, the springs related to the in-plane motion of the frame) but insensitive to the rotational springs about x-axis (i.e., substructure #10, the springs related to the out-of-plane motion of the frame). By investigating the detectability indices, the detectable substructures (i.e., the substructures which the modes are sensitive) along with their numbers were determined as follows: column(s) bottom ends (#1), column(s) mid-zones (#2), column(s) top ends (#3), beam ends (#7 and #8), beam mid-zone (#9), rotational springs about x-axis (#10), and rotational springs about y-axis (#11). Since the modes are insensitive to the other substructures (i.e., substructures #4, #5, #6, and #12), these substructures were eliminated. Thus, the number of substructures included in the updating procedure (i.e., design variables) was reduced from 12 to 8.

For the frame, the bending moment capacity ratio between the beam ends and the column(s) top ends is approximately 40% (i.e., columns are stronger than the beam in terms of flexural strength). That's why, theoretically, the plastic hinges are expected to first occur at beam ends (i.e., at weaker sections) instead of column(s) top ends. As a result of the plastic hinge mechanism, the moment transferred from beam ends to column(s) top ends is limited by the moment capacity of the beam ends. Since this transferred moment is lower than the moment capacity of the column(s) top ends, minor structural damage is expected to occur in these regions (confirmed by the damage observations presented later in this chapter). This is not the case for the column(s) bottom ends: As the moment due to the in-plane applied load increases, it must be resisted by the column(s) bottom ends. Therefore, major structural damage in these regions is expected to occur (also confirmed by the damage observations). The mid-zones of the beam and column members were not selected as design variables due to their relatively low internal moment levels (i.e., as stated before, a response sensitive to a parameter does not automatically imply that this parameter has to be included in the updating process). In addition, only insignificant damage occurrence was observed in these regions during visual damage inspections. Consequently, selecting 4 design variables were decided to be convenient for damage identification, namely column(s) bottom ends (#1), beam ends (#7-8), rotational springs about x-axis (#10), and rotational springs about y-axis (#11). Note that a common design variable was defined

for the adjacent elements for the beam ends at this stage (i.e., only one design variable instead of two for the elements designated as #7 and #8 in Figure 5.1 (b)).

The structural damages of the frame were defined by relative stiffness reduction factors (i.e., reduction in Young's modulus and/or spring stiffness values), and each progressively increasing damage state, the stiffness reduction factors of design variables were obtained by minimizing an objective function constructed as the differences between the modal parameters of the real structure (from OMA results discussed in Chapter Four) and the numerical model (from FE model). The updating process was conducted in two steps: (i) By using the experimentally identified modal parameters corresponding to the undamaged state, the initial FE model was updated to obtain a reliable reference model. In this step, the design variables were updated until a good match between numerically and experimentally identified modal parameters was obtained. (ii) The procedure was repeated by updating this reference model at each progressively increasing damage state (e.g., 0.50%, 1.00%, 1.40%, 2.20%, and 3.50%) to identify the damage, its location, and extent. Here, updating was performed always on the reference model instead of on the updated model of a previous damage state (e.g., damage results of 2.20% drift ratio were obtained by updating the reference model). This was done to ensure higher discrepancies for the optimization algorithm and to prevent probable cumulative errors between successive damage levels. In the second step, the rotational spring stiffnesses were excluded from the updating process (i.e., they were not updated and remained at their values that determined in the first step). Otherwise, they would attract most of the changes (i.e., damage) on themselves due to their higher detectabilities (see Figure 5.1) and would lead to unrealistic damage results for other substructures. Note that the constraints for the design variables were set to be ±1.0 (i.e., $\mathbf{l_b}$ = **-1.0** and $\mathbf{u_b}$ = **+1.0**) where (-) values mean stiffening and (+) values mean softening (or damage). The weighting factors were set to 1.0 for the out-of-plane and in-plane vibration frequencies, and for the in-plane mode shapes only, whereas the out-of-plane mode shapes were excluded from the updating process by setting their weighting factors to 0. This was done due to the high estimation uncertainty and complexity seen in these modes which might lead to unfavorable effects on the stability and performance of the optimization problem.

5.2.1 Updating for the Reference Model (Undamaged State)

The initial FE model was updated to obtain the reference model by using the modal data of the undamaged state. As stated before, the substructures column(s) bottom ends (#1), beam ends (#7-8), rotational springs about x-axis (#10), and rotational springs about y-axis (#11) were selected as design variables, thus n=4. The residual vector $\mathbf{r}$ [36x1] consists of 1x2=2 frequency residuals $\mathbf{r}_f$ and 17x2=34 mode shape residuals $\mathbf{r}_s$ (17 is the number of experimental measurement points, 2 is the number of modes that were included in the updating process). Note that 17 components of the $\mathbf{r}_s$, which are related to the out-of-plane mode shape, are equal to zero due to their weightings. The Jacobian matrix $\mathbf{J}_\mathbf{P}$ has dimensions of 36x4, where m=36 and n=4. Since n<m, an overdetermined problem occurs. Model order (d) was selected as 51 (i.e., all the numerical modes). The optimization problem was solved by Gauss-Newton method with trust region algorithm. Results are shown in Table 5.1.

As can be seen in Table 5.1, only the rotational springs were updated by the algorithm because of their relatively higher detectabilities (i.e., other design variables were not updated although they were involved in the updating procedure). Accordingly, the appropriate reference model was obtained when the spring stiffnesses about x- and y-axes became 5894 kNm/rad and 7444 kNm/rad, respectively. It is clear from Table 5.1 that the vibration frequencies of the reference FE model (updated model, 3rd column) and the experimentally identified ones (2nd column) match very well. Also, the MAC values calculated before (i.e., between the mode shapes of the initial FE model and the experimentally identified ones, 6th column) and after (between the mode shapes of the reference FE model and the experimentally identified ones, 7th column) updating exhibit very marginal improvements which indicate that the considered mode shapes have low sensitivities to the selected design variables (i.e., almost insensitive).

Table 5.1 Model updating results of the initial FE model to obtain the reference model using modal data of the undamaged state (F1 – bare frame)

(1) Initial FE Model Freq.	(2) Undamaged Frame Freq.	(3) Updated FE Model Freq.	(4) Freq. Differences Before Updating (1 - 2)	(5) Freq. Differences After Updating (3 - 2)	(6) MAC Before Updating (1 - 2)	(7) MAC After Updating (3 - 2)
[Hz]	[Hz]	[Hz]	[%]	[%]	[-]	[-]
6.16	5.58	5.58	10	0	0.99	0.99
15.70	15.10	14.98	4	1	0.95	0.96

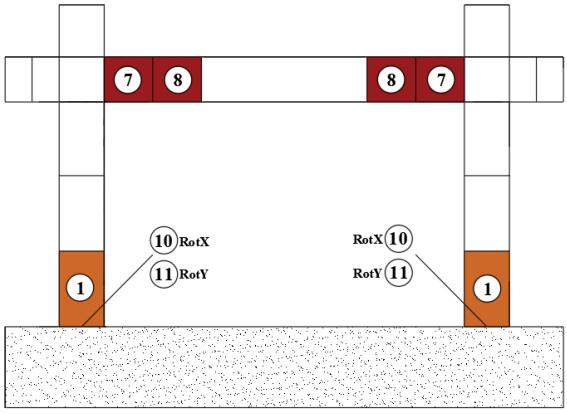

Design Variables
#1 Column(s) bottom ends
#7-8 Beam ends
#10 Rotational springs about x-axis (RotX)
#11 Rotational springs about y-axis (RotY)

	Initial	Ref. Model (Updated)
#10 RotX (kNm/rad):	9807	5894
#11 RotY (kNm/rad):	9807	7444

*Substructures #1 and #7-8 were also selected as design variables but not updated by the algorithm.

5.2.2 Damage Identification at Increasing Damage States

Damage identification of the frame at increasing damage states was performed by updating the reference model, which was obtained in the previous section. At each damage state, the corresponding experimental modal data were used. Two design variables were included in the updating process, namely the one at the column(s) bottom ends and the one at the beam ends (i.e., the substructures #1 and #7-8 in Table 5.1). Notice that the spring stiffnesses were kept fixed and excluded from the updating process as stated in Section 5.2. Since n=2 (i.e., two design variables), dimensions of the Jacobian matrix became 36x2 (i.e., n<m, an overdetermined problem occurs). It should be stated that the conditions not specified here were the same as the ones adopted in Section 5.2.1. The updating results with the dimensionless stiffness

reduction factors (in terms of p in percent) at different damage states with respect to the reference (undamaged) state are presented in Table 5.2.

Table 5.2 Model updating results of the reference model for increasing damage states using the modal data of the increasing damage states (F1 – bare frame)

Drifts [%]	(1) Reference FE Model Freq.	(2) Damaged Frame Freq.	(3) Updated FE Model Freq.	(4) Freq. Diff. Before Updating (1 - 2)	(5) Freq. Diff. After Updating (3 - 2)	(6) MAC Before Updating (1 - 2)	(7) MAC After Updating (3 - 2)
	[Hz]	[Hz]	[Hz]	[%]	[%]	[-]	[-]
0.50	5.58	5.41	5.41	3	0	0.99	0.99
	14.98	13.55	13.64	11	1	0.96	0.96
1.00	5.58	5.11	5.10	9	0	0.98	0.98
	14.98	11.11	11.22	35	1	0.98	0.98
1.40	5.58	4.57	4.55	22	0	0.98	0.98
	14.98	11.05	11.17	36	1	0.98	0.98
2.20	5.58	3.87	3.85	44	0	0.97	0.97
	14.98	9.62	9.73	56	1	0.99	0.98
3.50	5.58	3.64	3.62	54	0	0.99	0.98
	14.98	8.25	8.33	82	1	0.99	0.98

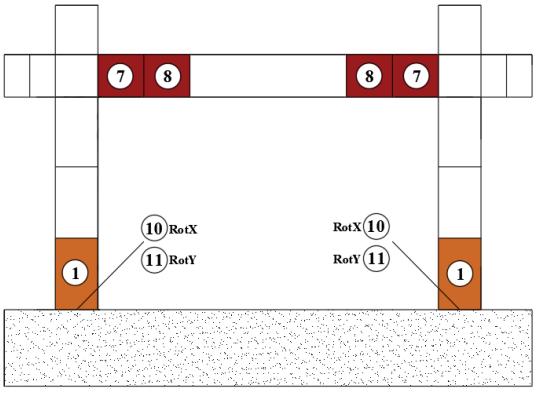

Design Variables

#1 Column(s) bottom ends

#7-8 Beam ends

Drifts [%]	Stiffness reduction factors with respect to the reference state (p%)	
	#1	#7-8
Reference	0	0
0.50	15	49
1.00	35	81
1.40	58	78
2.20	75	85
3.50	79	91

*Rotational spring stiffnesses #10 and #11 were not selected as design variables.

It is clear from Table 5.2 that the experimentally identified vibration frequencies (2nd column) and the ones of the updated FE model (3rd column) match almost perfectly. Especially for the 3.50% drift ratio, significant reduction from 82% to 1%

observed in the frequency differences calculated before and after updating (4^{th} and 5^{th} columns) reveals the effectiveness of the method. On the other hand, the MAC values calculated before and after updating (6^{th} and 7^{th} columns) are almost same due to their low sensitivities to the selected design variables (i.e., almost insensitive). The dimensionless stiffness reduction factors in Table 5.2 indicate that the severity of the structural damage increases as increasing drift level. This is because of the accumulation of damage on beam ends and column(s) bottom ends.

Contour plots of the objective function with respect to the changes in the design variables are presented in Figure 5.2 to examine the solution space of the optimization problem for different damage states. Note that these plots can be plotted since only two design variables were used for the updating. In Figure 5.2, x- and y-axes indicate the design variables used for beam and column(s) bottom ends (i.e., two design variables), whereas the z-axis (contours) represents the value of the objective function for a particular design parameter pair. The areas with darker blue zones indicate the global minimum (i.e., solution of the optimization problem). It can be said that the objective function has a flat surface in the vicinity of the solution. In other words, the global minimum lies within a wide interval (especially at low damage states); therefore, there exists no prominent solution for the optimization problem (i.e., it is difficult to find the global minimum point). As the damage level increases, the areas with darker blue zones shrink (i.e., the region indicating the global minimum narrows down), indicating that the solution becomes closer to a prominent one. This verifies that the chosen design parameters are convenient to represent the damage patterns observed at higher drift ratios.

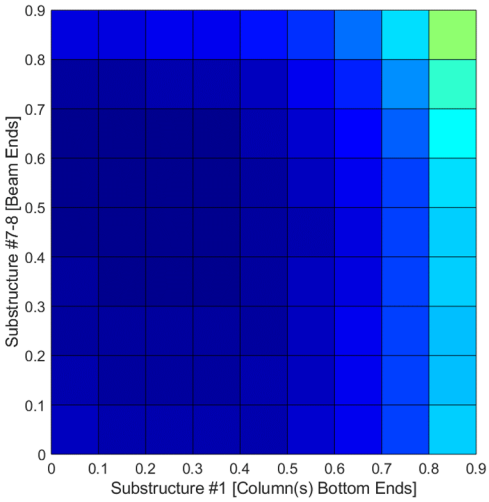

0.50% drift ratio

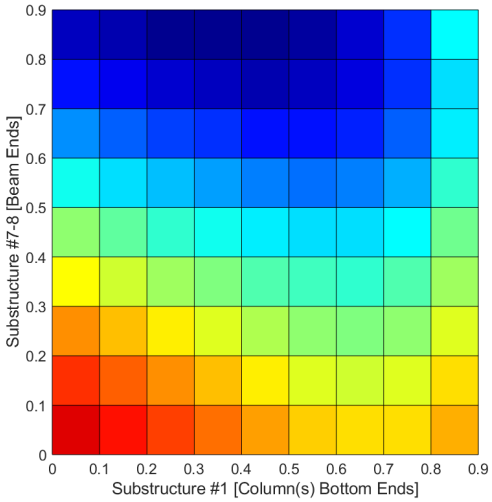

1.00% drift ratio

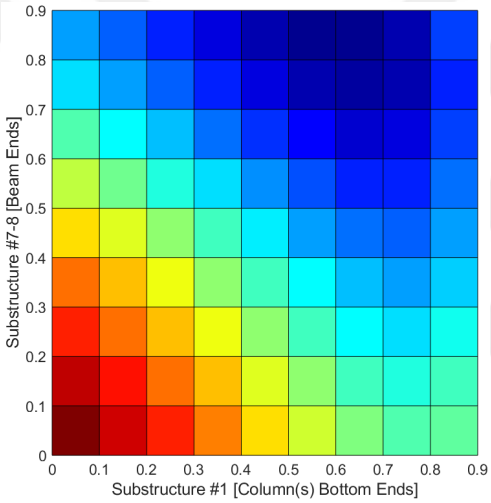

1.40% drift ratio

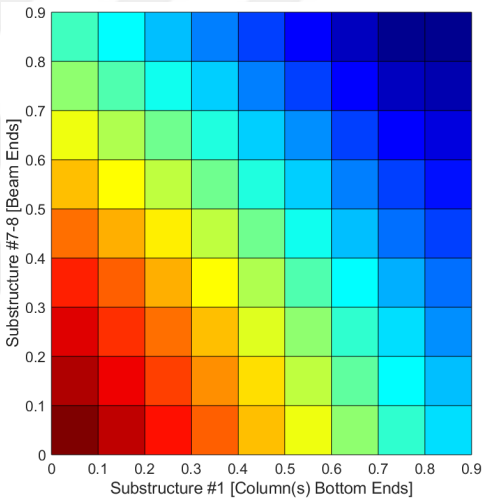

2.20% drift ratio

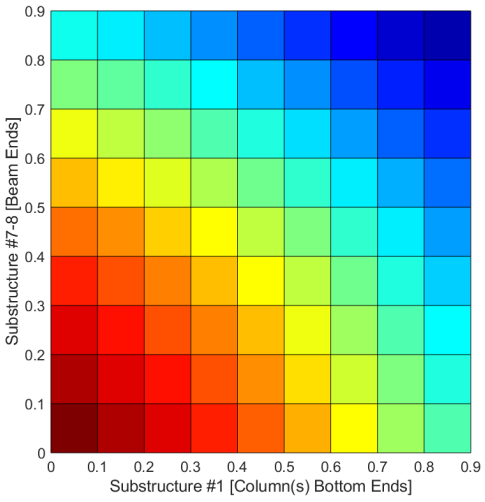

3.50% drift ratio

Figure 5.2 The contour plots of the objective function for increasing damage states (F1 – bare frame)

The damage identification results presented above were also supported by visual damage inspections made during quasi-static tests. In Figure 5.3 (a), the damage state of the frame at 3.50% drift ratio (i.e., the drift ratio where the design variables are more representative) is shown. Here, extensive and deep cracks were observed on the beam and the column(s) bottom ends, which are presented in Figures 5.3 (b) and (c), respectively. At this drift ratio, deep cracks and spalling of concrete were observed on the column(s) bottom ends, and more than 5 mm crack width was measured on the beam ends. In this damage level, the vibration frequencies of the frame were reduced by 35% and 45% for the first and the second modes with respect to the undamaged state, respectively. The damage observations during the tests are in good agreement with the damage identification results. Especially, structural damage is mainly concentrated on the beam ends and on the column(s) bottom ends, whereas there exists only minor damage on the other parts of the frame (i.e., column(s) top ends, column(s) mid-zones, and beam mid-zone). Note that the pictures presented in Figures 5.3 (b) and (c) are chosen to indicate the most damaged sides of the beam and column(s).

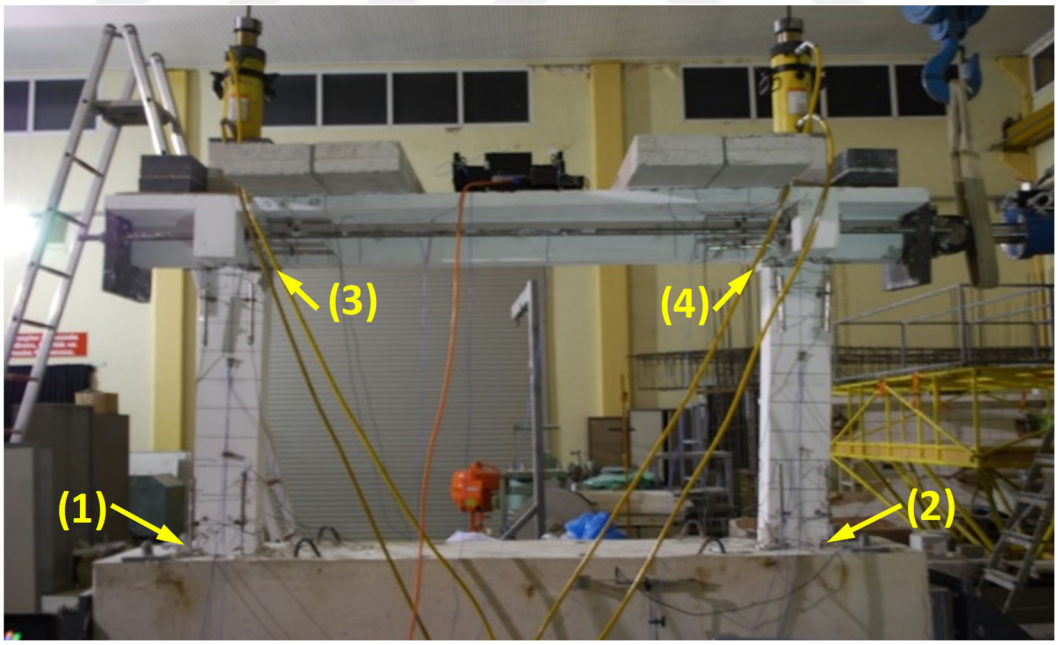

(a)

Figure 5.3 (a) General view of the frame, observed damages on the (b) beam ends and the (c) column(s) bottom ends at 3.50% drift ratio (Personal archive, 2016)

(b)

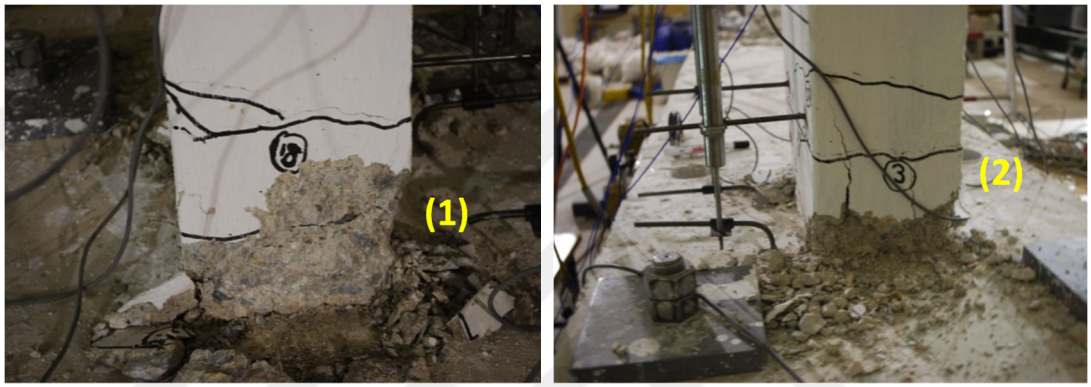

(c)

Figure 5.3 continues

5.3 Damage Identification of the Infilled Frames (F2 and F3)

In real-life situations, it is a known fact that the existence of infill walls has stiffening effects along the in-plane directions of structural systems. This means that the infilled structures have higher in-plane vibration frequencies than those of their counterparts without infills. Nevertheless, this is not the case for the tested frames (i.e., F1, F2, and F3) within the context of this thesis. By investigating the modal identification results presented in Section 4.6, it can be seen that the in-plane frequencies for the frames at undamaged state are very similar (i.e., minor differences may be due to variabilities in production, workmanship, concrete strength, axial load level, etc.), which implies that the infills are ineffective. This may be considered as a counter-intuitive result at a first glance, but it should be emphasized that the infill walls couldn't be excited properly during the dynamic tests due to the low excitation levels. In other words, the infill walls are too rigid to be excited by the excitation conditions

at hand. Namely, the excitation capacity of the shaker is limited due to its size and the ambient excitation is not sufficient and proper since the tests were conducted under closed (i.e., isolated) laboratory conditions without environmental effects (i.e., absence of usual ambient effects such as traffic, wind, etc.). Therefore, the recorded vibration data represent the dynamic characteristics of only the frame structure without the contributions of the infills. Note that although the infills are ineffective during the dynamic tests, they have a decisive role in the behaviors and damage formations of the frames during the quasi-static tests, which is revealed by damage observations presented in Chapter Four.

Since the dynamic characteristics of the infilled frames are very similar to the bare frame, therefore very similar to the FE model of the bare frame, considering the infill members in the modeling stage would lead to obtaining FE models which diverge from the experimental results. It is therefore impossible to develop realistic FE models, which are the representatives of the actual frame systems, for the infilled frames.

Based on the statements above, the initial FE model of the bare frame (refer to Section 5.2) was used for damage identification purposes of the infilled frames. Since it was not possible to perform damage identification of the infill walls (i.e., due to lack of the FE model with infills), effects of different types of infills on the frame structures' damage mechanisms were aimed to be investigated. In this context, the procedure applied on the bare frame (refer Section 5.2 for details) was adopted with some minor differences. Details and the obtained damage identification results are presented in the following sections.

5.3.1 Damage Identification of the Frame with Locked Infills (F2)

In this section, damage identification of the frame with locked infills (F2) is discussed. Due to the low-to-moderate (mild) level panel action, which occurs because of the sliding mechanism of the locked bricks over each other, the infill wall cannot resist the motion of the frame structure (i.e., the infill wall moves together with the surrounding frame during the cyclic tests). Therefore, minor damage is expected on

the frame structure caused by the infill wall. In addition, the locked infilled frame behaved almost similar to the bare frame during the quasi-static tests. Based on these findings, the design variables used for the bare frame were found to be appropriate also for this case. Consequently, column(s) bottom ends (#1), beam ends (#7-8), rotational springs about x-axis (#10), and rotational springs about y-axis (#11) were selected as design variables.

The initial spring stiffnesses were determined as 3236 kNm/rad (RotX) and 7355 kNm/rad (RotY) by manual updating procedure (i.e., trial-and-error method) for the purpose of bringing the numerical modal analysis results close to the experimentally identified ones; however, the ultimate spring stiffnesses were determined by automated model updating approach in Section 5.3.1.1 (i.e., by performing manual updating before, it was aimed to improve the converge performance of the automated updating). Different from the bare frame, the weighting factors for the in-plane mode shapes at 0.00% (i.e., undamaged state), 0.50%, 1.00%, 1.40%, 2.20%, and 3.50% drift ratios were set to 0.3, 0.3, 0.5, 0.7, 0.7, and 1.0, respectively. This was done due to the out-of-plane components of the experimentally identified mode shapes which have no counterparts in the initial FE model (i.e., the initial FE model has pure in-plane mode shapes, whereas the experimental in-plane mode shapes have out-of-plane components, which result in minimization difficulties in mode shape residuals). Weighting factors for the other responses (i.e., in-plane and out-of-plane vibration frequencies, and out-of-plane mode shapes) were selected the same as the ones adopted for the bare frame.

5.3.1.1 Updating for the Reference Model (Undamaged State)

The initial FE model was updated to obtain the reference model by using the modal data of the undamaged state. As stated before, the substructures column(s) bottom ends (#1), beam ends (#7-8), rotational springs about x-axis (#10), and rotational springs about y-axis (#11) were selected as design variables, thus n=4. Note that the model updating work was performed under the same conditions that were detailed for the

bare frame in Section 5.2.1 (e.g., constraints, model order, dimensions of residual vector and Jacobian matrix, etc.). Results are presented in Table 5.3.

Table 5.3 Model updating results of the initial FE model to obtain the reference model using modal data of the undamaged state (F2 – frame with locked infills)

(1) Initial FE Model Freq.	(2) Undamaged Frame Freq.	(3) Updated FE Model Freq.	(4) Freq. Differences Before Updating (1 - 2)	(5) Freq. Differences After Updating (3 - 2)	(6) MAC Before Updating (1 - 2)	(7) MAC After Updating (3 - 2)
[Hz]	[Hz]	[Hz]	[%]	[%]	[-]	[-]
4.77	4.57	4.57	4	0	0.96	0.96
14.95	14.50	14.46	3	0	0.78	0.78

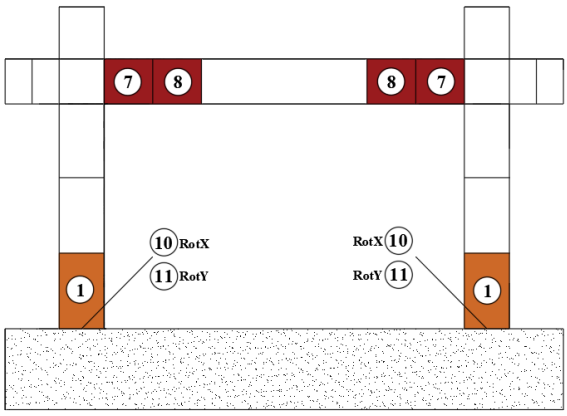

Design Variables
#1 Column(s) bottom ends
#7-8 Beam ends
#10 Rotational springs about x-axis (RotX)
#11 Rotational springs about y-axis (RotY)

	Initial	Ref. Model (Updated)
#10 RotX (kNm/rad):	3236	2824
#11 RotY (kNm/rad):	7355	6052

*Substructures #1 and #7-8 were also selected as design variables but not updated by the algorithm.

As can be seen, only the rotational springs were updated by the algorithm because of their relatively higher detectabilities (i.e., other design variables were not updated although they were involved in the updating procedure). Accordingly, the appropriate reference model was obtained when the spring stiffnesses about x- and y-axes became 2824 kNm/rad and 6052 kNm/rad, respectively (i.e., softer than those of the bare frame). It is clear from Table 5.3 that the vibration frequencies of the reference FE model (updated model, 3rd column) and the experimentally identified ones (2nd column) match very well. In addition, the MAC values calculated before (i.e., between the mode shapes of the initial FE model and the experimentally identified ones, 6th column) and after (between the mode shapes of the reference FE model and the

experimentally identified ones, 7th column) are almost same. This is mainly due to their relatively lower weighting factors, which drives the updating algorithm to emphasize more on matching the frequency responses, and/or their low sensitivities to the selected design variables (i.e., almost insensitive).

5.3.1.2 Damage Identification at Increasing Damage States

Damage identification of the frame at increasing damage states was performed by updating the reference model obtained in the previous section. Two design variables were included in the updating process, namely the one at the beam ends and the one at the column(s) bottom ends (i.e., the substructures #1 and #7-8 in Table 5.3), thus n=2 (i.e., here again, the spring stiffnesses were excluded from the updating process due to the same reason discussed before). Note that the model updating work was performed under the same conditions that were detailed for the bare frame in Section 5.2.2 (e.g., constraints, model order, dimensions of residual vector and Jacobian matrix, etc.). The updating results with the dimensionless stiffness reduction factors (in terms of p in percent) at different damage states with respect to the reference (undamaged) state are given in Table 5.4.

It is clear from Table 5.4 that the experimentally identified vibration frequencies (2nd column) and the ones of the updated FE model (3rd column) match almost perfectly. Especially for the 3.50% drift ratio, significant reduction from 62% to 1% observed in the frequency differences calculated before and after updating (4th and 5th columns) reveals the effectiveness of the method. On the other hand, the MAC values calculated before and after updating (6th and 7th columns) are almost same due to their weightings and/or low sensitivities to the selected design variables (i.e., almost insensitive). The dimensionless stiffness reduction factors in Table 5.4 indicate that the severity of the structural damage increases as increasing drift level. This is because of the accumulation of damage on beam and column(s) bottom ends.

Table 5.4 Model updating results of the reference model for increasing damage states using the modal data of the increasing damage states (F2 – frame with locked infills)

Drifts [%]	(1) Reference FE Model Freq.	(2) Damaged Frame Freq.	(3) Updated FE Model Freq.	(4) Freq. Diff. Before Updating (1 - 2)	(5) Freq. Diff. After Updating (3 - 2)	(6) MAC Before Updating (1 - 2)	(7) MAC After Updating (3 - 2)
	[Hz]	[Hz]	[Hz]	[%]	[%]	[-]	[-]
0.50	4.57	4.10	4.10	12	0	0.97	0.96
	14.46	13.88	13.91	4	0	0.81	0.81
1.00	4.57	4.08	4.08	12	0	0.97	0.97
	14.46	12.83	12.88	13	0	0.91	0.91
1.40	4.57	3.96	3.96	15	0	0.97	0.97
	14.46	12.45	12.50	16	0	0.93	0.92
2.20	4.57	3.74	3.74	22	0	0.98	0.98
	14.46	11.74	11.79	23	0	0.94	0.94
3.50	4.57	3.63	3.62	26	0	0.93	0.92
	14.46	8.91	8.97	62	1	0.98	0.97

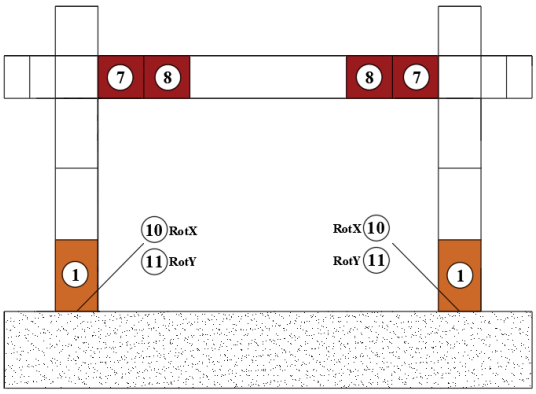

Design Variables

#1 Column(s) bottom ends

#7-8 Beam ends

Drifts [%]	Stiffness reduction factors with respect to the reference state (p%)	
	#1	#7-8
Reference	0	0
0.50	50	13
1.00	52	49
1.40	58	55
2.20	67	65
3.50	71	89

*Rotational spring stiffnesses #10 and #11 were not selected as design variables.

Contour plots of the objective function with respect to the changes in the design variables are presented in Figure 5.4 to examine the solution space of the optimization problem for different damage states (i.e., similarly to Figure 5.2). Here again, the global minimum lies within a wide interval (especially at low damage states); therefore, there exists no prominent solution for the optimization problem (i.e., it is difficult to find the global minimum point). As the damage level increases, the solution

becomes closer to a prominent one. This verifies that the chosen design parameters are convenient to represent the damage patterns observed at higher drift ratios.

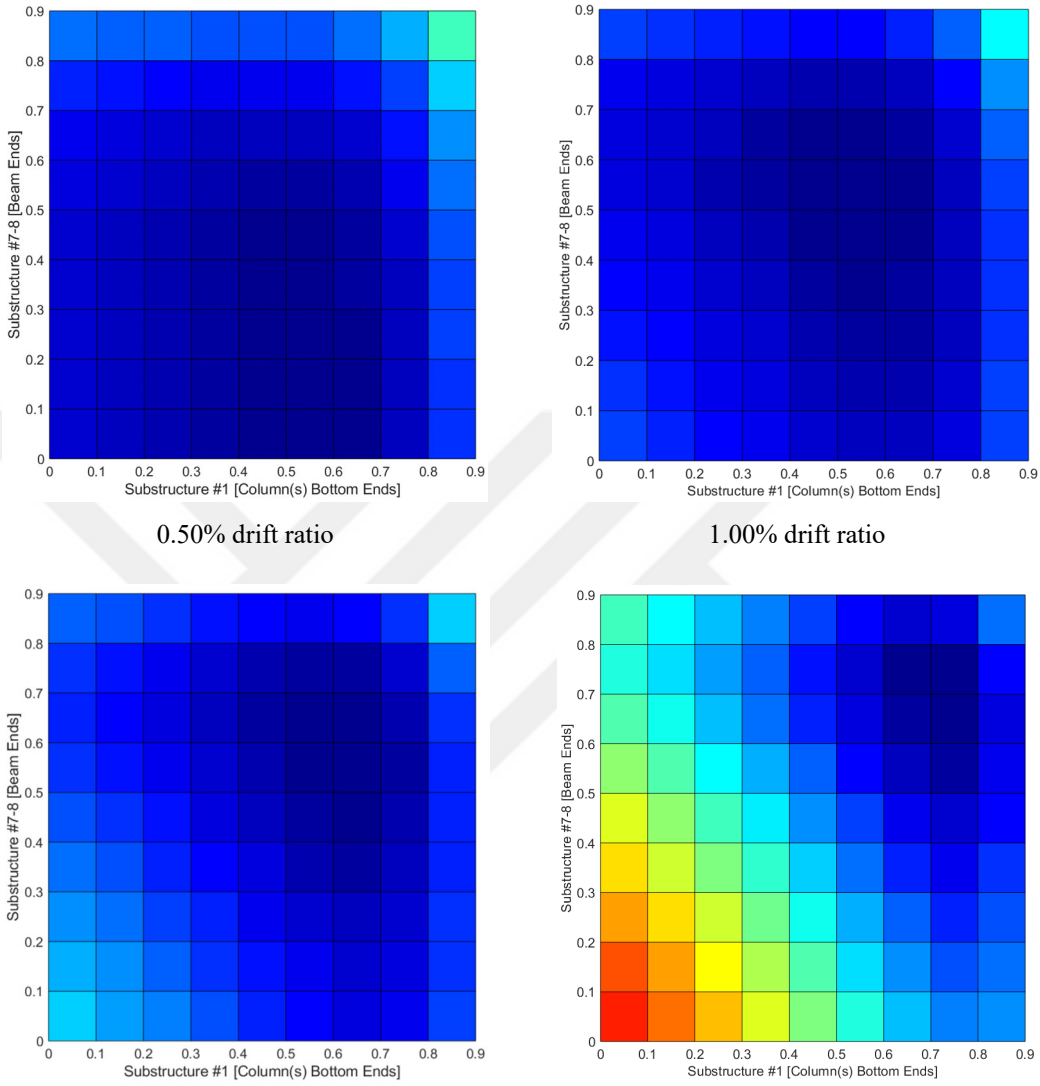

Figure 5.4 The contour plots of the objective function for increasing damage states (F2 – frame with locked infills)

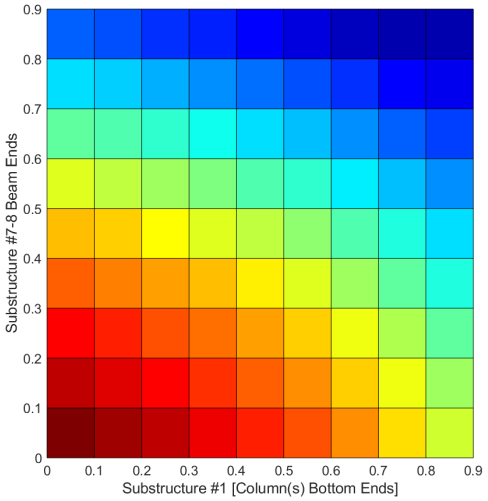

3.50% drift ratio

Figure 5.4 continues

The damage identification results presented above were also supported by visual damage inspections made during quasi-static tests. In Figure 5.5 (a), the damage state of the frame at 3.50% drift ratio (i.e., the drift ratio where the design variables are more representative) is shown. Here, extensive and deep cracks were observed on the beam and the column(s) bottom ends, which are presented in Figures 5.5 (b) and (c), respectively. At this drift ratio, deep cracks and spalling of concrete were observed on the column(s) bottom ends, and more than 4 mm crack width was measured on the beam ends. In this damage level, the vibration frequencies of the frame were reduced by 21% and 38% for the first and the second modes with respect to the undamaged state, respectively. The damage observations during the tests are in good agreement with the damage identification results. Especially, structural damage is mainly concentrated on the beam ends and on the column(s) bottom ends, whereas there exists only minor damage on the other parts of the frame (i.e., column(s) top ends, column(s) mid-zones, and beam mid-zone). It should be emphasized that the frame seems analogous to the bare frame in the sense of occurred damages. Note that the pictures presented in Figures 5.5 (b) and (c) are chosen to indicate the most damaged sides of the beam and column(s).

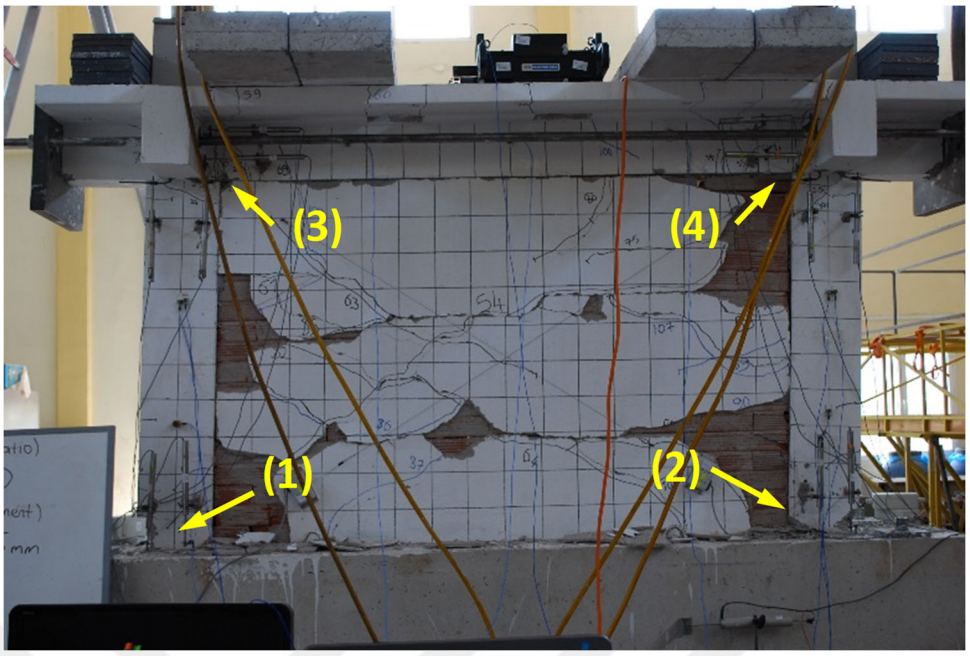

(a)

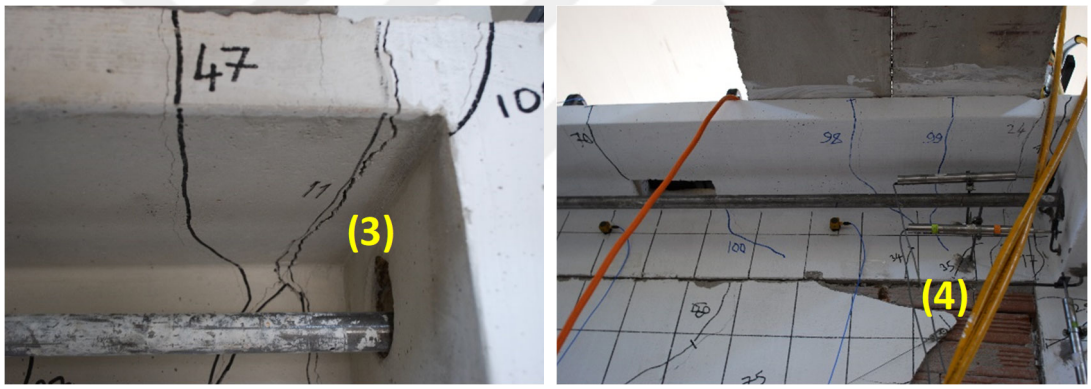

(b)

(c)

Figure 5.5 (a) General view of the frame, observed damages on the (b) beam ends (the picture on the left indicates the backside of the frame) and the (c) column(s) bottom ends at 3.50% drift ratio (Personal archive, 2016)

5.3.2 Damage Identification of the Frame with Standard Infills (F3)

This section presents the damage identification work of the frame with standard infills (F3). In this case, the infill wall acts like a rigid panel (i.e., high-level panel action due to using mortar on the bed and head-joints) and resists the motion of the surrounding frame system during the cyclic tests. Therefore, damage is likely to occur also on the column(s) mid-zones and top ends that are exposed to the resistance force of the infill wall. This approach can also be verified by the equivalent truss mechanism for a typical infilled frame where the infill wall is represented by a compressive diagonal strut element (Figure 5.6 (a)). Due to this mechanism, shear and compressive stresses occur on the loading corner along the contact length of the surrounding frame and the diagonal strut, as demonstrated in Figure 5.6 (b).

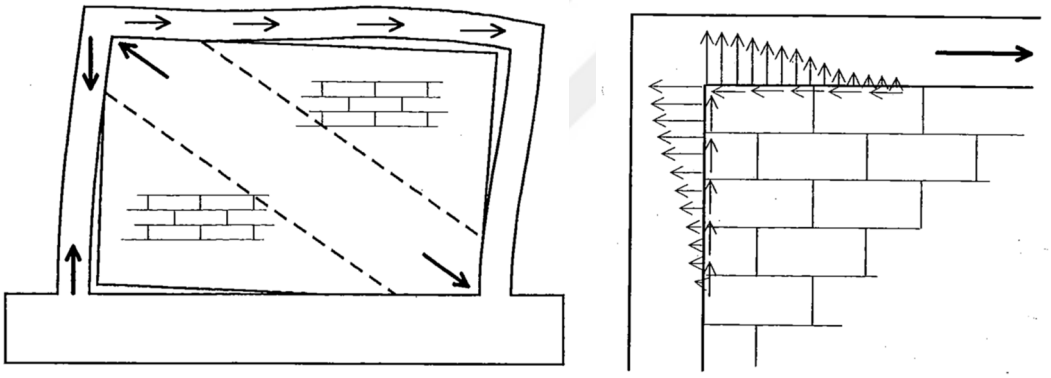

(a) (b)

Figure 5.6 (a) Equivalent truss mechanism for a typical infilled frame, and (b) the occurred compressive and shear stresses on the loading corner (Crisafulli, 1997)

By also considering the equivalent truss mechanism, the internal force diagrams (i.e., bending moment, shear force, and axial force) for the members of a typical infilled frame exposed to lateral loading along the beam are obtained as in Figure 5.7. It should be stated that the bending moments in the surrounding frame members are significantly smaller than they are in the bare frame for the same load level. This is due to the lateral force is mainly transmitted to the foundation by the truss mechanism. For example, the maximum bending moment at the bottom end of the right column in Figure 5.7 (a) is approximately six times smaller than that of the bare frame (Crisafulli, 1997).

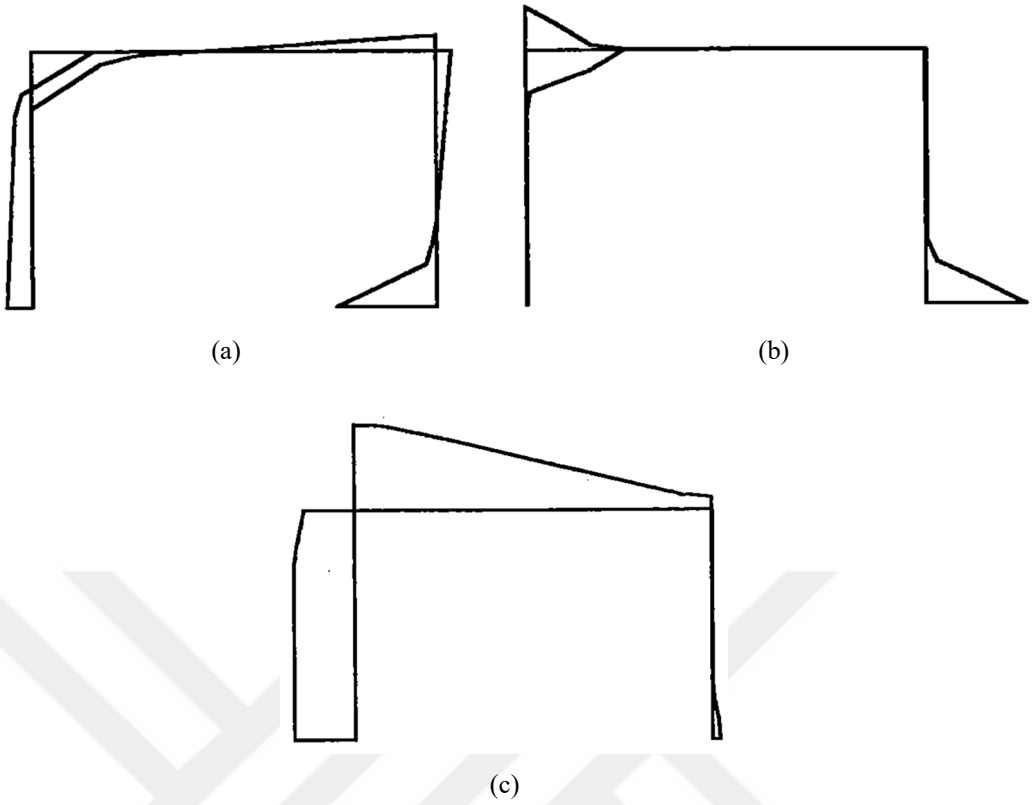

Figure 5.7 (a) Bending moment, (b) shear force, and (c) axial force diagrams for a typical infilled frame exposed to lateral loading along the beam (Crisafulli, 1997)

Based on the statements above and the approach that was used for the other frames (i.e., symmetry conditions, detectability indices, and internal moment levels occurred in the frame elements), column(s) bottom ends (#1), column(s) mid-zones (#2), column(s) top ends (#3), beam ends (#7-8), rotational springs about x-axis (#10), and rotational springs about y-axis (#11) were selected as design variables (i.e., 6 design variables were used, refer to Figure 5.1 (b)).

The initial spring stiffnesses were determined as 2824 kNm/rad (RotX) and 6052 kNm/rad (RotY) by manual updating procedure (i.e., trial-and-error method) for the purpose of bringing the numerical modal analysis results close to the experimentally identified ones; however, the ultimate spring stiffnesses were determined by automated model updating approach in Section 5.3.2.1. The weighting factors for the in-plane mode shapes at 0.00% (i.e., undamaged state), 0.50%, 1.00%, 1.40%, 2.20%, and 3.50% drift ratios were set to 0.2, 0.2, 0.5, 0.7, 1.0, and 1.0, respectively. This was done due to the same reason discussed in Section 5.3.1. Weighting factors for the other

responses (i.e., in-plane and out-of-plane vibration frequencies, and out-of-plane mode shapes) were selected the same as the ones used for the other frames.

5.3.2.1 Updating for the Reference Model (Undamaged State)

The initial FE model was updated to obtain the reference model by using the modal data of the undamaged state. As stated before, the substructures column(s) bottom ends (#1), column(s) mid-zones (#2), column(s) top ends (#3), beam ends (#7-8), rotational springs about x-axis (#10), and rotational springs about y-axis (#11) were selected as design variables, thus n=6. Note that the model updating work was performed under the same conditions that were detailed for the other frames. The only difference is the number of design variables (n=6), and therefore the dimensions of the Jacobian matrix (36x6). Since n<m, an overdetermined problem occurs. Results are given in Table 5.5.

As can be seen, only the rotational springs were updated by the algorithm because of their relatively higher detectabilities (i.e., other design variables were not updated although they were involved in the updating procedure). Accordingly, the appropriate reference model was obtained when the spring stiffnesses about x- and y-axes became 2528 kNm/rad and 5366 kNm/rad, respectively (i.e., softer than those of the other frames). It is clear from Table 5.5 that the vibration frequencies of the reference FE model (updated model, 3rd column) and the experimentally identified ones (2nd column) match very well. In addition, the MAC values calculated before (i.e., between the mode shapes of the initial FE model and the experimentally identified ones, 6th column) and after (between the mode shapes of the reference FE model and the experimentally identified ones, 7th column) are almost same. This is mainly due to their relatively lower weighting factors, which drives the updating algorithm to emphasize more on matching the frequency responses, and/or their low sensitivities to the selected design variables (i.e., almost insensitive).

Table 5.5 Model updating results of the initial FE model to obtain the reference model using modal data of the undamaged state (F3 – frame with standard infills)

(1) Initial FE Model Freq.	(2) Undamaged Frame Freq.	(3) Updated FE Model Freq.	(4) Freq. Differences Before Updating (1 - 2)	(5) Freq. Differences After Updating (3 - 2)	(6) MAC Before Updating (1 - 2)	(7) MAC After Updating (3 - 2)
[Hz]	[Hz]	[Hz]	[%]	[%]	[-]	[-]
4.57	4.41	4.41	4	0	0.97	0.97
14.46	14.22	14.18	2	0	0.77	0.77

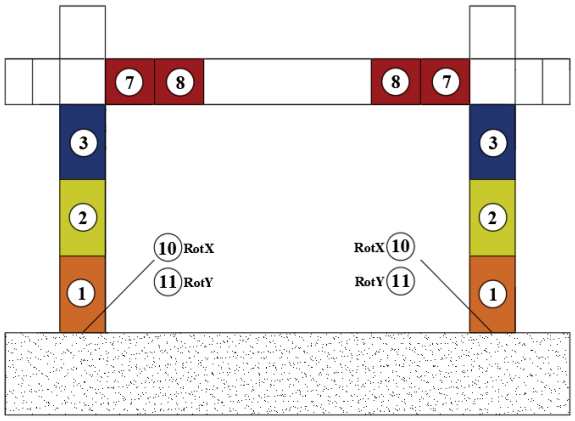

Design Variables

#1 Column(s) bottom ends
#2 Column(s) mid zones
#3 Column(s) top ends
#7-8 Beam ends
#10 Rotational springs about x-axis (RotX)
#11 Rotational springs about y-axis (RotY)

	Initial	Ref. Model (Updated)
#10 RotX (kNm/rad):	2824	2528
#11 RotY (kNm/rad):	6052	5366

*Substructures #1, #2, #3, and #7-8 were also selected as design variables but not updated by the algorithm.

5.3.2.2 Damage Identification at Increasing Damage States

Damage identification of the frame at increasing damage states was performed by updating the reference model obtained in the previous section. Four design variables were included in the updating process, namely the one at the column(s) bottom ends, the one at the column(s) mid-zones, the one at the column(s) top end, and the one at the beam ends (i.e., the substructures #1, #2, #3, and #7-8 in Figure 5.1 (b)), thus n=4 (i.e., here again, the spring stiffnesses were excluded from the updating process due to the same reason discussed before). Note that the model updating work was performed under the same conditions that were detailed for the other frames. The only difference is the number of design variables (n=4), and therefore the dimensions of the Jacobian matrix (36x4). Since n<m, an overdetermined problem occurs. The updating results

with the dimensionless stiffness reduction factors (in terms of p in percent) at different damage states with respect to the reference (undamaged) state are given in Table 5.6.

Table 5.6 Model updating results of the reference model for increasing damage states using the modal data of the increasing damage states (F3 – frame with standard infills)

Drifts [%]	(1) Reference FE Model Freq.	(2) Damaged Frame Freq.	(3) Updated FE Model Freq.	(4) Freq. Diff. Before Updating (1 - 2)	(5) Freq. Diff. After Updating (3 - 2)	(6) MAC Before Updating (1 - 2)	(7) MAC After Updating (3 - 2)
	[Hz]	[Hz]	[Hz]	[%]	[%]	[-]	[-]
0.50	4.41	4.06	4.06	9	0	0.97	0.97
	14.18	13.74	13.69	3	0	0.80	0.80
1.00	4.41	3.82	3.83	16	0	0.98	0.98
	14.18	12.45	12.45	14	0	0.90	0.90
1.40	4.41	3.77	3.77	17	0	0.99	0.98
	14.18	11.69	11.74	21	0	0.94	0.93
2.20	4.41	3.40	3.41	30	0	0.98	0.98
	14.18	10.86	10.83	31	0	0.95	0.95
3.50	4.41	3.05	3.06	45	0	0.99	0.98
	14.18	9.93	9.90	43	0	0.97	0.97

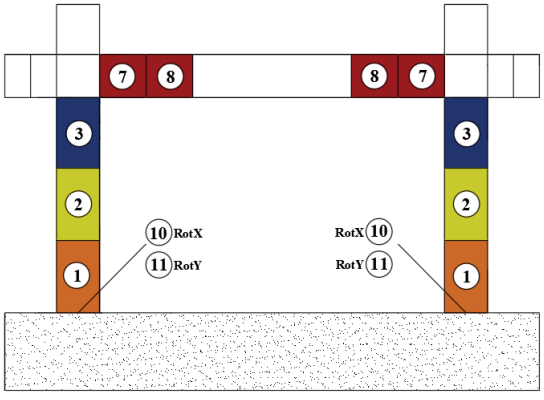

Design Variables

#1 Column(s) bottom ends
#2 Column(s) mid zones
#3 Column(s) top ends
#7-8 Beam ends

Drifts [%]	Stiffness reduction factors with respect to the reference state (p%)			
	#1	#2	#3	#7-8
Reference	0	0	0	0
0.50	44	3	5	8
1.00	57	20	25	35
1.40	59	23	40	45
2.20	73	30	54	50
3.50	82	35	62	60

*Rotational spring stiffnesses #10 and #11 were not selected as design variables.

It is clear from Table 5.6 that the experimentally identified vibration frequencies (2nd column) and the ones of the updated FE model (3rd column) match almost

perfectly. Especially for the 3.50% drift ratio, significant reduction from 45% to 0% observed in the frequency differences calculated before and after updating (4^{th} and 5^{th} columns) reveals the effectiveness of the method. On the other hand, the MAC values calculated before and after updating (6^{th} and 7^{th} columns) are almost same due to their weightings and/or low sensitivities to the selected design variables (i.e., almost insensitive). The dimensionless stiffness reduction factors in Table 5.6 indicate that the severity of the structural damage increases as increasing drift level. This is because of the accumulation of damage on structural elements. Since four design variables were used for the frame updating, the solution space of the optimization problem for different damage states cannot be visualized by contour plots as in the case of other frames (see Figures 5.2 and 5.4).

The damage identification results presented above were also supported by visual damage inspections made during the quasi-static tests. In Figure 5.8 (a), the damage state of the frame at 3.50% drift ratio is shown. Here, extensive and deep cracks were observed on the beam ends (Figure 5.8 (b)) and the column(s) bottom ends (Figure 5.8 (c)). At this drift ratio, deep cracks and spalling of concrete were observed on the column(s) bottom ends, and more than 5 mm crack width was measured on the beam ends. In addition, several cracks occurred on the column(s) top ends and mid-zones (Figures 5.8 (a) and (b)) because of the panel action of the infill wall. In this damage level, the vibration frequencies of the frame were reduced by 31% and 30% for the first and the second modes with respect to the undamaged state, respectively. The damage observations during the tests are in good agreement with the damage identification results. Especially for this frame, structural damage is concentrated on the column(s) bottom ends, mid-zones, top ends (i.e., throughout the column members), and beam ends (i.e., the damage formation is significantly different from the other frames). Note that the pictures presented in Figures 5.8 (b) and (c) are chosen to indicate the most damaged sides of the structural elements.

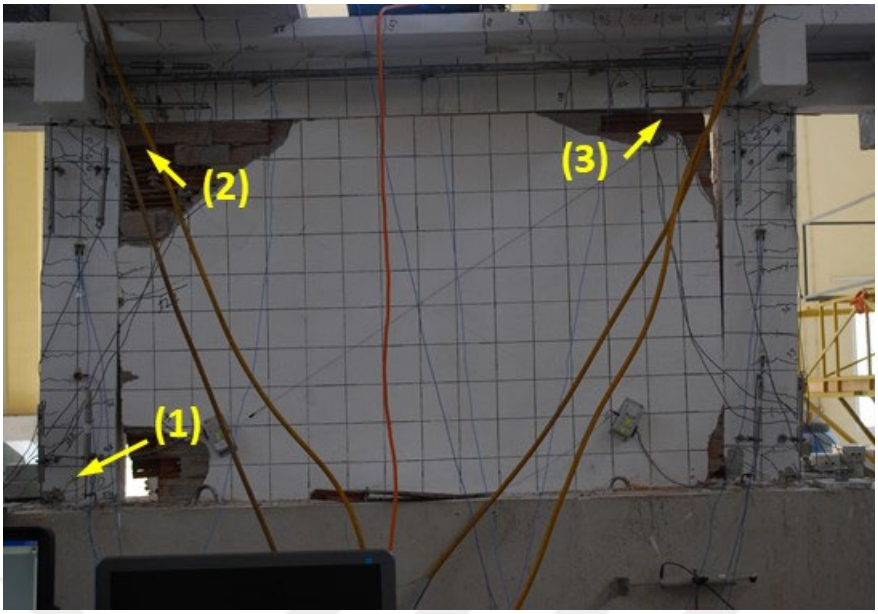

(a)

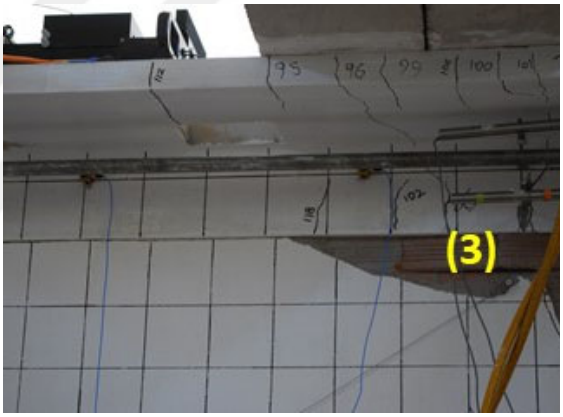

(b)

(c)

Figure 5.8 (a) General view of the frame, observed damages on the (b) column(s) top ends and beam ends, and the (c) column(s) bottom ends at 3.50% drift ratio (Personal archive, 2016)

CHAPTER SIX

MODEL CALIBRATION WORK PERFORMED ON THE UNREINFORCED MASONRY COURTYARD WALLS OF THE HISTORICAL ISABEY MOSQUE

6.1 Introduction

Historical masonry structures such as bridges, arches, buildings, towers (e.g., minarets), monuments (e.g., mosques, churches, basilicas) are shown as the symbols of cultural heritage and have great cultural and spiritual values for societies. They also significantly contribute to the economic development of countries by being tourist attractions. Therefore, it is important to ensure the structural safety of these unique cultural heritage pieces and hand them down to future generations.

Natural disasters (e.g., earthquakes, hurricanes, etc.), degeneration of materials in time, and dilapidation are the main reasons that threaten the safety of historical structures. Therefore, safety assessment and retrofitting/restoration are required to preserve them. Nowadays, especially for developed countries, interest in preservation and restoration of historical masonry structures, which requires also rigorous structural assessments, has increased. As the need for structural assessment increases, understanding the structural behavior of these structures has become an important field in engineering applications. One needs to obtain sufficiently accurate knowledge of the current state of the structural system to avoid erroneous interventions, and therefore confine the interventions within a minimal state in order to preserve the structure's historical value. The structural condition can be assessed by investigating structural integrity, geometry, boundary conditions, and material properties.

Finite element (FE) analysis is a popular tool for numerically modeling historical masonry structures, however, developing a reliable FE model is a difficult task. Challenges arise due to non-homogeneity of the masonry material, complicated cross-sectional properties (e.g., multi-leaf walls), uncertainty in boundaries, and mechanical/chemical characteristics of mortar layers. It is possible for an analyst to make some assumptions and simplifications in modeling and/or material

characteristics to overcome these aforementioned complexities. Generally, this modeling approach leads to erroneous FE models which do not accurately represent the real system. In this context, model calibration (a.k.a. model updating) has become a popular tool to correct these errors and to obtain a more reliable FE model which is more representative of the real structure (Friswell & Mottershead, 1995). Here, the calibration term refers to tuning the uncertain parameters of the numerical model such as Young's modulus, mass density, and boundary conditions by taking into account the in-situ measurements.

This chapter of the thesis presents the operational modal analysis (OMA) results and the sensitivity-based finite element model updating (FEMU) work performed on the unreinforced masonry courtyard walls of the historical Isabey Mosque. Two sets of ambient vibration tests were conducted using 12 uni-axial accelerometers which were deployed to register responses along the out-of-plane directions of the two perpendicularly positioned courtyard walls. The measured dynamic response data were then processed using a well-known output-only method called Enhanced Frequency Domain Decomposition (EFDD) embedded in ARTeMIS software (ARTeMIS, 2016). The initial numerical macro model of the system was developed in ABAQUS (ABAQUS, 2017) FE modeling environment by using the material properties obtained from the in-situ flat-jack tests and the relevant literature. Boundary conditions were defined by using individual translational springs in three directions. The initial stiffnesses of these springs were determined by performing manual updating work on the model so that the modal parameters of the initial numerical model capture the identified experimental results. In order to obtain a more reliable FE model which is more representative of the modal parameters estimated by the in-situ test, the initial FE model (i.e., initial numerical model) was updated using the sensitivity-based FEMU method in FEMtools software (FEMtools, 2017a). In this context, the model parameters, namely mass density, Young's modulus, and boundary conditions (i.e., translational springs) of the initial numerical model were calibrated in the sense of global parameter updating.

6.2 Description of the Historical Isabey Mosque

The historical Isabey Mosque was constructed by Aydinoglu Isa Bey as the work of architect Samlı Ali in 1375 in Selcuk, Izmir. It is evaluated as one of the oldest and most magnificent masterpieces of the Anatolian Principalities period. During its construction, stone and column members from the ruins of the nearby older civilizations (e.g., Ephesus and the Temple of Artemis) were also used. The mosque structure is composed of 4 walls forming the main building and 3 walls surrounding the courtyard (Figures 6.1 (a) and (b)). The courtyard walls have 1.80 m average thickness and 11.6 m free height. There is a ~3 m height difference between the ground levels of the interior and the exterior sides (i.e., the interior side is at a higher level). The courtyard walls are unreinforced. Herein, the upper half portion is made in three-layer stone masonry style where the middle layer is composed of rubble stones to fill the cavity between the outer layers, whereas the lower half portion is made in two-layer stone masonry style. The structural behaviors and damage types observed after past earthquakes revealed that the damage mechanism of historical masonry structures is predominantly along their out-of-plane directions (Augenti & Parisi, 2010; Dizhur et al., 2011; Dizhur & Ingham, 2015; Ismail et al., 2011). That's why the main motivation of this study is to research the out-of-plane behaviors of the West and North courtyard walls which are perpendicular to each other (Figures 6.1 (c) and (d)). These walls are particularly vulnerable to out-of-plane seismic loads due to lack of a slab forming a diaphragm to enable the walls to resist these loads altogether.

(a) (b)

Figure 6.1 (a) A general view of the historical Isabey Mosque, (b) main structure, (c) West, and (d) North courtyard walls (Personal archive, 2017)

(c)

(d)

Figure 6.1 continues

6.3 Field Measurements and Operational Modal Analysis Results

Dynamic characteristics of the courtyard walls were estimated by using ambient vibration (AV) response data. These tests were conducted in-situ using 16-channel Digitex portable data acquisition system with 16-bit sensitivity and 12 force-balanced uni-axial accelerometers with ±3g full range, noise floor bandwidth of 0.05-1500 Hz, and dynamic range greater than 110 dB. The AV tests were performed in two different sensor setups (i.e., Set-1 and Set-2) in order to measure the dynamic behavior of the wall system with a higher spatial resolution (i.e., response data acquired from more location). In Set-1, all of the accelerometers were placed on to the inner surface (facing courtyard) of the West wall along the out-of-plane direction (Figure 6.2 (a)). In Set-2, six of the accelerometers were kept as reference (R) sensors and the remaining six were relocated to the inner surface of the North wall in order to capture the out-of-plane responses of both walls simultaneously (Figures 6.2 (a) and (b)). Positions of the accelerometers, the number of accelerometers used in the test setups, and the selection of the reference accelerometers were determined by investigating the mode shapes of a preliminary numerical model (i.e., a coarse model having fixed support conditions and approximate material characteristics) in order to capture a sufficient number of out-of-plane modes of the wall system. For both of the test setups, approximately 14 minutes long AV response data were collected with a sampling rate of 250 Hz. The data acquisition system and one of the accelerometers deployed on the walls are presented in Figure 6.3.

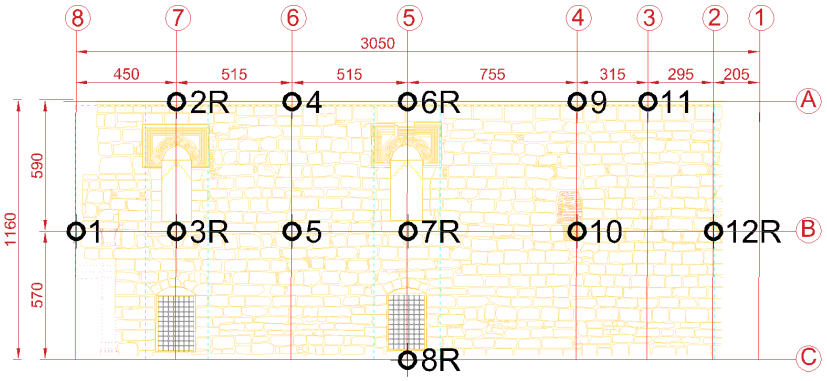

(a)

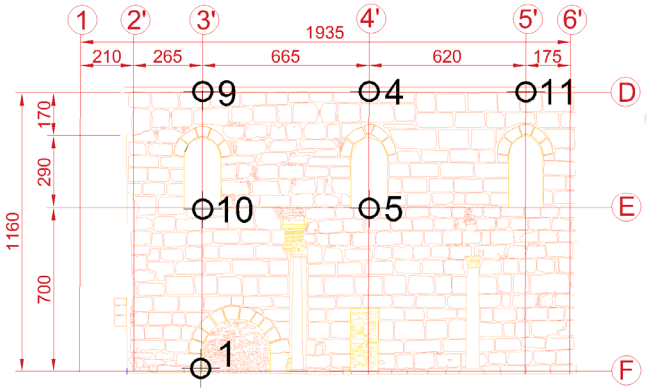

(b)

Figure 6.2 Accelerometer layouts of the inner surfaces (facing courtyard) of (a) West and (b) North courtyard walls (dimensions are in cm)

(a) (b)

Figure 6.3 (a) The data acquisition system and (b) one of the accelerometers deployed on the walls (Personal archive, 2017)

Pre-processing of the dynamic response data was performed in MATLAB. Operational modal analysis (OMA) was conducted in ARTeMIS software using the

EFDD method. The results are shown in Figure 6.4. It should be stated that only three out-of-plane modes were clearly identified from the collected experimental data. The vibration frequencies of these modes (i.e., 1st, 2nd, and 3rd experimentally identified out-of-plane modes) are estimated as 3.906 Hz, 8.960 Hz, and 21.265 Hz, respectively.

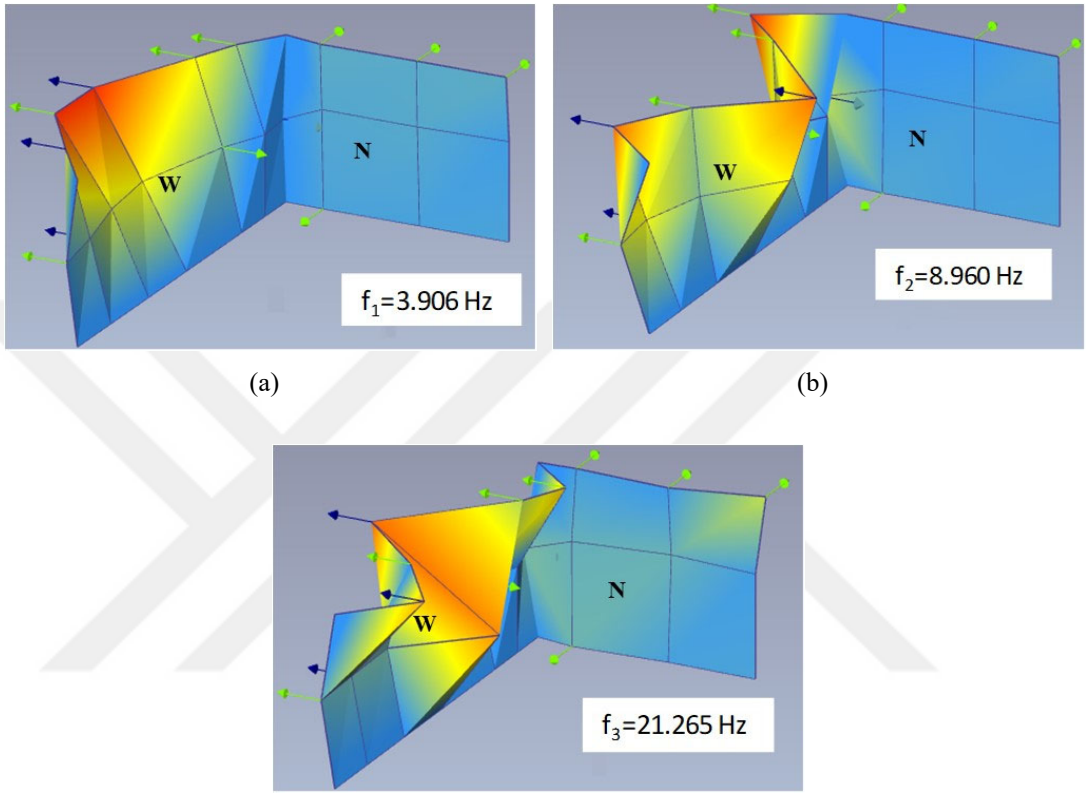

Figure 6.4 (a) 1st, (b) 2nd, and (c) 3rd experimentally identified out-of-plane modes of the courtyard wall system (W: West, N: North)

6.4 Initial FE Model of the Courtyard Walls

Mechanical characteristics of masonry structures may differ in different loading directions due to the variations in material properties and/or construction detailing. Therefore, making realistic assumptions in numerical modeling is essential to capture the actual structural system behavior. Mainly, three approaches are used in modeling masonry structures, namely micro modeling, simplified micro (meso) modeling, and macro modeling (Lourenço, 1996). Micro modeling is the detailed one in which masonry units and mortars (both bed and head-joints) are modeled separately (Figure 6.5 (a)). In meso modeling, masonry units are modeled together with their interface

relations and therefore there is no need to define mortars (Figure 6.5 (b)). In macro modeling, which is the coarsest and simplest one, a composite structural finite element (i.e., macro element) consisting of both the masonry unit and mortar layers is used (Figure 6.5 (c)).

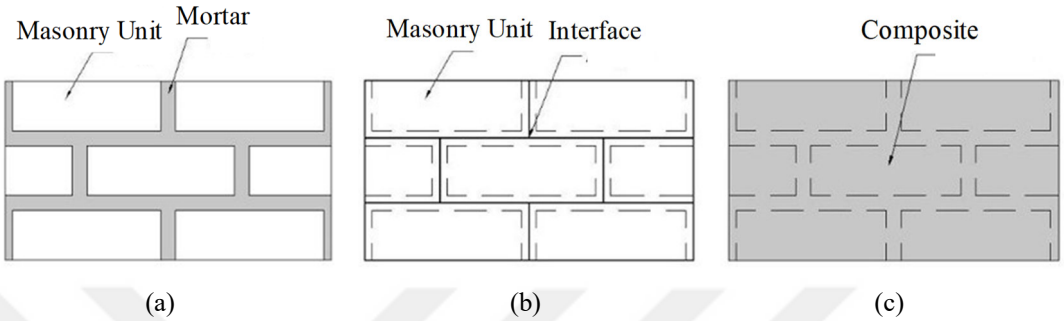

Figure 6.5 (a) Micro, (b) meso, and (c) macro modeling approaches for masonry structures (Lourenço, 1996)

In this research work, the macro modeling approach was used with a homogeneous material having equivalent mechanical properties representing both the masonry unit and the mortar to model the courtyard walls. This may seem to be too simplistic, but it is known that selecting a simple numerical model that represents the salient dynamic characteristics of the structure is very effective in dealing with convergence problems in model updating studies (Teughels, 2003; Teughels & De Roeck, 2004).

Due to the absence of shell and solid elements in FEDEASLab environment, the initial FE model (i.e., an extensive and realistic model than the preliminary model) of the West and North courtyard walls was developed in ABAQUS using 3-dimensional, 10-node quadratic tetrahedron (C3D10) continuous solid elements. Determining the optimum mesh size of a FE model is an important issue. Large meshes may lead to inaccurate and non-representative models, whereas small meshes may lead to unnecessarily complex and computationally expensive models. The optimum mesh size (therefore the optimum FE number) of the initial FE model was determined from convergence analysis which includes repeated frequency analyses for different mesh sizes. Note that the convergence analysis using the preliminary numerical model was performed before the field measurements discussed in Section 6.3. The relationship between the FE number and the 1st mode frequency is given in Figure 6.6 by a

convergence plot. Here, the optimum FE number is determined as 9405 from the first point where the frequency value remains almost constant. As a result, the initial FE model (i.e., initial numerical model) was created by 16356 nodes and 9405 elements.

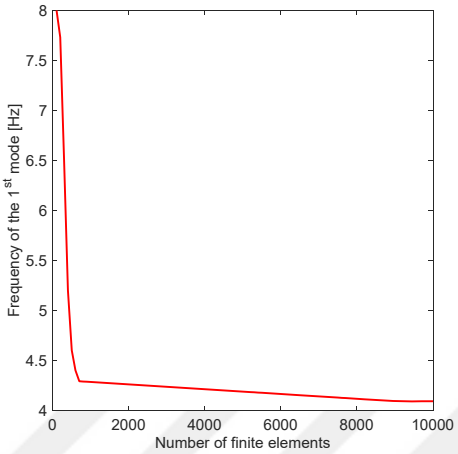

Figure 6.6 Convergence plot of the 1st mode of the preliminary numerical model

Mechanical characteristics of the wall system were determined by flat-jack tests (Figure 6.7) in accordance with ASTM C1197-04 (2004) and RILEM MDT.D.4 (2004), literature (Ceravolo et al., 2016; Mouyiannou et al., 2014; Ramos et al., 2005), and the findings of the similar structures that were previously investigated by the Turkish Republic Directorate General of Foundations. Based on these evaluations; mass density (ρ), Young's modulus (E), and Poisson's ratio (υ) of each macro element of the initial FE model were set to be 2400 kg/m^3, 4535 MPa, and 0.25, respectively.

(a) (b)

Figure 6.7 Flat-jack tests from (a) West and (b) North courtyard walls (Personal archive, 2018)

Boundary conditions (support conditions) were modeled by using translational springs in global X, Y, and Z directions with corresponding spring stiffnesses K_X, K_Y, and K_Z, respectively. The number of spring elements is 2649 in total (i.e., 883 spring elements for each X, Y, and Z direction). Note that the springs were divided into four distinct groups (regions) by their locations and designated as spring groups SGs. This way their different characteristics based on their locations could be considered in model updating (Figure 6.8). SG-1 was used for the zone where the North wall is interrupted by a doorway (Figure 6.8 (a), the doorway is not shown in the figure). SG-2 was used for the triangular interface between the North wall and the exterior stairs (Figure 6.8 (b)). SG-3 was used for the bases of both walls (soil-wall interface, Figure 6.8 (c)). Finally, SG-4 was used for the interface between the West wall and the minaret (Figure 6.8 (d)). No rotational springs were used in the modeling due to the definition of the solid elements (i.e., no rotational degree of freedom is available for solid elements due to their higher torsional and bending rigidities). In real-life cases, determining the actual stiffnesses of the springs representing the boundary conditions is practically impossible. Therefore, making educated guesses for assigning initial stiffness values for these springs under some assumptions is inevitable. Note that the final stiffness values will be obtained by updating these initial values. In this context, the initial spring stiffnesses were determined by a trial-and-error method (manual updating method without any optimization algorithm) so as to obtain an initial model with dynamic characteristics that are closely approximating the modal parameters obtained experimentally. Because of being the most uncertain model parameters (i.e., no prior knowledge exists), at this initial stage, only the spring values were manually updated, and the other parameters were set to be constant. This preliminary manual updating is very effective in overcoming potential convergence problems that may occur in the next stage of the model updating process using an optimization-based procedure.

Since the out-of-plane behavior of the wall system is the main motivation of this study, only the out-of-plane modes of the initial FE model were considered. No changes were observed in the modal properties when K_Y spring stiffnesses of SG-1, SG-2, and SG-3 were updated, which shows that the considered modes are insensitive to the aforementioned spring stiffnesses. Therefore, these springs were removed from

the model to increase the convergence performance of the updating problem. Also, note that only the out-of-plane modes (i.e., the modes that are the main motivation of the study) were extracted from the experimental data. Therefore, the model was set to be vertically fixed by assigning high values for K_Y spring stiffnesses of SG-4. This was done to prevent vertical modes to occur (not captured experimentally) and to reduce difficulties in pairing between the experimental and the numerical modes. Eventually, K_X and K_Z spring stiffnesses were manually calibrated to 18000 kN/m and 9000 kN/m for SG-1, 18000 kN/m and 9000 kN/m for SG-2, 18000 kN/m and 18000 kN/m for SG-3, 18000 kN/m and 18000 kN/m for SG-4, respectively.

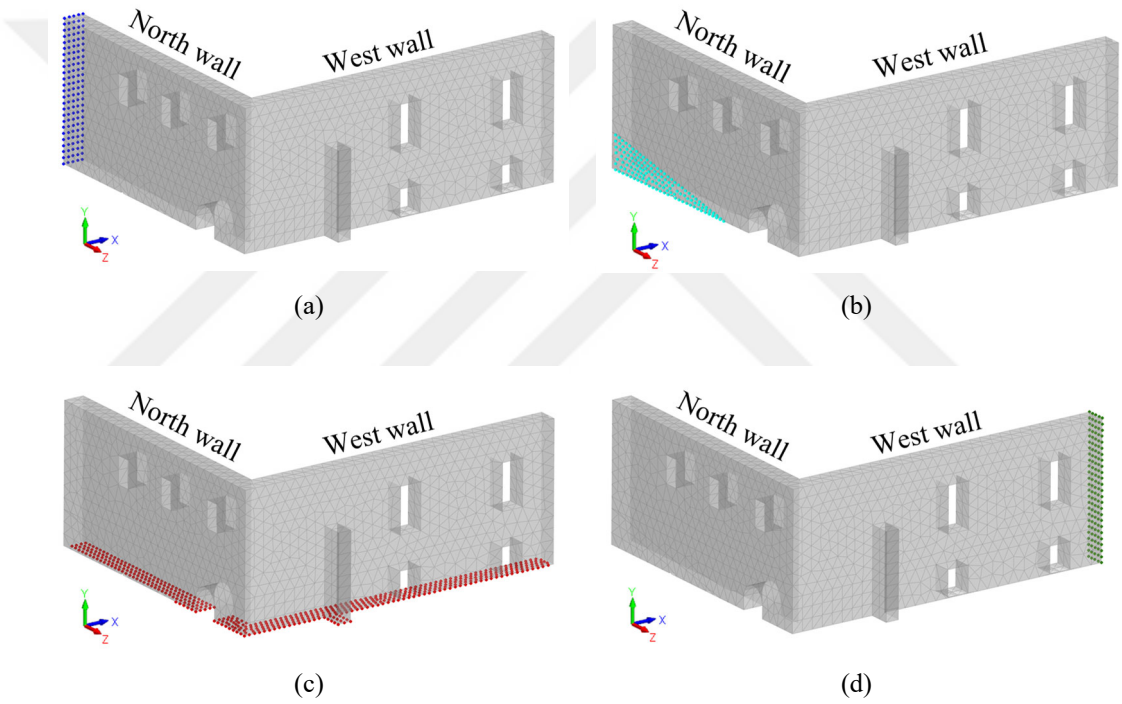

Figure 6.8 Spring groups (SGs) used for the numerical model: (a) SG-1, (b) SG-2, (c) SG-3, and (d) SG-4

Modal analysis of the initial FE model was conducted by ABAQUS standard module and the results are shown in Figure 6.9. Here, only the modes that correspond to the experimentally identified ones (see Figure 6.4) are presented (i.e., 1st, 5th, and 14th modes of the initial FE model). Vibration frequencies of these modes are obtained as 3.765 Hz, 9.208 Hz, and 19.848 Hz, respectively. Note that all of these modes are mainly the out-of-plane modes of the West wing of the courtyard wall system. It should be stated that almost all the modes between the 1st and 14th modes exhibit the out-of-

plane behavior of the wall system; however, these modes couldn't be extracted from the experimental data due to the spatial resolution of the present accelerometer layout.

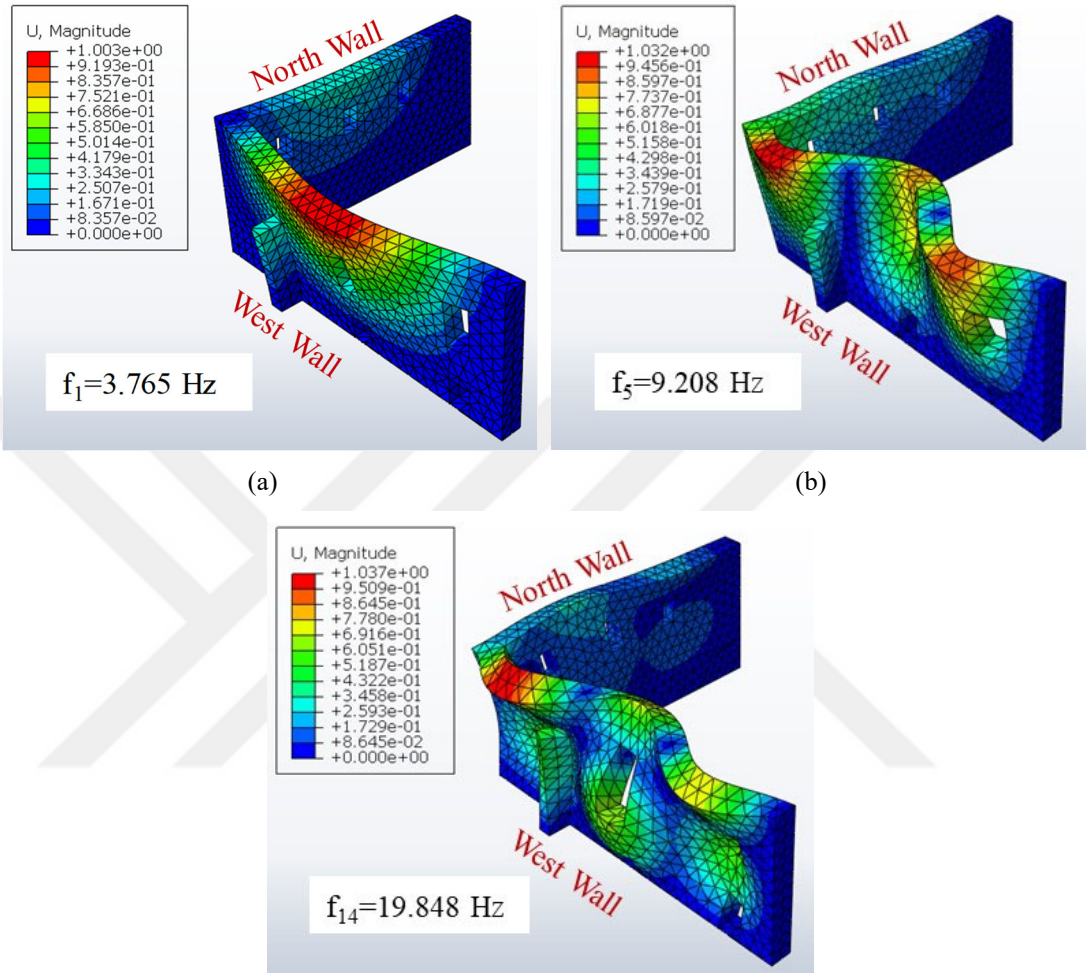

Figure 6.9 (a) 1st, (b) 5th, and (c) 14th modes of the initial numerical model

Modal analysis results identified using the initial numerical model (by the ABAQUS model) and the experimentally obtained counterparts (by the ARTeMIS model) are presented in Table 6.1 for comparison purpose. In the table, also the MAC values calculated between the experimental and numerical modes are given. Remind that a MAC value being close to unity denotes spatial similarity between the compared mode shapes (Allemang, 2003). It can be said that the numerically and experimentally obtained mode shapes are spatially similar to each other due to the fact that the smallest MAC value is at 78%. Nevertheless, large differences are seen for the frequency estimations (e.g., ~7% difference is calculated for the 3rd mode). Therefore, it can be

said that the initial numerical model needs updating to better represent the real structural system in terms of the estimated modal parameters. The updating will be done by calibrating some uncertain model parameters to match the numerical modal parameters with the experimental ones.

Table 6.1 Comparison of the modal parameters obtained using the initial numerical model and their experimental counterparts

Mode # [Num. vs. Exp.]	Init. Num. Model Freq. [Hz]	Experimental Freq. [Hz]	Freq. Diff. [%]	MAC [%]
1 - 1	3.765	3.906	-3.61	95.20
5 - 2	9.208	8.960	2.77	82.60
14 - 3	19.848	21.265	-6.66	78.30

6.5 Model Updating Work for the Initial FE Model

Model updating studies for the initial FE model of the courtyard walls were performed by FEMtools software using sensitivity-based finite element model updating method with Bayesian technique (FEMtools, 2017a). Here, the MATLAB based code (discussed in Chapters Four and Five) couldn't be used since the initial FE model was created in ABAQUS environment. A brief theoretical background of the updating method that is used in FEMtools is described below (FEMtools, 2017b).

The functional relationship between the responses and the model parameters can be written as follows

$$\{R_e\} = \{R_a\} + [S]\left(\{P_u\} - \{P_o\}\right) \quad \text{or} \quad \{\Delta R\} = [S]\{\Delta P\} \tag{6.1}$$

where $\{R_e\}$ is the response vector obtained from the experimental data, $\{R_a\}$ is the response vector of the numerical model for a given state $\{P_o\}$ of the model parameter values, $\{P_u\}$ is the vector of the updated model parameter values, $[S]$ is the sensitivity matrix, $\{\Delta R\}$ is the difference vector calculated between $\{R_e\}$ and $\{R_a\}$ response vectors, and $\{\Delta P\}$ is the parameter variation wanted to be identified. Note that the experimental and numerical responses must be accurately paired. Equation 6.1 can be

solved by least squares, weighted least squares, or Bayesian techniques, depending on the application of weighting factors used to weight the parameters and responses with respect to their importance, reliability (confidence), and amount of noise.

If the number of responses equals the number of updating parameters (i.e., in the case where $[S]$ is a square matrix), $\{\Delta P\}$ can be directly found by simple inversion of the sensitivity matrix as follows

$$\{\Delta P\} = [S]^{-1} \{\Delta R\} \tag{6.2}$$

Otherwise, the pseudo-inverse calculation is required where $[S]^{+}$ is the pseudo-inverse of the sensitivity matrix (Equation 6.3).

$$\{\Delta P\} = [S]^{+} \{\Delta R\} = \left([S]^{\mathrm{T}} [S] \right)^{-1} [S]^{\mathrm{T}} \{\Delta R\} \tag{6.3}$$

The least squares solution calculated from Equations 6.2 or 6.3 minimizes an objective function which can be written as follows

$$\{Obj.\,Func.\} = [S]\{\Delta P\} - \{\Delta R\} \tag{6.4}$$

For Bayesian techniques, the discrepancy between the experimental and numerical responses is defined by a weighted error as defined in Equation 6.5, where $[C_R]$ and $[C_P]$ are the diagonal weighting matrices representing the confidence in responses and model parameters, respectively. Note that if $[C_P] = 0$, (i.e., no error estimates on the model parameters are available, therefore there is no confidence in model parameters) the weighted least squares problem occurs, whereas if $[C_R] = 0$, (i.e., there is no confidence in the experimental data), then the model parameters are not updated since the experimental data are not used. In addition, if $[C_P] = 0$ and $[C_R] = \mathrm{I}$ (i.e., the responses are weighted similarly), a least squares problem occurs.

$$E = \{\Delta R\}^{\mathrm{T}} [C_R] \{\Delta R\} + \{\Delta P\}^{T} [C_P] \{\Delta P\} \tag{6.5}$$

Error given in Equation 6.5 can be minimized as follows

$$\{P_u\} = \{P_o\} + [G]\{-\Delta R\} \tag{6.6}$$

where $[G]$ is the gain matrix. In the case where there are more responses than parameters, $[G]$ is computed as Equation 6.7; otherwise, which is generally the case, Equation 6.8 is used.

$$[G] = \left([C_P] + [S]^{\mathrm{T}} [C_R][S] \right)^{-1} [S]^{\mathrm{T}} [C_R] \tag{6.7}$$

$$[G] = \left([C_P] \right)^{-1} [S]^{\mathrm{T}} \left([C_R]^{-1} + [S][C_P]^{-1} [S]^{\mathrm{T}} \right)^{-1} \tag{6.8}$$

As stated in Chapter Three, the weighting matrices, which depend on the structural characteristics, testing methods, and modeling strategies, can be determined based on a statistical approach like Gauss-Markov estimate. However, in practice, this statistical information is often not available, such that the appropriate weights are determined based on engineering judgements. Note that the absolute values of the elements within the weighting matrices are not meaningful alone, only their relative values with respect to each other are important. Sometimes, it is more useful to define statistical scatter values (Equation 6.9) instead of these matrices.

$$Scatter = \sigma / \mu \tag{6.9}$$

where σ and μ are the standard deviation and the mean of the considered model parameter or response, respectively. Note that low scatter results in low variance, high confidence, and high $[C_R]$ and $[C_P]$, whereas high scatter results in high variance, low confidence, and low $[C_R]$ and $[C_P]$. Model parameters with low scatters do not change too much during updating (i.e., parameters only change if the great majority of the responses indicate that these parameters should change), whereas the parameters

with high scatters are free to change (i.e., large parameter changes occur). Responses with low scatters lead to model parameter changes during updating (i.e., result in large parameter changes), whereas responses with high scatters only have effects if they all change the model parameters in the same way (i.e., result in small parameter changes). Since the mode shape estimations contain higher estimation uncertainty than frequency estimations due to having a limited number of sensors and estimation sensitivity to measurement noise, the strategy of assigning relatively higher scatter values to mode shape responses is suggested if they are thought to be unreliable.

Vibration frequencies and MAC values for the 1st, 5th, and 14th modes of the ABAQUS model and the 1st, 2nd, and 3rd experimental modes from ARTeMIS were selected as responses to be used for updating. Scatter values for the frequencies and MACs were selected as 1% and 30%, respectively. Note that relatively a higher scatter value was assigned to the MAC responses due to their higher estimation uncertainty. Mass density, Young's modulus, and boundary conditions (defined by translational springs) were selected as model parameters to be updated (i.e., parameters that are considered uncertain therefore require updating). The scatter values of 10%, 10%, and 25% were assigned to mass density, Young's modulus, and springs stiffnesses, respectively. Note that relatively a higher scatter value was assigned to the spring stiffnesses due to their higher uncertainty. Initial values used for these parameters are given in the previous sections. In order to obtain physically meaningful/feasible model parameter values after updating, bounds (i.e., change intervals during updating) were selected as ± 10%, ± 20%, and ± 60% for mass density, Young's modulus, and spring stiffnesses, respectively. Note that relatively a wider bound was used for spring stiffnesses due to their higher uncertainty.

Effects of mass density, Young's modulus, and spring stiffnesses on the vibration frequencies were investigated by a sensitivity analysis prior to updating the initial FE model. Based on the results of the sensitivity analysis, it is possible to investigate whether the model parameters should be updated individually for each finite element (local updating) or together for all finite elements with similar effects on modal parameters (global updating). Sensitivity plots of the vibration frequencies of the numerical model (i.e., 1st, 5th, and 14th modes) with respect to the mass density,

Young's modulus, and spring stiffnesses (i.e., K_X, K_Y, and K_Z) are shown in Figures 6.10 to 6.14, respectively. Note that the normalized sensitivities, independent on the units of the model parameters and responses, and thus can be compared for different model parameter types, are presented in the figures. From these results, it can be said that all finite elements of the model have similar effects (i.e., detectabilities), especially the Young's modulus, on the vibration frequencies (i.e., predominantly single color, red for mass density and blue for Young's modulus). There are patches of zones with different colors (i.e., sensitivities) but in order to have a well-conditioned overdetermined problem, it was decided to ignore them and perform global updating. (i.e., assigning a common model parameter for finite elements having similar detectabilities).

Similar results were observed for each SG (SG-1, SG-2, SG-3, and SG-4). Note that the insensitiveness of the modal parameters with respect to K_Y stiffnesses are also verified by the sensitivity analyses. Therefore, also for the spring stiffnesses, in order to obtain a well-conditioned optimization problem, global parameter updating was found to be appropriate. Consequently, model updating was performed by using 10 model parameters; namely one for mass density and Young's modulus of the entire model, and four for K_X and K_Z each having four separate spring groups (i.e., SG-1, SG-2, SG-3, and SG-4).

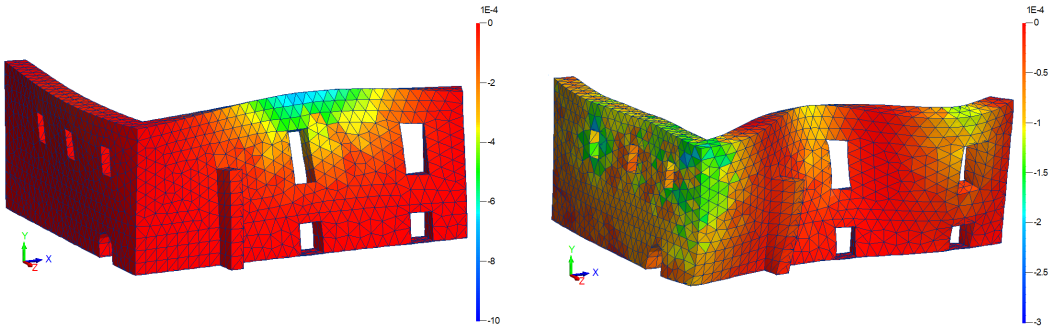

(a) (b)

Figure 6.10 Sensitivity plots of the (a) 1st, (b) 5th, and (c) 14th modes of the numerical model with respect to mass density

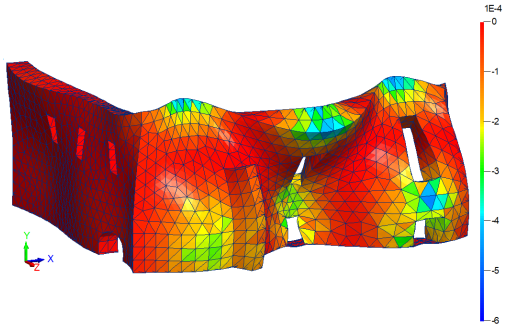

(c)

Figure 6.10 continues

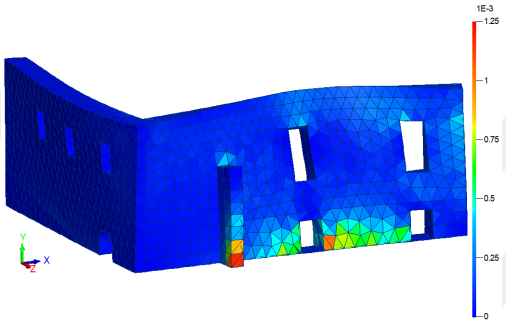

(a)

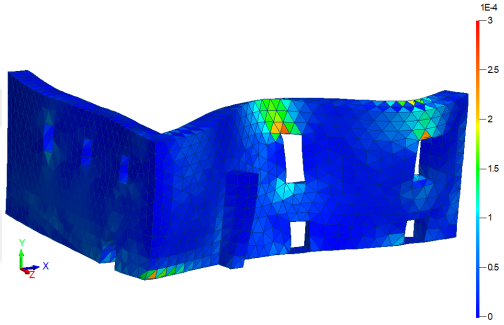

(b)

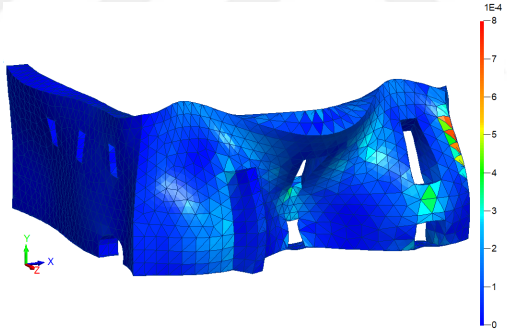

(c)

Figure 6.11 Sensitivity plots of the (a) 1st, (b) 5th, and (c) 14th modes of the numerical model with respect to Young's modulus

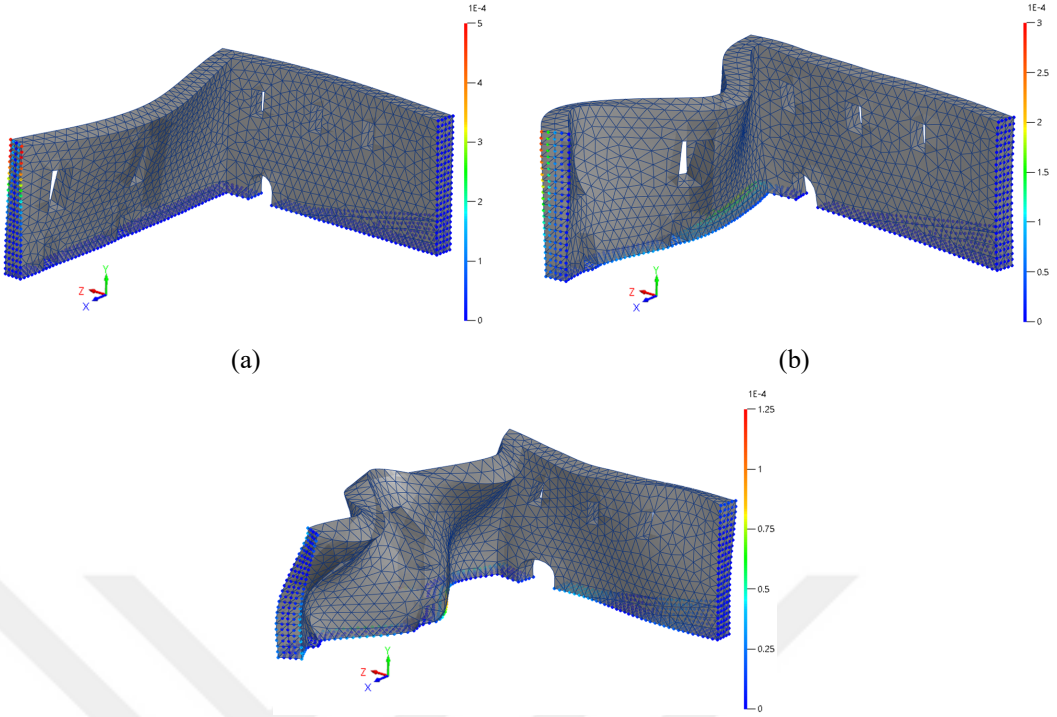

(a) (b)

(c)

Figure 6.12 Sensitivity plots of the (a) 1st, (b) 5th, and (c) 14th modes of the numerical model with respect to K_X

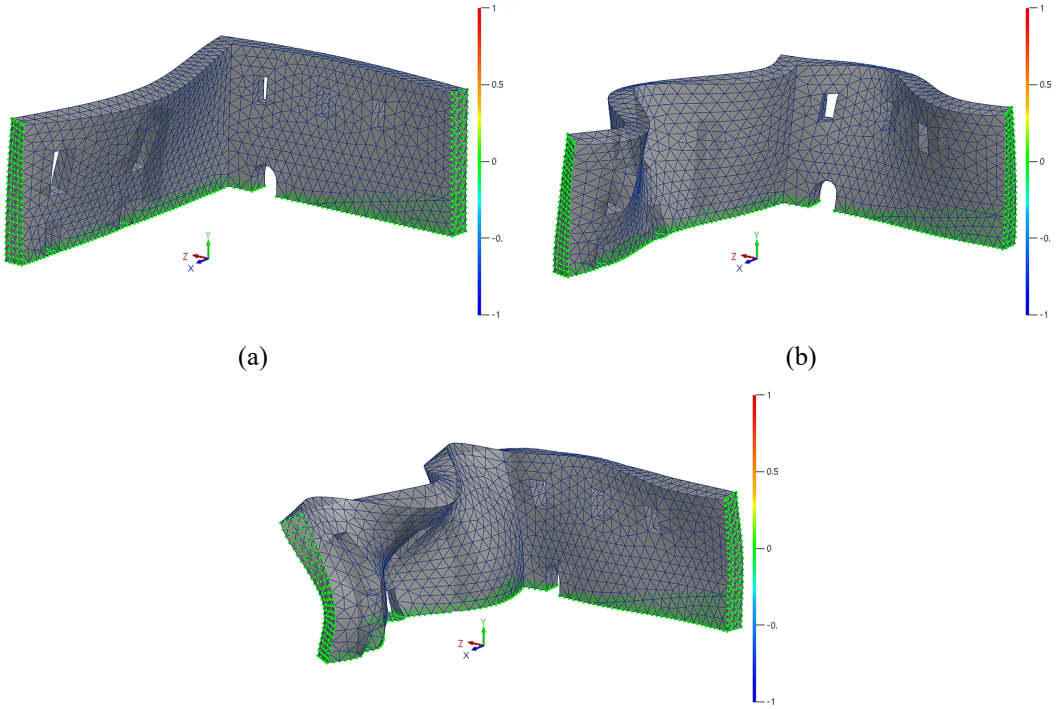

(a) (b)

(c)

Figure 6.13 Sensitivity plots of the (a) 1st, (b) 5th, and (c) 14th modes of the numerical model with respect to K_Y

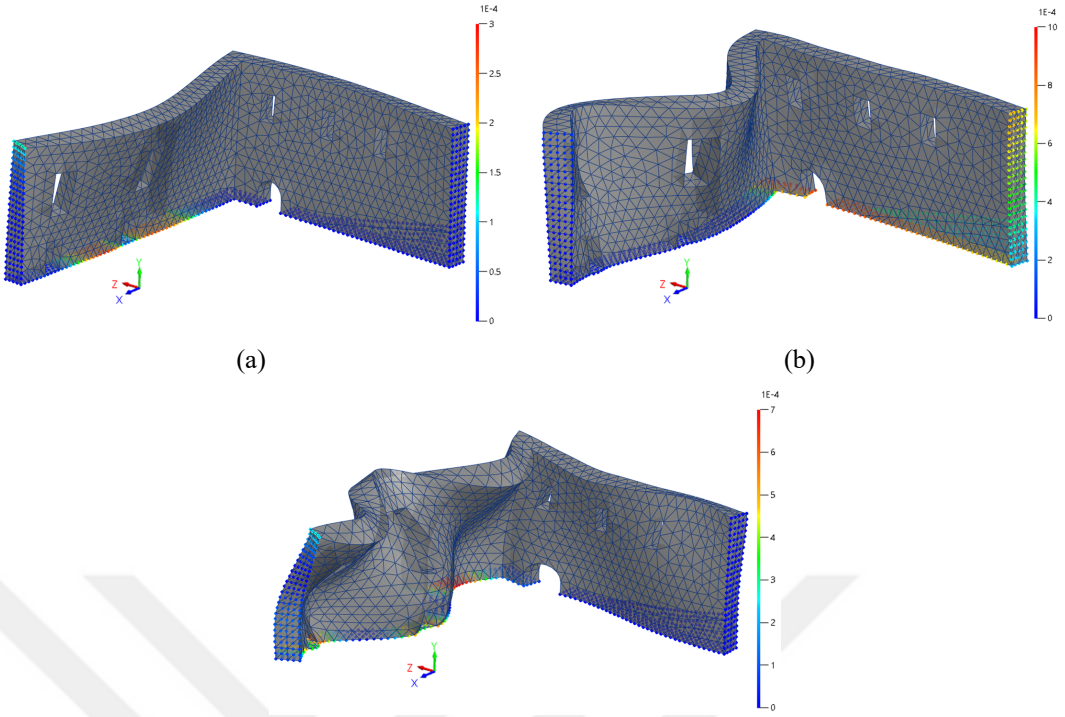

Figure 6.14 Sensitivity plots of the (a) 1st, (b) 5th, and (c) 14th modes of the numerical model with respect to K_Z

Modal parameters from the initial numerical model, experimental results, and the updated numerical model (the values in parentheses) are shown in Table 6.2.

Table 6.2 Modal parameters from the numerical models and experimental results

Mode # [Num. vs. Exp.]	**Numerical Model**	**Experimental**	**Freq. Diff. [%]**	**MAC [%]**
	Freq. [Hz]	**Freq. [Hz]**		
1 - 1	3.77 (3.93)	3.906	-3.61 (0.71)	95.20 (94.90)
5 - 2	9.21 (9.01)	8.960	2.77 (0.53)	82.60 (76.30)
14 - 3	19.85 (21.01)	21.265	-6.66 (-1.19)	78.30 (77.80)

From Table 6.2, it can be seen that significant improvements have been achieved between the frequencies computed before and after updating. On the other hand, the MAC values are not improved (i.e., are not increased in value) but rather slightly decreased. This is mainly because relatively higher scatter values were assigned to them which drives the updating algorithm to emphasize more on matching the frequency responses. Based on the updating results, the numerical model is calibrated

so that now it is more representative of the experimentally obtained modal parameters than the initial one. Consequently, the updated model can be used in the future for more in-depth analysis and assessment work.

Percentage changes of the model parameters with respect to their initially assigned values are shown in Figure 6.15 as contour plots. Besides, the model parameter values of the initial and updated numerical models are numerically presented in Table 6.3.

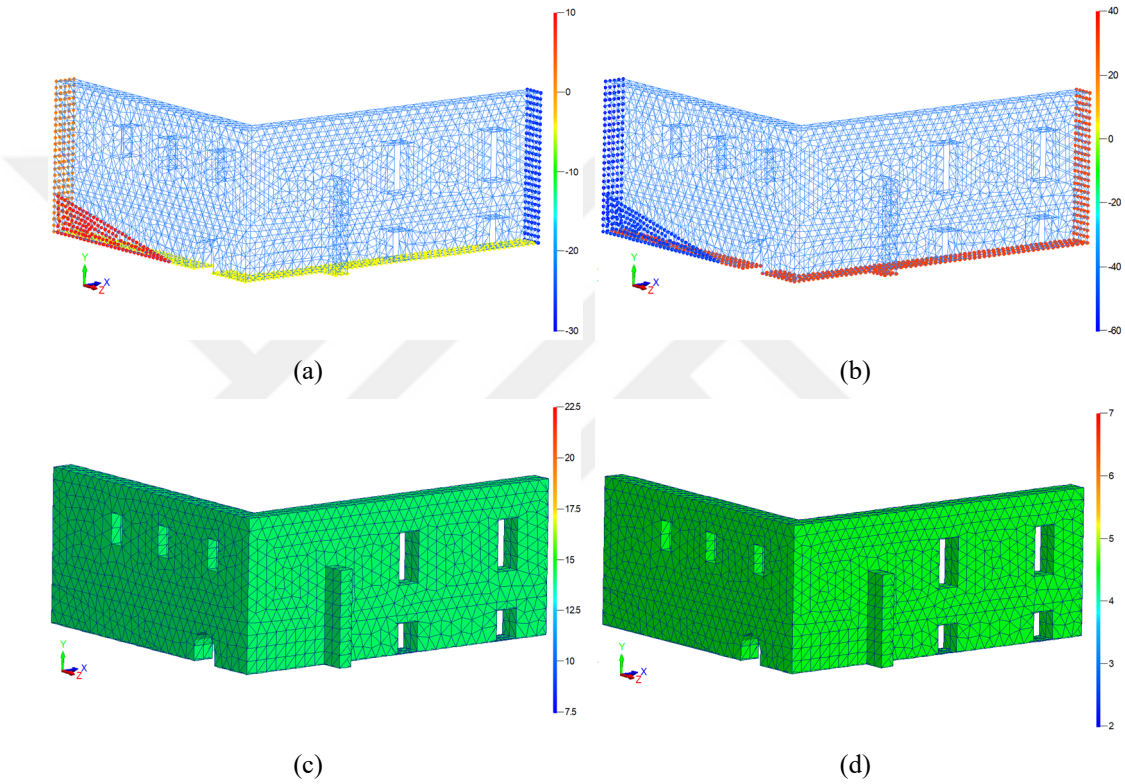

(a) (b)

(c) (d)

Figure 6.15 Percentage changes of (a) K_X, (b) K_Z, (c) Young's modulus, and (d) mass density with respect to their initially assigned values

By investigating the figure and the table together, it can be seen that all of the parameters are updated according to their updating strategy (i.e., global parameter updating), bounds, and scatter values. Another important issue is that the model parameters are updated well within the specified bounds, which means that the bounds are properly selected for the problem. Note that the updating results are heavily dependent on the updating strategy, initial parameters, parameter bounds, and scatters of model parameters and responses. Successive updating studies under different conditions may lead to different solutions, some of them even being unrealistic. That's

why all findings and results should be carefully evaluated by engineering judgement and insight, and then used if they are considered to be appropriate.

Table 6.3 Model parameters for the initial and updated numerical models

Model Parameter		Initial Value	Updated Value	Difference [%]
SG-1 [kN/m]	K_X	18000	18313	1.74
	K_Z	9000	3951	-56.10
SG-2 [kN/m]	K_X	18000	19487	8.26
	K_Z	9000	4418	-50.91
SG-3 [kN/m]	K_X	18000	17222	-4.32
	K_Z	18000	23366	29.81
SG-4 [kN/m]	K_X	18000	13129	-27.06
	K_Z	18000	23028	27.94
E [MPa]		4535	5177	14.15
ρ [kg/m^3]		2400	2507	4.44

6.6 Damage Scenario Study on the Courtyard Walls

It should be stated that damage scenario studies are beneficial tools that can be utilized for structural condition assessment of engineering structures. Namely, if the critical damage states for a structural system are known or foreseen (with extent and location information of the damages), they can be represented by using the reliable reference model of the system. Afterwards, it is possible to identify the modal parameters corresponding to each damage state, and by comparing these modal parameters to the ones that are extracted from the real-time monitoring data, it can be checked whether an undesired situation has occurred or not.

In the scope of this thesis, a damage scenario study was performed on the unreinforced masonry courtyard walls of the historical Isabey Mosque by using the updated/calibrated numerical model (i.e., reference model) obtained in the previous section. Here, the damaged case of the structural system was simulated numerically due to the impossibility to give controlled damage to the actual structure. But it must be stated that since the reference model was obtained by using the experimental data of the actual structure (i.e., the reference model is a representative of the actual

structural system), it can be employed to reflect any damage state of the actual structure as well.

The damaged case of the courtyard wall system was obtained by reducing the Young's modulus values of a specific region of the reference model by 70% (the blue colored zone denoted in Figure 6.16). This damaged region, which consists of 244 finite elements, was determined based on the first mode shape of the reference model which is presented in Figure 6.17. It should be stated that the constituted damaged model can be considered as representing an in-situ test of the courtyard wall system conducted after a damaging event. Since it reflects the dynamic characteristics of the damaged case, it is possible to carry out a damage identification study by using the outputs of the reference and damaged models.

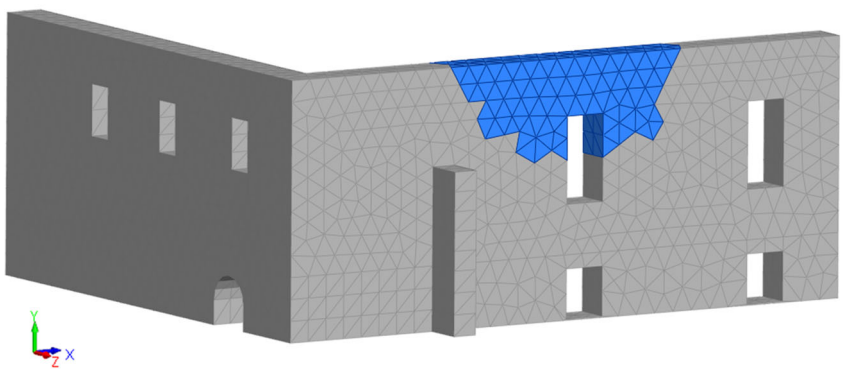

Figure 6.16 Damage scenario for the reference model of the courtyard walls

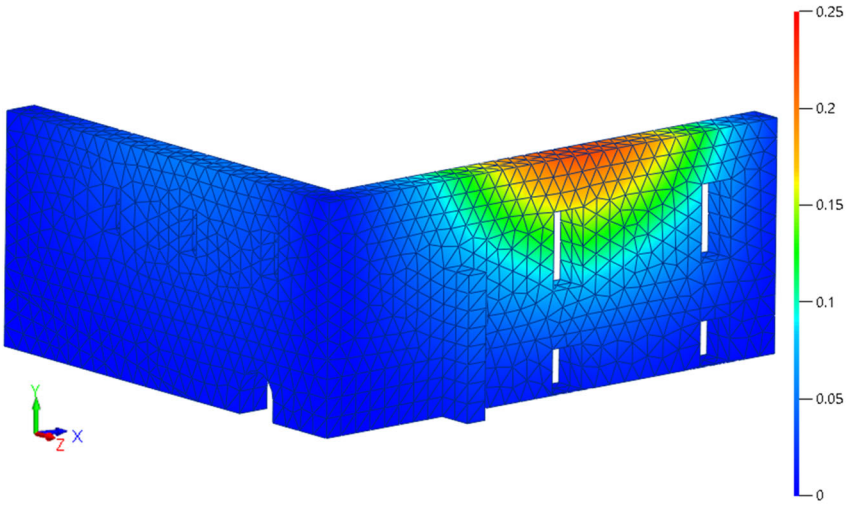

Figure 6.17 First mode shape of the reference model of the courtyard walls

The damaged zone of the wall system (see Figure 6.16) was tried to be detected by updating the reference model of the courtyard walls. In this context, the vibration frequencies and MAC values for the first 10 modes of both the models (i.e., the reference and damaged models) were selected as responses with scatter values of 1% and 10%, respectively. Only the Young's modulus values were selected as model parameters to be updated with a scatter value of 25%. Herein, local parameter updating strategy was adopted (i.e., model parameters were updated individually for each finite element, thus 9405 finite elements were updated). Bounds were selected as to be in 0-100% interval (i.e., only softening was allowed). Modal parameters from the reference, damaged, and updated models (i.e., values in parentheses are from the updated model) are given in Table 6.4.

Table 6.4 Modal parameters from the reference, damaged, and updated models

Mode # [Ref. vs. Dam.]	**Reference Model**	**Damaged Model**	**Freq. Diff. [%]**	**MAC [%]**
	Freq. [Hz]	**Freq. [Hz]**		
1 - 1	3.93 (3.84)	3.85	2.32 (-0.03)	99.80 (100)
2 - 2	4.77 (4.74)	4.75	0.49 (-0.04)	99.70 (100)
3 - 3	7.24 (6.90)	6.90	4.90 (-0.02)	98.90 (100)
4 - 4	8.41 (8.39)	8.39	0.26 (-0.02)	99.96 (100)
5 - 5	9.01 (8.91)	8.91	1.09 (-0.01)	98.70 (100)
6 - 6	10.28 (10.17)	10.17	1.13 (-0.03)	98.80 (100)
7 - 7	13.02 (12.46)	12.46	4.56 (-0.02)	20.40 (100)
8 - 8	13.03 (12.79)	12.79	1.91 (-0.01)	21.90 (100)
9 - 9	13.76 (13.73)	13.74	0.16 (-0.03)	99.00 (100)
10 - 10	16.07 (15.58)	15.59	3.12 (-0.01)	96.40 (100)

From Table 6.4, it can be seen that significant improvements have been achieved between the frequencies and MAC values computed before and after updating (i.e., an almost perfect match is obtained). Based on the updating results, the reference model is updated so that now it is more representative of the damaged state (i.e., damaged model). Percentage changes of the model parameters (i.e., Young's modulus values of

each finite element) with respect to their initial values are presented in Figure 6.18 as a contour plot. Actually, Figure 6.18 indicates the detected damages of the courtyard wall system. By investigating the figure, it can be concluded that the predefined damages are reasonably detected in terms of location and extent. Note that expecting a better result (i.e., the exact damage state shown in Figure 6.16) is nonsense since there exist many model parameters (i.e., 9405 model parameters) to be updated and the number of responses (i.e., first 10 modes) is limited. However, it is possible to enhance the results by limiting the number of model parameters by, for instance, updating only the vicinity of the damaged zone.

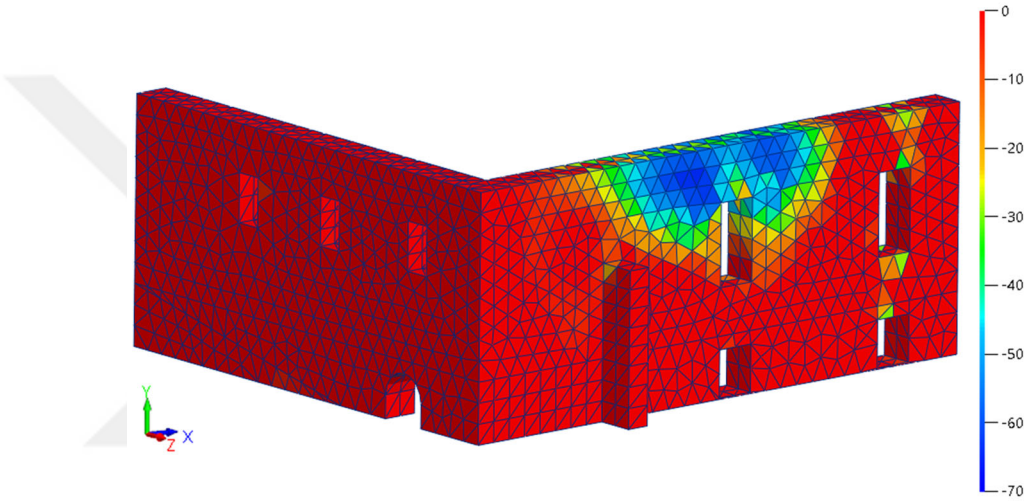

Figure 6.18 Detected damages of the courtyard walls

CHAPTER SEVEN
CONCLUSIONS AND FUTURE WORK

7.1 Conclusions

The research work presented in this thesis mainly concerned with three subjects: (i) System identification of half-scale, single-bay, single-story three R/C frames having different infill conditions at progressively increasing damage levels, (ii) damage identification of the frames by sensitivity-based finite element model updating method using the experimentally identified modal parameters, and (iii) system identification, model calibration, and damage scenario studies of the unreinforced masonry courtyard walls of the historical Isabey Mosque. Each of these subjects is summarized below.

In extensive experimental studies, half-scale, single-bay, single-story three R/C frames with different infill conditions, namely bare, locked type infilled, and standard type infilled, were quasi-statically tested under progressively increasing in-plane drifts, and after dynamically tested at some predetermined drifts. At different drift levels (i.e., at different damage states) AV and WN (having different excitation amplitudes) tests were conducted to estimate the modal parameters of the frames. WN tests were conducted by an electro-dynamic shaker positioned on top of the frames (i.e., on the slab level). The recorded dynamic response data at different damage states were processed by using three different output-only system identification methods, namely NExT-ERA, SSI-DATA, and EFDD. During the quasi-static tests, detailed visual damage inspections were conducted in order to classify the occurred damages, and their evolutions with respect to increasing damage levels were coupled with the corresponding modal identification results. A comparative study was performed for the frames at different damage states to reveal the effects of the different infill conditions. The main contributions and major findings of this research work are summarized as follows:

- For the frame with locked infills, stepped and horizontal cracks are mainly formed at brick-to-brick interfaces over a large portion of the infill wall due to the sliding

mechanism. Numerous and scattered plaster cracks (i.e., no concentration of crack patterns) occur and no significant brick crushing is observed.

- For the frame with standard infills, cracks are concentrated at corner zones where a bi-axial compression-compression stress state develops. This situation causes brick members to crush and spall around these zones (i.e., concentration of cracks).

- The additional lateral resistance imposed on the frames by the standard type infills is much higher than the additional resistance by the locked type infills. The frame with locked infills shows lower strength degradation than that of the frame with standard infills. Since the contribution of infills to the stiffness and lateral strength of a frame structure is not considered in most of the seismic codes, the behavior of the frame with locked infills seems analogous to the bare frame.

- The bare frame has the lowest initial stiffness value, whereas the standard infilled frame has the highest. The frame with locked infills has higher stiffness values at early stages but exhibits significant drops with increasing drift ratios due to overcoming the static friction threshold of the locked bricks and the shear failure of the mortar. The behavior of the frame with locked infills seems analogous to the bare frame in terms of stiffness degradation.

- The bare frame has the lowest energy dissipation capacity, whereas the standard infilled frame has the highest. The behavior of the frame with locked infills seems analogous to the bare frame in the sense of dissipated energy.

- The identified vibration frequencies are affected by the excitation levels considered in this research. Accordingly, AV test results exhibit the highest and WN wo/Offline test results exhibit the lowest frequency estimates. This shows that even for small RMS amplitude change in excitation level, modal parameter estimations are affected by the nonlinear behavior of R/C frames.

- Damping ratio estimations, which are the most uncertain estimations, are amplitude dependent and sensitive to SNR. Nevertheless, it can be said that AV tests result in lower and WN wo/Offline tests result in higher damping estimations.

- NExT-ERA, SSI-DATA, and EFDD methods give very close results for vibration frequency and mode shape estimations.

- NExT-ERA and SSI-DATA methods result in somewhat similar damping estimations; but the overall match among these methods is not as good as in the case of frequency and mode shape estimations. The damping estimations obtained by EFDD method differ considerably from the ones obtained by other two methods. Subjectiveness of the peak-picking and logarithmic decrement processes can be attributed as the reasons behind this higher variability in damping estimations.

- Very clear decreasing trends with increasing damage levels are observed in vibration frequency and MAC estimations for all excitation types and system identification methods. The identified damping ratios exhibit large variability and do not follow a clear trend that can be associated with increasing structural damage. Nevertheless, a slight increasing trend in damping estimations is noticeable as the structural damage increases (especially for the frame with locked infills).

- The decreasing trend in the frequency estimations with respect to increasing structural damage for the frame with locked bricks is slower than the other two. This may possibly be indicating that the extra damage that may be induced by frame-infill interaction is less severe for the frame with locked infills, due to low-to-moderate (mild) panel action, than for the frame with standard infills.

- The changes in MAC values as the structural damage increases are more pronounced for the infilled frames. This can be attributed to the infill wall-frame interaction in out-of-plane direction. The effect of infills on the mode shapes diminish as infill damage increases. The damage level does not change the classically damped nature of the mode shapes.

- Existence of infills adds out-of-plane components to the mode shapes. The out-of-plane components disappear as the infill damage increases, turning into almost perfectly in-plane mode shapes at higher damage levels.

- The dynamic excitation levels attained in this research work are not sufficient to excite the infill walls. Therefore, the modal identification results represent the dynamic characteristics of only the surrounding frame structure without the contributions of the infills. Although the infills are ineffective during the dynamic tests, they have a decisive role in the behaviors and damage formations of the frames during the quasi-static tests, which is revealed by damage observations.

- Closed (i.e., isolated) laboratory conditions that lack the usual ambient effects may lead to difficulties in the excitation of vibration modes for the test specimens. Especially in the case of rigid specimens, the present excitation conditions may not be sufficient to excite the specimens properly.

- The stiffness degradation values calculated using the estimated in-plane vibration frequencies indicate that the bare frame loses its lateral stiffness at a faster rate, whereas the frame with standard infills loses at a lower rate. Here again, the frame with locked infills seems analogous to the bare frame.

- Presence of infills initiates R/C member damages to occur earlier than the bare frame. In addition, it influences cracks on the R/C members and causes their numbers and widths to increase compared to the bare frame.

- Higher vibration modes cannot be identified clearly from the dynamic data due to low excitation levels and SNR.

- The identified out-of-plane modes are classically damped and have larger complex components due to low SNR values. That’s why they are considered as unreliable estimates.

Damage identification work of the frames having different infill conditions at gradually increasing damage states was performed by the sensitivity-based finite element model updating method. The initial FE models of the frames were developed in MATLAB based FEDEASLab software by using 3-D Bernoulli-Euler frame elements. Support conditions were represented by simple supports at column(s) bottom ends together with three rotational springs. Structural damages of the frames were defined by relative stiffness reduction factors. At each progressively increasing damage state, stiffness reduction factors of the predetermined design variables were obtained by minimizing an objective function constructed as the differences between the experimentally identified and the FE predicted modal parameters. In this context, modal parameter results of the EFDD method with WN w/Offline dataset were used. The model updating process was conducted in two steps: (i) First, a reliable reference model was obtained by using the experimentally identified modal parameters at the undamaged state, and then (ii) the procedure was repeated by updating this reference model at each progressively increasing damage state to identify the damage, its location, and extent. The number of design variables used for the updating procedure was reduced to ensure a well-conditioned optimization problem by taking into account symmetry conditions, detectability indices, and internal moment levels occurred in the frame elements. Finally, the identified damage results were verified using the visual damage observations made during the quasi-static tests. The main contributions and major findings of this research work are summarized as follows:

- Since it is very difficult to attain perfect fixity at supports in real-life situations, support conditions of numerical models should be represented by spring elements.

- Sensitivity of a mode can change from one element to another. In other words, detectability of an element can change from one mode to another.

- Detectable elements are the ones affected the most by the updating algorithm, this itself alone does not automatically imply that these elements have to be included in the updating process. In other words, if these elements are already adequately representing the actual values, then there is no reason to update them. Moreover,

excluding them from the updating process is beneficial in order to acquire well-conditioned optimization problems which in return lead to more accurate updating results.

- For the bare and locked infilled frames (i.e., frames with two design variables), the global minimum of the objective function lies within a wide interval at low damage states which indicates that the selected design variables do not provide a prominent solution; but provides a prominent one as damage level increases.

- It is clearly seen that the structural damage severity of all frames consistently increases as the frames are subjected to higher drift ratios.

- For the bare and locked infilled frames, structural damage is mainly concentrated on the beam ends and the column(s) bottom ends, whereas there exists only minor damage on the other parts of the frames. These damage observations are in good agreement with the damage identification results. Here again, the frame with locked infills seems analogous to the bare frame.

- For the frame with standard infills, structural damage is mainly concentrated on the column(s) bottom ends, mid-zones, top ends (i.e., throughout the column members), and beam ends. These damage observations are in good agreement with the damage identification results. It is clear that the presence of standard infills has significant effects on the damage formations of the frames.

Modal parameter identification and sensitivity-based finite element model updating studies were performed on the unreinforced masonry courtyard walls of the historical Isabey Mosque. Modal parameters of the walls were estimated from two sets of AV measurements using EFDD method embedded in ARTeMIS software. The initial numerical macro model of the courtyard walls was created in ABAQUS environment by using the material properties obtained from the flat-jack tests conducted on the walls as well as the values provided in the literature. Boundary conditions of the numerical model were divided into four substructures by taking into account their

locations on the walls. Translational springs were assigned to each substructure. Initial stiffnesses of the springs were determined by manual updating so that a numerical model having modal parameters representative of the actual courtyard wall system was obtained. Mass density, Young's modulus, and boundary conditions (i.e., translational springs) of the initial numerical model were calibrated using a global parameter updating method available in FEMtools software. Thus, a reliable FE model that is more representative than the initial one was obtained to be used in future numerical assessment studies. Finally, a damage scenario study was performed on the calibrated numerical model and the predefined damages were identified. The main contributions and major findings of this research work are summarized as follows:

- Boundary conditions are often the most uncertain parts of a structure, so they should be included in the updating process with relatively wider bound ranges and relatively higher scatter values to determine their actual states. Otherwise, unrealistic updating results may be obtained for the other updated model parameters due to the overcompensation problem.

- Existence of insensitive responses and/or linearly dependent model parameters may lead to having ill-conditioned problems with convergence difficulties. For a well-conditioned optimization problem with a unique solution, the number of model parameters to be updated must be limited in global parameter updating type approaches.

- Performing manual calibration prior to performing an optimization-based model updating proves itself to be beneficial in order to overcome potential convergence problems.

- Sensitivity analysis is always useful to find out whether a model parameter should be included in the updating process or not and also to decide a suitable updating strategy (i.e., local or global parameter updating) for a model.

- Mode shape estimations usually contain higher estimation uncertainty than frequency estimations due to having a limited number of sensors to estimate them and also due to measurement noise. Therefore, assigning relatively higher scatter values to mode shapes is suggested if they are thought to be unreliable.

- Model updating results are heavily dependent on the updating strategy, initial parameter values, parameter bounds, and scatters of model parameters and responses. Performing several updating works under different conditions may lead to different solutions, sometimes unrealistic ones. Therefore, all results should be carefully evaluated through engineering judgement, and used if they are decided to be appropriate.

7.2 Recommendations for Future Research

Based on the research work presented in this thesis, the following recommendations are made for future work:

- Effects of higher dynamic excitation levels than the ones achieved in this research work on system and damage identification results can be investigated.

- Frequency response functions, acceleration time histories, modal strains, modal curvatures, modal strain energies, and modal flexibilities can be considered as residuals in model updating method. Especially, using the modal flexibilities can be beneficial to identify local changes of the systems.

- The developed MATLAB based codes as part of the presented research work can further be extended in order to be capable of performing model updating studies on more complex structural systems (e.g., structural systems having planar elements, solid elements, etc.).

- Regularization methods can be studied to treat the ill-conditioning states of the optimization problems.

- Instead of engineering judgement and/or trial runs, statistical approaches can be used to determine the components of the weighting matrices. Thus, more objective results can be obtained.

- It is a known fact that the system identification results include uncertainty due to measurement errors (e.g., measurement noise, spatial density of the sensors, measurement length, excitation type and level, etc.). In addition, FEMU results include uncertainty because of the modeling errors, assumptions, and simplifications made during the development of numerical models, and the method itself (i.e., selection of design variables, residuals, weighting factors, and bounds may lead to uncertainty). Therefore, uncertainty quantification can be studied to determine the reliability of system identification and model updating results. In this context, non-probabilistic interval-based or Bayesian FEMU methods can be studied.

- Since all the real-life structures are inherently nonlinear, especially the damaged structures caused by strong excitations, nonlinear FEMU methods, that are based on the nonlinear responses of the structures, can be used. Since the nonlinear responses include more information about damage than linear ones, nonlinear FEMU methods provide more accurate damage identification results.

REFERENCES

ABAQUS (2017). *Dassault Systemes Simulia Corp*. Jonhston, USA.

Abdullah, M. M., Richardson, A., & Hanif, J. (2001). Placement of sensors/actuators on civil structures using genetic algorithms. *Earthquake Engineering & Structural Dynamics*, *30* (8), 1167-1184.

ACI 374.1-05 (2005). *Acceptance criteria for moment frames based on structural testing and commentary*. Michigan: American Concrete Institute.

Alkayem, N. F., Cao, M., Zhang, Y., Bayat, M., & Su, Z. (2018). Structural damage detection using finite element model updating with evolutionary algorithms: a survey. *Neural Computing and Applications*, *30* (2), 389-411.

Allemang, R. J. (2003). The modal assurance criterion-twenty years of use and abuse. *Sound and Vibration*, *37* (8), 14-23.

Alotto, P., Gaggero, M., Molinari, G., & Nervi, M. (1997). A "design of experiment" and statistical approach to enhance the "generalised response surface" method in the optimisation of multiminima problems. *IEEE Transactions on Magnetics*, *33* (2), 1896-1899.

Altunişik, A. C., Okur, F. Y., Genç, A. F., Günaydin, M., & Adanur, S. (2018). Automated model updating of historical masonry structures based on ambient vibration measurements. *Journal of Performance of Constructed Facilities*, *32* (1), 04017126.

Amani, M. G., Riera, J. D., & Curadelli, R. I. O. (2007). Identification of changes in the stiffness and damping matrices of linear structures through ambient vibrations. *Structural Control and Health Monitoring*, *14* (8), 1155-1169.

ARTeMIS Extractor Pro (2016). *Structural Vibration Solutions*. Aalborg, Denmark.

Asgarieh, E., Moaveni, B., & Stavridis, A. (2014). Nonlinear finite element model updating of an infilled frame based on identified time-varying modal parameters during an earthquake. *Journal of Sound and Vibration*, *333* (23), 6057-6073.

ASTM C1197-04 (2004). *Standard test method for in situ measurement of masonry deformability properties using the flatjack method*. USA: ASTM International.

Astroza, R., Ebrahimian, H., Conte, J. P., Restrepo, J. I., & Hutchinson, T. C. (2016a). System identification of a full-scale five-story reinforced concrete building tested on the NEES-UCSD shake table. *Structural Control and Health Monitoring*, *23* (3), 535-559.

Astroza, R., Ebrahimian, H., Conte, J. P., Restrepo, J. I., & Hutchinson, T. C. (2016b). Influence of the construction process and nonstructural components on the modal properties of a five-story building. *Earthquake Engineering & Structural Dynamics*, *45* (7), 1063-1084.

Astroza, R., Ebrahimian, H., Li, Y., & Conte, J. P. (2017). Bayesian nonlinear structural FE model and seismic input identification for damage assessment of civil structures. *Mechanical Systems and Signal Processing*, *93*, 661-687.

Augenti, N., & Parisi, F. (2010). Learning from construction failures due to the 2009 L'Aquila, Italy, earthquake. *Journal of Performance of Constructed Facilities*, *24* (6), 536-555.

Bajric, A., Brincker, R., & Georgakis, C. T. (2014). Evaluation of damping using time domain OMA techniques. In *Proceedings of the 2014 SEM Fall Conference and International Symposium on Intensive Loading and Its Effects, October 19-22, Beijing, China.* Retrieved June 30, 2020, from https://core.ac.uk/download/pdf/43245646.pdf.

Bajrić, A., Georgakis, C. T., & Brincker, R. (2015). Evaluation of damping using frequency domain operational modal analysis techniques. In J. Caicedo, & S. Pakzad, (Ed.), In *Dynamics of Civil Structures, volume 2* (351-355). Cham: Springer.

Bakir, P. G., Reynders, E., & De Roeck, G. (2007). Sensitivity-based finite element model updating using constrained optimization with a trust region algorithm. *Journal of Sound and Vibration*, *305* (1-2), 211-225.

Bartoli, G., Betti, M., & Giordano, S. (2013). In situ static and dynamic investigations on the "Torre Grossa" masonry tower. *Engineering Structures*, *52*, 718-733.

Bassoli, E., Vincenzi, L., D'Altri, A. M., de Miranda, S., Forghieri, M., & Castellazzi, G. (2018). Ambient vibration-based finite element model updating of an earthquake-damaged masonry tower. *Structural Control and Health Monitoring*, *25* (5), e2150.

Bayraktar, A., Altunişik, A. C., Birinci, F., Sevim, B., & Türker, T. (2010). Finite-element analysis and vibration testing of a two-span masonry arch bridge. *Journal of Performance of Constructed Facilities*, *24* (1), 46-52.

Beck, J. K., & Arnold, K. J. (1977). *Parameter estimation in engineering and science*. New York: John Wiley & Sons.

Behmanesh, I., Yousefianmoghadam, S., Nozari, A., Moaveni, B., & Stavridis, A. (2018). Uncertainty quantification and propagation in dynamic models using ambient vibration measurements, application to a 10-story building. *Mechanical Systems and Signal Processing*, *107*, 502-514.

Bendat, J. S., & Piersol, A. G. (2000). *Random data: Analysis and measurement procedures*. New York: Wiley.

Boller, C., Chang, F. K., & Fujino, Y. (2009). *Encyclopedia of structural health monitoring*. West Sussex: Wiley.

Boscato, G., Russo, S., Ceravolo, R., & Fragonara, L. Z. (2015). Global sensitivity-based model updating for heritage structures. *Computer-Aided Civil and Infrastructure Engineering*, *30* (8), 620-635.

Brincker, R., & Andersen, P. (2006). Understanding stochastic subspace identification. In *Proceedings of the 24th International Modal Analysis Conference (IMAC), January 30-February 2, St. Louis, Missouri.* Retrieved June 30, 2020, from https://core.ac.uk/download/pdf/60362355.pdf.

Brincker, R., & Ventura, C. (2015). *Introduction to operational modal analysis*. Chichester: John Wiley & Sons.

Brincker, R., Ventura, C., & Andersen, P. (2001a). Damping estimation by frequency domain decomposition. In *Proceedings of the 19th International Modal Analysis Conference (IMAC), February 5-8, Orlando, Florida,* 698-703.

Brincker, R., Zhang, L., & Andersen, P. (2001b). Modal identification of output-only systems using frequency domain decomposition. *Smart Materials and Structures*, *10* (3), 441-445.

Brownjohn, J. M. (2007). Structural health monitoring of civil infrastructure. *Philosophical Transactions of the Royal Society A: Mathematical, Physical and Engineering Sciences*, *365* (1851), 589-622.

Cabboi, A., Gentile, C., & Saisi, A. (2017). From continuous vibration monitoring to FEM-based damage assessment: application on a stone-masonry tower. *Construction and Building Materials*, *156*, 252-265.

Caicedo, J. M. (2011). Practical guidelines for the natural excitation technique (NExT) and the eigensystem realization algorithm (ERA) for modal identification using ambient vibration. *Experimental Techniques*, *35* (4), 52-58.

Caicedo, J. M., Dyke, S. J., & Johnson, E. A. (2004). Natural excitation technique and eigensystem realization algorithm for phase I of the IASC-ASCE benchmark problem: Simulated data. *Journal of Engineering Mechanics*, *130* (1), 49-60.

Carden, E. P., & Fanning, P. (2004). Vibration based condition monitoring: a review. *Structural Health Monitoring*, *3* (4), 355-377.

Carvalho, J., Datta, B. N., Gupta, A., & Lagadapati, M. (2007) A direct method for model updating with incomplete measured data and without spurious modes. *Mechanical Systems and Signal Processing*, *21* (7), 2715-2731.

Ceravolo, R., Pistone, G., Fragonara, L. Z., Massetto, S., & Abbiati, G. (2016). Vibration-based monitoring and diagnosis of cultural heritage: a methodological discussion in three examples. *International Journal of Architectural Heritage*, *10* (4), 375-395.

Chang, M., & Pakzad, S. N. (2013). Modified natural excitation technique for stochastic modal identification. *Journal of Structural Engineering*, *139* (10), 1753-1762.

Chase, J. G., Hwang, K. L., Barroso, L. R., & Mander, J. B. (2005). A simple LMS-based approach to the structural health monitoring benchmark problem. *Earthquake Engineering & Structural Dynamics*, *34* (6), 575-594.

Chen, W. H., Lu, Z. R., Lin, W., Chen, S. H., Ni, Y. Q., Xia, Y., & Liao, W. Y. (2011). Theoretical and experimental modal analysis of the Guangzhou New TV Tower. *Engineering Structures*, *33* (12), 3628-3646.

Chopra, A. K. (2012). *Dynamics of structures: theory and applications to earthquake engineering* (4th ed.). Englewood Cliffs, New Jersey: Prentice Hall.

Coleman, T. F., & Li, Y. (1996). An interior trust region approach for nonlinear minimization subject to bounds. *SIAM Journal on Optimization*, *6* (2), 418-445.

Compán, V., Pachón, P., Cámara, M., Lourenço, P. B., & Sáez, A. (2017). Structural safety assessment of geometrically complex masonry vaults by non-linear analysis. The Chapel of the Würzburg Residence (Germany). *Engineering Structures*, *140*, 1-13.

Conde, B., Ramos, L. F., Oliveira, D. V., Riveiro, B., & Solla, M. (2017). Structural assessment of masonry arch bridges by combination of non-destructive testing techniques and three-dimensional numerical modelling: Application to Vilanova bridge. *Engineering Structures*, *148*, 621-638.

Conn, A. R., Gould, N. I., & Toint, P. L. (2000). *Trust region methods*. Philadelphia: SIAM.

Costa, C., Arêde, A., Costa, A., Caetano, E., Cunha, Á., & Magalhães, F. (2015). Updating numerical models of masonry arch bridges by operational modal analysis. *International Journal of Architectural Heritage*, *9* (7), 760-774.

Costa, C., Ribeiro, D., Jorge, P., Silva, R., Arêde, A., & Calçada, R. (2016). Calibration of the numerical model of a stone masonry railway bridge based on experimentally identified modal parameters. *Engineering Structures*, *123*, 354-371.

Crisafulli, F. J. (1997). *Seismic behaviour of reinforced concrete structures with masonry infills*. Phd Thesis, University of Canterbury, Christchurch.

Ding, Z., Li, J., Hao, H., & Lu, Z. R. (2019). Structural damage identification with uncertain modelling error and measurement noise by clustering based tree seeds algorithm. *Engineering Structures*, *185*, 301-314.

Dizhur, D., & Ingham, J. (2015). *Seismic improvement of load bearing unreinforced masonry cavity walls*. External Research Report, University of Auckland, Porirua.

Dizhur, D., Ingham, J., Moon, L., Griffith, M., Schultz, A., Senaldi, I., Magenes, G., Dickie, J., Lissel, S., Centeno, J., Ventura, C., Leite, J. C., & Lourenço, P. B. (2011). Performance of masonry buildings and churches in the 22 February 2011 Christchurch earthquake. *Bulletin of the New Zealand Society for Earthquake Engineering*, *44* (4), 279-296.

Doebling, S. W., Farrar, C. R., & Prime, M. B. (1998). A summary review of vibration-based damage identification methods. *Shock and Vibration Digest*, *30* (2), 91-105.

Döhler, M., Andersen, P., & Mevel, L. (2011a). Data merging for multi-setup operational modal analysis with data-driven SSI. In T. Proulx, (Ed.), In *Structural Dynamics, volume 3* (443-452). New York: Springer.

Döhler, M., Reynders, E., Magalhaes, F., Mevel, L., De Roeck, G., & Cunha, A. (2011b). Pre-and post-identification merging for multi-setup OMA with covariance-driven SSI. In T. Proulx, (Ed.), In *Dynamics of Bridges, volume 5* (57-70). New York: Springer.

Ebrahimian, H., Astroza, R., Conte, J. P., & de Callafon, R. A. (2017). Nonlinear finite element model updating for damage identification of civil structures using batch Bayesian estimation. *Mechanical Systems and Signal Processing*, *84*, 194-222.

Ercan, E. (2018). Assessing the impact of retrofitting on structural safety in historical buildings via ambient vibration tests. *Construction and Building Materials*, *164*, 337-349.

Ewins, D. J. (2000). *Modal testing: theory, practice and application* (2nd ed.). Baldock, Hertfordshire: Research Studies Press Ltd.

Fan, W., & Qiao, P. (2011). Vibration-based damage identification methods: a review and comparative study. *Structural Health Monitoring*, *10* (1), 83-111.

Fang, S. E., Perera, R., & De Roeck, G. (2008). Damage identification of a reinforced concrete frame by finite element model updating using damage parameterization. *Journal of Sound and Vibration*, *313* (3-5), 544-559.

Farrar, C. R., & Lieven, N. A. J. (2007). Damage prognosis: The future of structural health monitoring. *Philosophical Transactions of the Royal Society A: Mathematical, Physical and Engineering Sciences*, *365* (1851), 623-632.

Felber, A. J. (1993). *Development of a hybrid bridge evaluation system*. Phd Thesis, University of British Columbia, Vancouver.

FEMtools (2017a). *Dynamic Design Solutions.* Leuven, Belgium.

FEMtools (2017b). *FEMtools model updating theoretical manual, version 4.0.0.* Leuven: Dynamic Design Solutions.

Filippou, F. C., & Constantinides, M. (2004). *FEDEASLab getting started guide and simulation examples*. Retrieved August 31, 2004, from http://www.neesgrid.org/news/documents.php.

Foti, D., Diaferio, M., Giannoccaro, N. I., & Mongelli, M. (2012). Ambient vibration testing, dynamic identification and model updating of a historic tower. *NDT & E International*, *47*, 88-95.

Fox, R. L., & Kapoor, M. P. (1968). Rates of change of eigenvalues and eigenvectors. *AIAA Journal*, *6* (12), 2426-2429.

Friswell, M. I., Mottershead, J. E. (1995). *Finite element model updating in structural dynamics*. Dordrecht: Kluwer Academic Publishers.

Fritzen, C. P., Jennewein, D., & Kiefer, T. (1998). Damage detection based on model updating methods. *Mechanical Systems and Signal Processing*, *12* (1), 163-186.

Garcia-Palencia, A. J., Santini-Bell, E., Sipple, J. D., & Sanayei, M. (2015). Structural model updating of an in-service bridge using dynamic data. *Structural Control and Health Monitoring*, *22* (10), 1265-1281.

Gentile, C., & Gallino, N. (2008). Ambient vibration testing and structural evaluation of an historic suspension footbridge. *Advances in Engineering Software*, *39* (4), 356-366.

Goksu, C., Inci, P., Demir, U., Yazgan, U., & Ilki, A. (2017). Field testing of substandard RC buildings through forced vibration tests. *Bulletin of Earthquake Engineering*, *15* (8), 3245-3263.

Grip, N., Sabourova, N., & Tu, Y. (2017). Sensitivity-based model updating for structural damage identification using total variation regularization. *Mechanical Systems and Signal Processing*, *84*, 365-383.

Guo, Y. L., Ni, Y. Q., & Chen, S. K. (2017). Optimal sensor placement for damage detection of bridges subject to ship collision. *Structural Control and Health Monitoring*, *24* (9), e1963.

He, L. X., Wu, C., & Li, J. (2019). Post-earthquake evaluation of damage and residual performance of UHPSFRC piers based on nonlinear model updating. *Journal of Sound and Vibration*, *448*, 53-72.

He, X., Moaveni, B., Conte, J. P., Elgamal, A., & Masri, S. F. (2009). System identification of Alfred Zampa Memorial Bridge using dynamic field test data. *Journal of Structural Engineering*, *135* (1), 54-66.

Holland, J. (1975). *Adaptation in natural and artificial systems*. Michigan: University of Michigan Press.

Ibán, N., Castaño, J., Cara, J., Fernández, J., Cacho-Pérez, M., Muñoz, I., & Lorenzana, A. (2015). Finite element model updating of a lively footbridge. In *Proceedings of the 6th International Operational Modal Analysis Conference (IOMAC'15), May 12-14, Gijón, Spain*. Retrieved June 30, 2020, from http://iomac.eu/iomac/2015/pdf/507_Paper_Iban.pdf.

Ibanez, P., Vasudevan, R., & Smith, C. B. (1976). Experimental and theoretical analysis of buildings. In *Proceedings of the ASCE-EMD Specialty Conference UCLA Extension, March 30-31, Los Angeles, California,* 412-430.

Ismail, N., Griffith, M., & Ingham, J. (2011). Performance of masonry buildings during the 2010 Darfield (New Zealand) earthquake. In *Proceedings of the 11th North American Masonry Conference*, *June 5-8, Minneapolis, USA.* Retrieved June 30, 2020, from https://researchspace.auckland.ac.nz/handle/2292/6807.

Jaishi, B., & Ren, W. X. (2005). Structural finite element model updating using ambient vibration test results. *Journal of Structural Engineering*, *131* (4), 617-628.

Jaishi, B., & Ren, W. X. (2006). Damage detection by finite element model updating using modal flexibility residual. *Journal of Sound and Vibration*, *290* (1-2), 369-387.

James, III G. H., Carne, T. G., & Lauffer J. P. (1993). *The natural excitation technique (NExT) for modal parameter extraction from operating wind turbines.* Report SAND92-1666, Sandia National Labs, Albuquerque.

Ji, X., Fenves, G. L., Kajiwara, K., & Nakashima, M. (2011). Seismic damage detection of a full-scale shaking table test structure. *Journal of Structural Engineering*, *137* (1), 14-21.

Joshi, S., & Boyd, S. (2009). Sensor selection via convex optimization. *IEEE Transactions on Signal Processing*, *57* (2), 451-462.

Juang, J. N., & Pappa, R. S. (1985). An eigensystem realization algorithm for modal parameter identification and model reduction. *Journal of Guidance, Control, and Dynamics*, *8* (5), 620-627.

Kammer, D. C. (1991). Sensor placement for on-orbit modal identification and correlation of large space structures. *Journal of Guidance, Control, and Dynamics*, *14* (2), 251-259.

Kirkpatrick, S., Gelatt, C. D., & Vecchi, M. P. (1983). Optimization by simulated annealing. *Science*, *220* (4598), 671-680.

Leyder, C., Dertimanis, V., Frangi, A., Chatzi, E., & Lombaert, G. (2018). Optimal sensor placement methods and metrics-comparison and implementation on a timber frame structure. *Structure and Infrastructure Engineering*, *14* (7), 997-1010.

Li, X. Y., & Law, S. S. (2010). Adaptive Tikhonov regularization for damage detection based on nonlinear model updating. *Mechanical Systems and Signal Processing*, *24* (6), 1646-1664.

Lourenço, P. B. (1996). *Computational strategies for masonry structures*. Phd Thesis, Delft University of Technology, Delft.

Luco, J. E., Ozcelik, O., & Conte, P. (2010). Acceleration tracking performance of the UCSD-NEES shake table. *Journal of Structural Engineering, 136* (5), 481-490.

Magalhães, F., Caetano, E., Cunha, Á., Flamand, O., & Grillaud, G. (2012). Ambient and free vibration tests of the Millau Viaduct: Evaluation of alternative processing strategies. *Engineering Structures*, *45*, 372-384.

Magalhães, F., Cunha, Á., Caetano, E., & Brincker, R. (2010). Damping estimation using free decays and ambient vibration tests. *Mechanical Systems and Signal Processing*, *24* (5), 1274-1290.

Maia, N. M. M., Silva, J. M., He, J., Lieven, N. A. J., Lin, R. M., Skingle, G. W., To, W. -M., & Urgueira, A. P. V. (1997). *Theoretical and Experimental Modal Analysis*. Somerset: Research Studies Press.

Marwala, T. (2010). *Finite element model updating using computational intelligence techniques: applications to structural dynamics*. London: Springer.

Masciotta, M. G., Ramos, L. F., Lourenço, P. B., Vasta, M., & De Roeck, G. (2016). A spectrum-driven damage identification technique: Application and validation through the numerical simulation of the Z24 Bridge. *Mechanical Systems and Signal Processing*, *70*, 578-600.

MATLAB (2017). *The MathWorks Inc.* Massachusetts, USA.

Meo, M., & Zumpano, G. (2005). On the optimal sensor placement techniques for a bridge structure. *Engineering Structures*, *27* (10), 1488-1497.

Misir, S., Ozcelik, O., Girgin, S. C., & Kahraman, S. (2012). Experimental work on seismic behavior of various types of masonry infilled RC frames. *Structural Engineering and Mechanics*, *44* (6), 763-774.

Moaveni, B. (2007). *System and damage identification of civil structures*. Phd Thesis, University of California, San Diego.

Moaveni, B., Stavridis, A., Lombaert, G., Conte, J. P., & Shing, P. B. (2013). Finite-element model updating for assessment of progressive damage in a 3-story infilled RC frame. *Journal of Structural Engineering*, *139* (10), 1665-1674.

Mor´e, J. J., & Wright, S. J. (1993). *Optimization software guide, volume 14 of frontiers in applied mathematics.* Philadelphia: SIAM.

Mota, M. (2011). *Shake table acceleration tracking performance impact on dynamic similitude.* Phd Thesis, Drexel University, Philadelphia.

Mottershead, J. E., & Friswell, M. I. (1993). Model updating in structural dynamics: A survey. *Journal of Sound and Vibration*, *167* (2), 347-375.

Mottershead, J. E., Link, M., & Friswell, M. I. (2011). The sensitivity method in finite element model updating: A tutorial. *Mechanical Systems and Signal Processing*, *25* (7), 2275-2296.

Mouyiannou, A., Rota, M., Penna, A., & Magenes, G. (2014). Identification of suitable limit states from nonlinear dynamic analyses of masonry structures. *Journal of Earthquake Engineering*, *18* (2), 231-263.

Nocedal, J., & Wright, S. J. (1999). *Numerical optimization*. New York: Springer.

Nozari, A., Behmanesh, I., Yousefianmoghadam, S., Moaveni, B., & Stavridis, A. (2017). Effects of variability in ambient vibration data on model updating and damage identification of a 10-story building. *Engineering Structures*, *151*, 540-553.

Ozcelik, O., Gundogan, M., & Kahraman, S. (2013). Modal parameter estimation of model steel bridge using system identification methods. *Technical Journal of Turkish Chamber of Civil Engineers, 405,* 6471-6478 (in Turkish).

Ozcelik, O., Misir, I. S., Amaddeo, C., Yucel, U., & Durmazgezer, E. (2015). Modal identification results of quasi-statically tested RC frames at different damage levels. In M. Mains, (Ed.), In *Topics in Modal Analysis, volume 10* (215-226). Cham: Springer.

Ozcelik, O., Yucel, U., & Durmazgezer, E. (2018) Modal parameter identification of progressively damaged reinforced concrete frames with various infill conditions. Ingegneria Sismica, *35* (4), 114-135.

Pahner, U. (1998). *A general design tool for the numerical optimisation of electromagnetic energy transducers*. Phd Thesis, Katholieke Universiteit Leuven, Leuven.

Papadimitriou, C. (2004). Optimal sensor placement methodology for parametric identification of structural systems. *Journal of Sound and Vibration*, *278* (4-5), 923-947.

Papadimitriou, C., Beck, J. L., & Au, S. K. (2000). Entropy-based optimal sensor location for structural model updating. *Journal of Vibration and Control*, *6* (5), 781-800.

Papadopoulos, M., & Garcia, E. (1998). Sensor placement methodologies for dynamic testing. *AIAA Journal*, *36* (2), 256-263.

Park, H. S., Kim, J., & Oh, B. K. (2019). Model updating method for damage detection of building structures under ambient excitation using modal participation ratio. *Measurement*, *133*, 251-261.

Park, S. (1997). *Development of a methodology to continuously monitor the safety of complex Structures*. Phd Thesis, Texas A & M University, College Station.

Park, S., Bolton, R. W., & Stubbs, N. (2006). Blind test results for nondestructive damage detection in a steel frame. *Journal of Structural Engineering*, *132* (5), 800-809.

Peeters, B. (2000). *System identification and damage detection in civil engineering*. Phd Thesis, Katholieke Universiteit Leuven, Leuven.

Peeters, B., & De Roeck, G. (2001). Stochastic system identification for operational modal analysis: a review. *Journal of Dynamic Systems, Measurement, and Control, 123* (4), 659-667.

Petersen, Ø. W., & Øiseth, O. (2017). Sensitivity-based finite element model updating of a pontoon bridge. *Engineering Structures*, *150*, 573-584.

Qureshi, Z. H., Ng, T. S., & Goodwin, G. C. (1980). Optimum experimental design for identification of distributed parameter systems. *International Journal of Control*, *31* (1), 21-29.

Rainieri, C., & Fabbrocino, G. (2014). *Operational modal analysis of civil engineering structures: an introduction and guide for applications.* New York: Springer.

Ramos, L. F., Lourenço, P. B., & Costa, A. C. (2005). Operational modal analysis for damage detection of a masonry construction. In *Proceedings of the 1st International Operational Modal Analysis Conference, April 26-27, Copenhagen, Denmark.* Retrieved June 30, 2020, from https://repositorium.sdum.uminho.pt/handle/1822/4958.

Ramos, L. F., Marques, L., Lourenço, P. B., De Roeck, G., Campos-Costa, A., & Roque, J. (2010). Monitoring historical masonry structures with operational modal analysis: two case studies. *Mechanical Systems and Signal Processing*, *24* (5), 1291-1305.

Reynders, E. (2012). System identification methods for (operational) modal analysis: review and comparison. *Archives of Computational Methods in Engineering*, *19* (1), 51-124.

Reynders, E., & De Roeck, G. (2010). A local flexibility method for vibration-based damage localization and quantification. *Journal of Sound and Vibration*, *329* (12), 2367-2383.

Reynders, E., Magalhaes, F., De Roeck, G., & Cunha, A. (2009). Merging strategies for multi-setup operational modal analysis: application to the Luiz I steel arch bridge. In *Proceedings of IMAC-XXVII, February 9-12, Orlando, Florida.* Retrieved June 30, 2020, from https://www.academia.edu/17375367.

RILEM MDT.D.5 (2004). In-situ stress-strain behavior tests based on the flat jack. *Materials and Structures, 37,* 497-501.

Rytter, A. (1993). *Vibration based inspection of civil engineering structures*. Phd Thesis, Aalborg University, Denmark.

Shi, Z. Y., & Law, S. S. (1998). Structural damage localization from modal strain energy change. *Journal of Sound and Vibration*, *218* (5), 825-844.

Simoen, E., De Roeck, G., & Lombaert, G. (2015). Dealing with uncertainty in model updating for damage assessment: A review. *Mechanical Systems and Signal Processing*, *56-57*, 123-149.

Sohn, H., & Law, K. H. (1997). A Bayesian probabilistic approach for structure damage detection. *Earthquake Engineering & Structural Dynamics*, *26* (12)*,* 1259-1281.

Sohn, H., Farrar, C. R., Hemez, F. M., Shunk, D. D., Stinemates, D. W., Nadler, B. R., & Czarnecki, J. J. (2003). *A review of structural health monitoring literature: 1996-2001.* Report No: LA-13976-MS, Los Alamos National Laboratory, USA.

Song, M., Moaveni, B., Papadimitriou, C., & Stavridis, A. (2019). Accounting for amplitude of excitation in model updating through a hierarchical Bayesian approach: Application to a two-story reinforced concrete building. *Mechanical Systems and Signal Processing*, *123*, 68-83.

Stubbs, N., Kim, J. T., & Tople, K. (1992). An efficient and robust algorithm for damage localization in offshore platforms. In *Proceedings of the ASCE 10th Structures Congress*, *April 13-15, San Antonio, Texas,* 543-546.

Stubbs, N., Park, S., Sikorsky, C., & Choi, S. (2000). A global non-destructive damage assessment methodology for civil engineering structures. *International Journal of Systems Science*, *31* (11), 1361-1373.

Suykens, J. A. K., & Vandewalle, J. (2002). Coupled local minimizers: alternative formulations and extensions. In *Proceedings of the 2002 World Congress on Computational Intelligence - International Joint Conference on Neural Networks IJCNN'02*, *May 12-17, Honolulu, USA,* 2039-2043.

Suykens, J. A. K., Vandewalle, J., & De Moor, B. (2001). Intelligence and cooperative search by coupled local minimizers. *International Journal of Bifurcation and Chaos*, *11* (08), 2133-2144.

Teughels, A. (2003). *Inverse modelling of civil engineering structures based on operational modal data.* Phd Thesis, Katholieke Universiteit Leuven, Leuven.

Teughels, A., De Roeck, G., & Suykens, J. A. (2003). Global optimization by coupled local minimizers and its application to FE model updating. *Computers & Structures*, *81* (24-25), 2337-2351.

Teughels, A., & De Roeck, G. (2004). Structural damage identification of the highway bridge Z24 by FE model updating. *Journal of Sound and Vibration*, *278* (3), 589-610.

Thoen, B. K., & Laplace, P. N. (2004). Offline tuning of shaking tables. In *Proceedings of the 13th World Conference on Earthquake Engineering, August 1-6, Vancouver, Canada.* Retrieved June 30, 2020, from https://www.iitk.ac.in/nicee/wcee/article/13_960.pdf.

Titurus, B., & Friswell, M. I. (2008). Regularization in model updating. *International Journal for Numerical Methods in Engineering*, *75* (4), 440-478.

Torres, W., Almazán, J. L., Sandoval, C., & Boroschek, R. (2017). Operational modal analysis and FE model updating of the Metropolitan Cathedral of Santiago, Chile. *Engineering Structures*, *143*, 169-188.

Twitchell, B. S., & Symans, M. D. (2003). Analytical modeling, system identification, and tracking performance of uniaxial seismic simulators. *Journal of Engineering Mechanics, 129* (12), 1485-1488.

Udwadia, F. E. (1994). Methodology for optimum sensor locations for parameter identification in dynamic systems. *Journal of Engineering Mechanics*, *120* (2), 368-390.

Van Overschee, P., & De Moor, B. L. (1996). *Subspace identification for linear systems.* Dordrecht: Kluwer Academic Publishers.

Weber, B., Paultre, P., & Proulx, J. (2007). Structural damage detection using nonlinear parameter identification with Tikhonov regularization. *Structural Control and Health Monitoring*, *14* (3), 406-427.

Weber, B., Paultre, P., & Proulx, J. (2009). Consistent regularization of nonlinear model updating for damage identification. *Mechanical Systems and Signal Processing*, *23* (6), 1965-1985.

Yang, Y. B., & Chen, Y. J. (2009). A new direct method for updating structural models based on measured modal data. *Engineering Structures, 31* (1), 32-42.

Yao, L., Sethares, W. A., & Kammer, D. C. (1993). Sensor placement for on-orbit modal identification via a genetic algorithm. *AIAA Journal*, *31* (10), 1922-1928.

Yi, T. H., Li, H. N., & Zhang, X. D. (2012). Sensor placement on Canton Tower for health monitoring using asynchronous-climb monkey algorithm. *Smart Materials and Structures*, *21* (12), 125023.

Yucel, U. (2014). *Developing offline-tuning technique to be used for damage level assessment of a model frame type structure and application of system identification methods*. MSc Thesis, Dokuz Eylül University, İzmir.

Yuen, K. V., & Kuok, S. C. (2015). Efficient Bayesian sensor placement algorithm for structural identification: a general approach for multi-type sensory systems. *Earthquake Engineering & Structural Dynamics*, *44* (5), 757-774.

Zhang, G., Ma, J., Chen, Z., & Wang, R. (2014). Automated eigensystem realisation algorithm for operational modal analysis. *Journal of Sound and Vibration*, *333* (15), 3550-3563.

Zhang, J., Maes, K., De Roeck, G., Reynders, E., Papadimitriou, C., & Lombaert, G. (2017). Optimal sensor placement for multi-setup modal analysis of structures. *Journal of Sound and Vibration*, *401*, 214-232.

APPENDICES

APPENDIX-1: List of Symbols

Chapter Two

$\mathbf{y}(t)$	Dynamic response, Response of a system
$\mathbf{A}$	True mode shapes matrix, State matrix of the state-space model, Mode shape matrix (modal matrix)
$\mathbf{q}(t)$	True modal coordinates vector, Modal coordinates
$\hat{\mathbf{A}}$	Estimated modal matrix
$\hat{\mathbf{q}}(t)$	Estimated modal coordinates
$\hat{\mathbf{A}}^{+}$	Pseudo inverse of $\hat{\mathbf{A}}$
$\mathbf{I}$	Identity matrix
V	Value of the sensor placement
$\mathbf{a}$	True mode shape
$\hat{\mathbf{a}}$	Each of the estimated mode shapes in $\hat{\mathbf{A}}$
$\{X_i\}$	Random vector
σ	Standard deviation
a_i	Elements of the true mode shape $\mathbf{a}$
ε	Relative uncertainty parameter
D	Number of test setups
N_{ref}	Common (overlapping) set of DOFs (reference sensors)
N_{rov}	Remaining (non-overlapping) set of DOFs (roving sensors)
$\{\phi^{k}_{ref,i}\}$	Partitions of the k^{th} mode shape estimated from the i^{th} setup at N_{ref}
$\alpha^{k}_{1,i}$	Scaling factor

$\{\phi^k\}$	Total (merged) mode shape
ξ	Modal damping factor
f_{min}	Lowest vibration frequency value in Hz
T	Measurement duration in seconds
$\mathrm{y}(\mathrm{n})$	Filtered signal
$\mathrm{a}(\mathrm{k})$	Filter coefficients
na	Number of filter coefficients
$\mathrm{x}(\mathrm{n})$	Input to the filter
f_1, f_2	Filter cut-off frequencies
$\mathbf{M}$	Mass matrix
$\mathbf{C}$	Damping matrix
$\mathbf{K}$	Stiffness matrix
$\mathbf{x}(\mathrm{t})$	Displacement vector
$\dot{\mathbf{x}}(\mathrm{t})$	Velocity vector
$\ddot{\mathbf{x}}(\mathrm{t})$	Acceleration vector
$\mathbf{f}(\mathrm{t})$	Externally applied force vector
$\mathbf{X}(\mathrm{t})$	Displacement stochastic vector process
$\dot{\mathbf{X}}(\mathrm{t})$	Velocity stochastic vector process
$\ddot{\mathbf{X}}(\mathrm{t})$	Acceleration stochastic vector process
$\mathbf{F}(\mathrm{t})$	Stochastic excitation vector process
$\mathrm{X}_{\mathrm{i}}(\mathrm{s})$	Reference scalar response process
$E[.]$	Expectation operator
$\mathbf{R}(.)$	Correlation function vector

$\mathbf{u}(k)$	Vector of system inputs
$\mathbf{x}(k)$	Vector of states
$\mathbf{y}(k)$	Vector of system outputs, Output measurement responses in time domain, Free decay
$\mathbf{B}$	Input matrix of the state-space model
$\mathbf{C}$	Output matrix of the state-space model
$\mathbf{D}$	Feed-through matrix of the state-space model
$\mathbf{H}(k)$	Hankel matrix
$\mathbf{Y}(k)$	Impulse response vector
N	Number of sensors
s	Number of rows in the Hankel matrix
m	Number of columns in the Hankel matrix
$\mathbf{R}$	Left eigenvectors of $\mathbf{H}(0)$
$\mathbf{S}$	Right eigenvectors of $\mathbf{H}(0)$
$\mathbf{\Sigma}$	Diagonal matrix of singular values
g	System order
$\mathbf{\Lambda}$	Eigenvalues of the matrix $\mathbf{A}$
ω_i	Vibration frequencies
ξ_i	Damping ratios
N_s	Number of modes
Δt	Sampling period
ϕ_i	Mode shapes
$\mathbf{\Gamma}$	Eigenvectors of the matrix $\mathbf{A}$, Observability matrix
$\mathbf{R}_q(\tau)$	Correlation function matrix of the modal coordinates

$\mathbf{R}_y(\tau)$	Correlation function matrix of $\mathbf{y}(t)$
$\mathbf{G}_y(f)$	Spectral density matrix of $\mathbf{y}(t)$
$\mathbf{G}_q(f)$	Spectral density matrix of $\mathbf{q}(t)$
$\mathbf{a}_n$	Mode shapes
Υ_n	Modal participation vectors
λ_n	Poles
c_n	A positive constant
$\mathbf{Z}$	Diagonal matrix holding the singular values z_n^2 (auto-spectral densities of the modal coordinates)
$\mathbf{U}$	Singular vector
$\mathbf{P}$	Observation matrix
$\mathbf{G}$	Discrete time system matrix
$\mathbf{u}_0$	State-space initial conditions of the free decay
np	Number of data points
$\mathbf{H}_1$	Upper part of the Hankel matrix (the past)
$\mathbf{H}_2$	Lower part of the Hankel matrix (the future)
$\mathbf{O}$	Projection matrix
$\mathbf{T}_{21}$, $\mathbf{T}_{11}$	Block Toeplitz matrices
$\mathbf{X}$	Matrix of Kalman states
$\mathbf{W}_1$, $\mathbf{W}_2$	Real-valued weight matrices

Chapter Three

$\mathbf{p}_k$	Unknown model parameter set
$\mathbf{p}_0$	Initial values of the model parameter set

$\mathbf{r}$, $\mathbf{r}(\mathbf{p})$	Residual vector
$z(\mathbf{p}_k)$	Numerically obtained quantities
$\tilde{z}$	Experimentally obtained quantities
$\mathbf{J}_{\mathbf{P}_k}$, $\mathbf{J}_{\mathbf{P}}$	Sensitivity (Jacobian) matrix
$\mathbf{p}_{k+1}$	Updated model parameter values
$\mathbf{p}$	Design variables
n	Number of design variables, Number of damage functions
$z_j(\mathbf{p})$	Numerically obtained modal quantities
$\tilde{z}_j$	Experimentally obtained modal quantities
r_j	Residuals
m	Number of residuals
$\mathbf{l}_b$	Lower bounds (constraints)
$\mathbf{u}_b$	Upper bounds (constraints)
$\mathbf{r}_f(\mathbf{p})$	Frequency (eigenfrequency) residuals
$\mathbf{r}_s(\mathbf{p})$	Mode shape residuals
$\|.\|$	Euclidean norm
m_f	Number of eigenfrequencies
m_s	Number of modal displacements
ϕ_i	Numerical modal vectors
$\bar{\phi}_j$	Experimental modal vectors
θ	Angle between modal vectors
λ_i , $\lambda_j(\mathbf{p})$	Numerical eigenvalues
$\bar{\lambda}_j$	Experimental eigenvalues
f_j	Eigenfrequency
ϕ_j	Numerical modal vector
$\tilde{\phi}_j$	Experimental modal vector

ϕ_j^l	l^{th} (any arbitrary) component of vector ϕ_j
ϕ_j^{ref}	Reference component of vector ϕ_j
$ndof_j$	Number of DOFs used for mode ϕ_j
N_{mode}	Number of considered modes
$\mathbf{W}$	Weighting matrix
w_j	Weighting factor of r_j
X^e	Value of a physical parameter X in element e
X_{ref}^e	Reference value of X^e
a_X^e, a^e, $\mathbf{a}$	Dimensionless correction factor
$\mathbf{K}^e$	Updated element stiffness matrix
$\mathbf{K}_{ref}^e$	Reference element stiffness matrix
$\mathbf{K}$	Global system stiffness matrix
$\mathbf{K}^U$	Stiffness matrix of the non-updated elements
n_e	Number of elements wanted to be updated
p_i, $\boldsymbol{p}$	Multiplication factors
N_i, $\mathbf{N}$	Damage function
x^e	Geometrical coordinate of the center of element e
$\mathbf{M}$	System mass matrix
d	Order of the analytical model
$\mathbf{F}_j^e$	Nodal forces
$\Delta\mathbf{p}$	Sufficiently small design parameter step
D_j	Detectability index
$\mathbf{S}_j$	j^{th} column vector of the sensitivity matrix
$f(\mathbf{p}_k)$	Function to be minimized (objective function)
$q_k(\mathbf{z})$	Quadratic model of truncated Taylor series
$\mathbf{z}$	Step vector from $\mathbf{p}_k$
$\nabla f(\mathbf{p}_k)$	Gradient of the objective function

$\nabla^2 f(\mathbf{p}_k)$	Hessian of the objective function
$\mathbf{p}^*$	Local solution
$\mathbf{z}_k$	Search direction
α_k	Step length (distance to move along $\mathbf{z}_k$)
m_k	Model function
Δ	Radius of the trust region

Chapter Four

f_i, f_j	Identified frequencies for models of successive orders *i* and *j*
ξ_i, ξ_j	Damping ratios for models of successive orders *i* and *j*
ϕ_i, ϕ_j	Mode shapes for models of successive orders *i* and *j*
MAC_{ϕ_i,ϕ_j}	Modal assurance criteria calculated between ϕ_i and ϕ_j
$\oplus$	A pole with stable frequency, damping, and mode shape
.d	A pole with stable frequency and damping
.v	A pole with stable frequency and mode shape
.f	A pole with stable frequency only
ω	Vibration frequency
ξ	Damping ratio
SD_i^j	Stiffness degradation
f_{ND}^j, $f_{D,i}^j$	Identified frequencies for a particular frame *j* at the undamaged and various damaged levels *i*, respectively

Chapter Five

$\mathbf{l_b}$, $\mathbf{u_b}$	Constraints for the design variables
$\mathbf{r}$	Residual vector
$\mathbf{r}_f$	Frequency residuals
$\mathbf{r}_s$	Mode shape residuals
$\mathbf{J_P}$	Jacobian matrix

Chapter Six

ρ	Mass density
E	Young's modulus
υ	Poisson's ratio
K_X, K_Y, K_Z	Translational springs in global X, Y, and Z directions, respectively
$\{R_e\}$	Response vector obtained from the experimental data
$\{R_a\}$	Response vector of the numerical model for a given state $\{P_o\}$ of the model parameter values
$\{P_u\}$	Vector of the updated model parameter values
$[S]$	Sensitivity matrix
$\{\Delta R\}$	Difference vector calculated between $\{R_e\}$ and $\{R_a\}$ response vectors
$\{\Delta P\}$	Parameter variation
$[S]^+$	Pseudo-inverse of the sensitivity matrix
$[C_R]$, $[C_P]$	Diagonal weighting matrices representing the confidence in responses and model parameters, respectively
$[G]$	Gain matrix
σ	Standard deviation of the considered model parameter or response
μ	Mean of the considered model parameter or response

APPENDIX-2: Publications

Some of the material in this thesis was included in article and/or conference papers as follows:

Durmazgezer, E., Yucel, U., & Ozcelik, O. (2018). Damage identification studies of a reinforced concrete portal frame by sensitivity-based finite element model updating method. In *Proceedings of the 13th International Congress on Advances in Civil Engineering*, *September 12-14, Izmir, Turkey,* 1-9.

Durmazgezer, E., Yucel, U., & Ozcelik, O. (2019). Damage identification of a reinforced concrete frame at increasing damage levels by sensitivity-based finite element model updating. *Bulletin of Earthquake Engineering*, *17* (11), 6041-6060.

Mısır, İ. S., Özçelik, Ö., Durmazgezer, E., Yücel, U., Amaddeo, C., Kuran, F., Tuna, E., Yücel, G., & Youssouf, I. B. (2017). Tarihi yığma binaları oluşturan üç tabakalı taş yığma duvarların düzlem dışı etkilere göre model kalibrasyonu: İsabey Camii örneği. *Uluslararası Katılımlı 6. Tarihi Yapıların Korunması ve Güçlendirilmesi Sempozyumu, 2-4 Kasım, Trabzon, Türkiye*, 483-492 (in Turkish).

Ozcelik, O., Misir, I. S., Amaddeo, C., Yucel, U., & Durmazgezer, E. (2015). Modal identification results of quasi-statically tested RC frames at different damage levels. In M. Mains, (Ed.), In *Topics in Modal Analysis, volume 10* (215-226). Cham: Springer.

Ozcelik, O., Misir, I. S., Yucel, U., Girgin, O., Durmazgezer, E., Amaddeo, C., Kuran, F., Tuna, E., Yucel, G., & Youssouf, I. B. (2018). Model updating studies of a masonry courtyard wall of Isabey Mosque using out-of-plane ambient vibration measurements. In *Proceedings of the 13th International Congress on Advances in Civil Engineering*, *September 12-14, Izmir, Turkey,* 1-8.

Ozcelik, O., Yucel, U., & Durmazgezer, E. (2018). Modal parameter identification of progressively damaged reinforced concrete frames with various infill conditions. *Ingegneria Sismica*, *35* (4), 114-135.

Özçelik, Ö., Amaddeo, C., Mısır, İ. S., Durmazgezer, E., & Yücel, U. (2015). Modal identification results of RC frames at different damage levels. In *Proceedings of the Third Conference on Smart Monitoring, Assessment and Rehabilitation of Civil Structures, September 7-9, Antalya, Turkey.* Retrieved June 30, 2020, from https://data.smar-conferences.org/SMAR_2015_Proceedings/papers/80.pdf.

Özçelik, Ö., Mısır, İ. S., Amaddeo, C., Yücel, U., & Durmazgezer, E. (2015). Betonarme çerçevelerin farklı hasar seviyelerindeki modal parametre tahmin sonuçları. *Ulusal Yapı Mekaniği Laboratuvarları Toplantısı*, *29-30 Mayıs, Kayseri, Türkiye*, 73-74 (in Turkish).